

AN EXPERIMENTAL INVESTIGATION
OF A RESONANCE MECHANISM
IN A TWO-DIMENSIONAL
TURBULENT JET

By

KOMBUPALAYAM MALAYANAN KUMARAVEL PRAKASH

Bachelor of Engineering

Anna University

Madras, India

1984

Submitted to the Faculty of the Graduate College
of the Oklahoma State University
in partial fulfillment of the requirements
for the Degree of
MASTER OF SCIENCE
July, 1986

Thesis
1986
P893e
Cp 2



AN EXPERIMENTAL INVESTIGATION
OF A RESONANCE MECHANISM
IN A TWO-DIMENSIONAL
TURBULENT JET

Thesis Approved:

Flint O. Thomas

Thesis Adviser

A. J. Ghajar

P. M. Morelli

Norman N. Durham

Dean of the Graduate College

1259941

PREFACE

I wish to thank the faculty members in the Mechanical and Aerospace Engineering Department at Oklahoma State University who have helped me to further my education.

I am deeply indebted to my advisor, Dr. F. O. Thomas for all the guidance and encouragement he has given me throughout my academic curriculum. I also thank him for involving me in the NSF project and giving me a chance to do experimental oriented investigation work which I had always wanted to do. Besides, I also thank him for helping me analyze the experimental measurements and in writing the thesis material. He has extended such help irrespective of time and place in all matters and I am very grateful for that. I also thank him for helping me to get financial assistance which helped me in my studies to a great extent.

My thanks go to Mr. Ron Delahoussaye and Mr. K. S. Suresh Rao for their graphics package which helped me in analyzing much of the experimental data. My deep appreciation also goes to Sankaran Mohan for his timely assistance and to Mrs. Daleene Caldwell for typing and coordinating the final draft of my thesis.

I also thank my father and mother, Mr. and Mrs. Malayanan and my sisters, Rani and Jayanthi, for their continued moral support which helped me to attain what I have looked forward to in my academic career at Oklahoma State University.

TABLE OF CONTENTS

Chapter	Page
I. INTRODUCTION	1
II. MEASUREMENT APPARATUS AND FLOWFIELD	6
III. BASIC FLOW DEVELOPMENT	10
3.1. Mean Flow Development	10
3.2. Longitudinal Velocity Fluctuation	21
IV. EXPERIMENTAL INVESTIGATION OF JET DEVELOPMENT	29
4.1. Spectral Measurement Techniques	29
4.1.1. Linear Region	30
4.1.2. Nonlinear Transition Region	40
4.2. Longitudinal Space-Time Correlations	71
4.3. Spectral Coherence and Phase Angle Measurements	100
V. EVIDENCE OF FEEDBACK	140
5.1. Global Resonance Model	140
5.2. Comparison of Global Resonance Model Predictions with Experiment	147
5.3. Conclusions	151
5.4. Recommendations	152
REFERENCES	154
APPENDICES	157
APPENDIX A - COMPUTER PROGRAM LISTINGS	158
APPENDIX B - UNCERTAINTY ANALYSIS	177

LIST OF TABLES

Table	Page
I. Mean Flow Properties for Planar Jets	20
II. Measurements of Linear Amplification in Free Shear Layers	33

LIST OF FIGURES

Figure	Page
1. Two-Dimensional Jet	2
2. Schematic of Experimental Arrangement	7
3. Mean Flow Velocity Profile at $x/D = 0.25, 0.5$ and 1.0	11
4. Mean Flow Velocity Profile at $x/D = 1.5, 2$ and 3.0	12
5. Mean Flow Velocity Profile at $x/D = 4, 5$ and 7.0	13
6. Mean Flow Velocity Profile at $x/D = 7, 9$ and 11.0	14
7. Mean Flow Velocity Profile at $x/D = 13, 15, 17$ and 20	15
8. Comparison of Actual Data With Hyperbolic Tangent Profile	16
9. Jet Widening	17
10. Mean Velocity Decay	19
11. Longitudinal Fluctuation Intensity Profile at $x/D = 0.25, 0.5$ and 1.0	22
12. Longitudinal Fluctuation Intensity Profile at $x/D = 1.5, 2.0$ and 3.0	23
13. Longitudinal Fluctuation Intensity Profile at $x/D = 4, 5$ and 7.0	24
14. Longitudinal Fluctuation Intensity Profile at $x/D = 7, 9$ and 11.0	25
15. Longitudinal Fluctuation Intensity Profile at $x/D = 1, 15, 17$ and 20	26
16. Longitudinal Fluctuation Intensity Variation with x/D (Linear Ordinate)	27
17. Longitudinal Fluctuation Intensity Variation with x/D (Logarithmic Ordinate)	28
18. Comparison of Michalke's Theory With Experimental Data	32

Figure	Page
19. Growth and Decay of the Most Amplified Fundamental Instability Wave (Bandwidth of 10 Hz)	33
20. Growth of Shear Layer Thickness	35
21. Power Spectrum at $x/D = 0.25$	37
22. Amplitude Variation of Low Frequency Mode near 20 Hz (Bandwidth of 5 Hz) Across the Jet	38
23. Shear Layer Power Spectra at $x/D = 1.0$ and 1.25	41
24. Shear Layer Power Spectra at $x/D = 1.25$ and 1.5	42
25. Shear Layer Power Spectra at $x/D = 1.5$ and 1.75	43
26. Shear Layer Power Spectra from a Different Trial at $x/D = 1.25$ and 1.50	45
27. Shear Layer Power Spectra from a Different Trial at $x/D = 1.5$ and 1.75	46
28. Shear Layer Power Spectrum at $x/D = 2.00$	48
29. Shear Layer Power Spectrum at $x/D = 2.25$	49
30. Comparison of the Growth of ≈ 750 Hz (Bandwidth 10 Hz) and ≈ 250 Hz (Bandwidth 10 Hz) at the Shear Layer	51
31. Growth and Decay of ≈ 250 Hz (Bandwidth 10 Hz) and 125 Hz (Bandwidth 10 Hz) at the Shear Layer	52
32. Shear Layer Power Spectra at $x/D = 2$ and 3.0	53
33. Shear Layer Power Spectra at $x/D = 3$ and 4.5	54
34. Shear Layer Power Spectrum at $x/D = 6$	55
35. Shear Layer Power Spectrum at $x/D = 7$	56
36. Shear Layer Power Spectrum at $x/D = 8$	57
37. Shear Layer Power Spectrum at $x/D = 9$	59
38. Shear Layer Power Spectrum at $x/D = 10$	60
39. Shear Layer Power Spectrum at $x/D = 12$	61
40. Shear Layer Power Spectrum at $x/D = 20$	62
41. Centerline Power Spectrum at $x/D = 2.0$	63

Figure	Page
42. Centerline Power Spectrum at $x/D = 3.0$	64
43. Centerline Power Spectrum at $x/D = 4.0$	65
44. Centerline Power Spectrum at $x/D = 5.0$	66
45. Centerline Power Spectrum at $x/D = 6.0$	67
46. Centerline Power Spectra at $x/D = 7, 8, 9$ and 10	68
47. Centerline Power Spectrum at $x/D = 12.0$	69
48. Centerline Power Spectrum at $x/D = 20.0$	70
49. Probe Arrangement for Space-Time Correlation Measurements . .	72
50. Space-Time Correlation Function at $x/D = 25.0$	74
51. Space-Time Correlation Function at $x/D = 0.25$	76
52. Space-Time Correlation Function at $x/D = 0.5$	77
53. Space-Time Correlation Function at $x/D = 0.75$	78
54. Space-Time Correlation Function at $x/D = 1.0$	79
55. Space-Time Correlation Function at $x/D = 2.0$	81
56. Space-Time Correlation Function at $x/D = 2.5$	82
57. Space-Time Correlation Function at $x/D = 3.0$	83
58. Space-Time Correlation Function at $x/D = 4.0$	84
59. Space-Time Correlation Function at $x/D = 5.0$	85
60. Space-Time Correlation Function at $x/D = 6.0$	86
61. Comparison of Correlation Function at $x/D = 7.0$ and 8.0 . . .	88
62. Comparison of Correlation Function at $x/D = 8.0$ and 9.0 . . .	89
63. Comparison of Correlation Function at $x/D = 9.0$ and 10.0 . . .	90
64. Space-Time Correlation Function at $x/D = 12.0$	91
65. Space-Time Correlation Function at $x/D = 14.0$	92
66. Space-Time Correlation Function at $x/D = 16.0$	93
67. Space-Time Correlation Function at $x/D = 17.0$	94

Figure	Page
68. Space-Time Correlation Function at $x/D = 18.0$	95
69. Space-Time Correlation Function at $x/D = 20.0$	96
70. Space-Time Correlation Function at $x/D = 40.0$	97
71. Space-Time Correlation Function at $x/D = 60.0$	98
72. Correlation Coefficient at Zero Time Delay with Downstream Distance	99
73. Probe Arrangement for Coherence Measurements	102
74. Frequency of Maximum Coherence with Downstream Distance . . .	104
75. Variation of Coherence of the Mode Near 250 Hz (Bandwidth 10 Hz) with Downstream Distance	105
76. Variation of Coherence of the Mode Near 125 Hz (Bandwidth 10 Hz) with Downstream Distance	107
77. Variation of Coherence of the Mode Near 60 Hz (Bandwidth 10 Hz) with Downstream Distance	108
78. Variation of Coherence of the Mode Near 20 Hz (Bandwidth 10 Hz) with Downstream Distance	109
79. Comparison of Coherence Measurements of the Set: Probes Placed Side by Side at $x/D = 8.0$ with the Set: One Probe Fixed at Nozzle Exit, the Other Probe Placed at $x/D = 8.0$	111
80. Comparison of Coherence Measurements of the Set: Probes Placed Side by Side at $x/D = 16.0$ with the Set: One Probe Fixed at Nozzle Exit, the Other Probe Placed at $x/D = 16.0$	112
81. Coherence Spectrum at $x/D = 0.25$	114
82. Coherence Spectrum at $x/D = 0.5$	115
83. Coherence Spectrum at $x/D = 1.0$	117
84. Coherence Spectrum at $x/D = 1.5$	118
85. Phase Spectrum at $x/D = 0.25$	119
86. Phase Spectrum at $x/D = 0.5$	120
87. Phase Spectrum at $x/D = 1.0$	121
88. Phase Spectrum at $x/D = 1.5$	122

Figure	Page
89. Space-Time Correlation of the Two Signals Presented in Equations 4-3.4 and 4-3.5	124
90. Coherence Spectrum at $x/D = 2.0$	125
91. Coherence Spectrum at $x/D = 2.5$	127
92. Coherence Spectrum at $x/D = 3.0$	128
93. Coherence Spectrum at $x/D = 4.0$	129
94. Coherence Spectrum at $x/D = 5.0$	130
95. Phase Spectrum at $x/D = 2.5$	131
96. Phase Spectrum at $x/D = 3.0$	132
97. Phase Spectrum at $x/D = 4.0$	133
98. Variation of Coherence of the Mode Near 20 Hz (Bandwidth 10 Hz) with Downstream Distance (Both Probes Set Side By Side)	134
99. Variation of Coherence of the Mode Near 60 Hz (Bandwidth 10 Hz) with Downstream Distance (Both Probes Set Side By Side)	135
100. Variation of Coherence of the Mode Near 125 Hz (Bandwidth 10 Hz) with Downstream Distance (Both Probes Set Side By Side)	136
101. Variation of Coherence of the Mode Near 250 Hz (Bandwidth 10 Hz) with Downstream Distance (Both Probes Set Side By Side)	137
102. Variation of Momentum Thickness with Downstream Distance . . .	139
103. Schematic of Structural Patterns in the Flow	143
104. Geometrical Representation of the Shear Layer and the Potential Core Regions	146
105. Comparison of Theoretically Predicted Frequencies and Locations for Structural Events with Experimentally Measured Coherence Based Values	150

NOMENCLATURE

A	constant in equation (2-1)
$A_1(t)$	modelled anemometer signal
$A_2(t)$	modelled anemometer signal
a	acoustic speed
a_1	amplitude (power spectral density) of 20 Hz
a_2	amplitude (power spectral density) of 60 Hz
B	constant in equation (2-1)
b	mean velocity half-width
C_1	geometric virtual origin in equation (3-1)
C_2	kinematic virtual origin
C_{xy}	coincident spectral density
D	nozzle slot width
E	mean hot-wire voltage signal
f	frequency
f_{res}	resonance frequency
f_{pc}	structural passage frequency at the end of potential core
f_i	structural passage frequency associated with the i^{th} event
f_{res_i}	resonance frequency for the i^{th} structural event
f_{max}	highest frequency expected in the data
G_{xy}	cross spectrum function of signals $x(t)$ and $y(t)$
G_x	power spectral density function of signal $x(t)$
G_y	power spectral density function of signal $y(t)$
H	shape factor

K	$U_c/U_m \approx 0.6$
K_1	jet widening rate
K_2	mean velocity decay rate
N	integer
Q_{xy}	quadrature spectral density
R_u	correlation function
Re_{δ^*}	Reynolds number based on displacement thickness
Re_{δ^*crit}	critical Reynolds number based on displacement thickness
St	Strouhal number
t	time variable
T	correlation function time period
U	mean longitudinal velocity
U_c	average mean velocity across the shear layer
U_m	local centerline mean velocity
U_o	nozzle unit mean velocity
u	instantaneous longitudinal velocity
v	instantaneous lateral velocity
x	longitudinal spatial co-ordinate
x_0	streamwise near exit location for the feedback node
x_i	downstream location for the i^{th} structural event
x_{pc}	length of potential core
y	lateral spatial co-ordinate
z	vertical spatial co-ordinate
η	Ratio of lateral spatial co-ordinate to the maximum slope shear layer thickness
δ	maximum slope shear layer thickness
β	dimensionless frequency ($\frac{2\pi f\delta}{U}$)

$-\alpha_i$	spatial amplification rate
θ	momentum thickness of free shear layer
Δy	lateral flapping amplitude
τ	time delay
ρ	correlation coefficient
γ_{xy}	spectral coherence
ϕ_{xy}	phase angle spectrum
α	jet half angle
Δt	sampling time
ω_1	angular frequency corresponding to 20 Hz
ω_2	angular frequency corresponding to 60 Hz

CHAPTER I

INTRODUCTION

A schematic of the two-dimensional turbulent jet flow field along with the relevant co-ordinate system is shown in Figure 1. The flow field may be conveniently divided into three primary regions; the initial region, the interaction region and the similarity region. The initial region consists of two free shear layers originating at each of the nozzle lips that bound a core of irrotational fluid known as the potential core. The shear layers widen with downstream distance and approximately six to seven nozzle widths ($x/D = 6-7$) downstream they engulf the potential core. The resulting interaction region consists of that part of the flow in which the interacting shear layers adjust to one another and a condition of dynamic equilibrium is approached. This region extends approximately to twenty slot widths ($x/D = 20$) downstream. For $x/D > 20$ the flow exhibits self-similar behavior such that the velocity profiles when scaled with appropriate velocity and length scales all collapse to a single profile shape. The appropriate velocity scale is the local mean centerline velocity, U_m , and the length scale is the local mean velocity half-width, b . This is the lateral distance required for the mean velocity to fall to one-half its local centerline value.

Traditionally turbulent flows have been viewed as essentially random processes, which could only be described statistically.

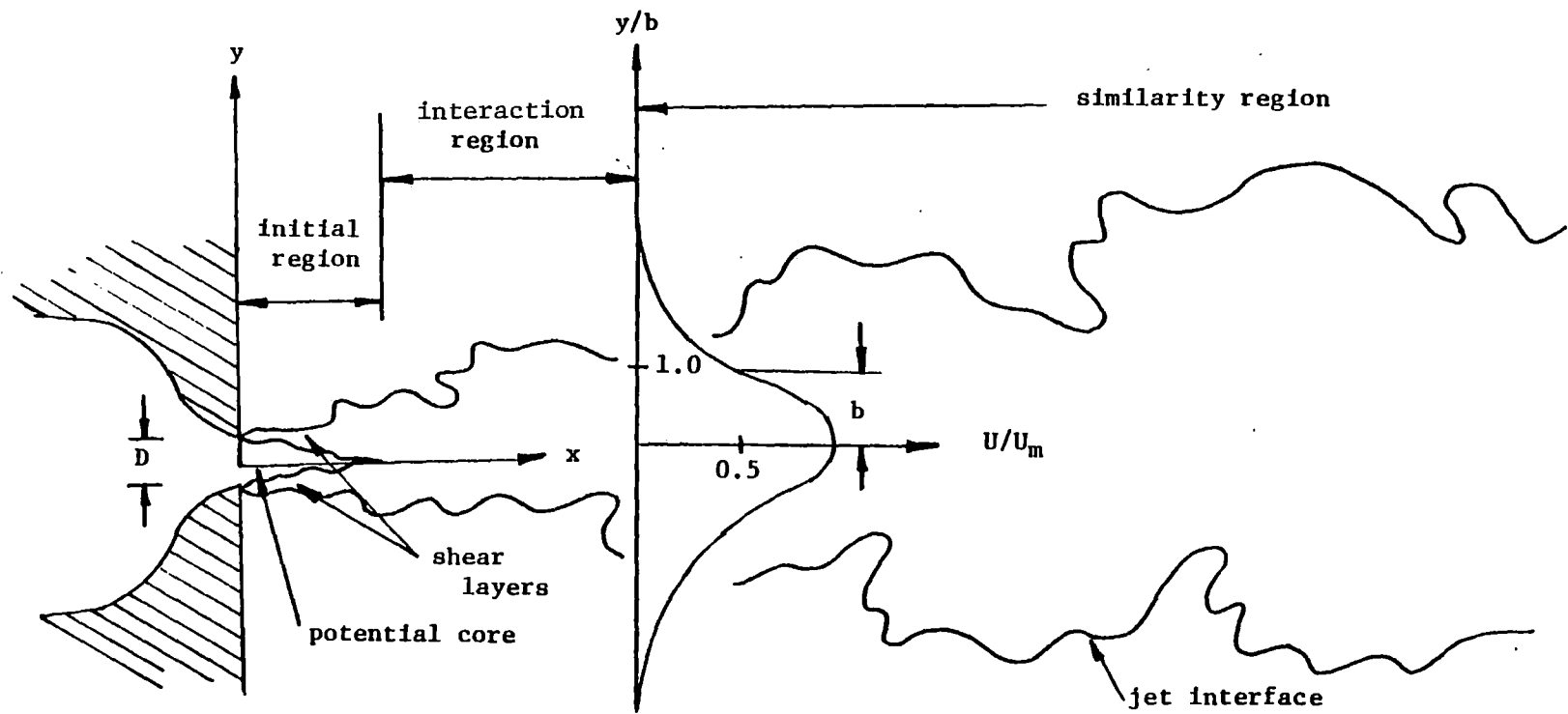


Figure 1. Two-Dimensional Jet

Recently, however, a number of studies have suggested the presence of large-scale quasi periodic vortex structures in many turbulent shear flows. The dynamics of such "coherent structures", as they are often called, seems likely to play an important role in the transport of mass, momentum and heat as well as in the generation of aerodynamic noise. Hence, they have recently received much attention from researchers.

Brown and Roshko (1974), Browand and Weidmann (1976) and Dimotakis and Brown (1976) confirmed that large scale coherent structures were indeed intrinsic features of turbulent mixing layers at high Reynolds numbers. In fact, Winant and Browand (1974) showed that the pairing of coherent structures in the mixing layer is directly responsible for its widening.

Lau, Fisher and Fuchs (1972) performed an experimental study in the initial region of a turbulent axisymmetric jet. Velocity fluctuation measurements were obtained in both the potential core and entrainment regions of the jet. It was felt that events occurring in the mixing region induced corresponding fluctuations in the entrainment region and potential core. In this manner the fluctuations due to the coherent structure in the developing jet mixing layer could be inferred without the high levels of turbulence that tend to obscure the signal there. The result of their study was a strong indication of the existence of coherent underlying motion in the jet. Lau and Fisher (1975) using wave reduction techniques and H. H. Bruun (1977) using flow visualization techniques provided conclusive evidence as to the presence of large-scale toroidal structures in the initial region of the round jet. The influence of such structures on aerodynamic noise generation was studied by C. T. Moore (1976) and Kibens (1979). It was found that the

frequencies of the far field jet noise corresponded exactly to the vortex formation frequencies in the flow field. Despite rather thorough investigation in the initial region, comparatively little work has been done on determining the form of the coherent structures in the similarity region of an axisymmetric jet. This is largely due to the high degree of phase randomization which makes large-scale structure detection very difficult.

The strongest indication of the existence of large-scale structure in planar jets is the so called "flapping phenomenon" which has been noted by Bradshaw and Goldschmidt (1973), Weir and Bradshaw (1975) and Cervantes and Goldschmidt (1981). This involves the negative instantaneous correlation of longitudinal velocity fluctuations from probes located laterally on opposite side of the jet centerline. Early studies of this phenomenon suggested that the jet flaps much as a flag does. More recent studies by Oler and Goldschmidt (1982), Mumford (1982), Antonia et al (1983), Thomas and Goldschmidt (1986) and Thomas and Brehob (1986) indicate the apparent flapping is due to the presence of an anti-symmetric array of vortical structures which propagate through the similarity region of the jet. Measurements by Antonia et al (1983) and Thomas and Goldschmidt (1986) suggest these structures originate in the form of instability waves occurring in the nascent jet shear layers which grow exponentially with downstream distance and then roll up into a symmetric array of vortices. A symmetry breaking mechanism occurs in the interaction region and leads to the development of the anti-symmetric self-preserving mode which is observed in the similarity region. The nature of the symmetry breaking mode is currently not fully understood.

Recent studies by Ho and Nossier (1981) of an axisymmetric jet operating at high subsonic Mach number impinging on a flat plate placed normal to the mean flow direction, attribute the excitation of the instability waves in the initial shear layer and subsequent large-scale structural development to an upstream propagating pressure wave generated by the impingement of the downstream coherent structures on the plate. Because of the above phenomenon they put forth the idea that the initial region and the downstream regions of the flow are actually coupled by a resonance mechanism.

Laufer (1981) has questioned whether a similar resonance mechanism could occur in a free jet without the presence of a plate. In fact, measurements by Laufer and Monkewitz (1980), in a round jet have shown that initial shear layer hot-wire signals exhibit modulation at a frequency corresponding to the downstream vortex passage frequency. Related work by Thomas and Goldschmidt (1985) have suggested the possibility of a similar resonance mechanism occurring in the two-dimensional jet.

The primary goal of the reported research is to search for evidence of the presence of a resonance mechanism operating in a free two-dimensional planar turbulent jet.

CHAPTER II

MEASUREMENT APPARATUS AND FLOW FIELD

The experimental facility shown schematically in figure 2 is powered by a three-stage centrifugal blower which supplies air to a large cubic plenum chamber of 1.2 m on a side. The blower and plenum are coupled by means of a flexible rubber duct which serves to prevent blower motor vibrations from being transmitted to the flow field. A fiberglass insulation slab, 12.7 cm thick, was used within the plenum to filter the air and also to decouple the flow field from any blower pulsation. A rectangular duct 0.76 m long, 45.7 cm in height, and 20.3 cm wide connects the plenum chamber to the nozzle assembly. The duct contained a section of flow straighteners followed by three turbulence reducing screens. The two-dimensional nozzle has a contraction ratio of 16 to 1 and ends in a slot that is 1.27 cm wide and 45.7 cm in height. The nozzle contour was based on a design by Jordinson (1961).

The flow field was formed by two large horizontal plywood plates 2.13 m in length and 1.52 m wide separated by a 0.457 m air gap (see Figure 2). These horizontal plates were designed to keep the basic flow two-dimensional in nature. All other sides of the flow field remained open. The entire set-up was supported by a sturdy angle iron frame to which a probe support mechanism was attached which allowed probe positioning in three-dimensions accurate to 0.8mm. An optional micrometer attachment allowed for lateral probe positioning accurate to 0.25 mm.

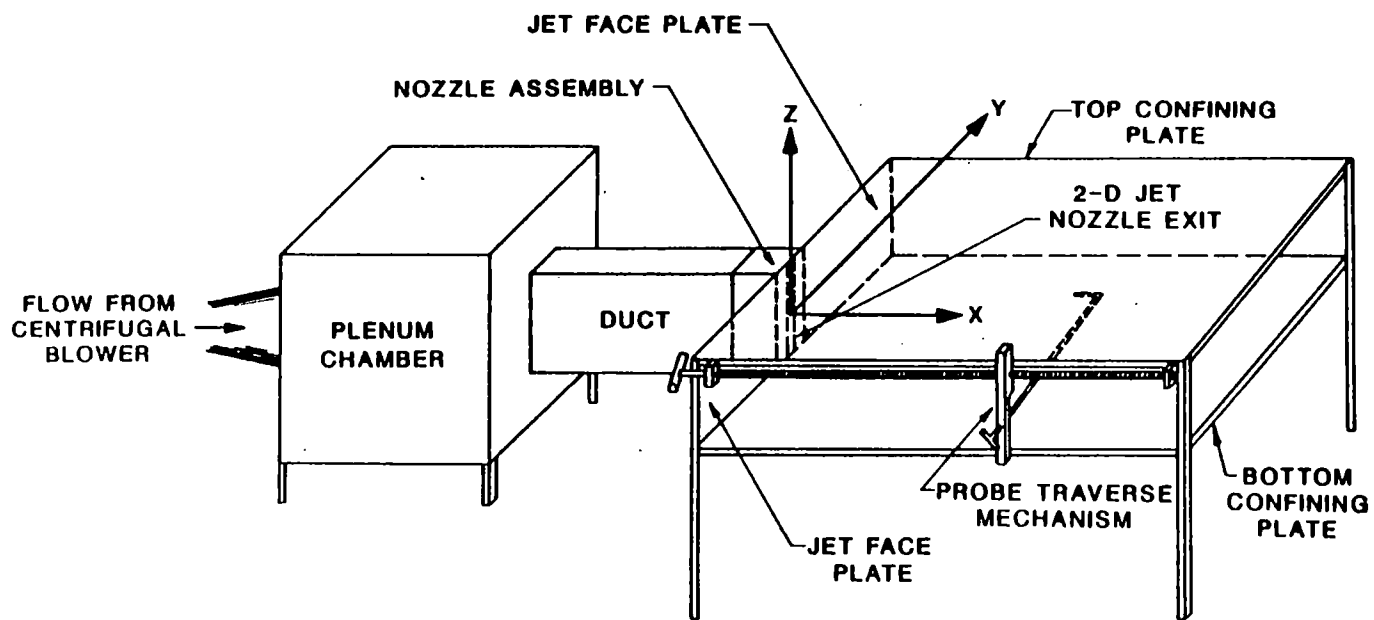


Figure 2. Schematic of Experimental Arrangement

All measurements made involved digital data acquisition and for this purpose DISA 56C01 anemometers operated in the constant temperature mode with DISA 56C17 CTA bridges were used. For measurement of the instantaneous longitudinal velocity component, DISA 55P01 standard straight wire probes were used. These probes were operated at an over-heat ratio of approximately 1.6, which corresponds to a wire temperature of 220 °C. The analog signals from the anemometers were passed through DISA 55D25 anti-alias filters and then digitized with an HP-98640A analog/digital conversion board. The digitized signals were then processed on line with an HP-9920S microcomputer which performed all data reduction.

Calibration of the probes was performed by use of a calibration jet which was constructed in house. The calibration rig was essentially an axisymmetric jet powered by compressed air and had an exit diameter of 0.6 inches. The calibrator had a hot wire bracket stand for mounting a probe such that its sensor was contained in the potential core of the calibrating jet and normal to the mean flow direction. A pressure tap on the calibrator was used to connect it to a Dwyer Micromanometer with an accuracy of ± 0.005 inches of water. A valve on the calibrator was then used with the manometer to set the calibration jet velocity to any desired value. The anemometer D.C. bridge voltage was then recorded for each velocity setting of the calibration jet. The resulting datum points were then least squares fitted to a Collis and Williams (1959) correlation of the form

$$E^2 = A + BU^{0.45} \quad (2-1)$$

where E is the anemometer D.C. bridge voltage, U is the mean velocity and A, B are calibration constants.

In the work to be reported, all measurements were made at an exit Reynolds number of 7700 (based on nozzle slot width and mean exit velocity). This corresponds to an exit velocity of 8.84 m/s. The exit velocity was set and monitored throughout the experiment with a pitot-static tube connected to a Dwyer micromanometer with an accuracy of 0.02". The probe is located near the nozzle exit plane on the jet centerline and 6.4 cm below the top confining plate. The exit mean velocity profile was flat and the exit fluctuation velocity near centerline was quite low; 0.3 percent. The nozzle exit boundary layers were laminar and had a momentum thickness of 0.0085 cm. The displacement thickness was 0.0232 cm.

CHAPTER III

BASIC FLOW DEVELOPMENT

This chapter presents the experimental results which document the general development of the jet with respect to its mean flow and longitudinal velocity fluctuations. Section 3.1 presents the mean flow development while Section 3.2 presents the development of longitudinal fluctuation intensities.

3.1 Mean Flow Development

The mean flow development of the jet is presented in Figures 3-7. The initial mean velocity profile exhibit a "top-hat" shape out to $x/D = 1.5$. The profiles are flat except for a very thin shear layer. The mean velocity variation in the shear layer is closely approximated by a hyperbolic tangent type profile as is evidenced from Figure 8. In this figure the abscissa is $\eta = y/\delta$ where y is the lateral spatial coordinate and δ is the maximum slope shear layer thickness ($\delta = 0.043$ cm.) The initial mean velocity development is characterized by the widening of the shear layer bounding the potential core, resulting in a "shearing down" of the initially flat profile. Approximate mean velocity similarity is noted to be reached by $11 \leq x/D \leq 13$ as seen in Figures 6 and 7.

The widening of the jet with downstream distance is shown in Figure 9. For $x/D > 11$ the widening rate is linear and exhibits the self-

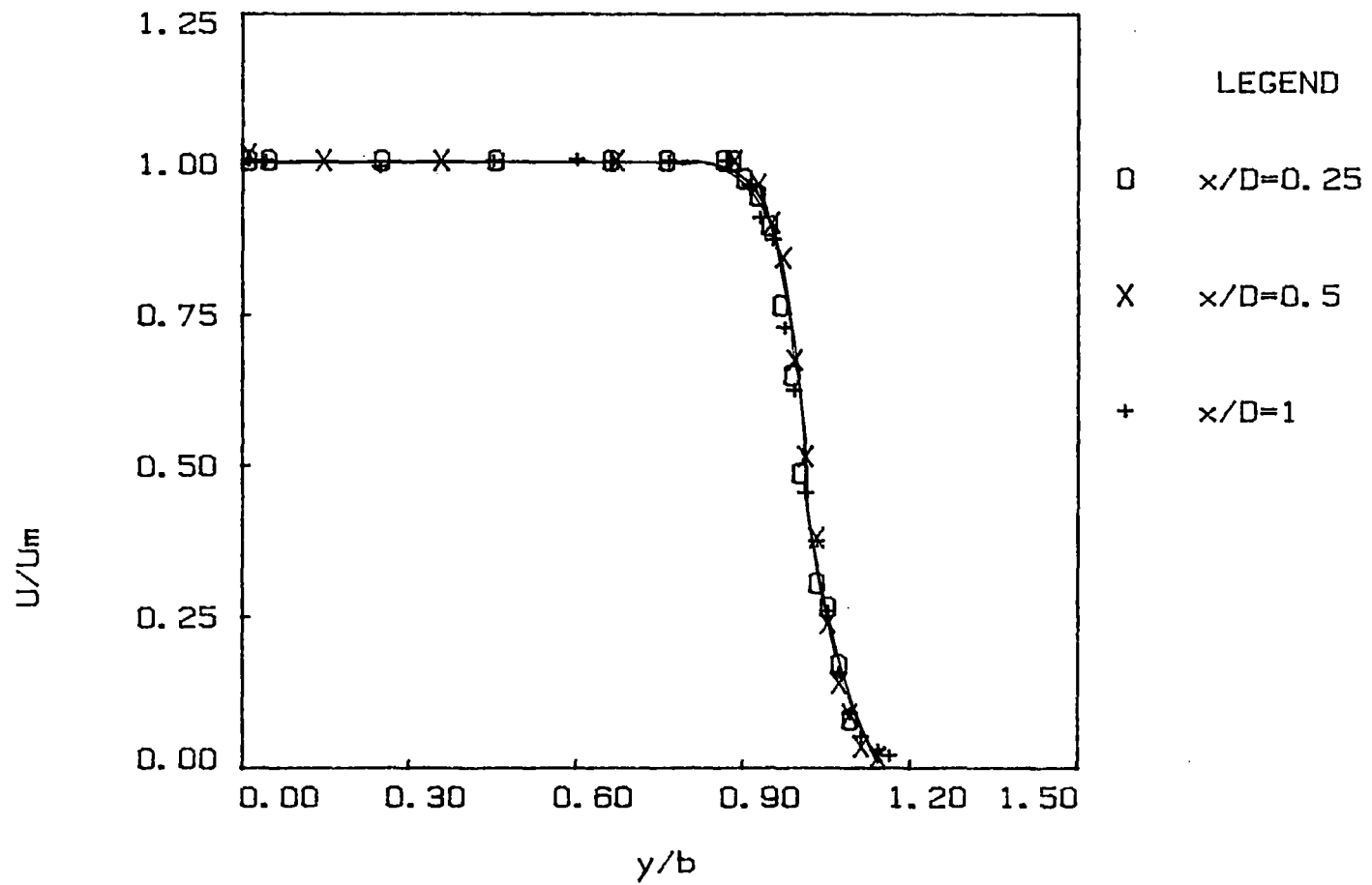


Figure 3. Mean Flow Velocity Profile at $x/D = 0.25, 0.5$ and 1.0

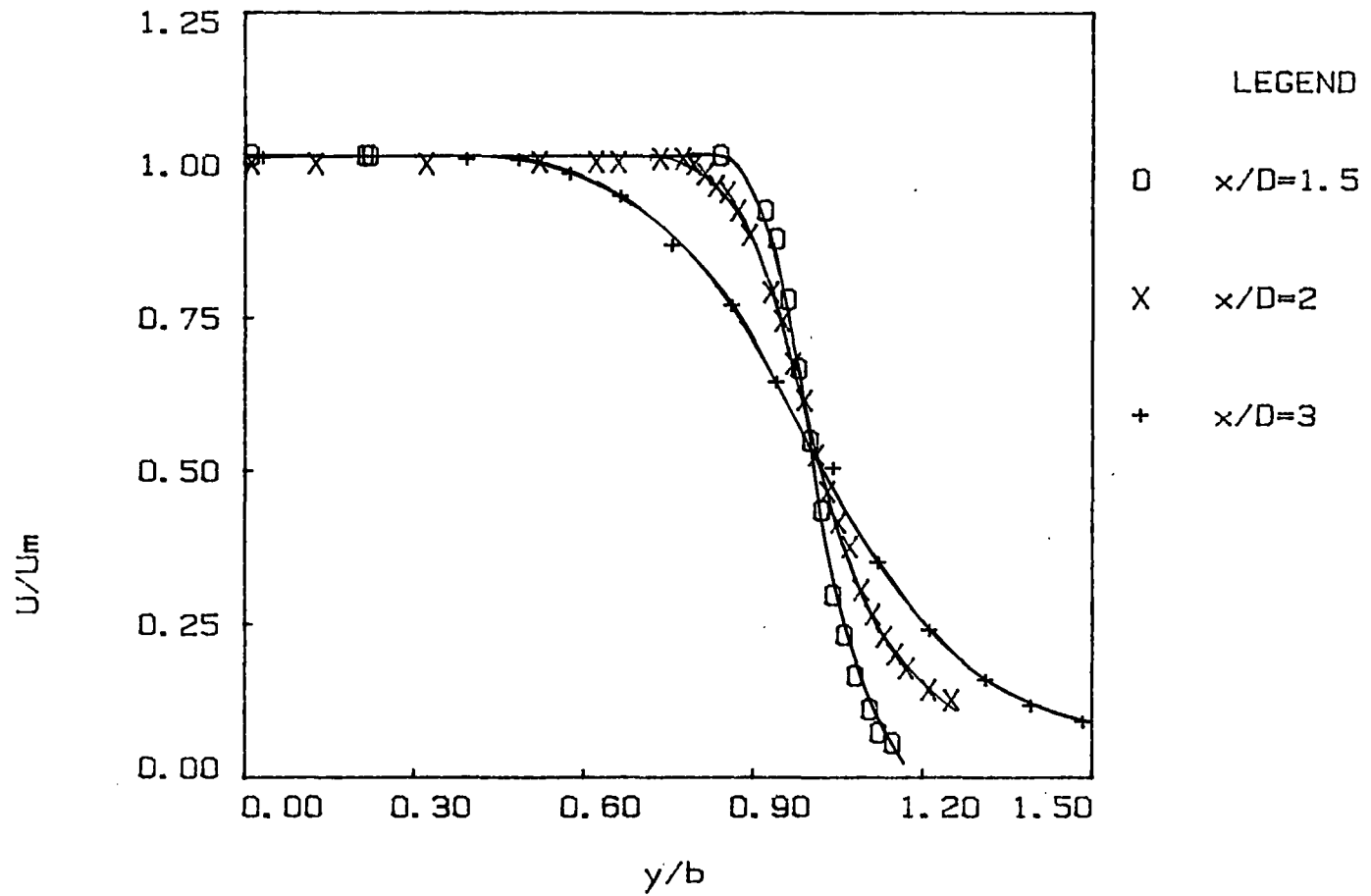


Figure 4. Mean Flow Velocity Profile at $x/D= 1.5, 2$ and 3.0

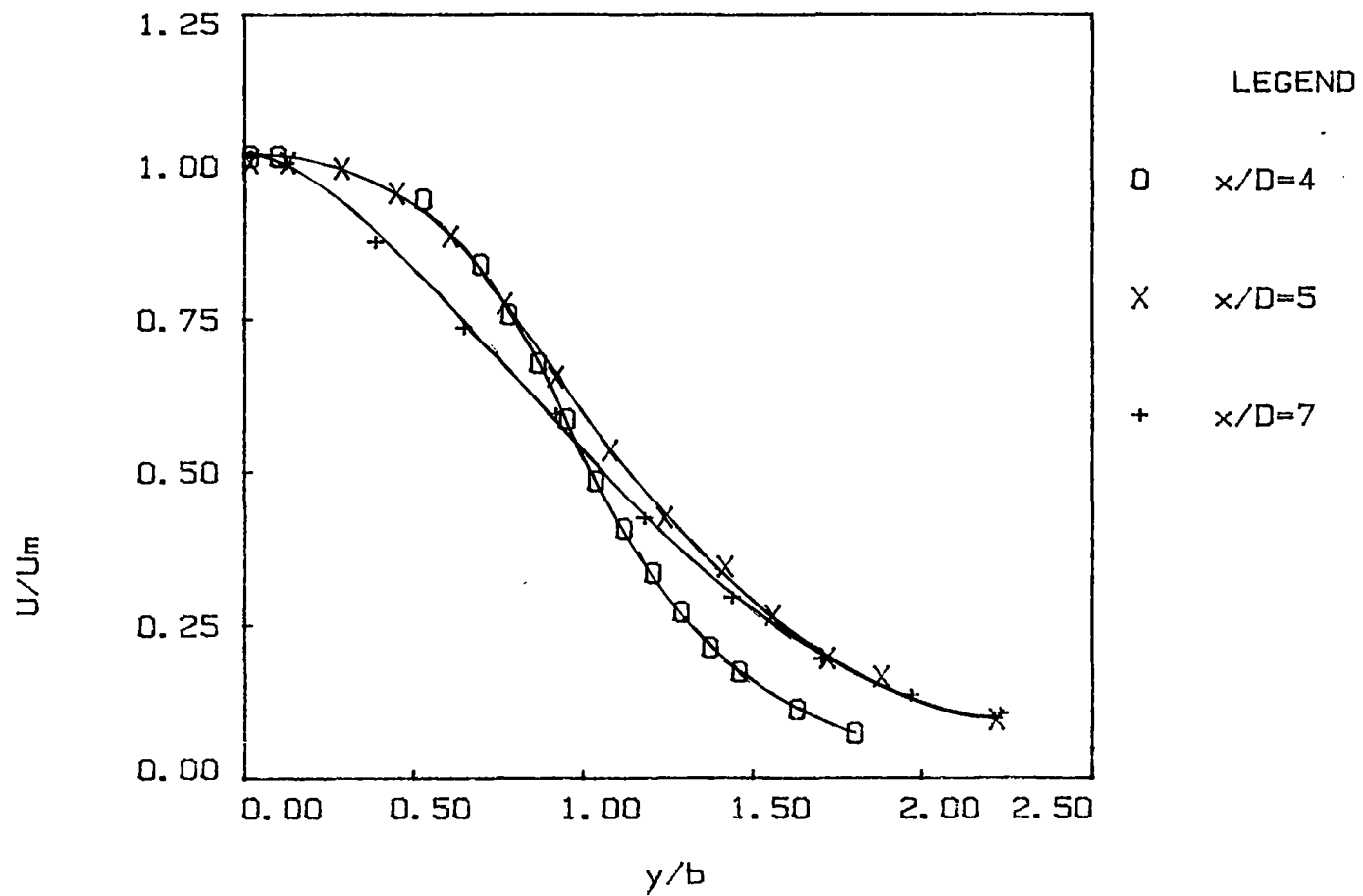


Figure 5. Mean Flow Velocity Profile at $x/D = 4, 5$ and 7.0

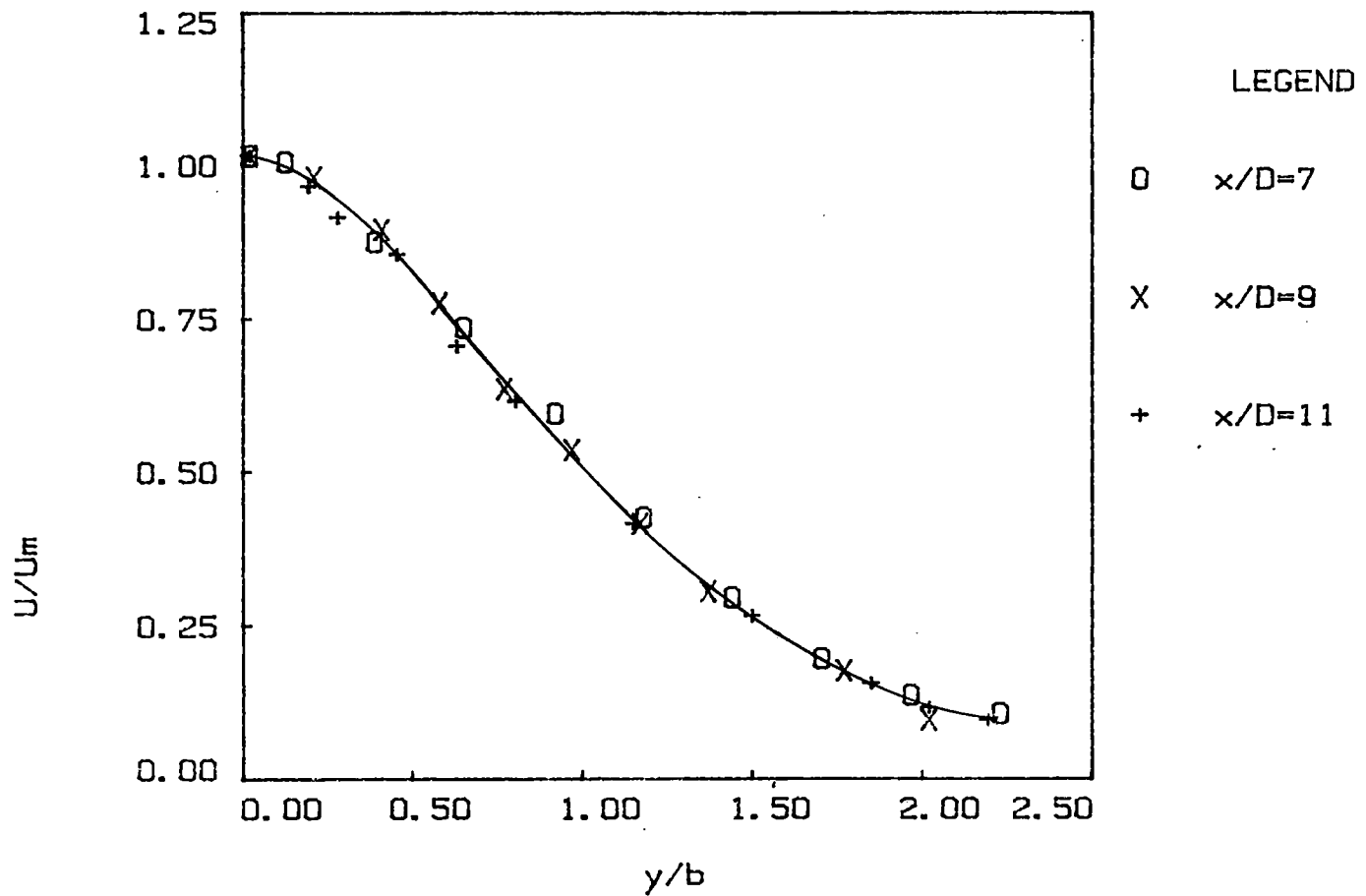


Figure 6. Mean Flow Velocity Profile at $x/D = 7, 9$ and 11.0

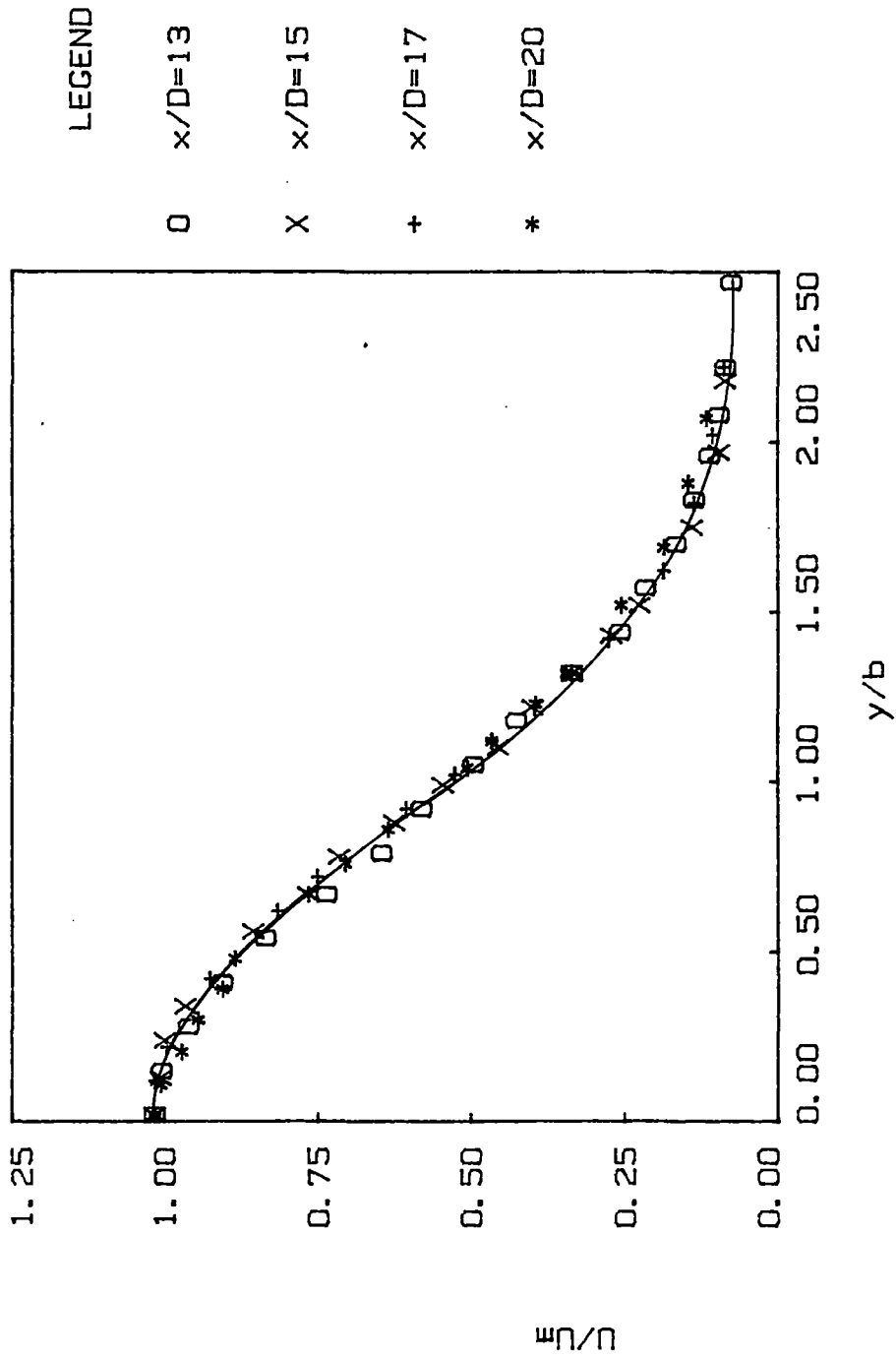


Figure 7. Mean Flow Velocity Profile at
x/D = 13, 15, 17 and 20

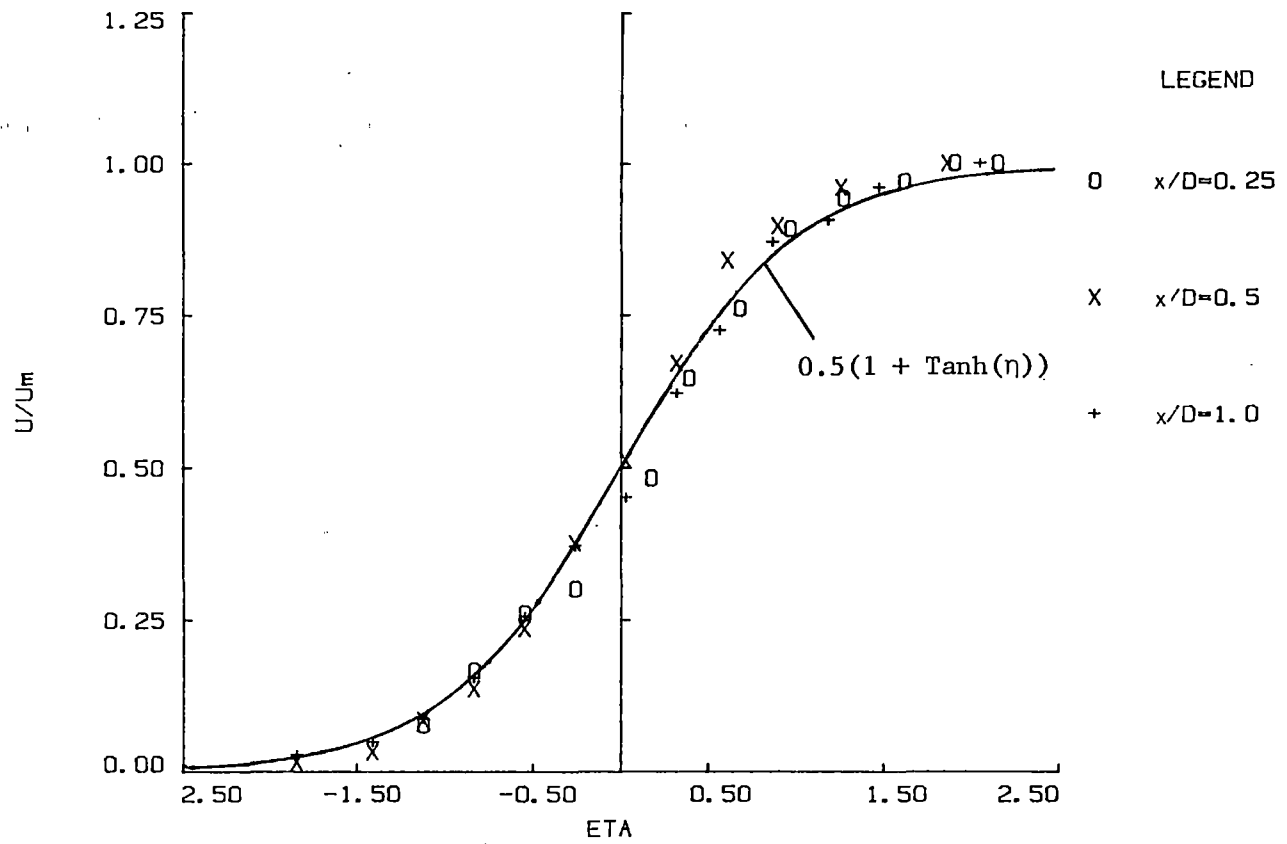


Figure 8. Comparison of Actual Data With Hyperbolic Tangent Profile

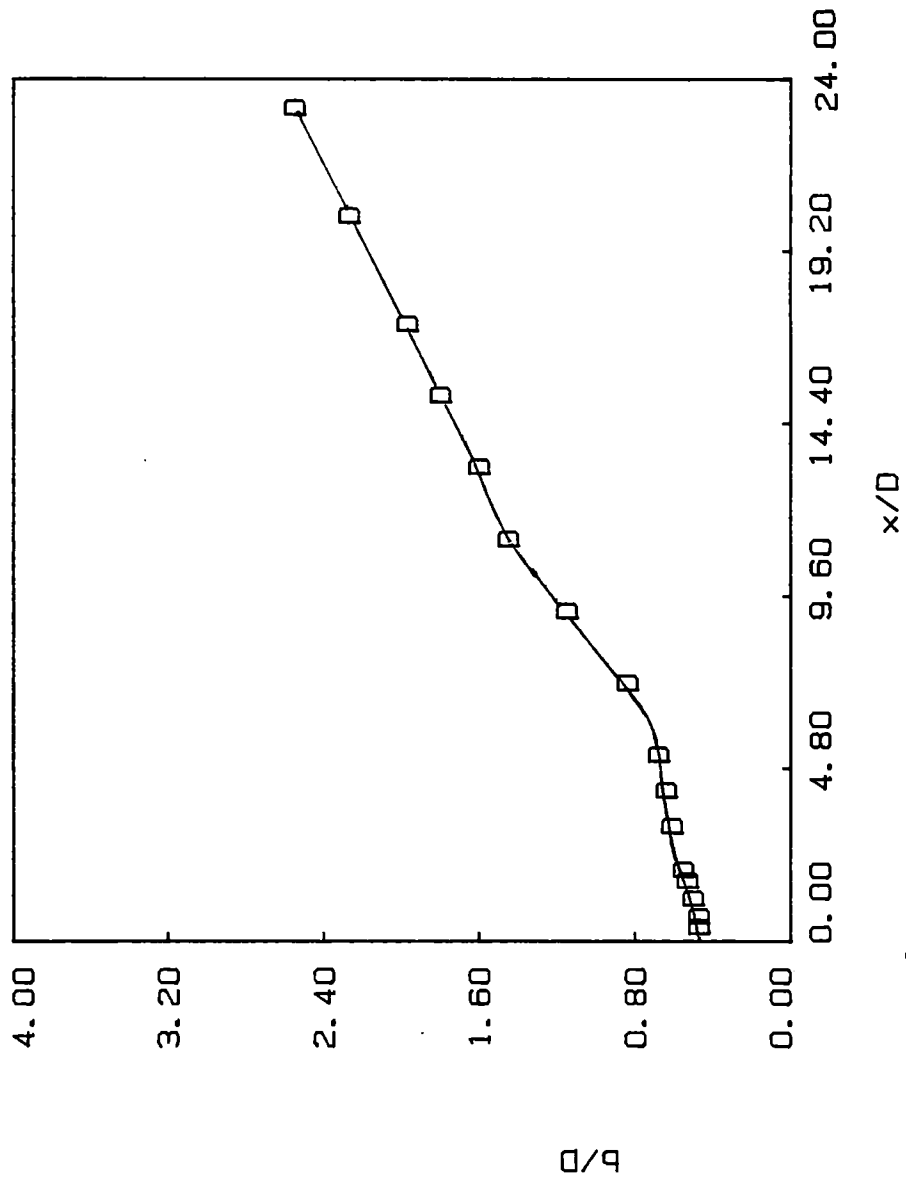


Figure 9. Jet Widening

preserving form

$$b/D = k_1(x/D - C_1) \quad (3-1)$$

where $k_1 = d(b/D)/d(x/D) = 0.104$, $C_1 =$ virtual origin based upon jet widening = -1.8. The widening rate near the jet exit is due primarily to the widening of the nascent jet shear layers. A rather abrupt increase in jet widening is noted to occur near $x/D = 3$. This is likely to be due to large-scale vortical structure interactions in the developing jet shear layer and will be addressed further in Section 4. Another increase in the widening rate in the region $x/D = 5$ to $x/D = 9$ seems to be associated with the end of potential core and the onset of the interaction region. Figure 10 shows the centerline mean velocity decay with downstream distance. For $x/D > 11$ a linear decay rate characteristic of the similarity region is obtained and is given by

$$\left(\frac{U_m}{U_0}\right)^{-2} = K_2(x/D - C_2) \quad (3-2)$$

where $K_2 = d((U_m/U_0)^{-2})/d(x/D) = 0.18$, $C_2 =$ virtual origin based upon velocity decay = 0.354. Near the jet exit the centerline velocity remains essentially constant until the developing shear layer engulfs the potential core, after which a gradual approach to the self-similar form is noted.

Table I. lists the jet widening rates and geometric origins as measured by a number of researchers along with the current values. The widening rate compares well with the other values but the virtual origins show some scatter which may be attributed to the upstream plenum turbulence levels (see Flora and Goldschmidt (1969)).

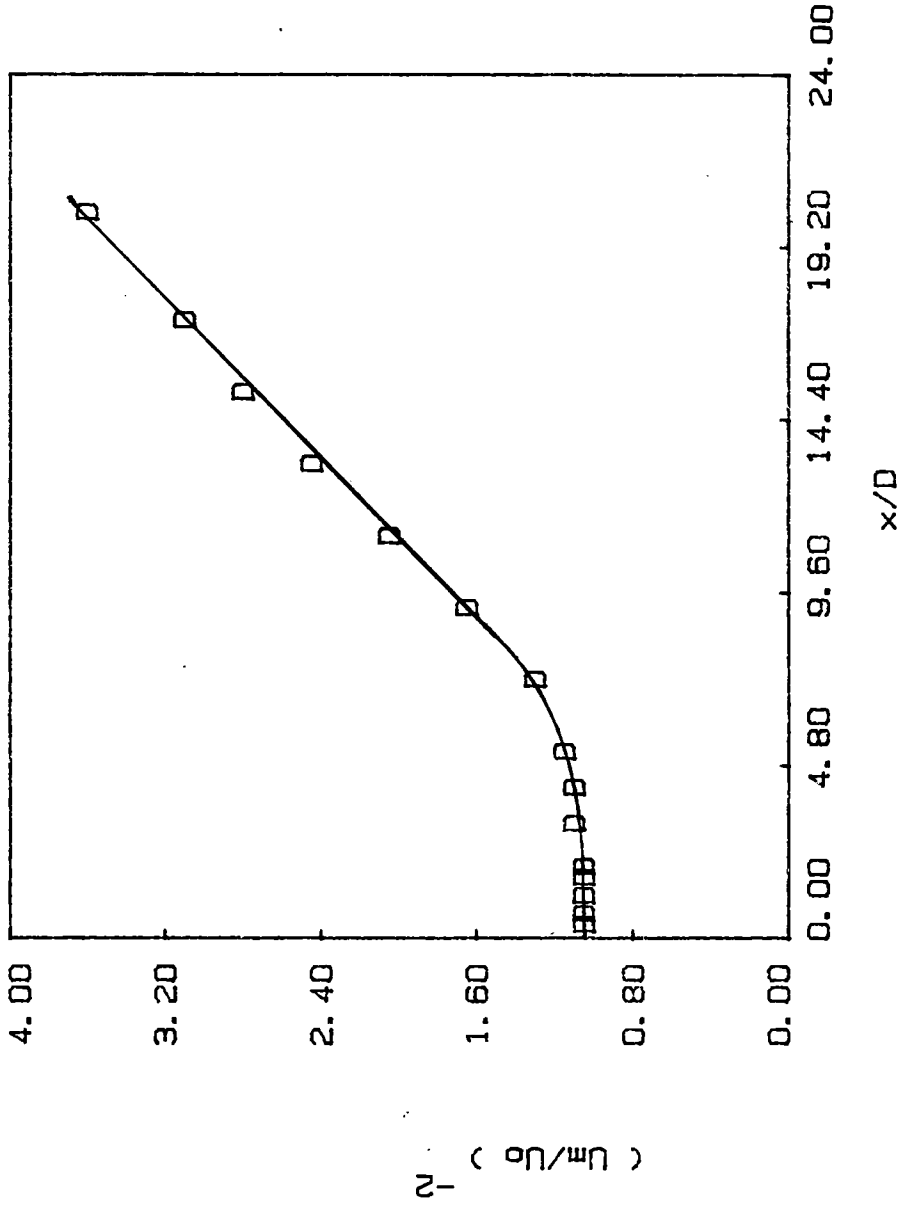


Figure 10. Mean Velocity Decay

TABLE I
MEAN FLOW PROPERTIES FOR PLANAR JETS

Reference	Re_D	K_1	K_2	C_1	C_2
Flora (1969)	2.00×10^4 to 3.00×10^4	0.109 to 0.130	0.158 to 0.227	-15.000	2.000
van der Hegge Zijnen (1958)	1.33×10^4	0.100	0.205	0.000	-1.700
Foss (1965)	5.50×10^4	0.085	0.257	-2.000	6.500
Kaiser (1971)	6.00×10^3	0.101	0.208	-2.600	0.000
Ott (1972)	1.00×10^4	0.097	0.228	-3.000	7.000
Jenkins (1974)	1.45×10^4	0.085	0.160	-6.100	4.000
Mulej (1975)	1.60×10^4	0.095	0.185	-0.789	13.200
Gutmark and Wagnanski (1976)	3.00×10^4	0.100	0.170	-2.000	4.700
Cervantes (1978)	1.00×10^4	0.083	0.240	-6.600	4.500
Chambers (1977)	6.00×10^3	0.100	0.190	-3.500	-3.200
Thomas (1980)	6.00×10^3	0.106	0.214	-3.500	-0.913
Thomas (1983)	6.00×10^3	0.100	0.220	-3.200	-1.600
Thomas and Brehob (1986)	1.50×10^4	0.086	0.253	-4.711	10.371
Current	7.00×10^3	0.104	0.180	-1.800	-0.354

3.2 Longitudinal Velocity Fluctuations

Figures 11-15 show the development of lateral profiles of longitudinal fluctuation intensity. This intensity is defined as the ratio of the r.m.s. longitudinal velocity fluctuation to the local centerline velocity. The longitudinal fluctuation intensity is noted to originate at $y/b = 1.0$ corresponding to the location of maximum mean shear. In the potential core of the jet, a comparatively low turbulence intensity of 0.3 percent was measured. The fluctuation level on the centerline increased as the effect of turbulence which originates in the shear layers gradually propagates toward the center of the flow. By $x/D \approx 20$ the intensity profile attains a general saddle shape characteristic of other published data (see Gutmark and Wygnanski (1976)). Figures 16 and 17 show the variation of longitudinal fluctuation intensity with x/D in the shear layer at $y/b = 1.0$ and at the centerline. There is a difference in the growth of the fluctuating intensities in the shear layer and on the centerline; the reason being the presence of a steep velocity gradient in the shear layer. In addition Figure 11 reveals that the fluctuations in the shear layer become fully developed earlier than on the jet centerline.

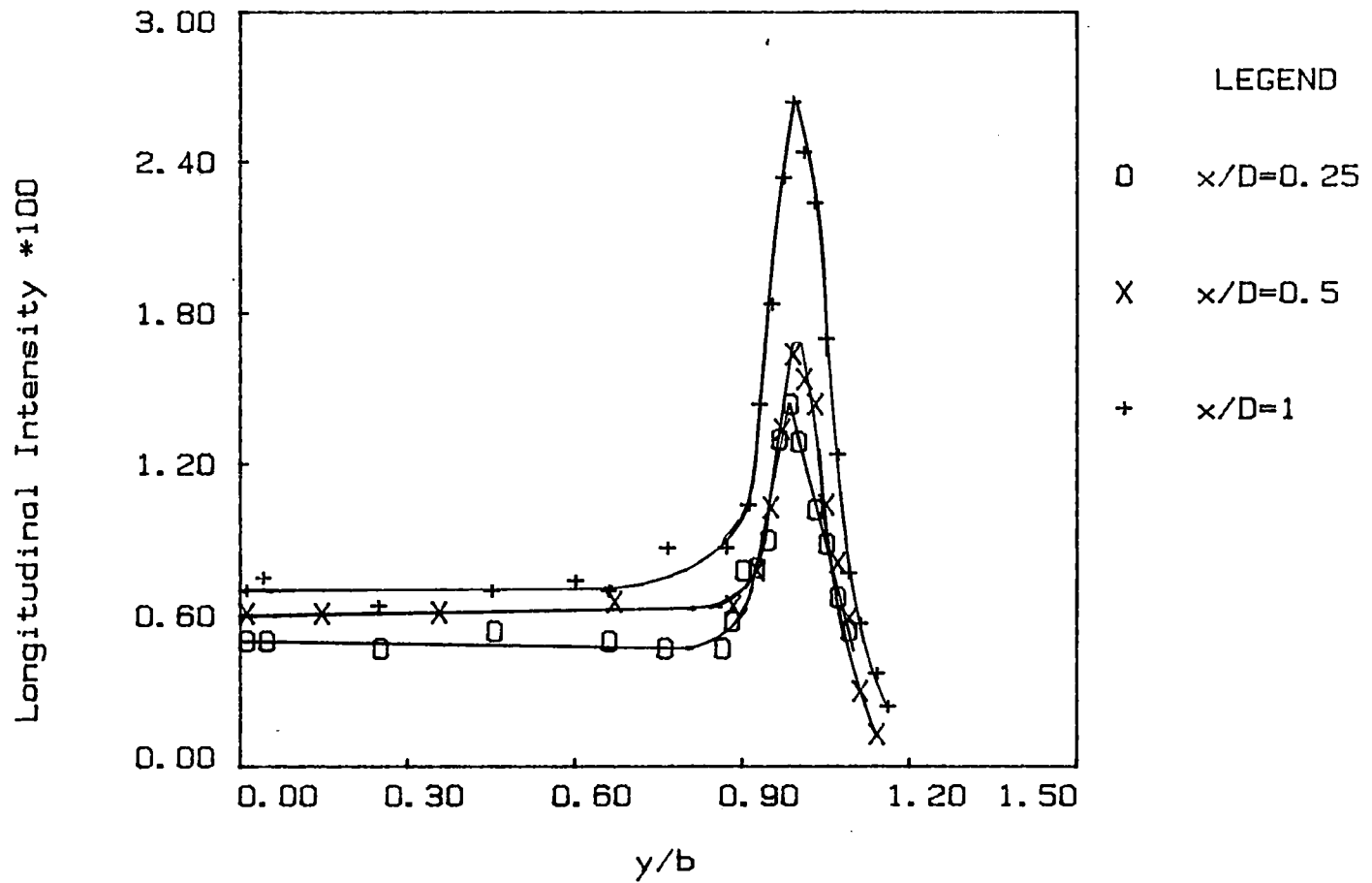


Figure 11. Longitudinal Fluctuation Intensity Profile at $x/D = 0.25, 0.5$ and 1.0

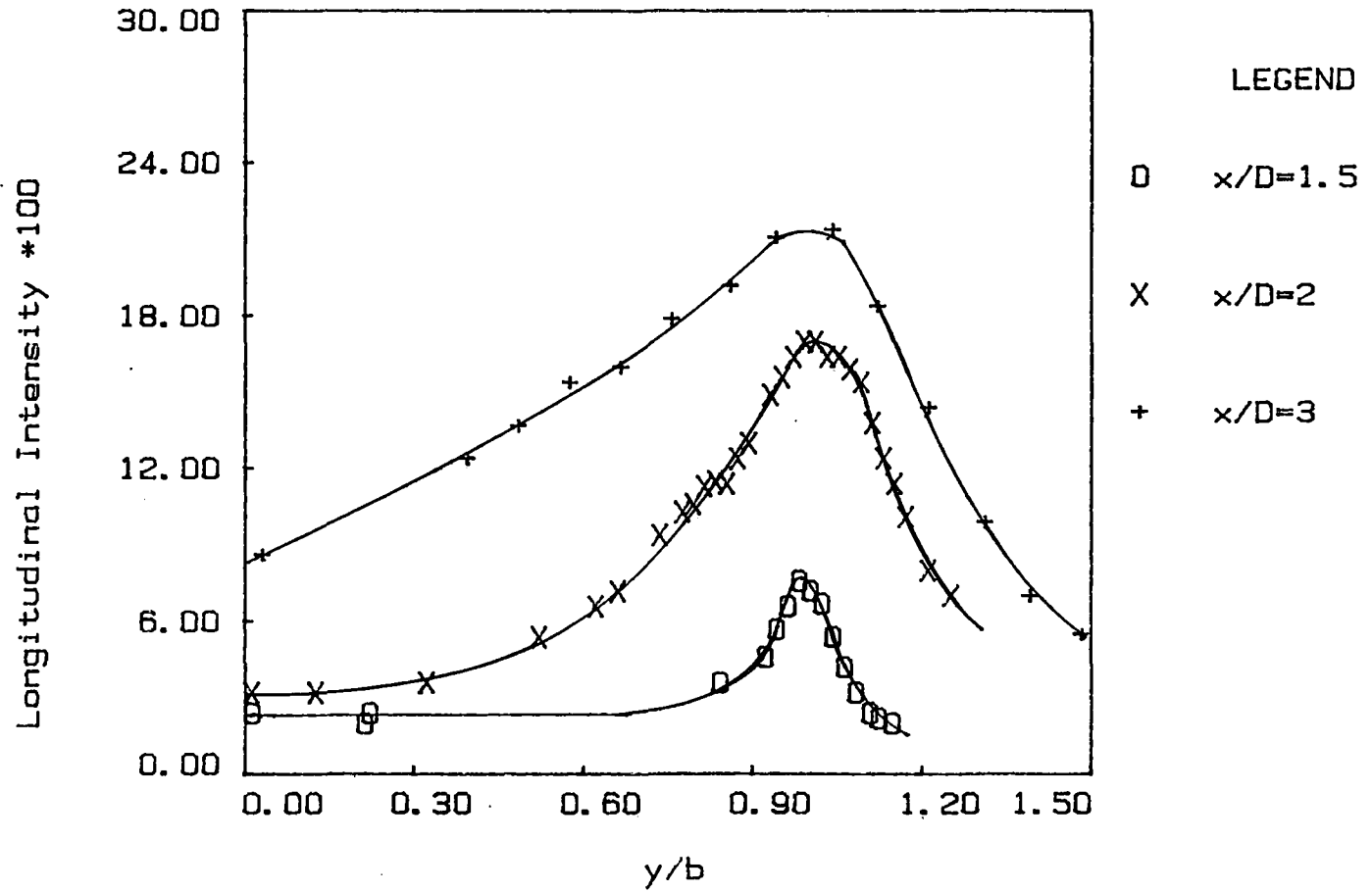


Figure 12. Longitudinal Fluctuation Intensity Profile at $x/D = 1.5, 2.0$ and 3.0

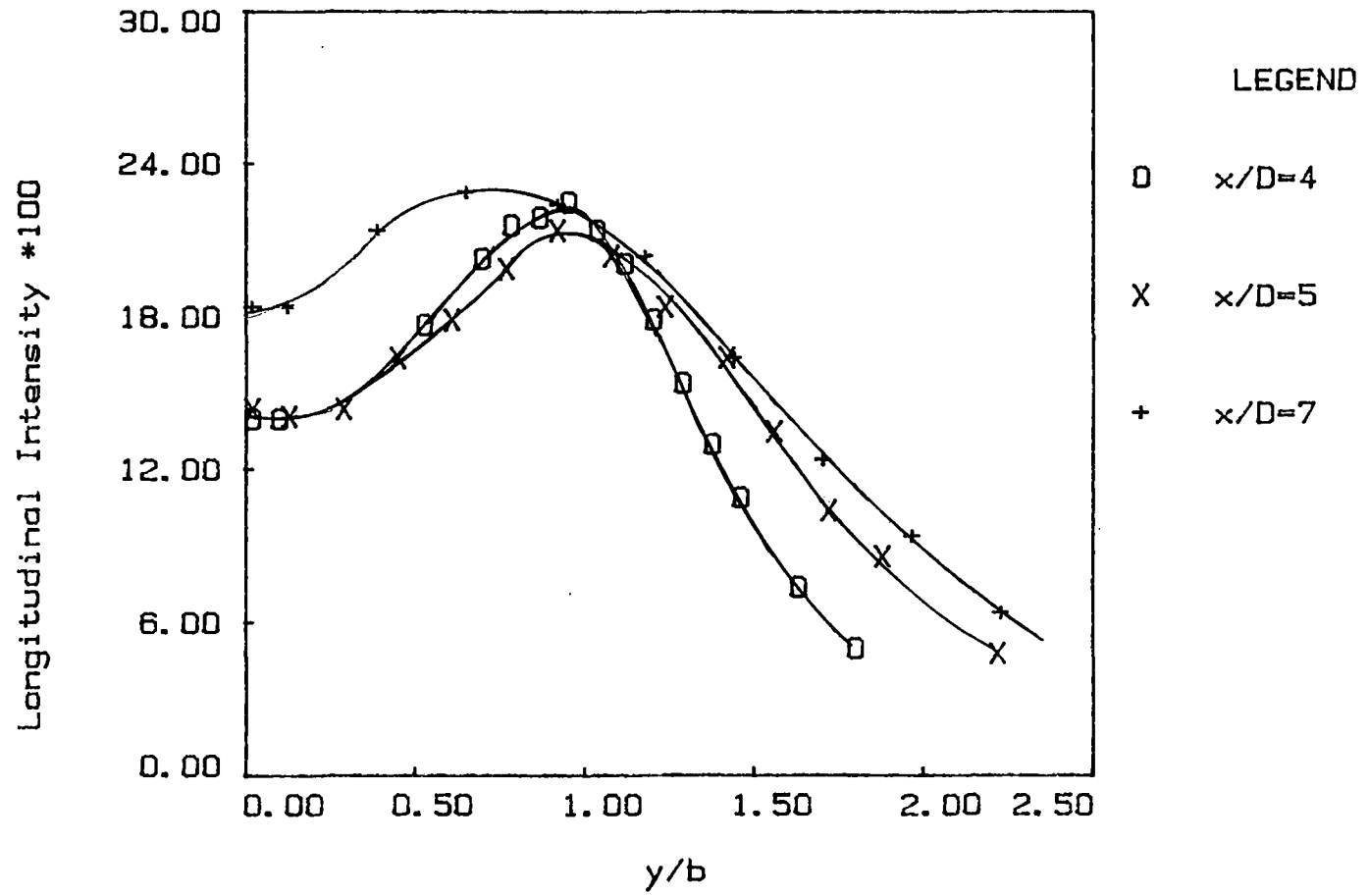


Figure 13. Longitudinal Fluctuation Intensity Profile at $x/D = 4, 5$ and 7

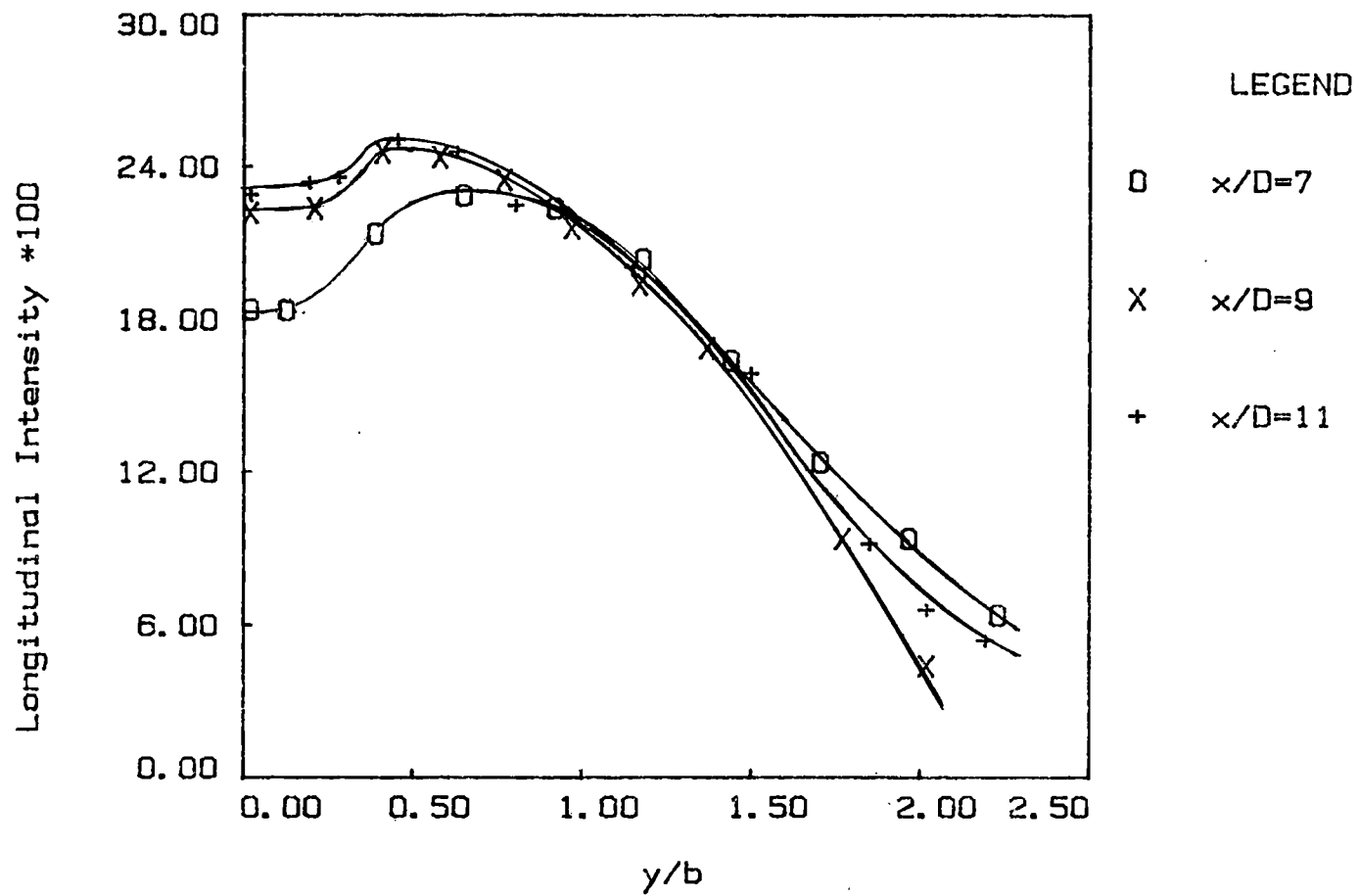


Figure 14. Longitudinal Fluctuation Intensity Profile at $x/D = 7, 9$ and 11

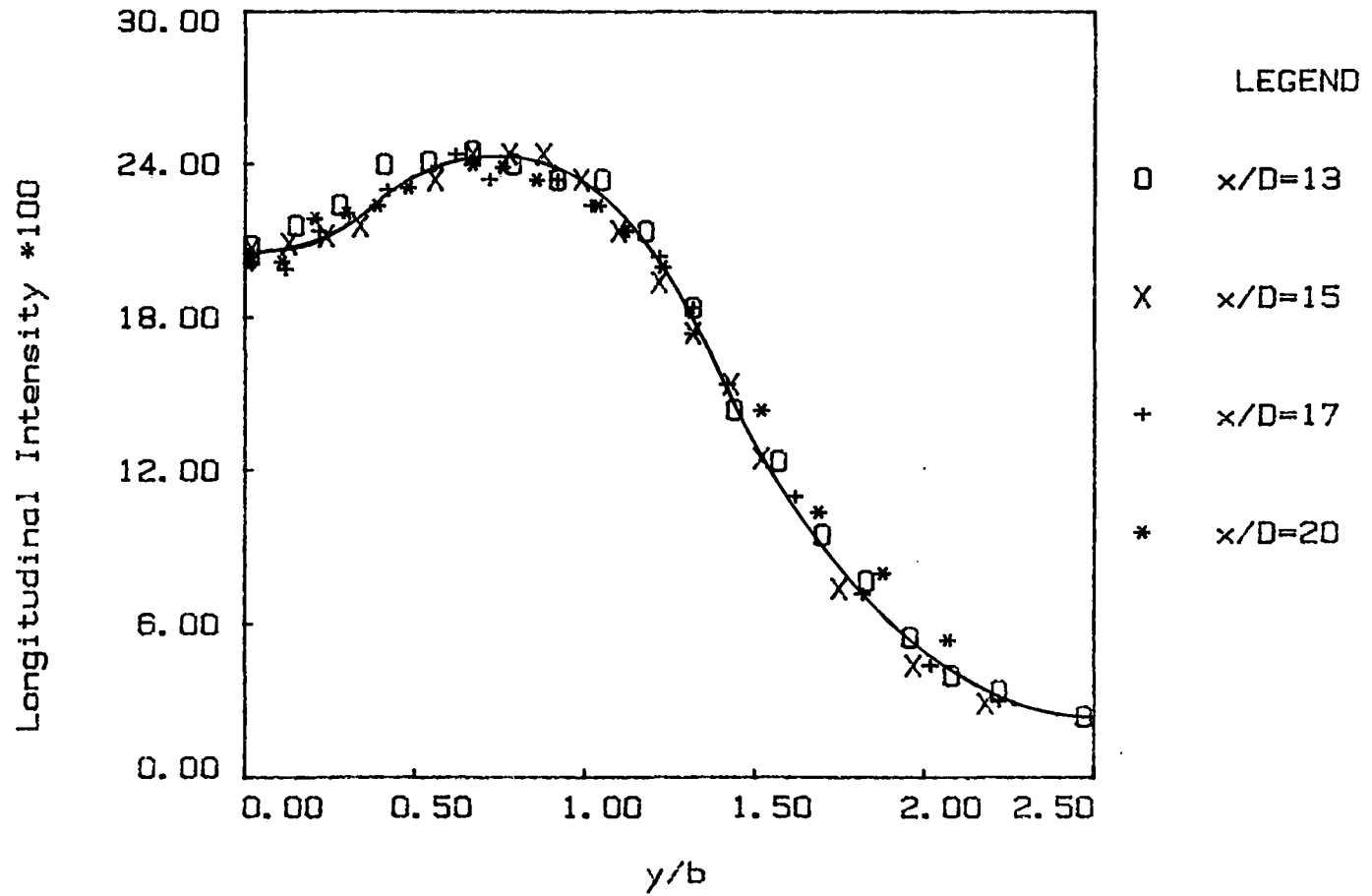


Figure 15. Longitudinal Fluctuation Intensity Profile at $x/D = 13, 15, 17$ and 20

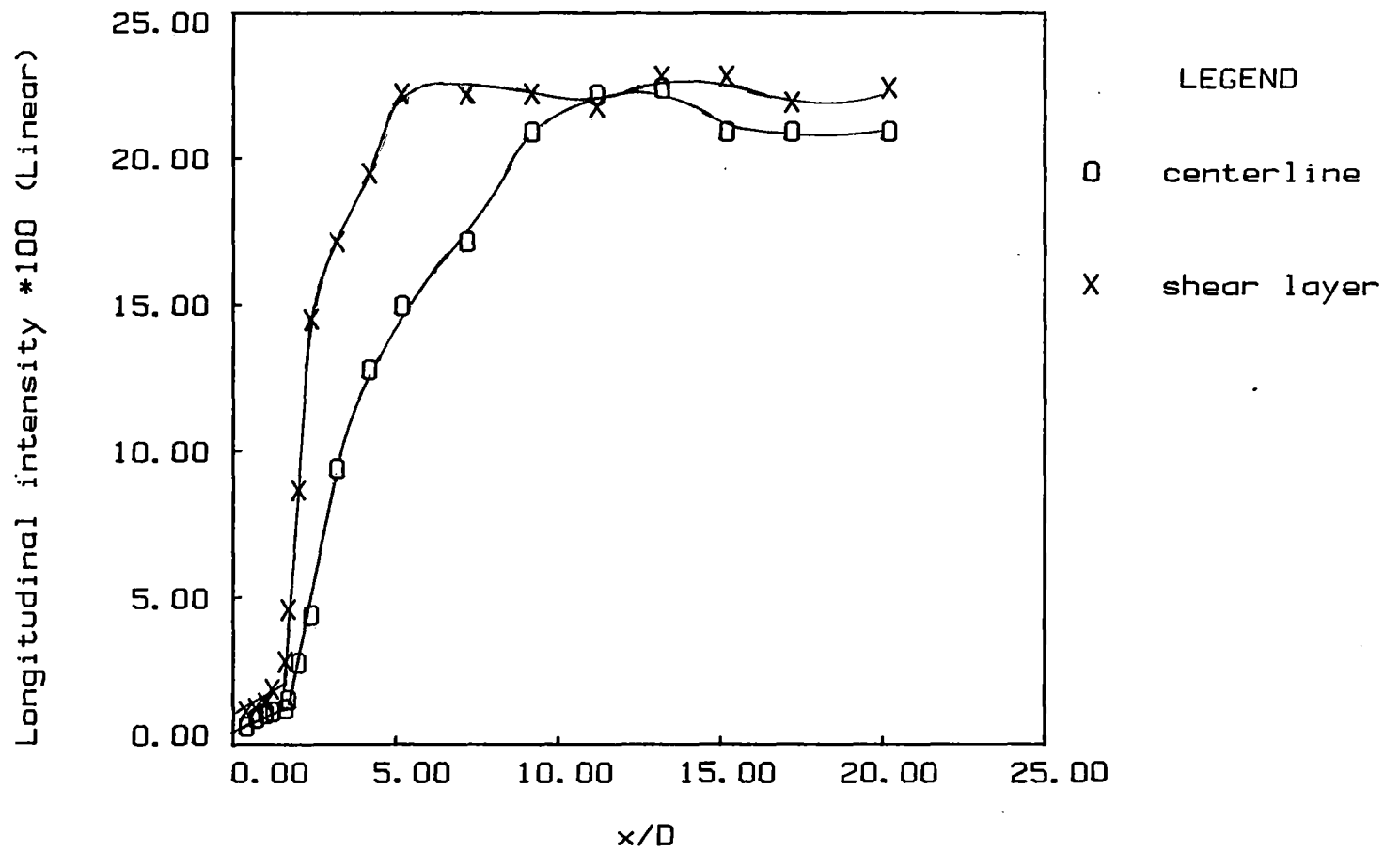


Figure 16. Longitudinal Fluctuation Intensity Variation with x/D(Linear Ordinate)

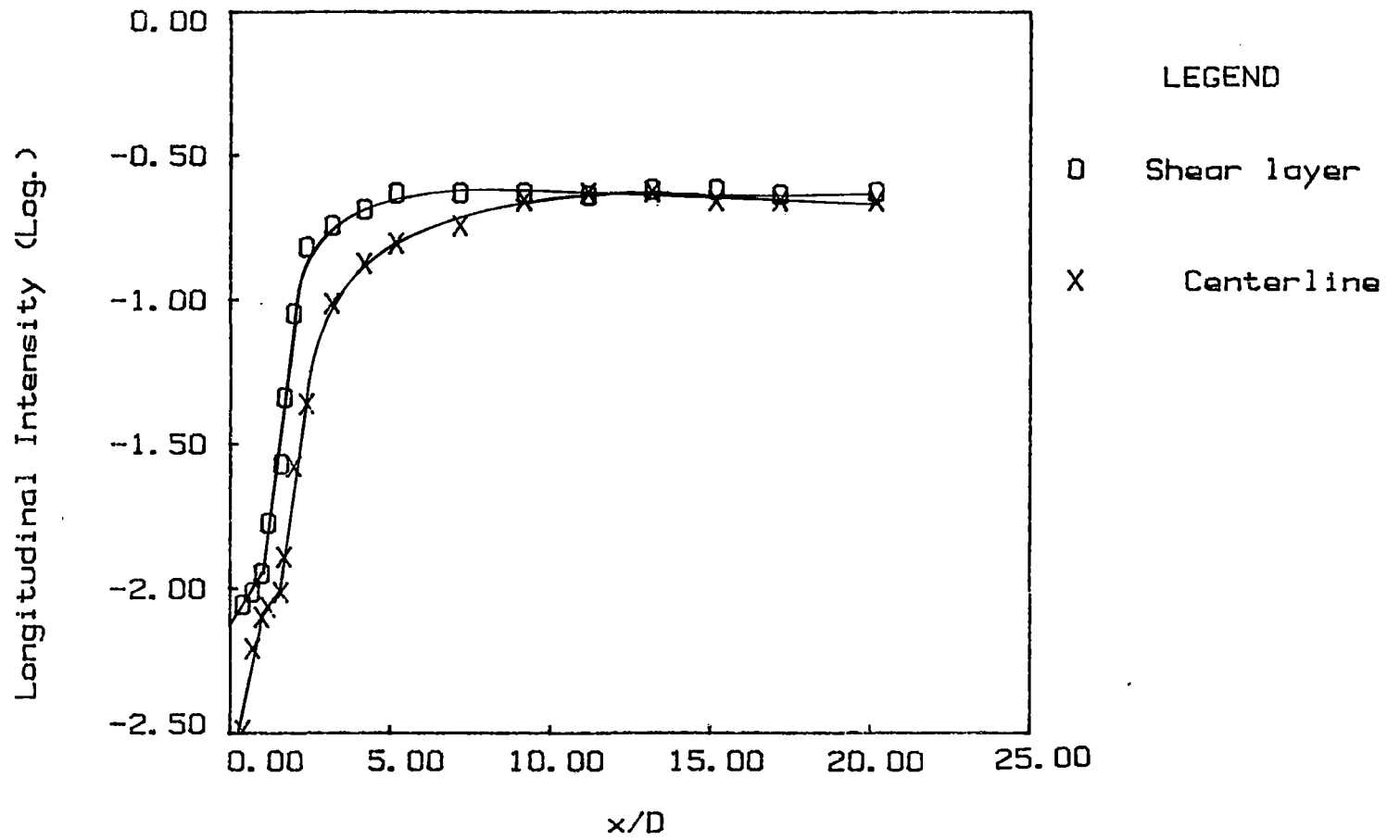


Figure 17. Longitudinal Fluctuation Intensity
Variation with x/D(Logarithmic Ordinate)

CHAPTER IV
EXPERIMENTAL INVESTIGATION OF
JET DEVELOPMENT

This chapter presents the results of measurements that detail the development of structural patterns in the two-dimensional turbulent jet. Section 4.1 presents detailed measurements of energy spectra obtained throughout the developing region. In following sections detailed correlations, coherence and phase spectra measurements are also presented. These measurements are used to infer the structural development of the planar turbulent jet.

4.1 Spectral Measurement Techniques

Spectral measurements of the longitudinal velocity fluctuations were made both on the centerline of the jet and in the jet shear layer ($y/b = 1.0$) at several selected streamwise locations ($1/4 \leq x/D \leq 20$). The purpose of such measurements is to document the spatial evolution of the time-averaged frequency distribution of energy of the longitudinal velocity fluctuations.

For these measurements a standard "straight wire" probe was used. The signal from the hot-wire was first passed through a DISA 55D25 anti-alias filters and then digitized with an HP-98640A analog/digital conversion board. In order to obtain repeatable, smooth spectra the measurements were ensemble averaged typically over 200 ensembles. The

sampling rate was selected to be sufficiently rapid so as to satisfy the Nyquist criterion which requires a sampling rate $\Delta t = 1/2f_{\max}$, where f_{\max} is the highest frequency expected in the data and Δt is the sampling time. Typically a cutoff frequency of 2000 Hz was used. The hot-wire used for the above measurements were either aligned vertically (in an x-z plane) or horizontally (in an x-y plane) depending on the streamwise location. For $x/D < 2.75$ the shear layers are very thin and the probe sensor was positioned normal to the mean flow and in the plane of the jet shear layer in order to obtain satisfactory spatial resolution (the hot-wire sensor diameter is $5\mu\text{m}$). For greater downstream distances ($x/D > 2.75$) the probe sensor was aligned perpendicular to the plane of the jet shear layer so that the measurement of longitudinal fluctuations would not be significantly contaminated by the lateral fluctuating velocity component. For measurement of the spectra a Fast Fourier Transformation algorithm was used to compute the power spectral density functions directly from the sampled digital hot-wire signal. A listing of the power spectrum program used in the analysis is presented in Appendix A.

4.1.1. Linear Region

The linear instability region specifies the near exit, nascent jet shear layers in which infinitesimal perturbations grow exponentially with downstream distance but do not appreciably interact with each other. As is shown in Figure 8, the mean velocity distribution across the jet shear layers bounding the potential core for $0 \leq x/D \leq 2$ is closely approximated by a hyperbolic tangent profile. Michalke (1965) applied linear stability theory to investigate the stability

characteristics of a hyperbolic tangent profile for spatially amplified disturbances. Theoretical spatial amplification rates from Michalke's (1965) theory and experimentally measured values obtained for the growth of different spectral components are compared in Figure 18. In the figure $\beta = \text{dimensionless frequency} = 2\pi f\delta/U_0$ and $-\alpha_i = \text{spatial amplification rate of the disturbance}$. Note that δ is the maximum-slope shear layer thickness. It may be noted from Figure 18 that a generally favorable comparison between theory and experiment exists, supporting the existence of a linear amplification region near the jet exit. Table II. presents a comparison of theoretical and experimental values relating to linear amplification in free shear layers based on an assumed hyperbolic tangent profile. In this table the linear amplification in different free shear layers is compared in terms of a Strouhal Number and amplification rate. The Strouhal Number is a dimensionless frequency given by $f\theta/U_c$ where $f = \text{disturbance fundamental frequency}$, $\theta = \text{momentum thickness of the free shear layer}$ and $U_c = \text{average mean velocity across the shear layer}$. The current values are seen to be in general agreement with the other tabulated values. Figure 19 shows the growth of the most amplified instability with downstream distance as determined from measured shear layer spectra. This corresponds to a disturbance frequency of 750 Hz. It may be noted from the figure that the region of linear growth extends approximately to $x/D = 1$. Figure 20 shows the variation of measured maximum-slope jet shear layer thickness with downstream distance. It is seen from the figure that the flow remains essentially parallel to a downstream distance of approximately $x/D = 1$, which is one of the key assumptions made in linear instability theory.

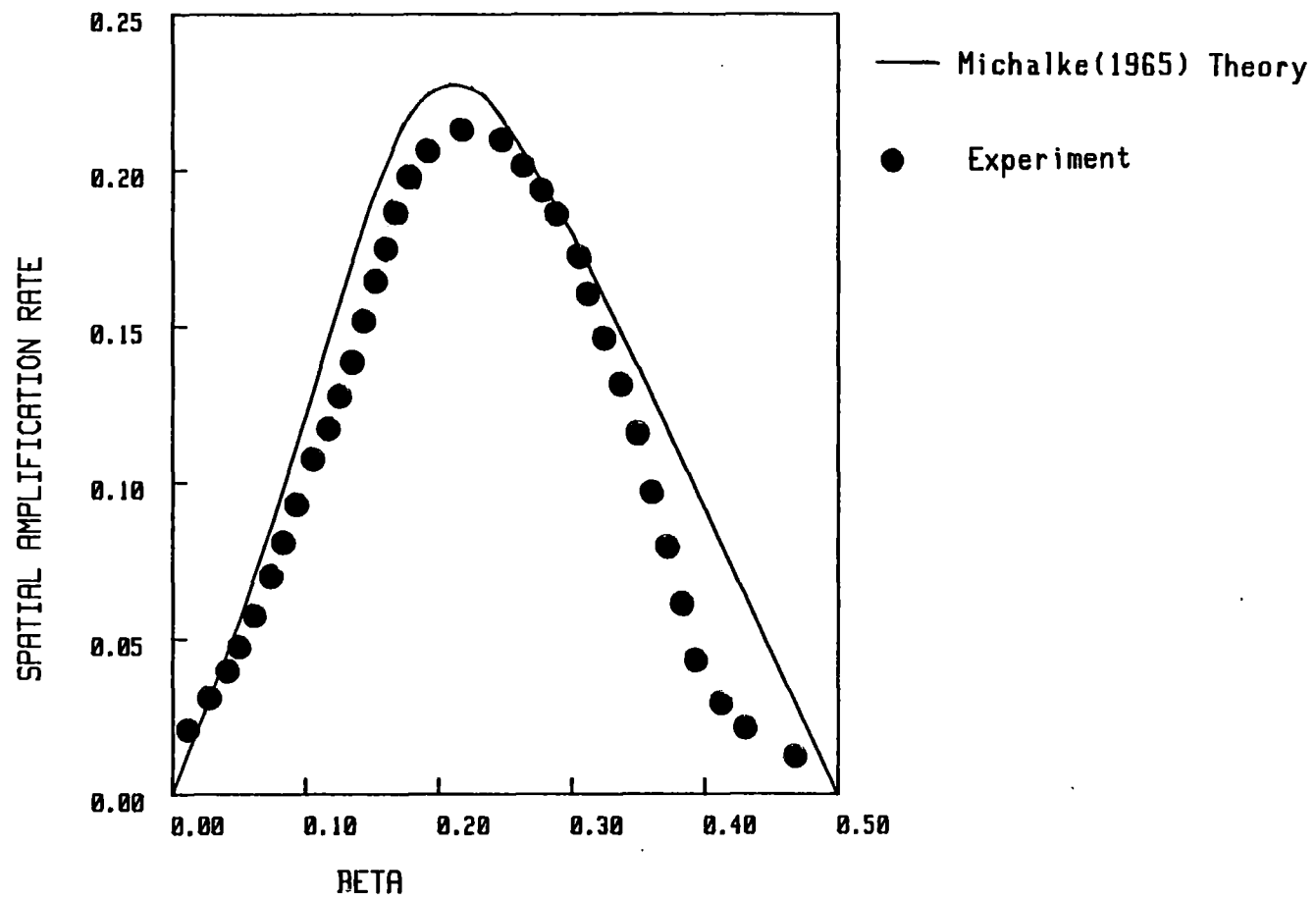


Figure 18. Comparison of Michalke's Theory With Experimental Data

TABLE II.

MEASUREMENTS OF LINEAR AMPLIFICATION IN FREE SHEAR FLOWS

Reference	Strouhal Number		Amplification Rate ($-\alpha\theta$)	
	Theory	Expt.	Theory	Expt.
Freytmuth (1966), Round jet	0.033	0.034	0.114	0.09
Browand (1966), Free shear layer	0.033	0.021	0.114	0.131
Miksad (1972), Free shear layer	0.034	0.035	0.07	0.197
Ho & Huang (1982), Free shear layer	0.035	0.031	0.03	0.029
Gutmark & Ho (1980), Round jet	0.033	0.034	-	-
Current, Planar jet	0.0282	0.027	0.089	0.085

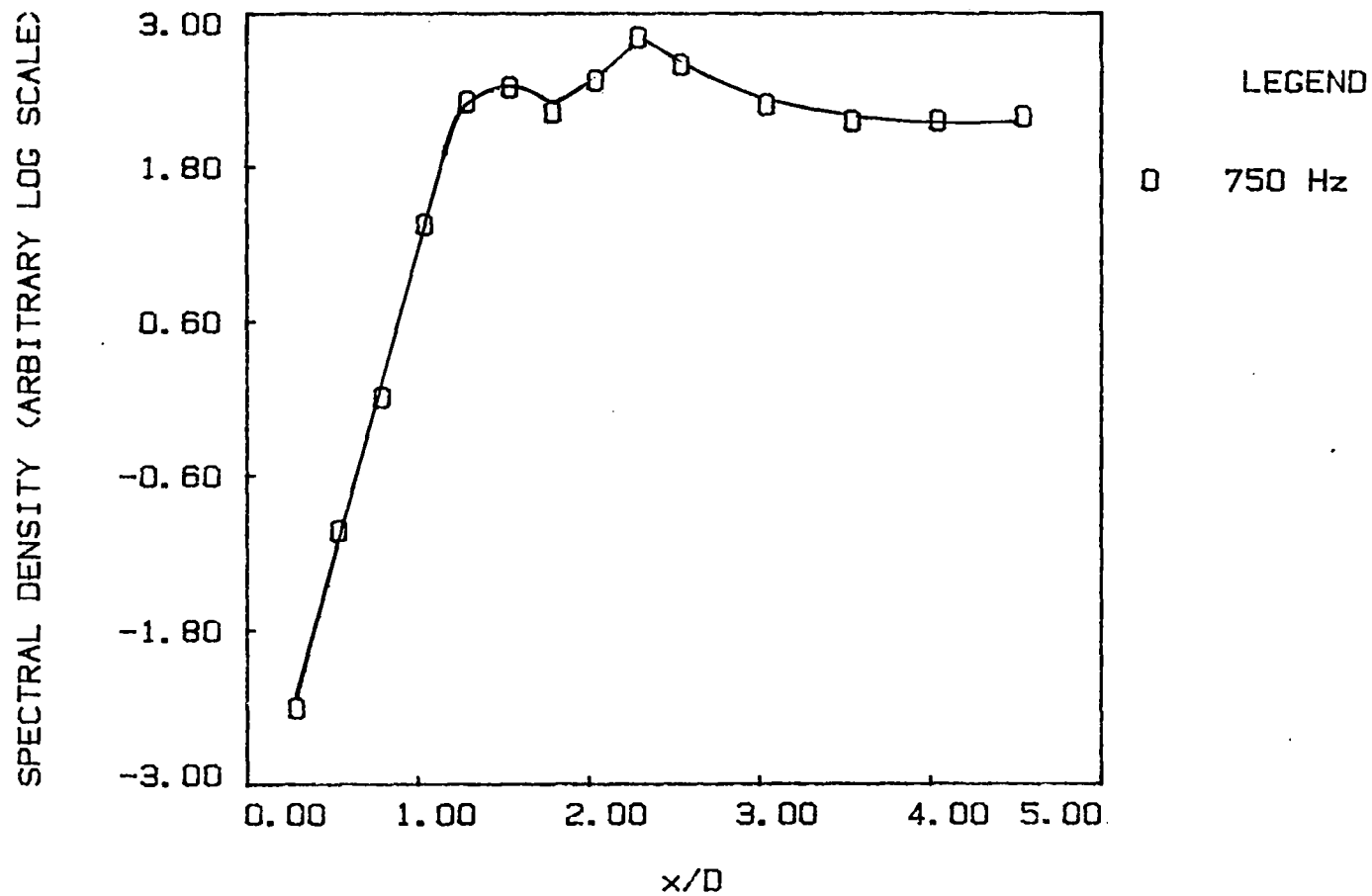


Figure 19. Growth and Decay of the Most Amplified Fundamental Instability Wave (Bandwidth 10 Hz)

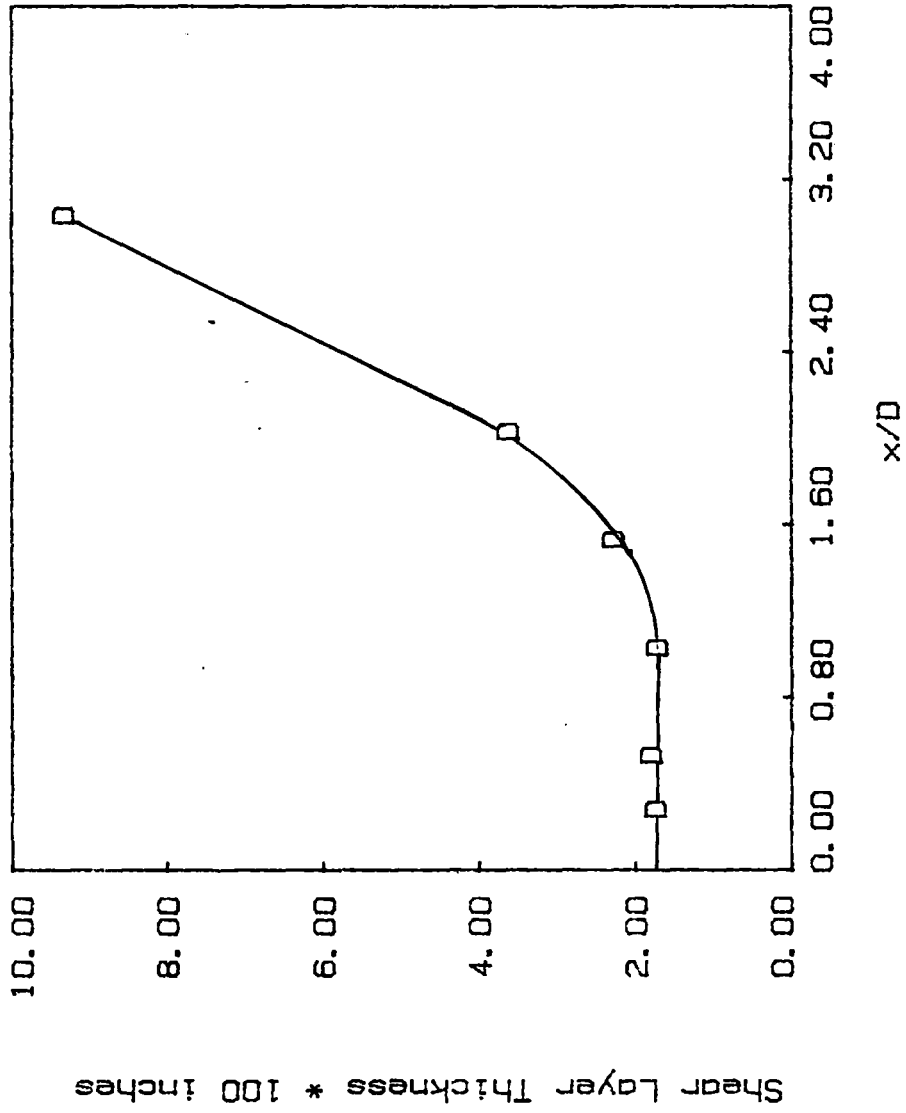


Figure 20. Growth of Shear Layer Thickness

One unexpected and somewhat surprising result of energy spectra obtained in the initial region is shown in Figure 21. This figure shows the power spectrum obtained in the shear layer at $x/D = 0.25$, in which a dominant low level peak at approximately 20Hz is noted. This low frequency mode is very uncharacteristic of thin shear layer instability frequencies for it is an order of magnitude less than the expected values (recall the frequency of maximum amplification is 750 Hz). The dimensionless frequency for this mode may be calculated to be $\beta = 5.95 \times 10^{-3}$ which from Figure 18 is shown to be a neutral mode and downstream in the linear amplification region ($x/D < 1$) the spectra show no growth of this mode. Plausible sources for the production of this unexpected low frequency wave were investigated and are discussed below.

Pulsing of the exit flow by a mechanism such as an upstream plenum resonance could be a very likely source for causing low frequency pulsations at the jet exit which in turn would show up in the power spectral measurements as a low frequency mode. Profiles of spectral modes obtained by laterally traversing the hot-wire at $x/D = 0.5$ were made in order to investigate this possibility. Figure 22 shows the amplitude variation of the low frequency mode ($\approx 20\text{Hz}$) across the jet exit. It is clearly seen from this figure that the low frequency wave is localized in the jet shear layers with the potential core being basically free of any such disturbance. Hence, pulsing of the exit flow can be ruled out as a possible source for the presence of the low frequency wave in the shear layers.

The low frequency wave under consideration could possibly originate as a boundary layer instability wave growing inside the nozzle. The

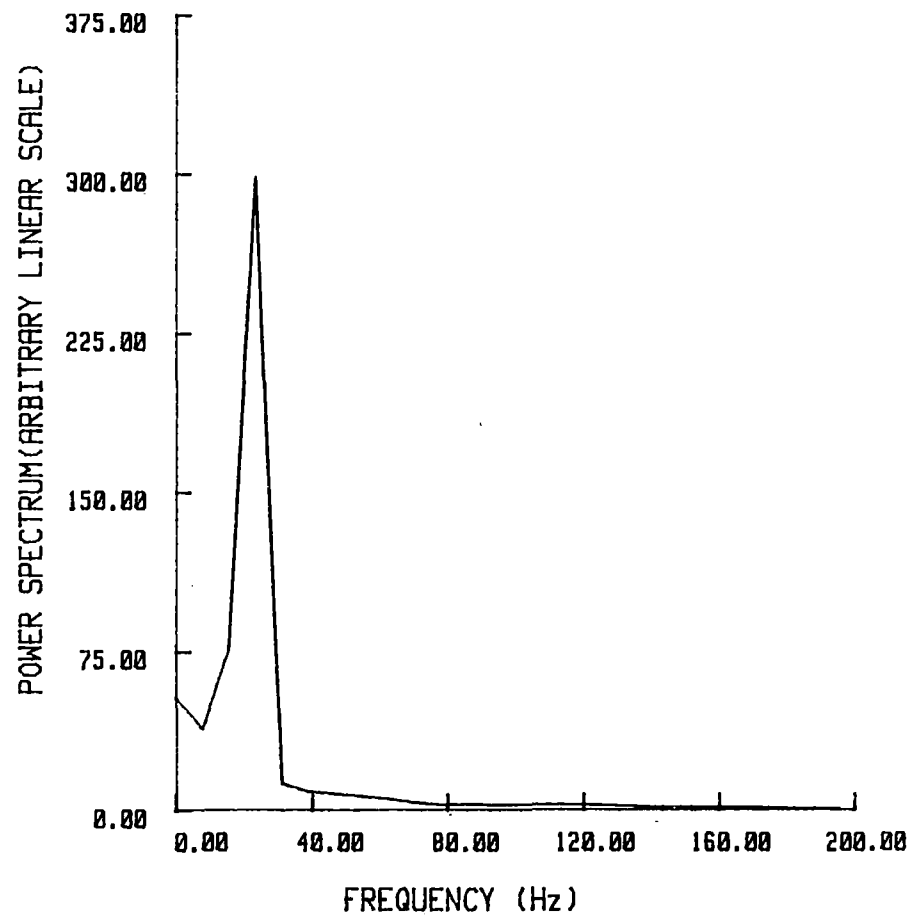


Figure 21. Shear Layer Power Spectrum at $x/D = 0.25$

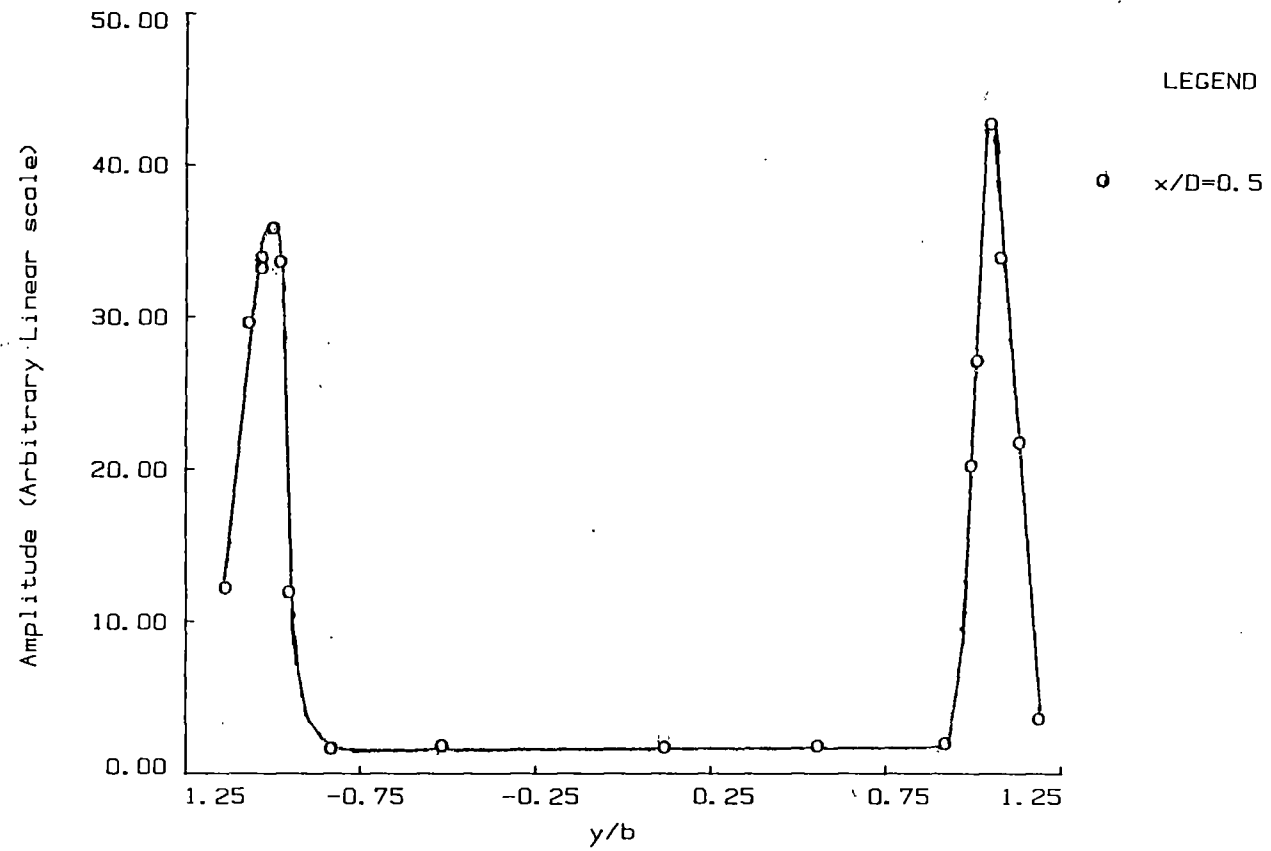


Figure 22. Amplitude Variation of Low Frequency Mode near 20 Hz (Bandwidth of 5 Hz) Across the Jet

boundary layer of the nozzle as presented in Chapter II was measured to be laminar, exhibiting a shape factor $H = 2.73$ which is similar to the Blasius solution value of 2.6. The Reynolds Number based on displacement thickness is $Re_{\delta^*} = 139$. The instability characteristics of the Blasius-flat plate boundary layer were computed by Wazzan, Skmura and Smith (1968). From their analysis the critical Reynolds Number (based on displacement thickness) for amplification of disturbances was noted to be $Re_{\delta^*} = 520$. Thus, the possibility that the nozzle boundary layers are the source for the low frequency wave may be ruled out since the measured Re_{δ^*} is far below Re_{δ^*crit} .

Another possible source for the low frequency wave could be due to a kinematic effect arising because of a lateral flapping of the shear layer past the stationary probe. In order to evaluate the existence of the above phenomenon the parameters $\Delta y/\delta$ and $\Delta y/\theta$ were calculated, where $\Delta y =$ lateral flapping amplitude $= \sqrt{\overline{u^2}} / (\partial U/\partial y)_{max}$, $\delta =$ maximum slope free shear layer thickness $= 0.017$ inch and $\theta =$ momentum thickness of the free shear layer $= 0.0069$ inch. The computed values of $\Delta y/\delta$ at $x/D = 0.25, 0.5$ and 1.0 were 0.033, 0.029 and 0.05 respectively and $\Delta y/\theta$ at $x/D = 0.25, 0.5$ and 1.0 were 0.081, 0.071 and 0.12 respectively. Since these values of $\Delta y/\delta$ and $\Delta y/\theta$ are so small we may safely conclude that the low frequency wave is not due to any lateral flapping of the shear layer.

From the above investigation it may be concluded that the low frequency wave is highly localized in the two developing jet shear layers adjoining the potential core and is not linked to any source external to the flow field. As expected, it may also be noted that this neutral wave has no effect on the amplification of other shear layer

instabilities in the linear region. In the later sections of this chapter evidence is presented which suggests a source for this low frequency wave within the jet.

4.1.2. Non Linear Transition Region

As is seen in Figure 19 the exponential growth of the most amplified instability wave saturates by approximately $x/D = 1.25$. This location marks the end of linear growth and the onset of nonlinear interaction between fluctuations. This distance for saturation of the most amplified mode corresponds to approximately 2.6 initial instability wavelengths. The onset of nonlinear effects is to be expected from the large increase in peak shear layer fluctuation intensity as evidenced from Figure 11 and 12. In fact the criterion for the onset of nonlinear effects suggested by Sato (1960) is met since $\sqrt{\overline{u^2}} / U_m > 4\%$ shortly beyond $x/D = 1.25$.

Previous research in free shear layers has indicated that the onset of non-linear effects is marked by the rolling up of the most amplified instability wave into a periodic array of compact spanwise vortices. Since the initial region of the planar jet basically consists of two free shear layers it seems natural to expect similar behavior. Indeed, in the linear region the behavior has been demonstrated to be quite similar (see Figure 18). However, the results of spectral measurements for nonlinear planar jet transition indicate some important differences which will next be discussed.

The longitudinal fluctuation spectra presented in Figures 23, 24, and 25 clearly show the growth of the most amplified frequency (≈ 750 Hz) with downstream distance and indicate that by $x/D = 1.5$ a

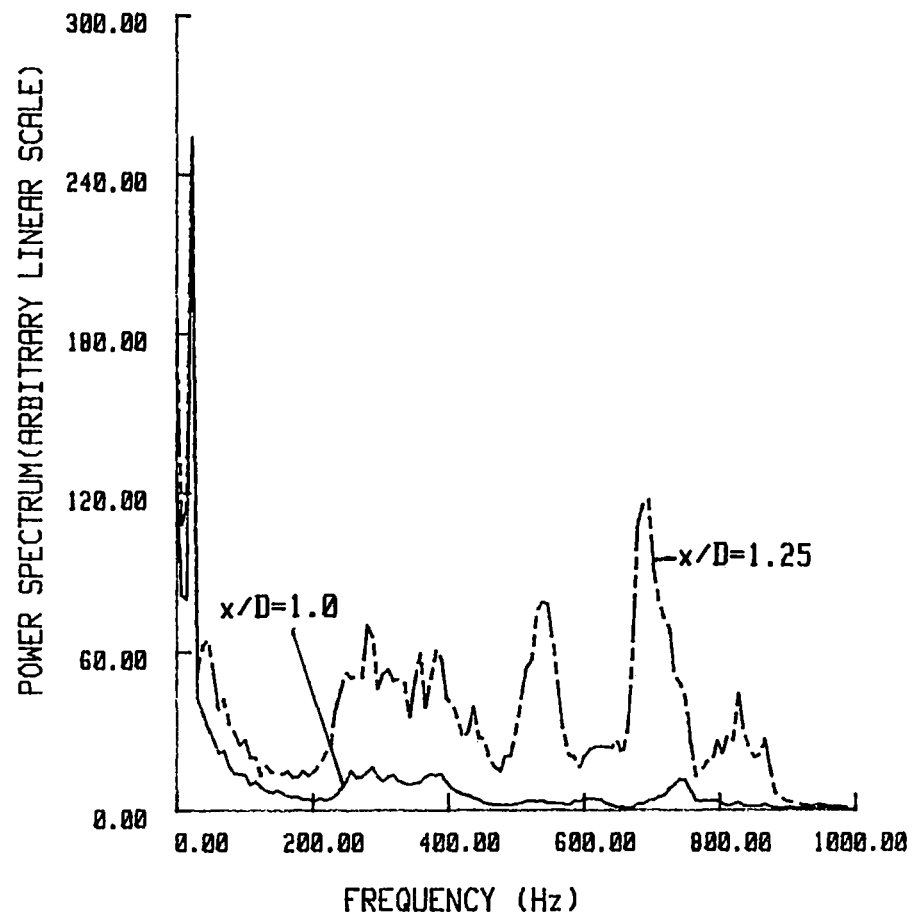


Figure 23. Shear Layer Power Spectra at $x/D = 1.0$ and 1.25

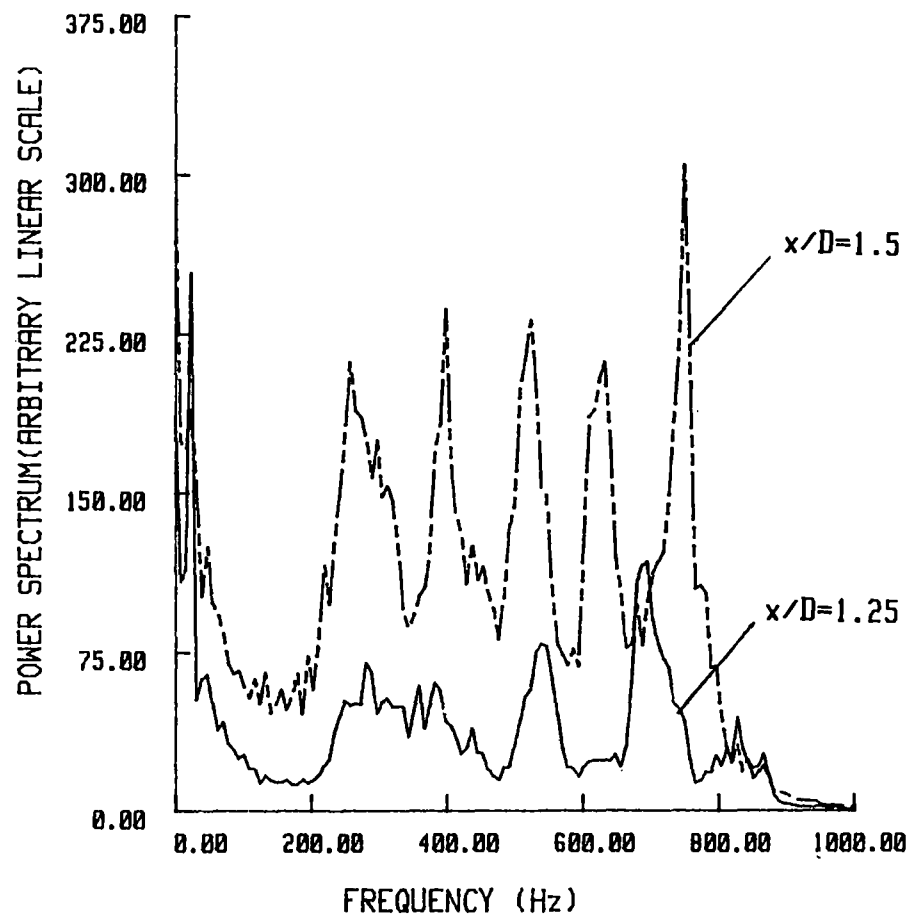


Figure 24. Shear Layer Power Spectra at $x/D = 1.25$ and 1.5

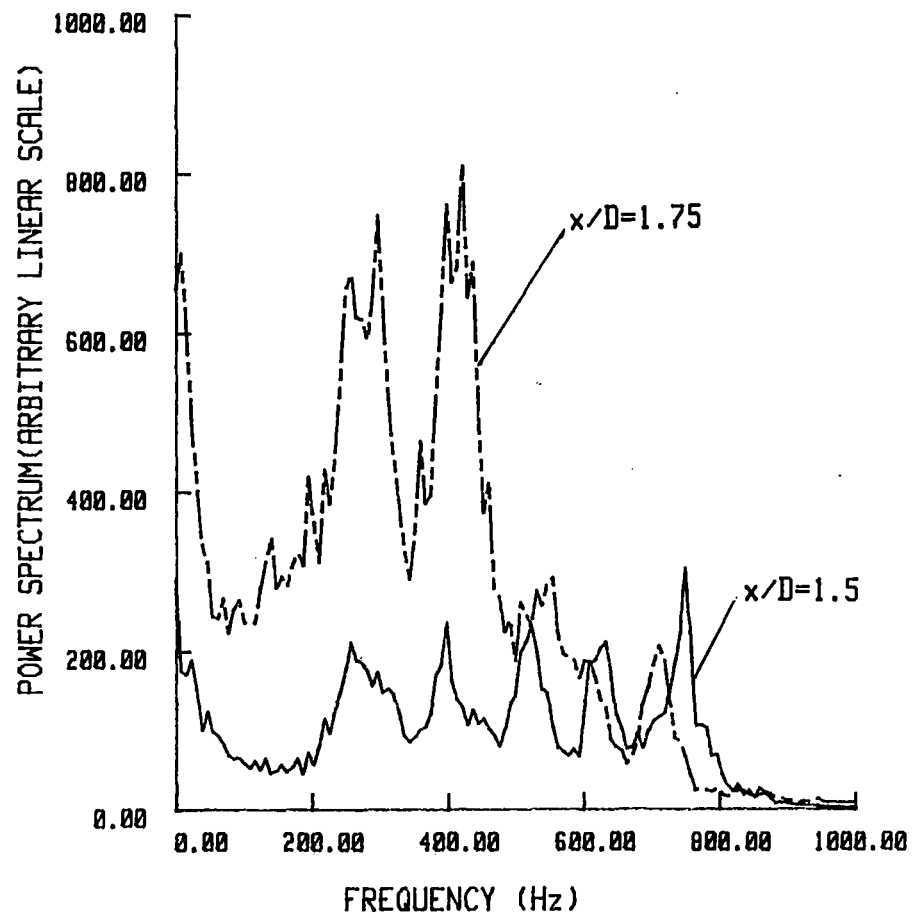


Figure 25. Shear Layer Power Spectra at $x/D = 1.5$ and 1.75

saturation state for this mode is attained. This saturation of the fundamental at 750 Hz (seen also in Figure 19) is associated with the growth of modes at approximately 260, 400, 525 and 630 which are all seen to be separated on average by 123 Hz. With increasing downstream distance the two modes at 260 Hz and 400 Hz are seen to grow as evidenced from Figure 25 (the frequency resolution for these measurements is approximately 9 Hz). The cause for the growth of these two modes is more thoroughly investigated in Chapter V. Figure 25 also shows the development of 'sidebands' on both the primary modes. The frequency spacing between the sidebands corresponds to the low frequency mode at approximately 23 Hz which is also seen in the same figure. Thus, the presence of the sidebands on the 260 Hz and 400 Hz mode as seen in Figure 25 indicates modulation by the low frequency mode. Discussion of the nature of this low frequency mode was presented in the previous section. This mode originally appeared in the power spectra very near the nozzle exit as a neutral mode exhibiting negligible growth throughout the linear region. Similar spectral measurements reported in the literature for free shear layers have not shown similar low frequency modulation effects. However, work by Laufer and Monkewitz (1980) has demonstrated a similar modulation effect in the initial region of a round jet while Miksad et al (1982) considered the effects of modulation on two-dimensional wake transition.

Figures 26 and 27 present results of shear layer spectral measurements at the same streamwise locations as presented earlier, but for a different trial. It may be seen from these figures that all the dominant spectral peaks exhibit stronger sideband structure at an earlier x/D station compared with those in Figures 24 and 25. The

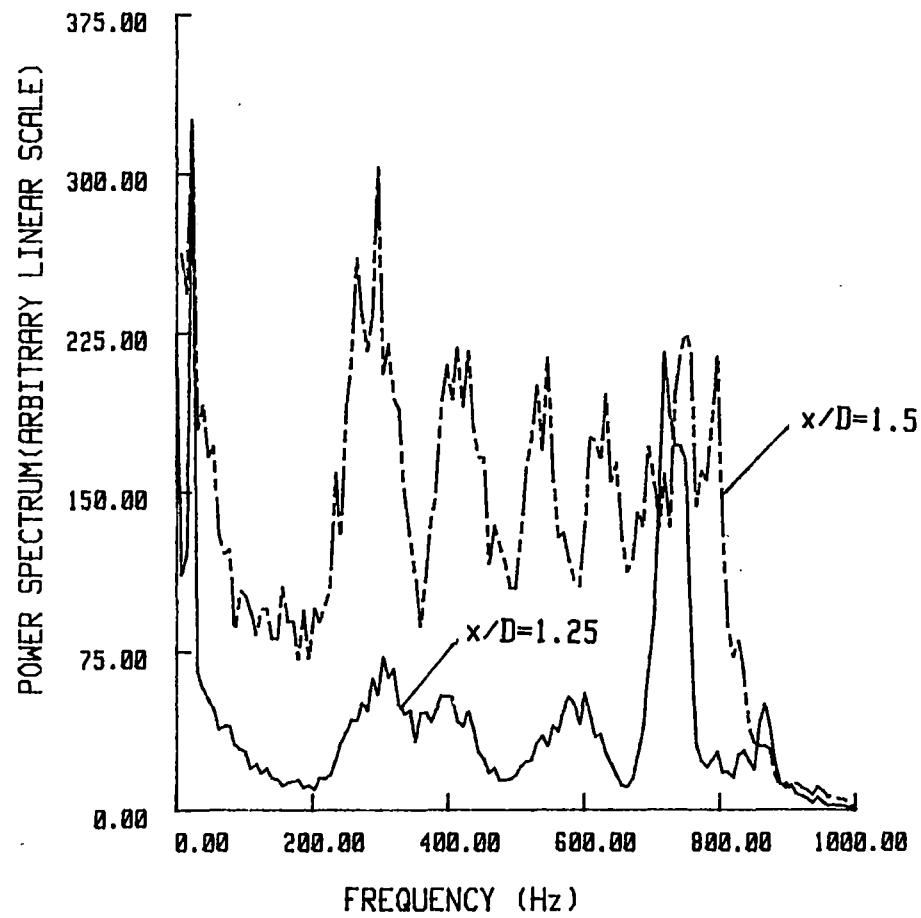


Figure 26. Shear Layer Power Spectra from a Different Trial at $x/D = 1.25$ and 1.5

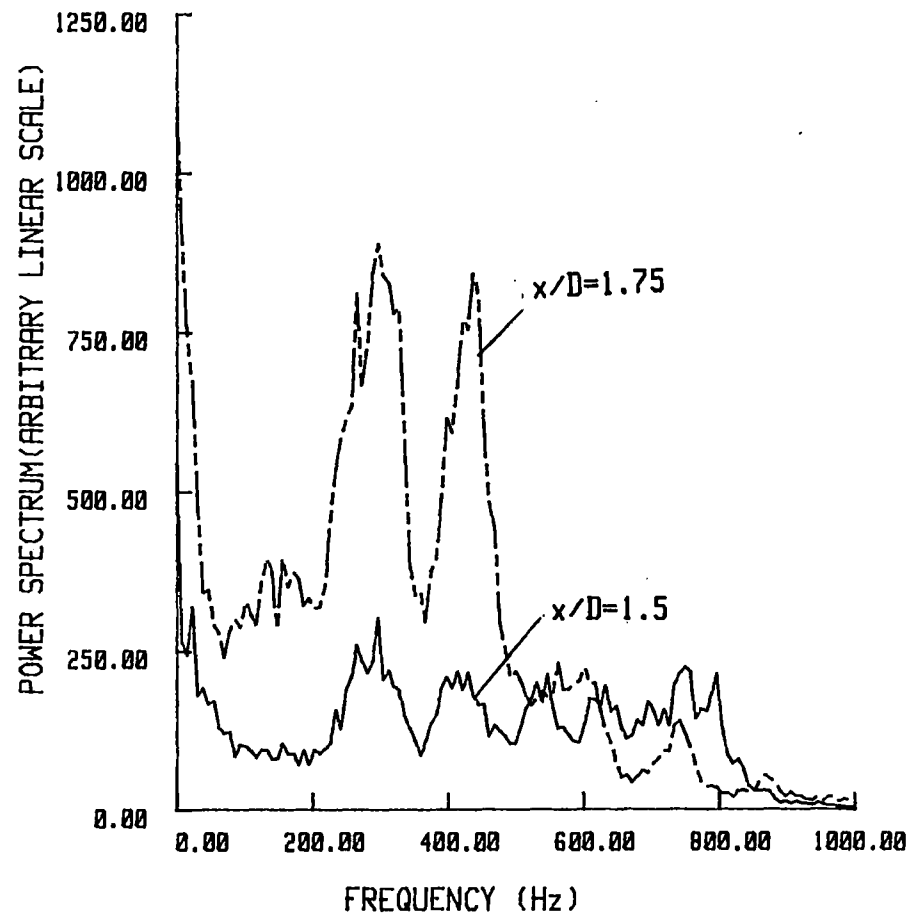


Figure 27. Shear Layer Power Spectra from a Different Trial at $x/D = 1.5$ and 1.75

presence of stronger sidebands is due to the fact that the modulating mode was somewhat higher in amplitude in this set of measurements as compared with the Figures 24 and 25. In general, this low frequency mode, though always present, did exhibit some variation in near exit amplitude which led to corresponding modification of sideband evolution. The data to be presented are considered typical of several trials, however. Irrespective of the amplitude of the low frequency mode there is always a transformation of energy to the two dominant modes near 260 and 400 Hz at a downstream location of $x/D \approx 1.5$.

The frequency resolution for these spectral measurements as mentioned earlier is 9 Hz and hence it is possible for a particular spectral mode to exhibit some variation as to its measured frequency. Such a variation is seen in Figure 28 where a spectral peak near 250 Hz is the mode previously referred to as 260 Hz. In all future references this mode is referred to as 250 Hz. Figures 28 and 29 demonstrate the continued growth of the mode near 250 Hz which becomes dominant over the 400 Hz mode. The 250 Hz mode reaches a saturation state near $x/D \approx 2.25$. The nonlinear formation and growth of the mode near 250 Hz is very suggestive of the vortex roll-up process that has often been visualized in free shear layers. Ho and Huerre (1984) related the completion of the roll-up process to the downstream location where the fundamental frequency reaches its maximum amplitude. It must be noted that for free shear layers, roll-up will occur at the initially most amplified frequency (see Ho and Huang (1982), Ho and Huerre (1984)). This is obviously not the case for the planar jet as the spectral data has indicated that the most amplified frequency saturates quickly ($x/D \approx 1.50$) at a comparatively low amplitude while the slower growing mode

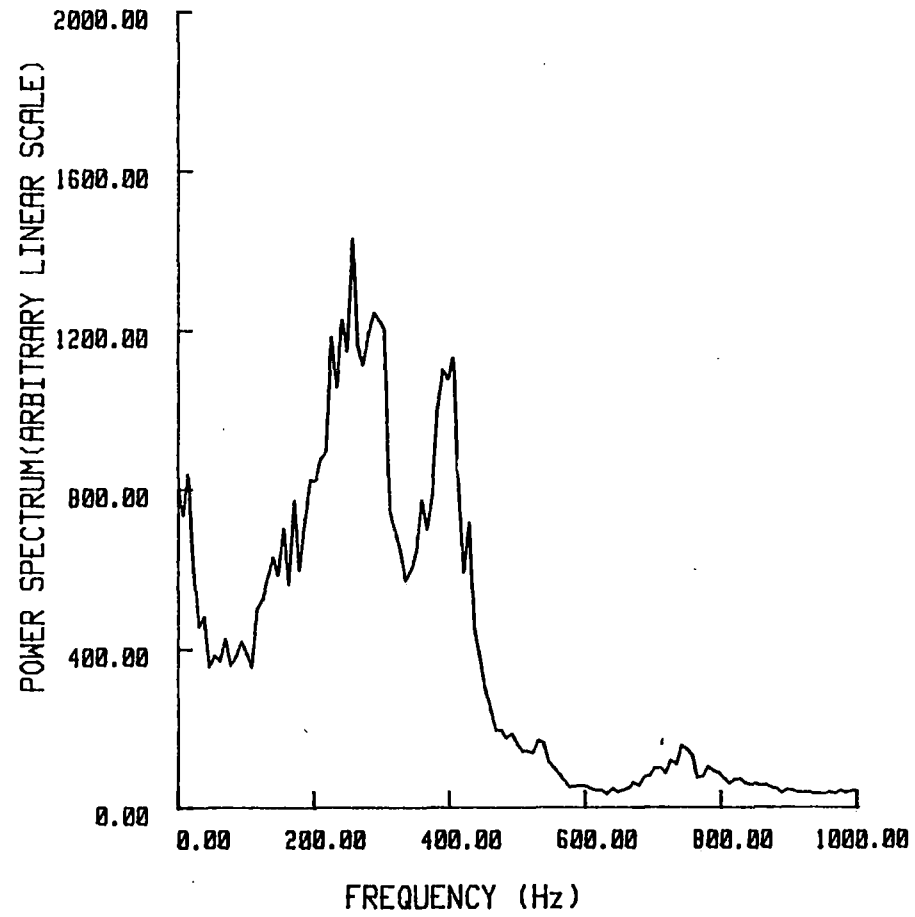


Figure 28. Shear Layer Power Spectrum at $x/D = 2.0$

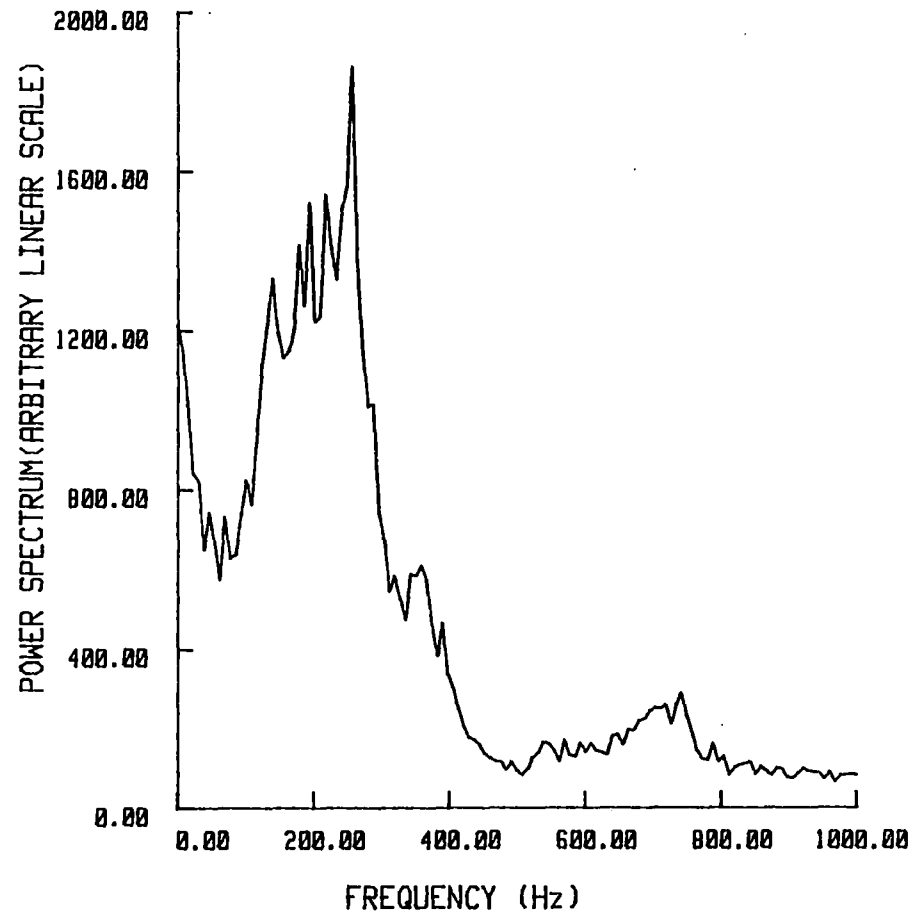


Figure 29. Shear Layer Power Spectrum at $x/D = 2.25$

near 250 Hz eventually reaches much higher amplitude and suggests vortex formation occurs, on average, near that frequency. Figure 30 compares the streamwise growth of these two modes in the developing jet shear layer (bandwidth 10 Hz). This substantial deviation of the jet shear layer behavior from that reported for mixing layers is likely be due to the fact that the jet contains an additional imposed length scale which is the jet slot width D . This will be elaborated upon in Chapter V.

Ho and Huang (1982) have demonstrated that the location of subharmonic saturation corresponds to the streamwise location where vortex pairing is accomplished in free shear layers, though it is difficult to pinpoint a particular location since it requires some streamwise distance to occur. Figure 31 shows the streamwise growth and decay of the 250 Hz mode along with its subharmonic at approximately 125 Hz. In this figure the 125 Hz mode is seen to saturate at $x/D \approx 4.5$ indicating a vortex pairing event occurs near that approximate location. Figures 32 and 33 present the power spectra in the shear layer from $x/D = 2$ to 4.5. These figures clearly show a sequence involving the approximate halving of modal frequency which suggests the pairing of vortical structures over these streamwise locations as described above. With increasing distances downstream there is a gradual shift in the energy to lower frequencies as seen in Figures 34 to 36. Modulation effects have been shown to play an important role in this energy transfer phenomenon, which is characterized by the formation of multiple sidebands. These sidebands are asymmetric about the principle mode they modulate, generally favoring the low frequency side. Miksad (1972) noted that nonlinear interaction between modes at two different frequencies in a free shear layer resulted in the

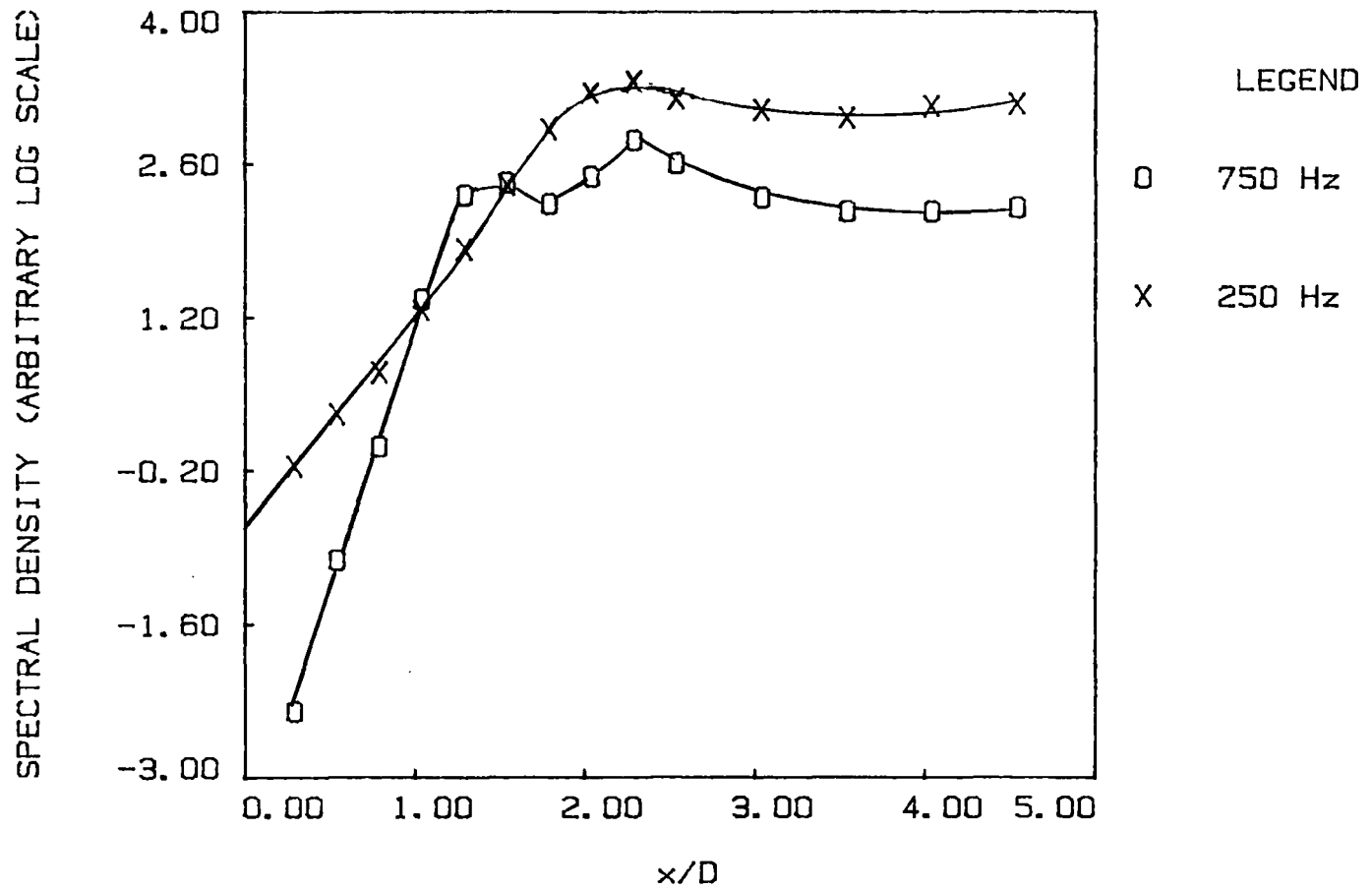


Figure 30. Comparison of The Growth of 750 Hz
 (Bandwidth of 10 Hz) and 250 Hz (Bandwidth
 10 Hz) at the Shear Layer

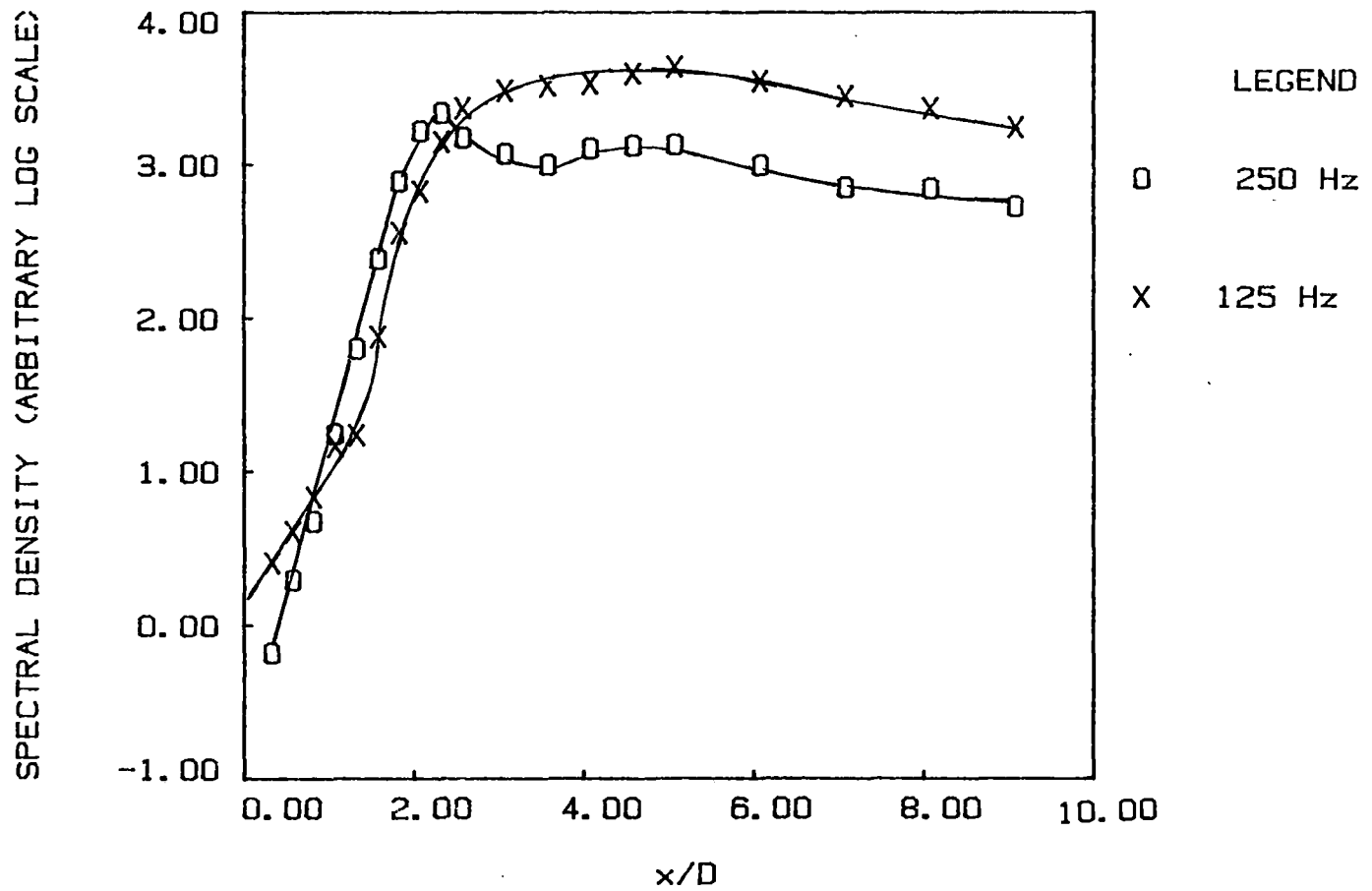


Figure 31. Growth and Decay of 250 Hz (bandwidth 10 Hz) and 125 Hz (bandwidth 10 Hz) at the Shear Layer

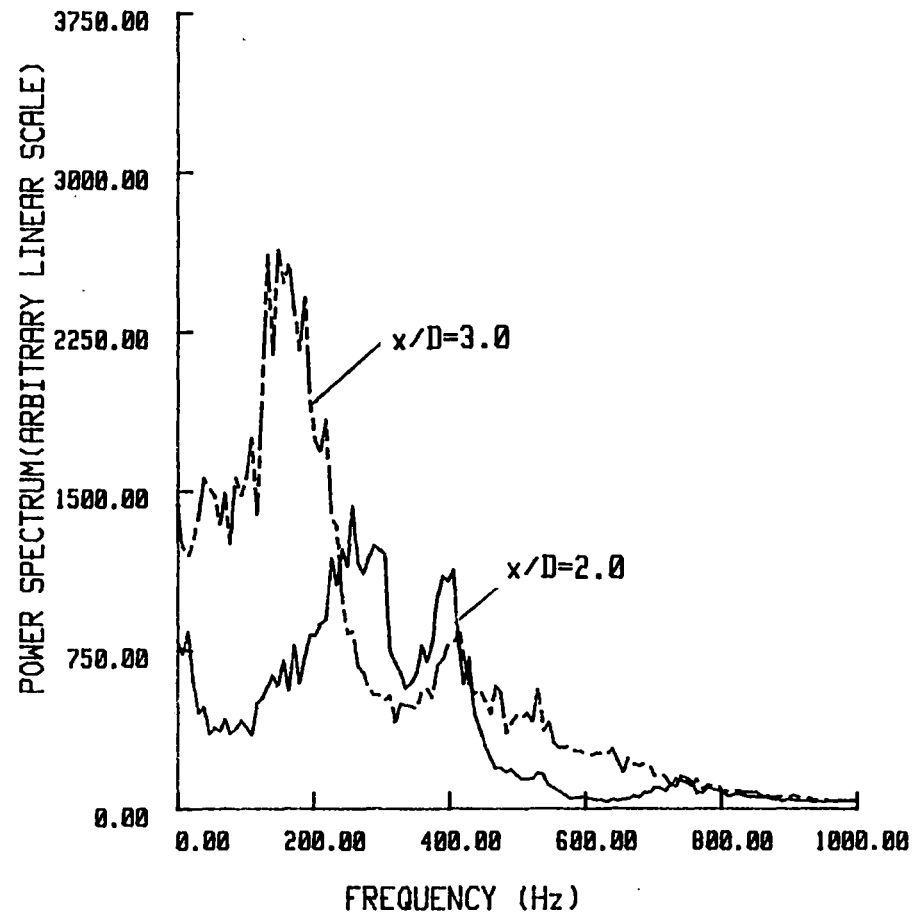


Figure 32. Shear Layer Power Spectra at $x/D = 2$ and 3

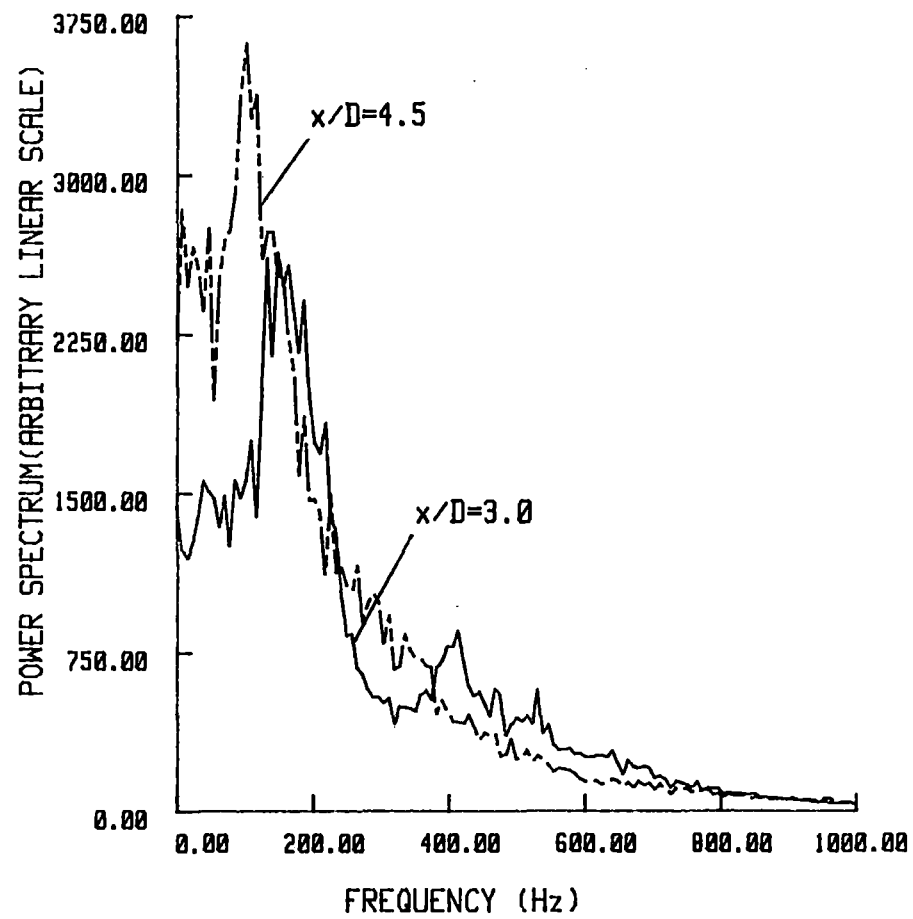


Figure 33. Shear Layer Power Spectra at
 $x/D = 3$ and 4.5

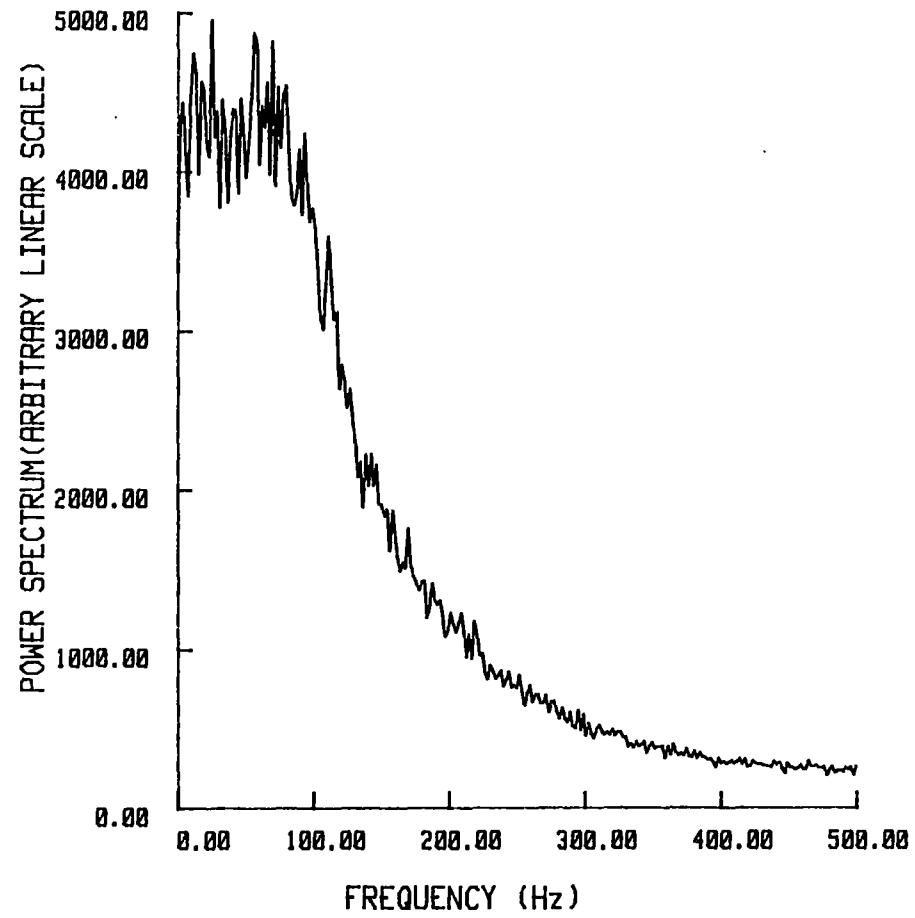


Figure 34. Shear Layer Power Spectrum
at $x/D = 6$

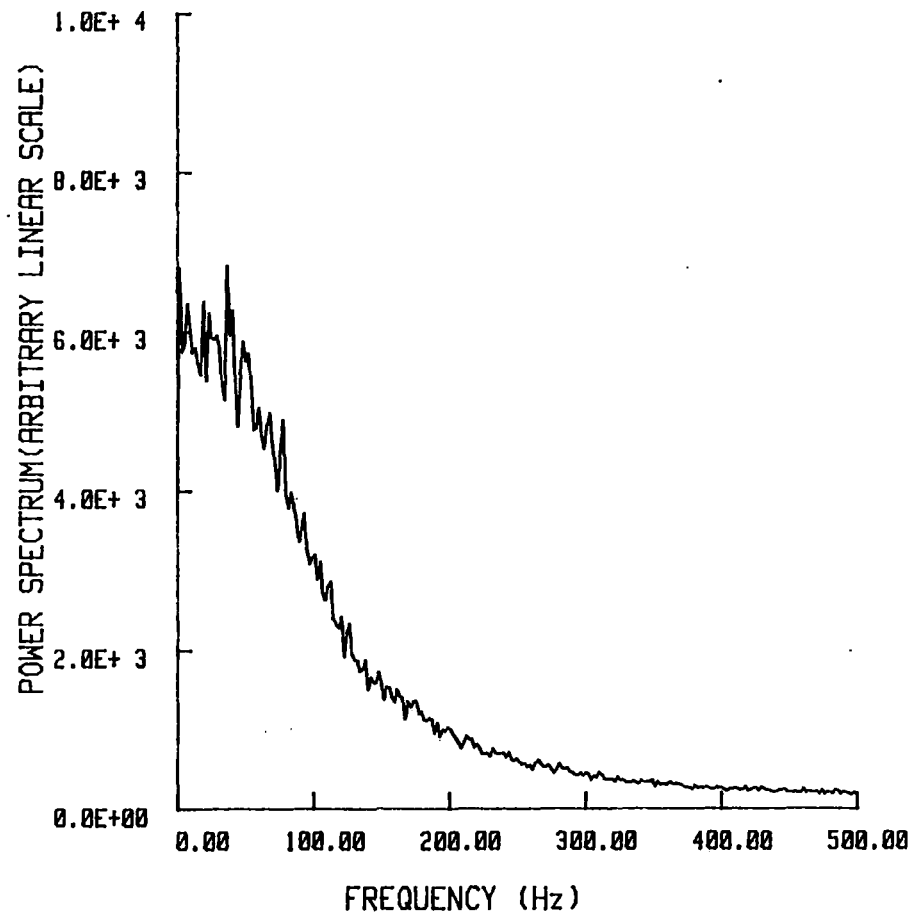


Figure 35. Shear Layer Power Spectrum at $x/D = 7$

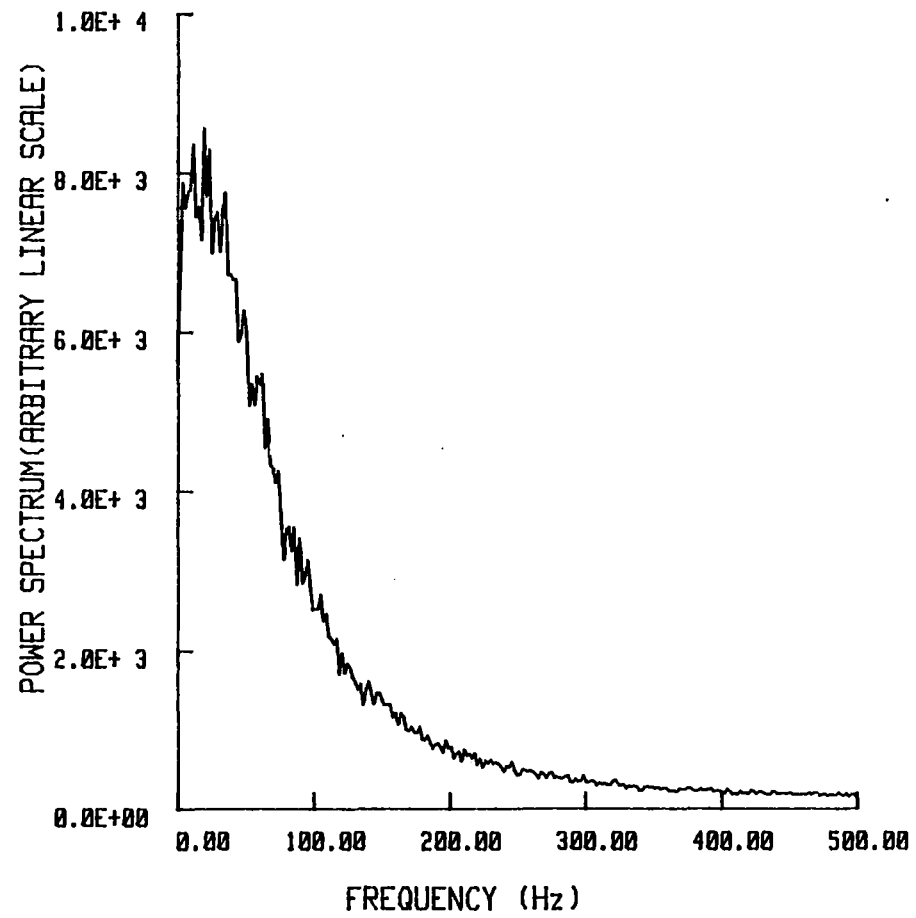


Figure 36. Shear Layer Power Spectrum at $x/D = 8$

formation of sum and difference modes as well as the harmonics and subharmonics of the interacting waves. Such nonlinear interactions between sidebands appears to be a primary cause for the energy transfer to lower frequencies noted in the jet shear layer spectra. The shear layer spectra at $x/D = 9, 10, 12,$ and 20 are presented in Figure 37 through 40. They are basically broadband in nature which is indicative of the flow being turbulent at these locations.

Spectra of longitudinal velocity fluctuations obtained on the jet centerline are sequentially presented in Figures 41 through 48. It is expected that velocity fluctuations in the jet potential core are induced by the large-scale structural events occurring in the shear layers. Hence, the centerline power spectra show more distinct peaks as compared to those of shear layer spectra which are obscured by high levels of fine grain turbulence. From Figures 43 through 45 a gradual halving in the peak spectral frequency is noted to occur over the downstream distance $4 < x/D < 7$. This halving appears to correspond to the merging of structures noted to occur in the shear layer from $x/D = 2.00$ to 4.5 (Figures 32 and 33). If it is assumed that the fluctuations in the potential core are manifestations of events occurring in the jet shear layers then it is expected that the frequency halving seen in the centerline spectra would occur some distance downstream of the actual location of vortex merging in the shear layers. The mean velocity profile as presented in Figures 5 and 6 show the disappearance of the "flat profile shape" (characteristic of a potential core) by approximately $x/D = 7.0$ giving strong evidence as to the location of the end of the potential core. This results in the merging of the two shear layers and an interaction between the structures emanating from them. Evidence

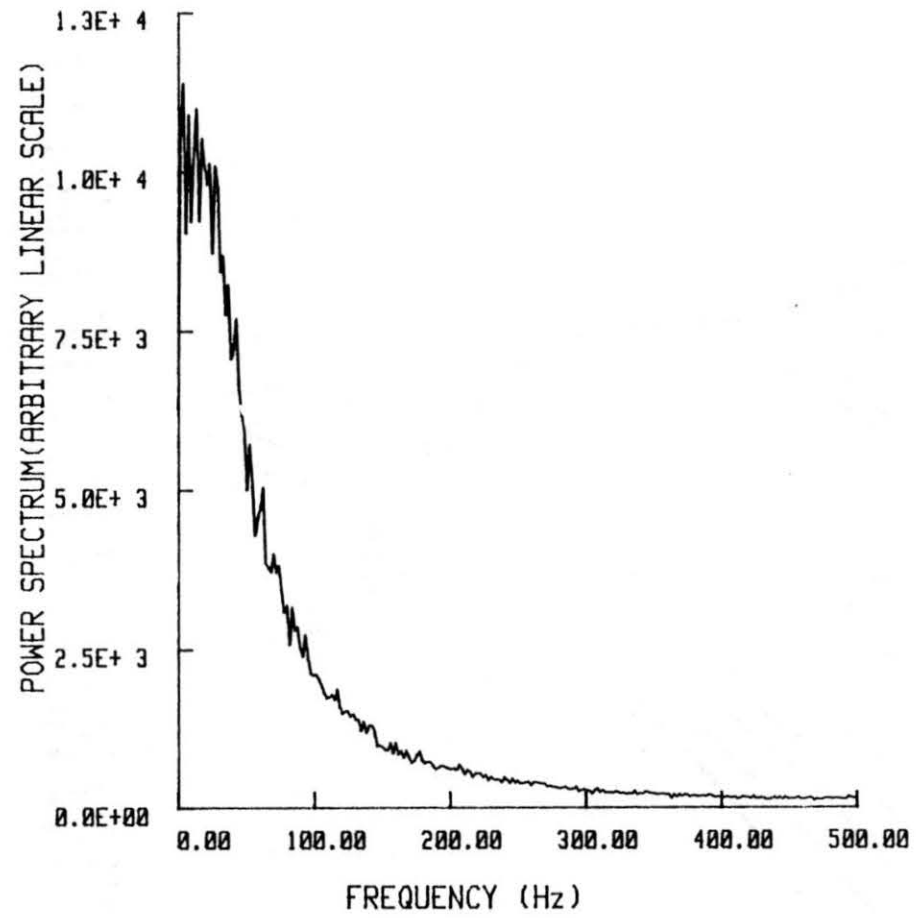


Figure 37. Shear Layer Power Spectrum at $x/D = 9$

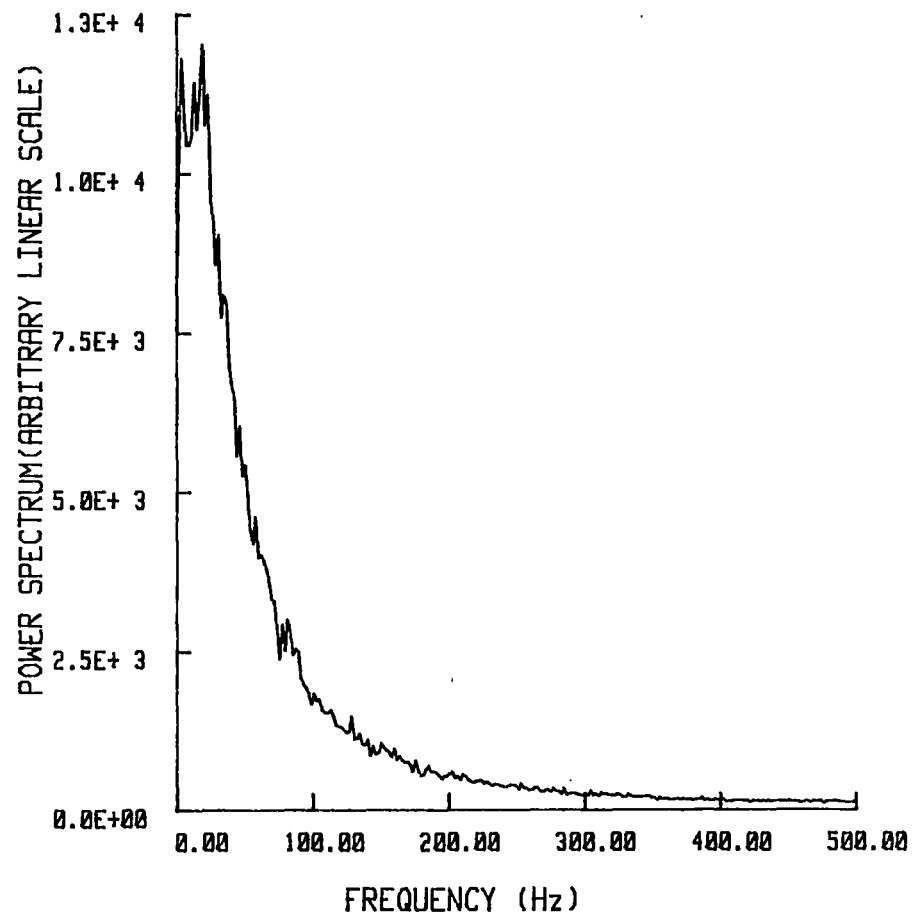


Figure 38. Shear Layer Power Spectrum at
 $x/D = 10$

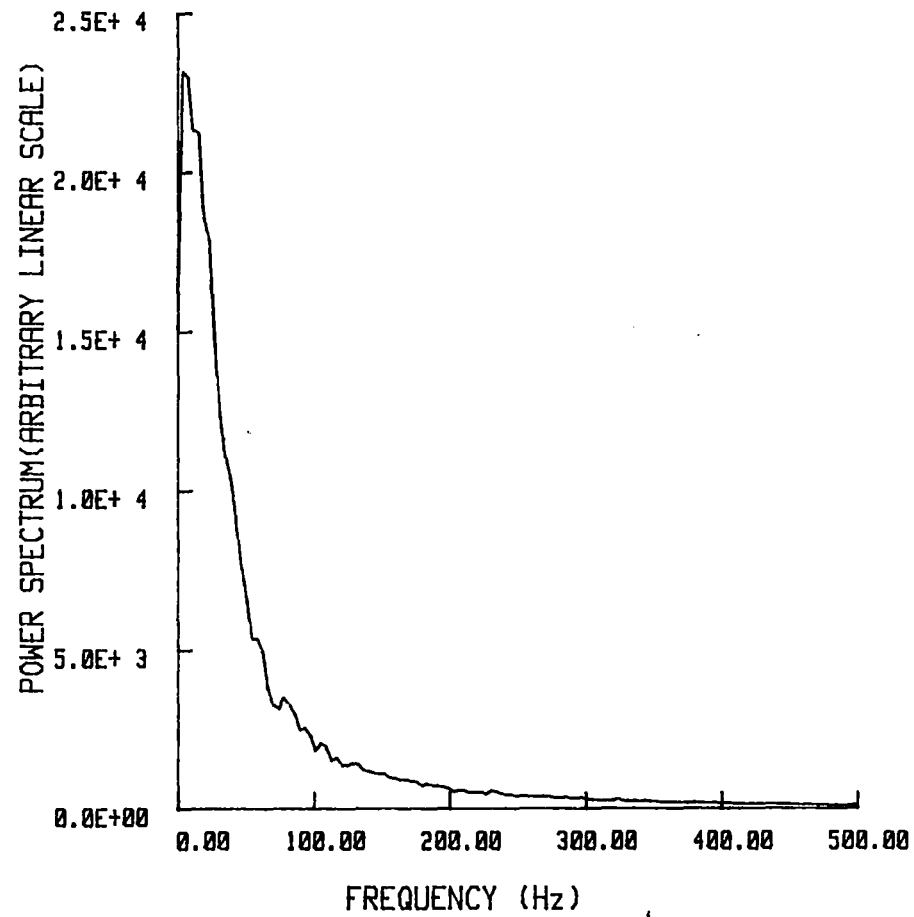


Figure 39. Shear Layer Power Spectrum at
 $x/D = 12$

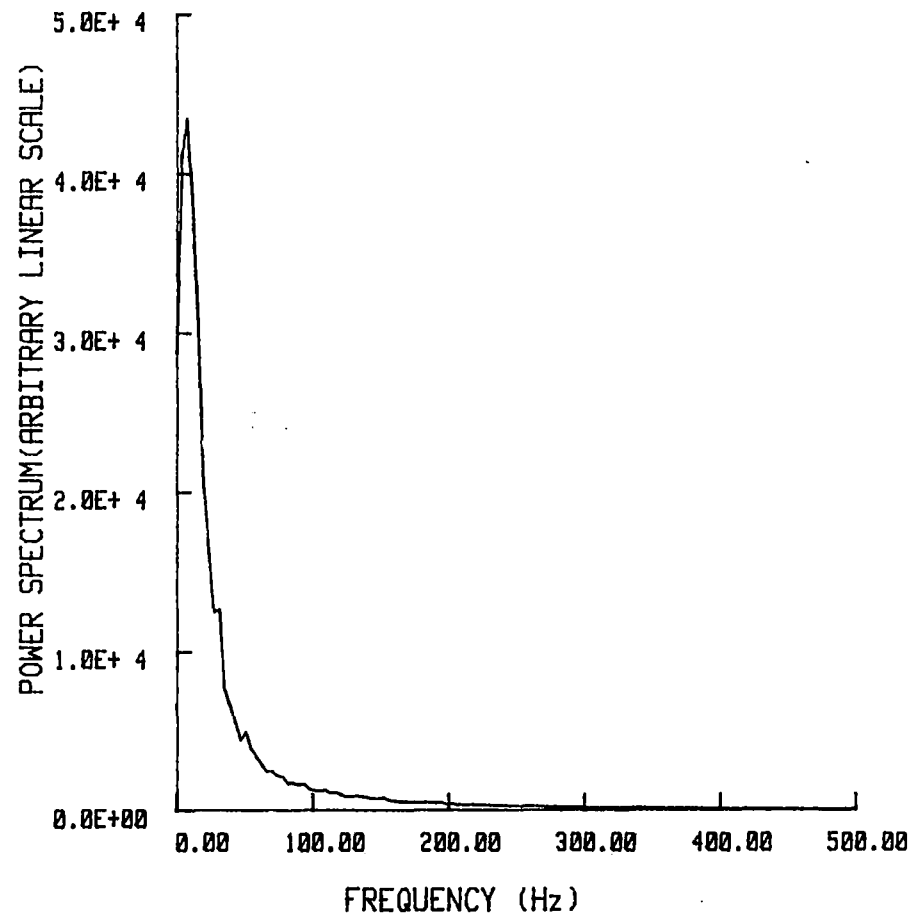


Figure 40. Shear Layer Power Spectrum at $x/D = 20$

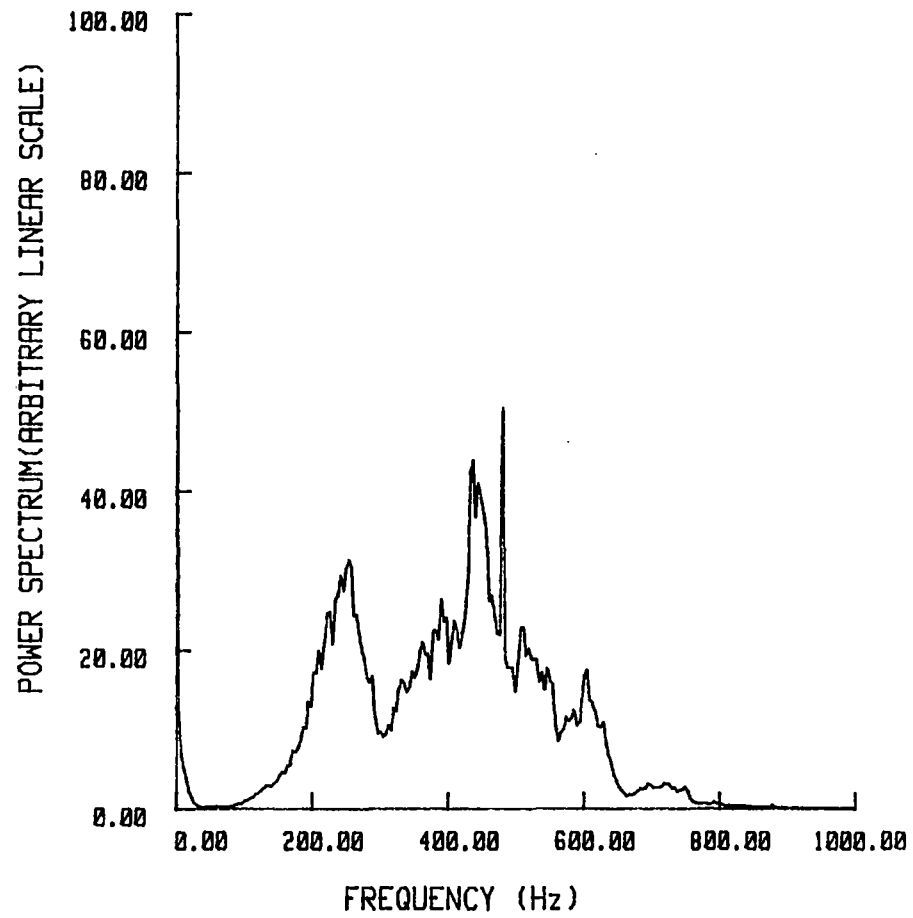


Figure 41. Centerline Power Spectrum at
 $x/D = 2$

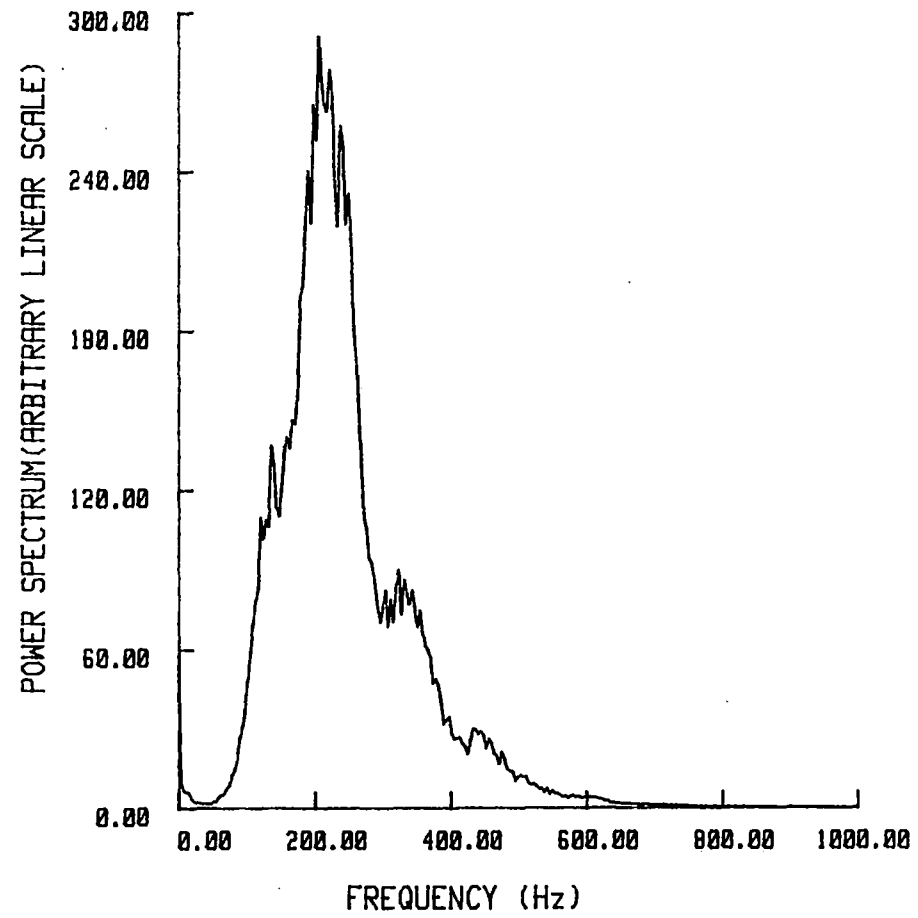


Figure 42. Centerline Power Spectrum at
 $x/D = 3$

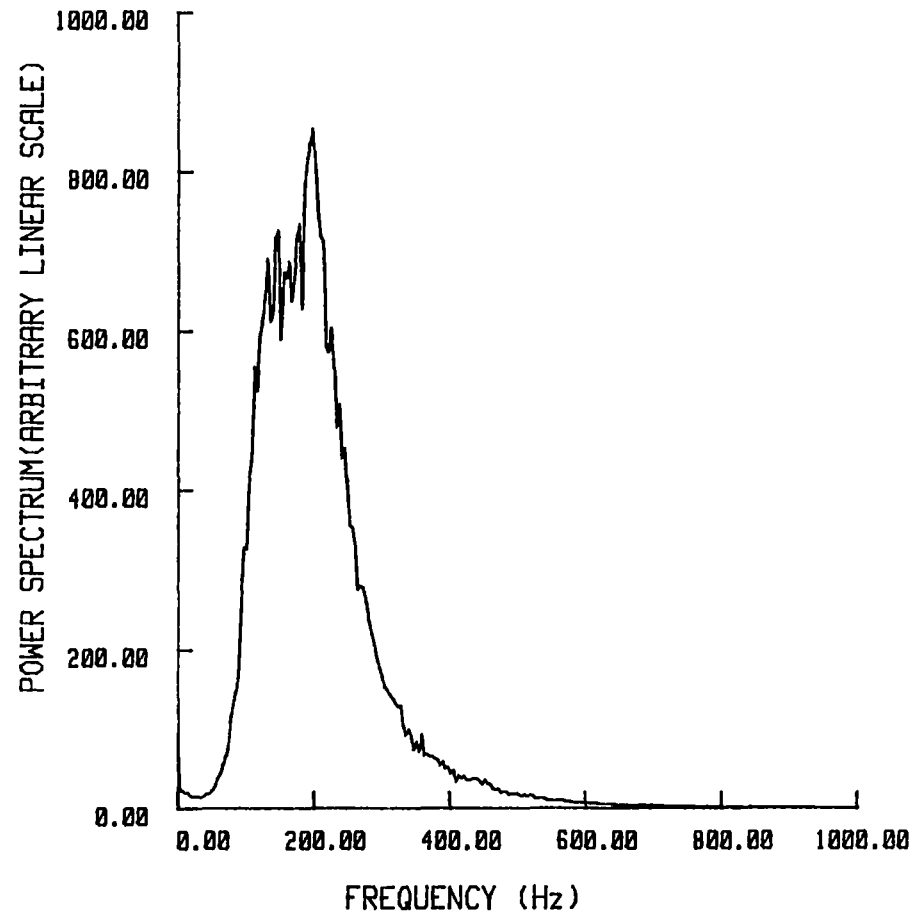


Figure 43. Centerline Power Spectrum at
 $x/D = 4$

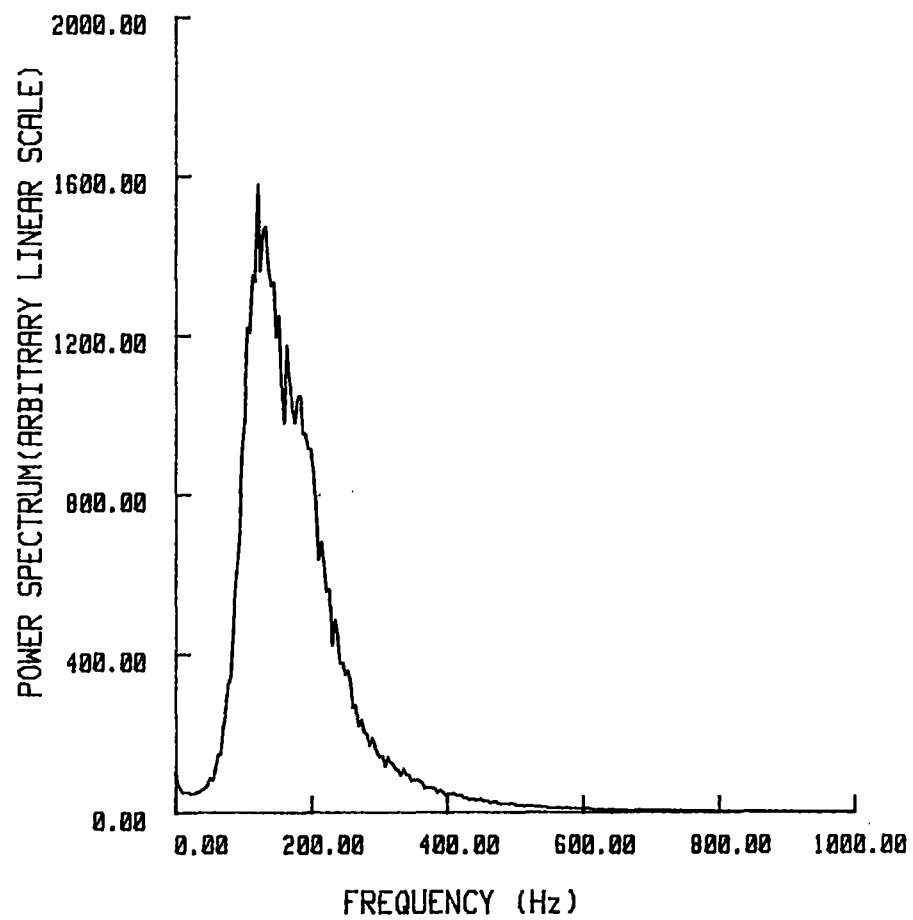


Figure 44. Centerline Power Spectrum at
 $x/D = 5$

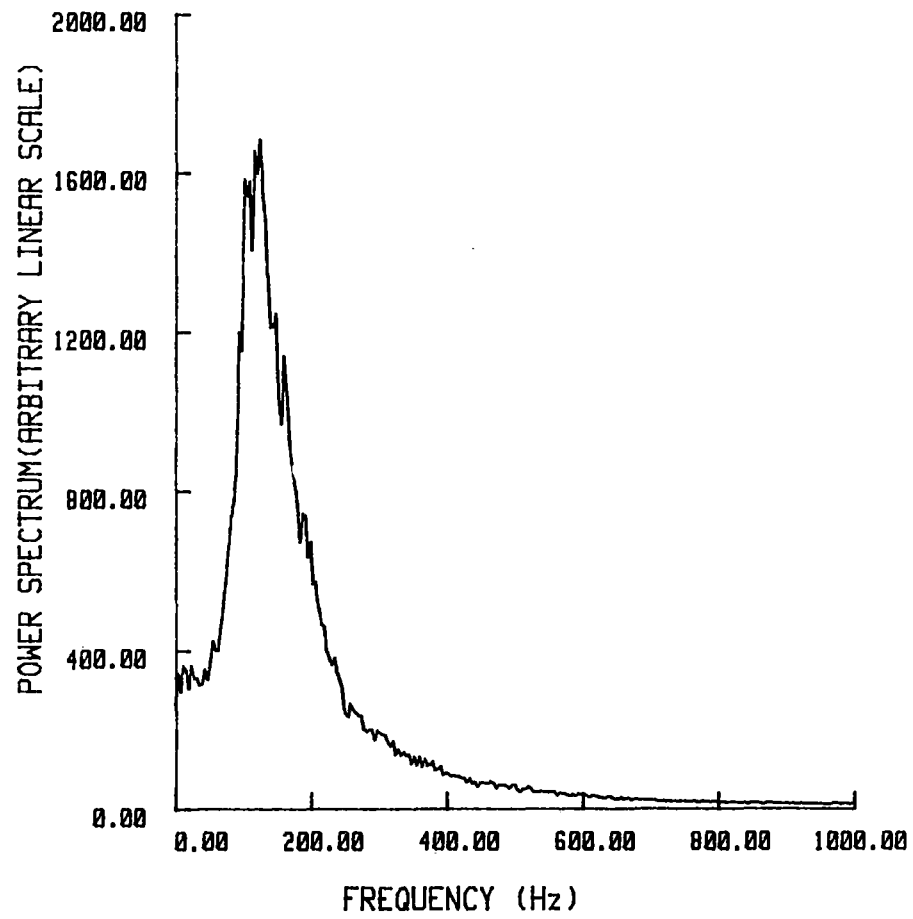


Figure 45. Centerline Power Spectrum at $x/D = 6$

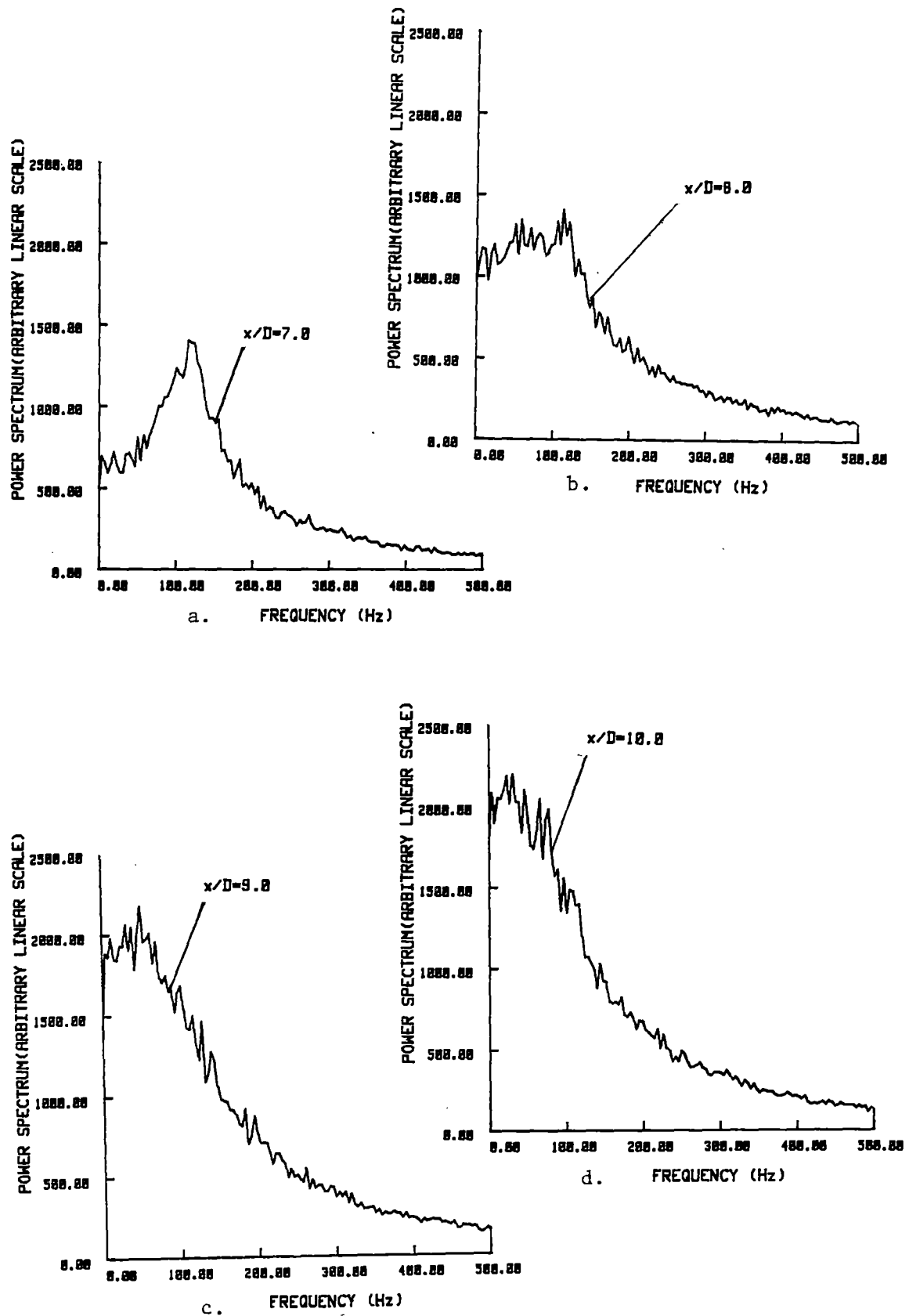


Figure 46. Centerline Power Spectra at $x/D = 7, 8, 9$ and 10

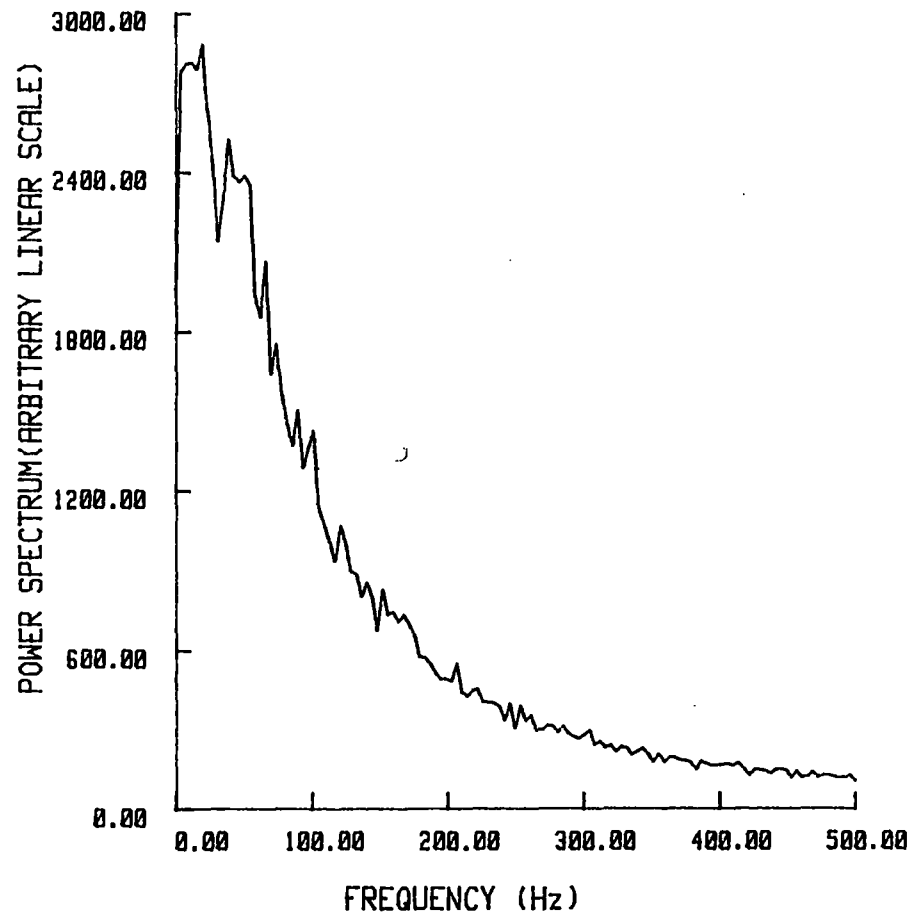


Figure 47. Centerline Power Spectrum at
 $x/D = 12$

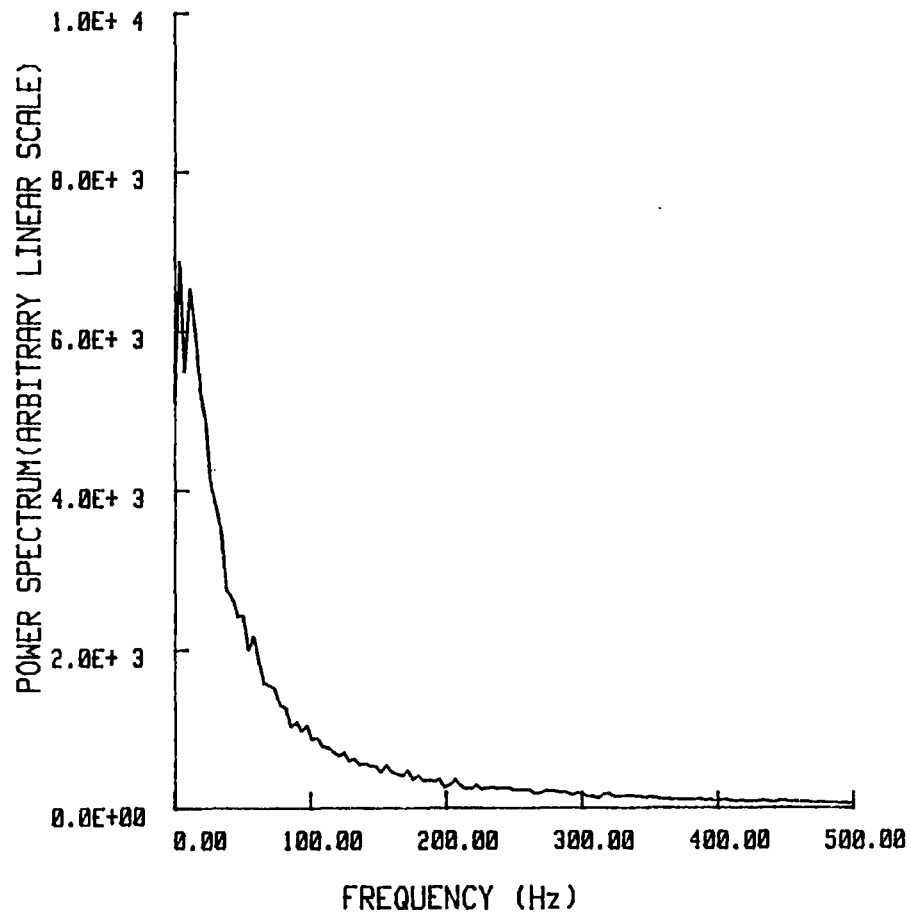


Figure 48. Centerline Power Spectrum at
 $x/D = 20$

of structural interaction is clearly seen from the centerline spectra at $x/D = 7, 8, 9,$ and 10 as presented in the sequence of Figure 46. Also from the figure two consecutive halvings in frequency are seen, giving indication of a multiple merging/destruction event involving the interacting large-scale structures. Such an event is obscured in the shear layer spectra due to the presence of high turbulence levels. The centerline spectra at $x/D = 12$ and 20 as seen in Figures 47 and 48 are broadband in nature. The high level turbulence present at these locations makes it difficult to discern the large-scale flow structures even though they are present, as will be demonstrated in measurements to be presented in the following sections.

The next section presents two point correlation measurements between fluctuations in the jet shear layers obtained for selected streamwise locations within the region $1/4 < x/D < 20$. These measurements will provide more insight as to the relationship of the structural patterns in the two developing jet shear layers.

4.2 Longitudinal Space-Time Correlation

Space-time correlation of longitudinal fluctuations were made to provide additional information concerning the structural patterns in the flow. For this purpose two conventional straight-wire probes were positioned on opposite sides of the jet centerline at $y/b = \pm 1.0$ as shown schematically in Figure 49 at selected streamwise locations in the developing jet. This lateral probe separation is large compared to the length scales of the fine grained velocity fluctuations and hence such a measurement is expected to highlight mainly the effects of the large-scale flow. The space-time correlation between two velocity

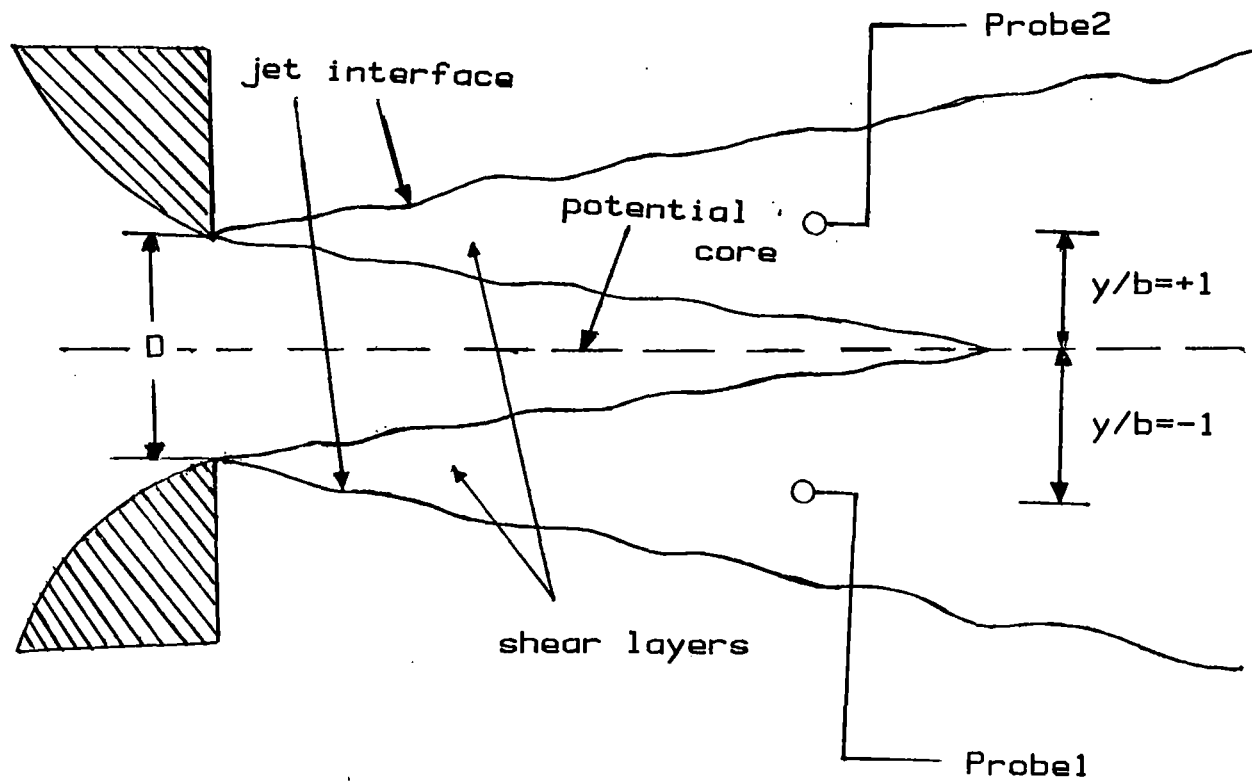


Figure 49. Probe Arrangement for Space-Time Correlation Measurements

fluctuations u_1 and u_2 is defined in Equation 4-1.

$$R_u(\Delta y, \tau) = \lim_{T \rightarrow \infty} \frac{1}{T} \int_0^T u(y=b, t) u(y=-b, t+\tau) dt \quad (4-1)$$

where Δy is the lateral probe separation, τ is the time delay between the two signals and T is the time period over which the correlation will be averaged. The form of the equation for digital signals which corresponds to Equation 4-1 is Equation 4-2.

$$R_{12}(r\Delta t) = 1/N-r \sum_{n=1}^{N-r} (e_1)_n (e_2)_{n+r} \quad (4-2)$$

where Δt is the sampling rate and r is the number of data points shift between signals e_1 and e_2 (which is analogous to τ). The factor $1/N-r$ appears in the equation to account for fewer datum points being available for correlation as the time-delay is increased. Normalizing the correlation function by the rms velocity fluctuations of the two signals results in the correlation coefficient.

$$\rho_{12}(r\Delta t) = \frac{R_{12}(r\Delta t)}{\sqrt{\overline{e_1^2}} \sqrt{\overline{e_2^2}}} \quad (4-3)$$

The advantage of using the correlation coefficient is that this quantity is bounded by 1 and -1. The PASCAL computer algorithm used to calculate the correlation function from sampled signals is presented in Appendix A.

Figure 50 presents a typical correlation function obtained in the jet similarity region. The correlation functions in the initial region

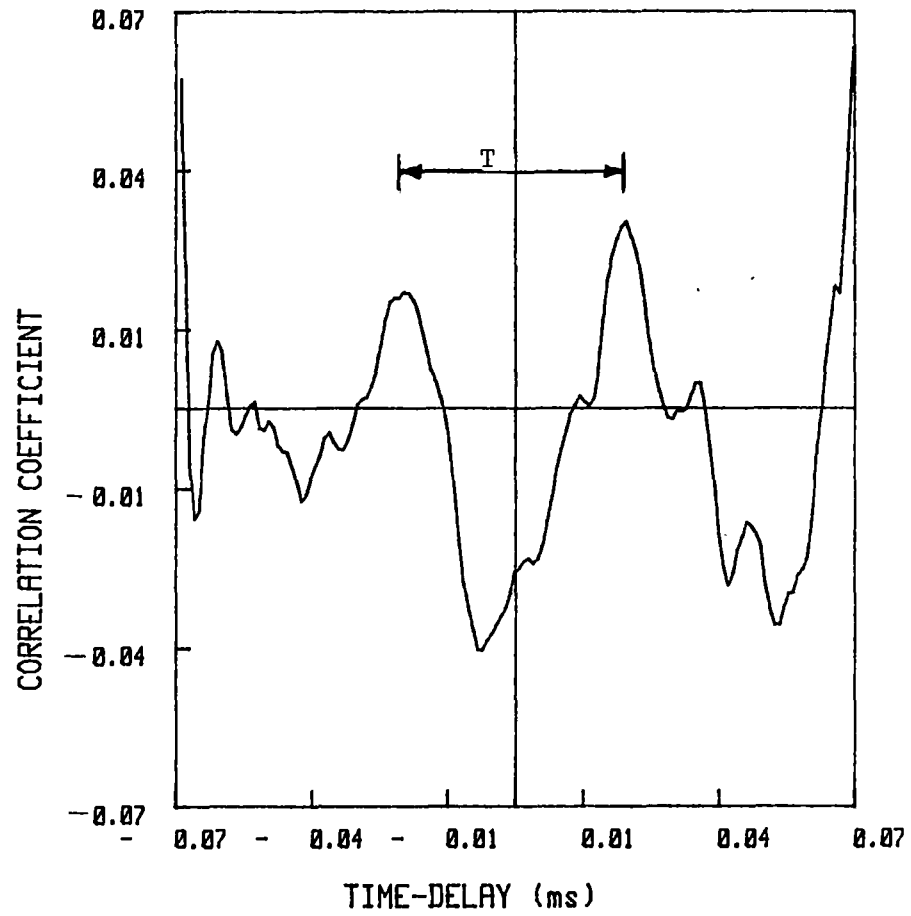


Figure 50. Space-Time Correlation Function
at $x/D = 25$

are different in functional form from those in the similarity region but a general method used to analyze these functions can be described by considering the correlation function presented in Figure 50. A time period for each correlation function could be specified by defining one period of the function T to be the time interval between two consecutive maximum points as shown in Figure 50. The reciprocal of this time period is defined to be the correlation frequency. Thomas and Brehob (1986), Thomas and Goldschmidt (1986) and Cervantes and Goldschmidt (1981) have presented evidence which suggests that the correlation frequency is a measure related to the passage frequency of large scale structures in the flow.

Space-time correlation functions obtained in the linear-region from $x/D = 0.25$ to 0.75 is presented in Figures 51 to 53. These correlation functions are characterized by a strong negative correlation at zero time delay with a correlation frequency of approximately 60 Hz. This negative correlation indicates that the two shear layer longitudinal velocity fluctuation signals on average exhibit opposite signs instantaneously. This strongly suggests the presence of antisymmetric near exit fluctuations in the flow. Such a finding is also in accordance with the shear layer spectra in the linear region (Figure 21) which show the fluctuations energy content to be concentrated in a dominant low frequency neutral mode. Though the correlation frequency estimate is not equal to the frequency of the dominant spectral mode both are at least an order of magnitude below the characteristic instability frequency and are likely related to a similar mechanism which will be discussed in the next section.

Figure 54 shows the correlation obtained at $x/D = 1.0$ which

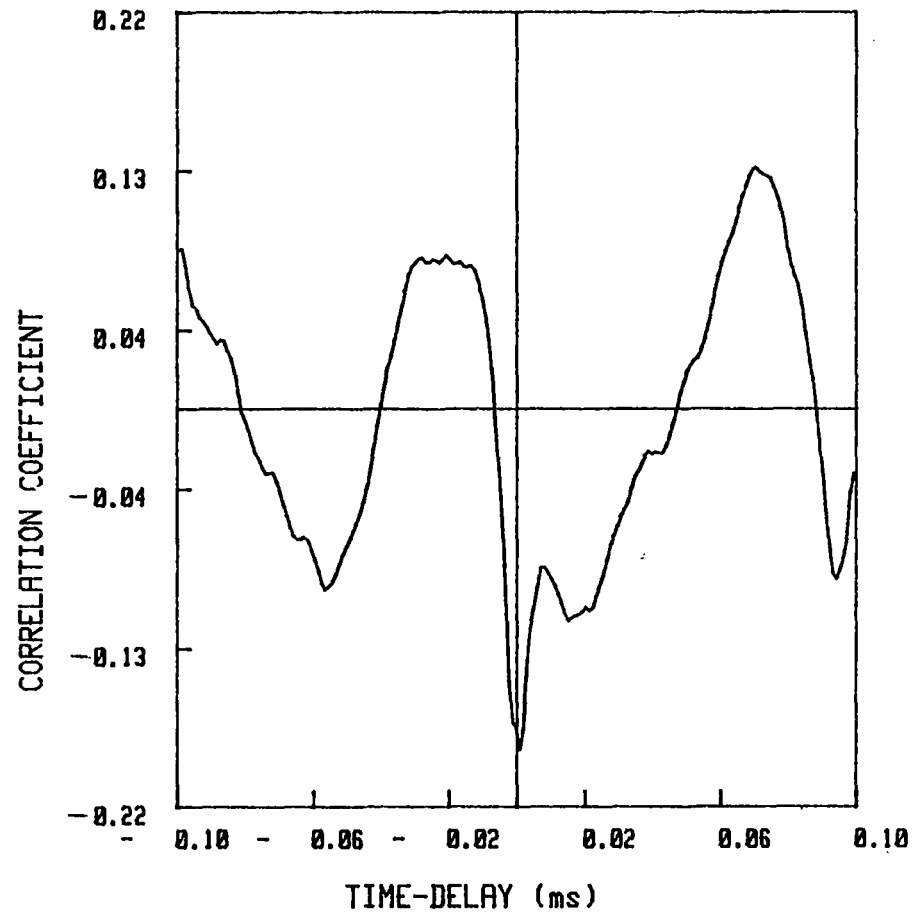


Figure 51. Space-Time Correlation Function
at $x/D = 0.25$

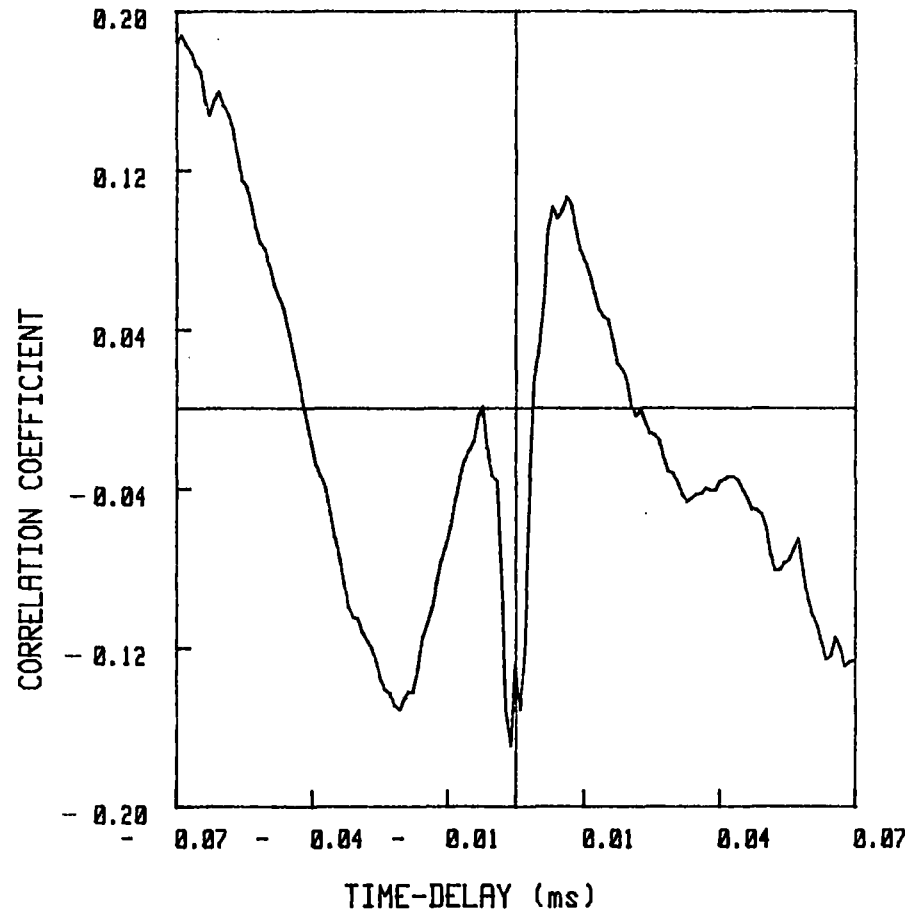


Figure 52. Space-time Correlation Function
at $x/D = 0.5$

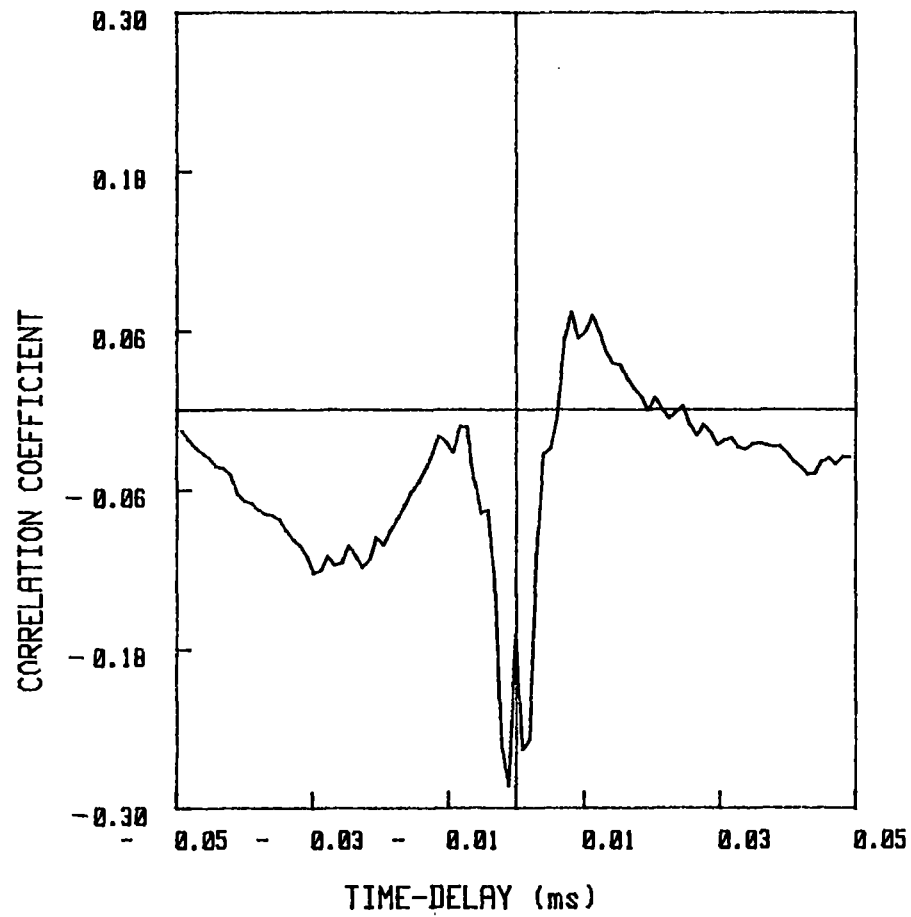


Figure 53. Space-time Correlation Function
at $x/D = 0.75$

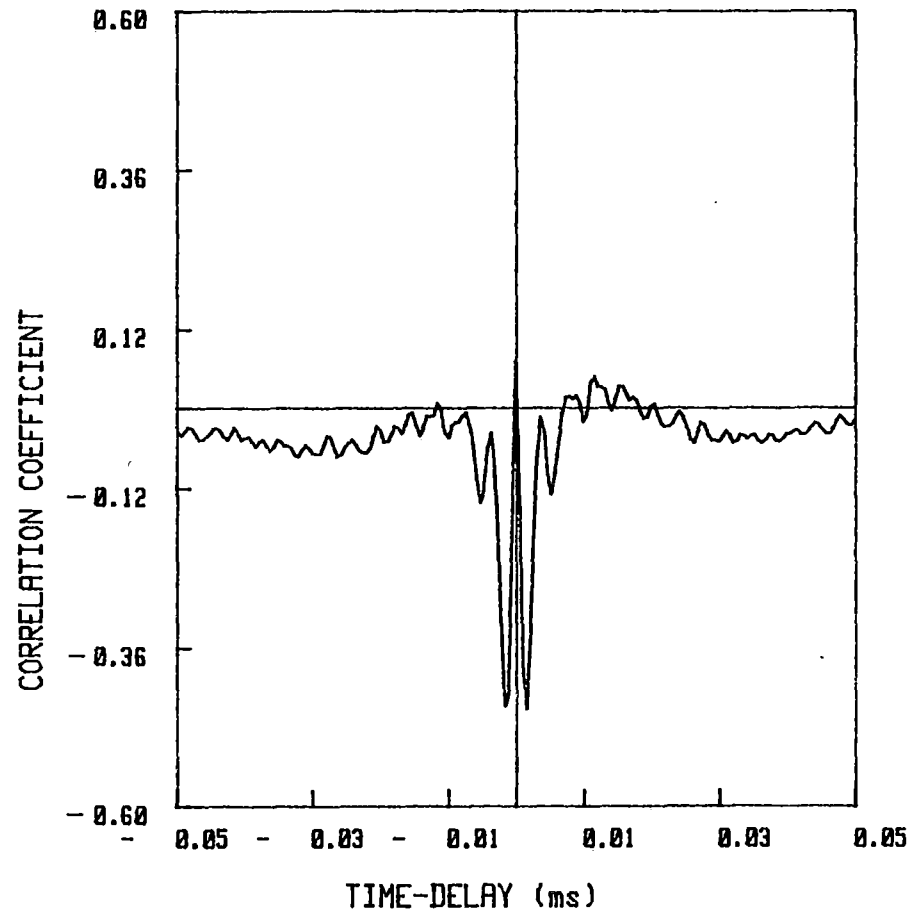


Figure 54. Space-Time Correlation Function
at $x/D = 1.0$

indicates the continued presence of the anti-symmetric mode at this location along with the development of a high frequency mode. Here it should be noted that the time resolution used in these measurements was ≈ 0.002 seconds which corresponds to a frequency of 500 Hz. Hence, any signal with a frequency higher than 500 Hz would be seen in the correlation function plot as 500 Hz. Thus, the high frequency mode (500 Hz) seen in Figure 54 is representative of the most amplified instability wave near 750 Hz which is seen to be symmetrical from the positive correlation exhibited at zero time delay. Figures 55 through 60 present the development of the correlation function for $2.0 \leq x/D \leq 6$. An increase in the positive correlation coefficient at zero time delay by $x/D = 2$ is seen from the Figures 54 and 55. This increase is indicative of the growth of the high frequency symmetric wave which grows to eventually mask the low frequency anti-symmetric wave. A reduction in the correlation frequency to approximately 245 Hz is seen to occur at the x/D locations 2 to 2.5 from Figures 55 and 56. This frequency (245 Hz) agrees well with power spectral measurements at those locations thus providing evidence regarding the approximate location of structural formation. The positive correlation at zero time delay suggests these structures form symmetrically in both jet shear layers. As expected there is a slight decrease in the positive correlation due to the increasing randomization of the waveforms as the flow progresses downstream (which was also noted in a spectral sense as broadening of spectral peaks). A further decrease in the positive correlation with downstream distance is noticeable from Figures 57, 58, 59 and 60. A halving in frequency is noticed at $x/D = 4.0$, but still the symmetric distribution of the structural pattern is well

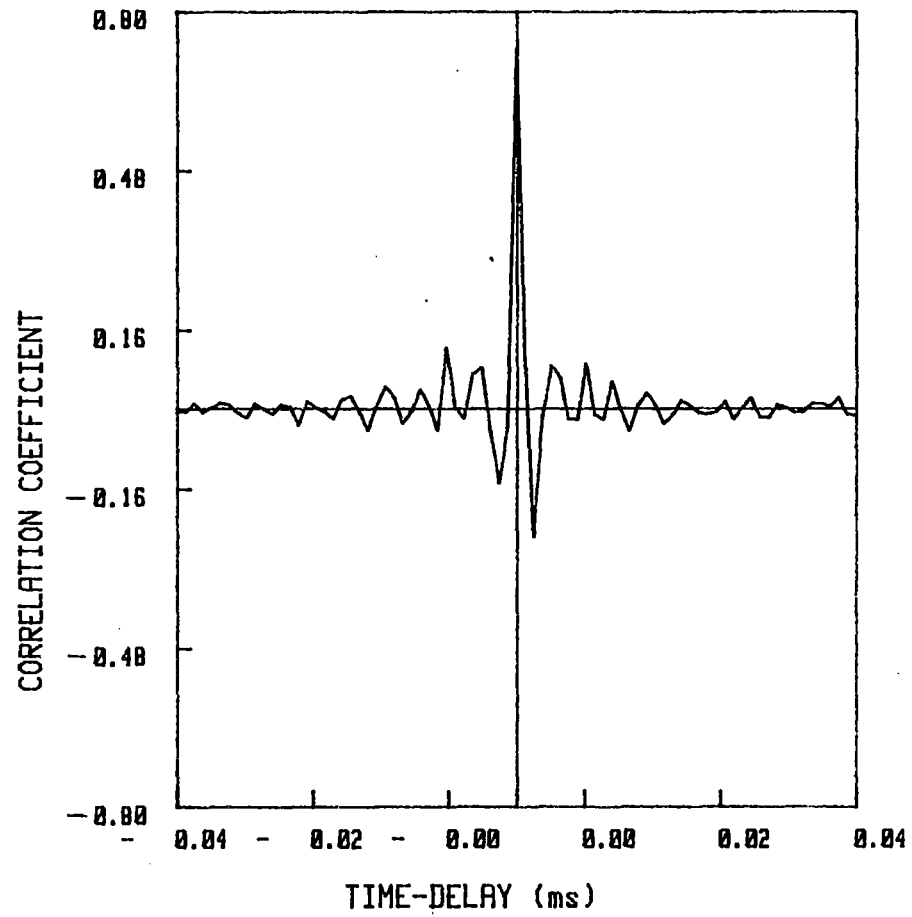


Figure 55. Space-time Correlation Function
at $x/D = 2$

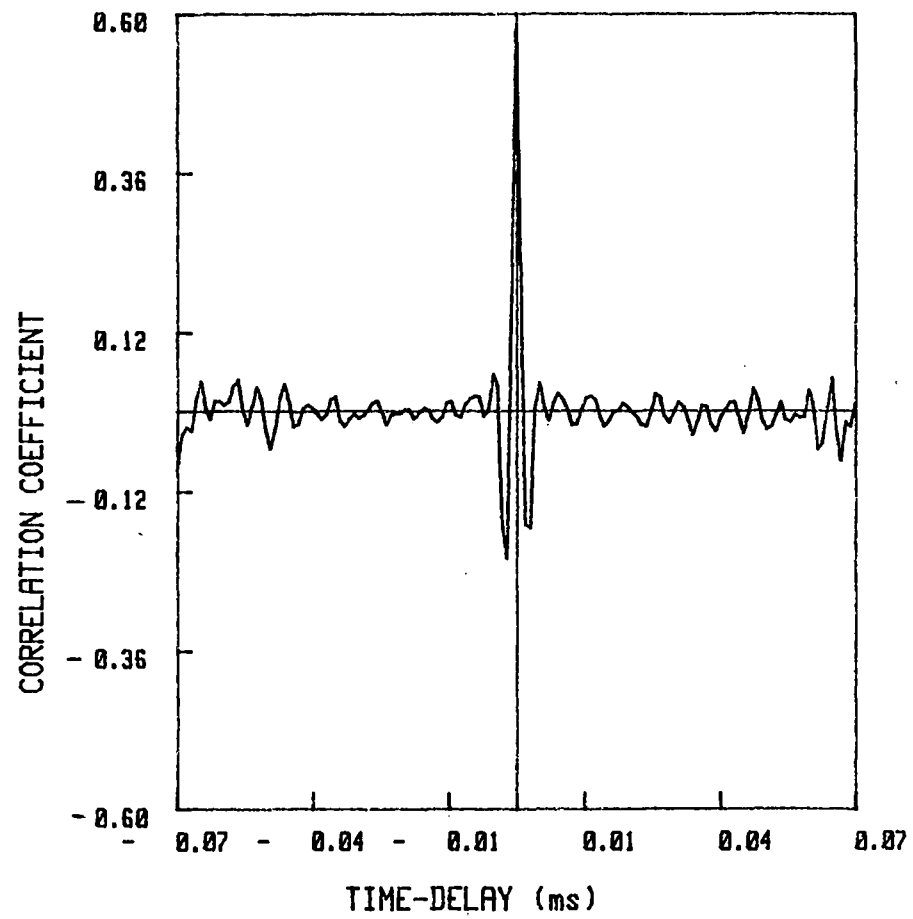


Figure 56. Space-time Correlation Function
at $x/D = 2.5$

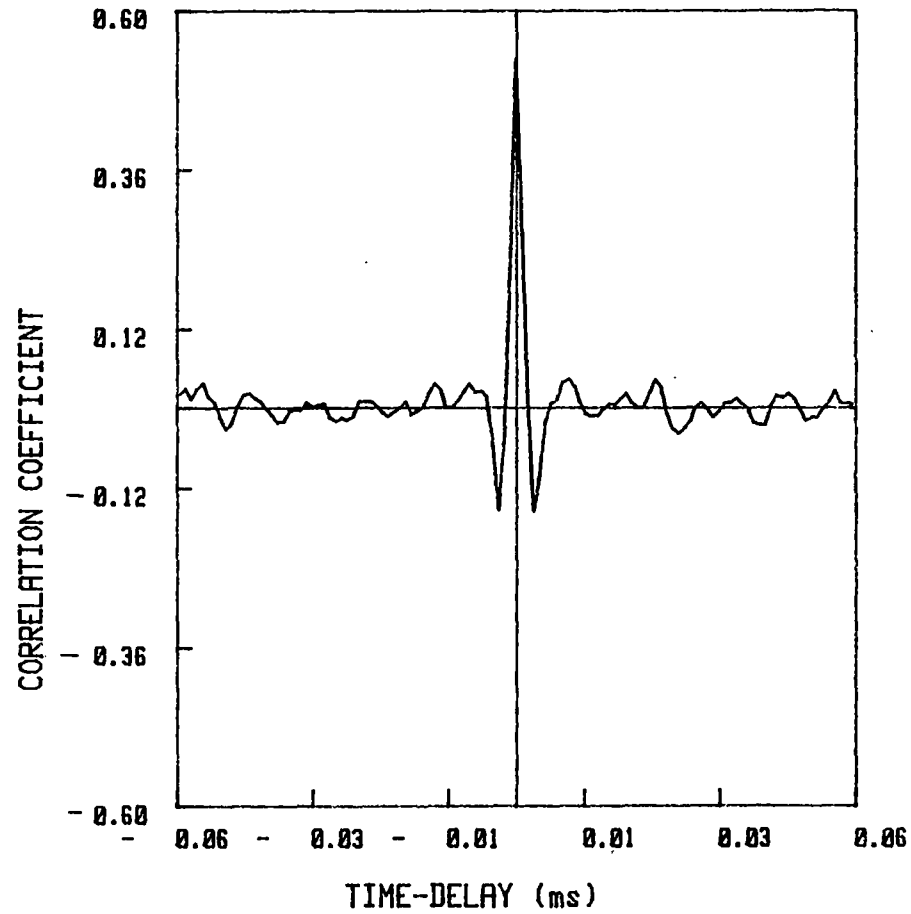


Figure 57. Space-Time Correlation Function
 $x/D = 3$

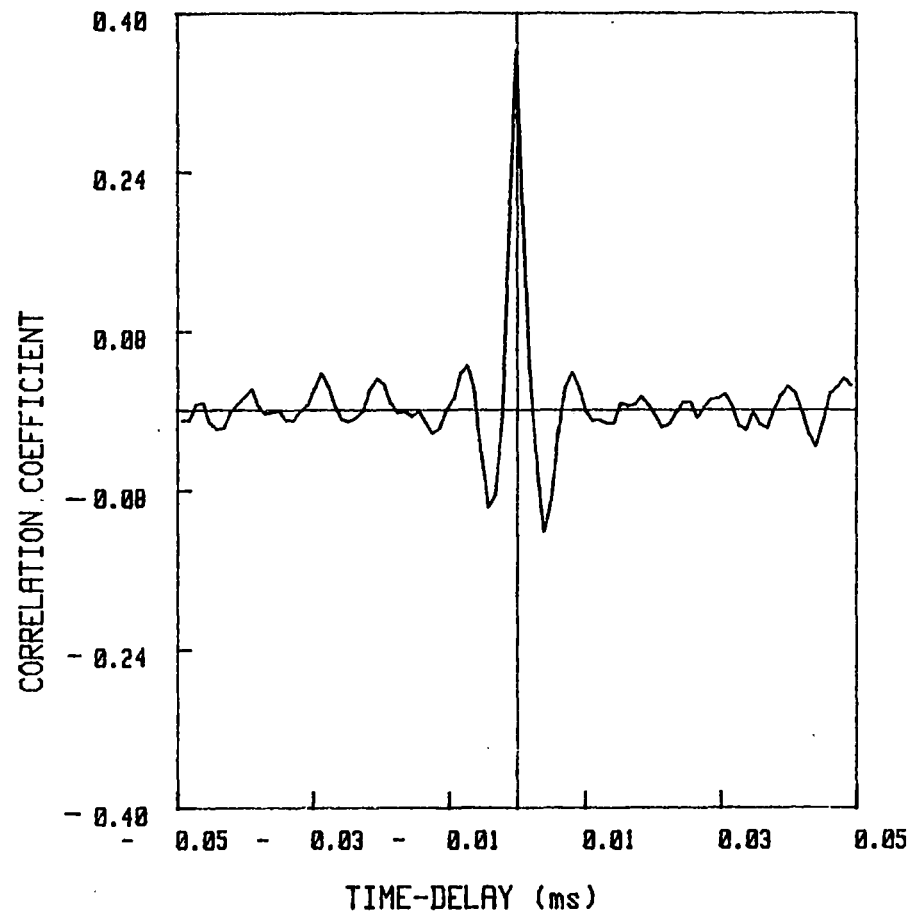


Figure 58. Space-Time Correlation Function
 $x/D = 4$

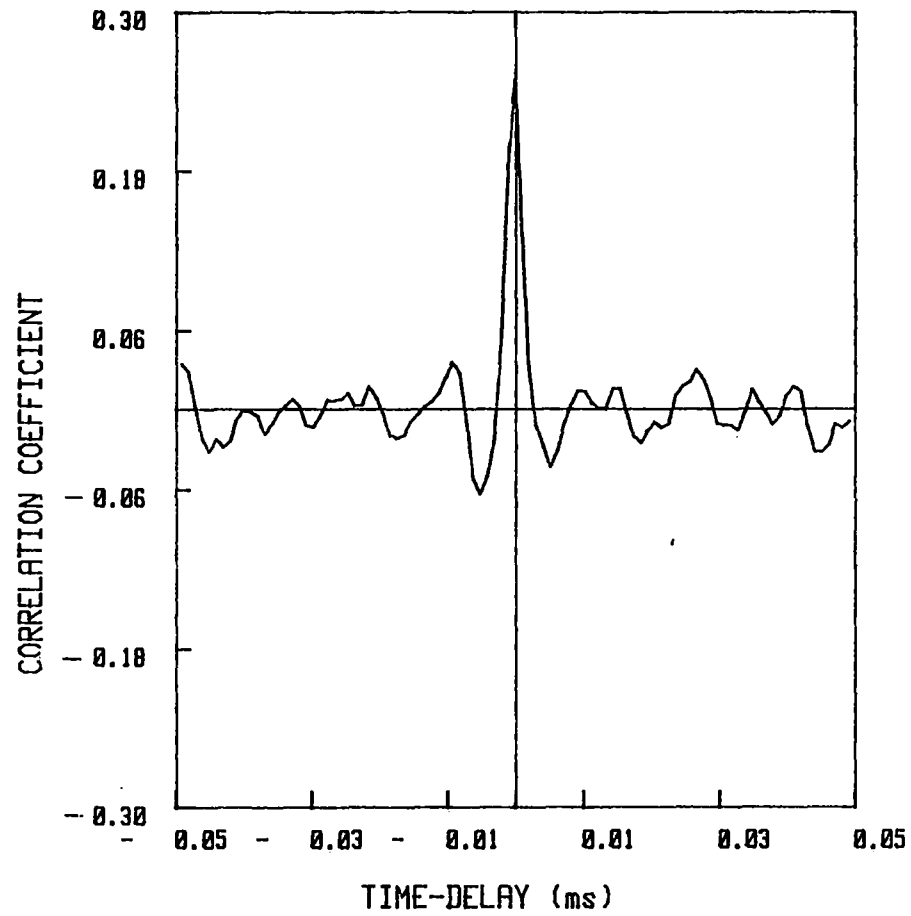


Figure 59. Space-Time Correlation Function
at $x/D = 5$

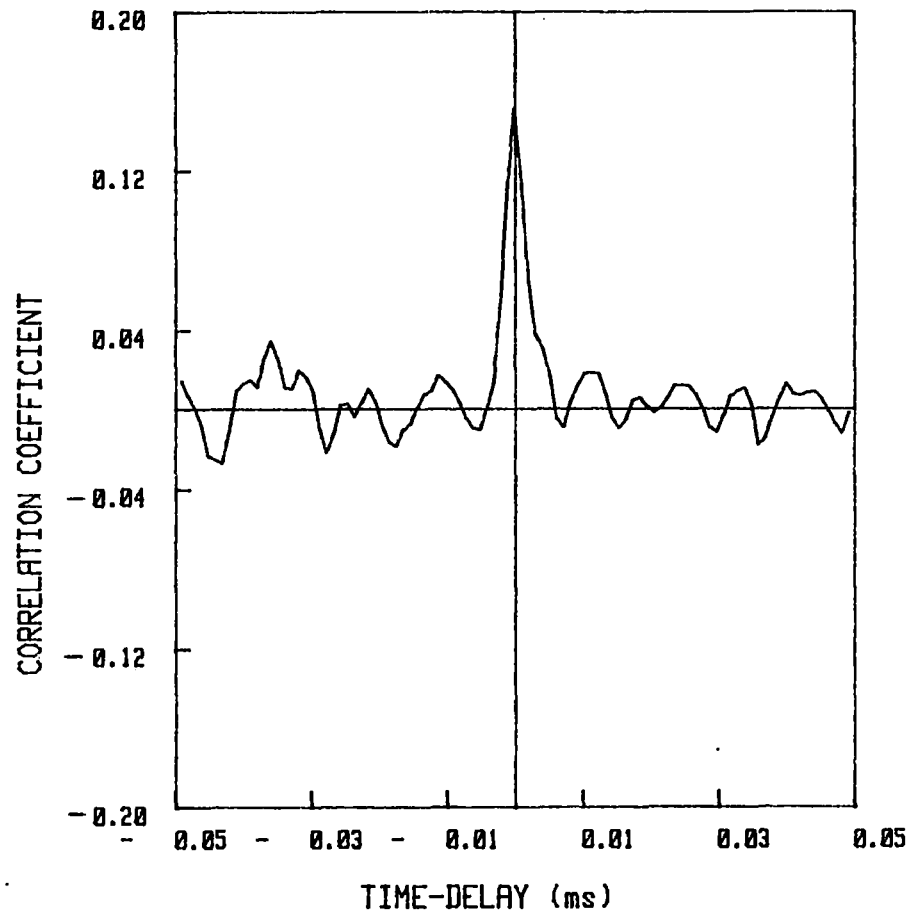


Figure 60. Space-Time Correlation Function
at $x/D = 6$

maintained. This halving in frequency corresponds well to a similar halving noticed in the shear layer spectra at $x/D \approx 4.0$ providing further evidence of a merging event between structures as mentioned in the previous section. The loss of the symmetric structural pattern due to the merging of the two shear layers at the end of the potential core is well illustrated in the sequence of correlation plots in Figures 61 through 63. The sequence of figures show gradual loss in the positive correlation and by $x/D = 10$ the organization of the symmetric structural array appears completely lost as the correlation is nearly zero indicating reorganization of the flow due to the merging of the two shear layers at the end of the potential core. The location from $x/D \approx 10$ to $x/D \approx 16$ seems to be a region of renewed structural development as evidenced by the Figures 64 and 65 which show the onset of negative correlation at zero time delay. By $x/D \approx 16.0$ the flow has clearly organized itself to form an antisymmetric structural pattern as shown in Figure 66. Figures 67 through 70 show the development and maintenance of this antisymmetric pattern. In fact, Figure 71, which is a space-time correlation function plot at $x/D = 60$ made by Brehob and Thomas (1986) well into the similarity region in the same setup but at a higher Reynolds number, shows very strong resemblance to the present measurement. That work along with Thomas and Goldschmidt (1986) has indicated that such a self-preserving anti-symmetric structural array is an inherent feature of the similarity region of a two-dimensional turbulent jet.

Figure 72 presents the variation of correlation coefficient at zero time delay with downstream distance. The flow pattern in the two shear layers adjoining the potential core with respect to each other is well

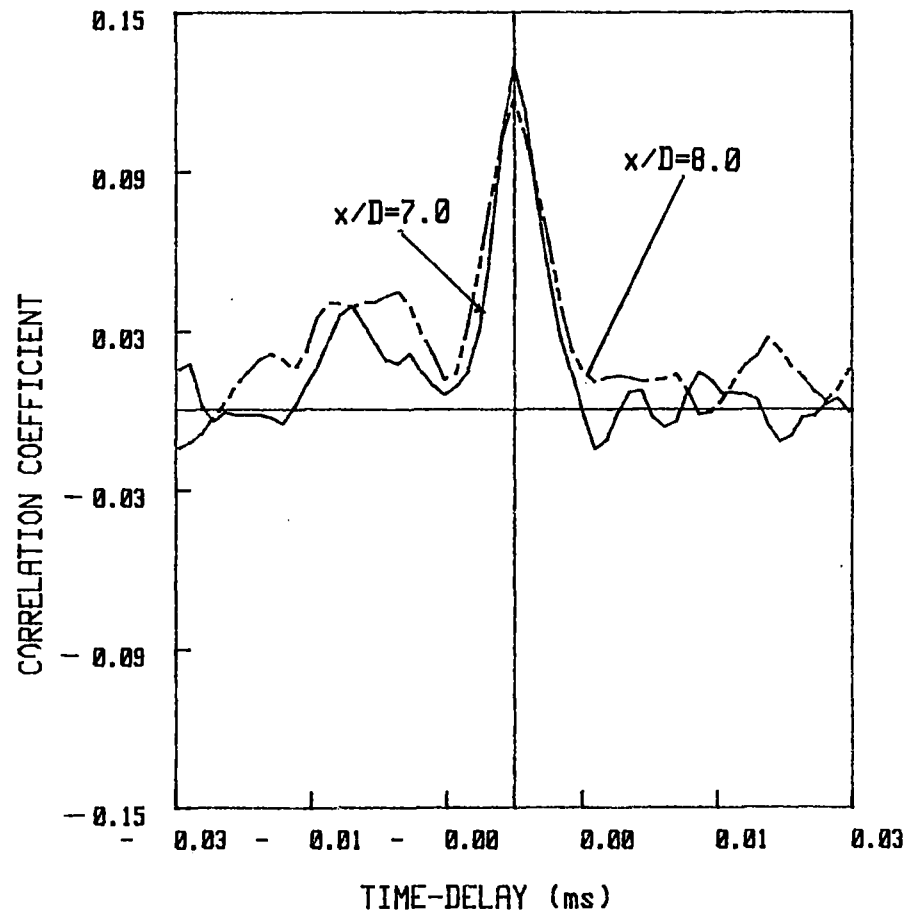


Figure 61. Comparison of Correlation Function at $x/D = 7$ and 8

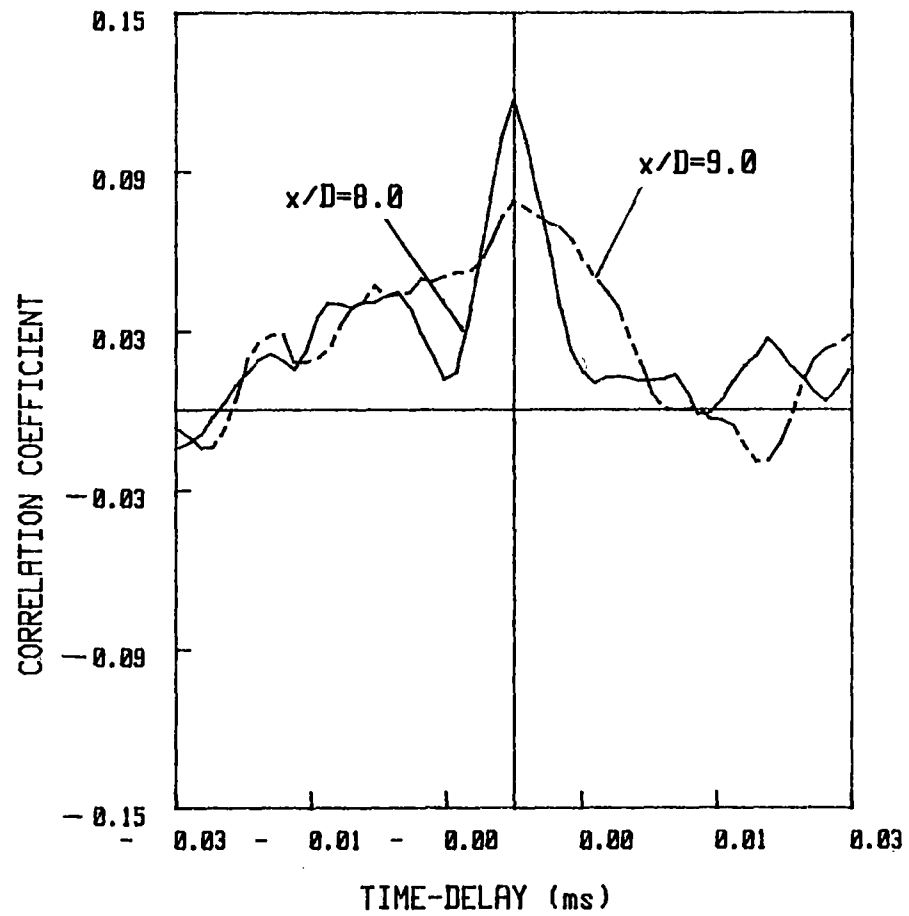


Figure 62. Comparison of Correlation Function at $x/D = 8$ and 9

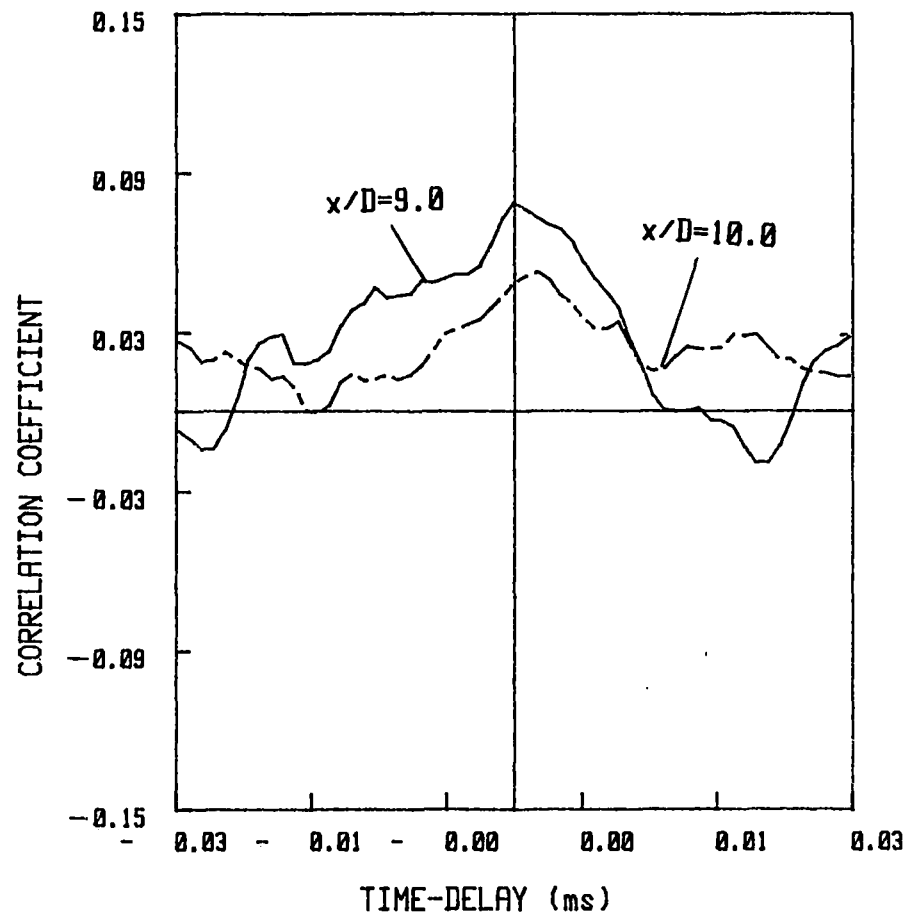


Figure 63. Comparison of Correlation Function at $x/D = 9$ and 10

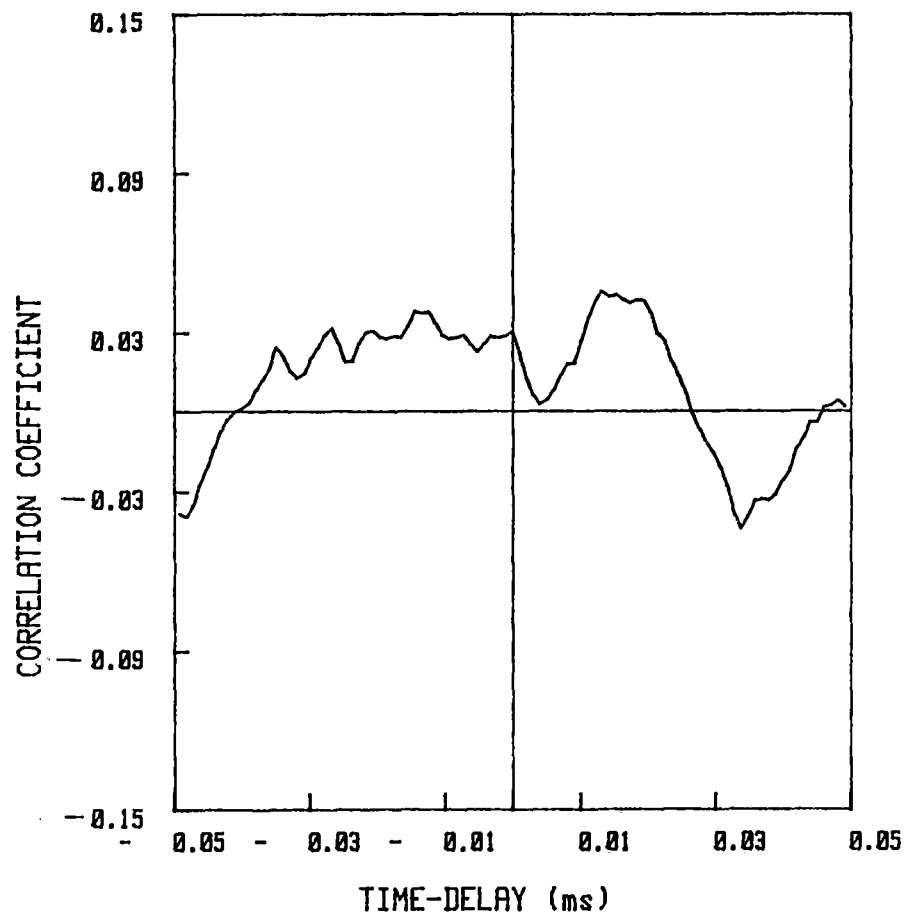


Figure 64. Space-Time Correlation Function
at $x/D = 12$

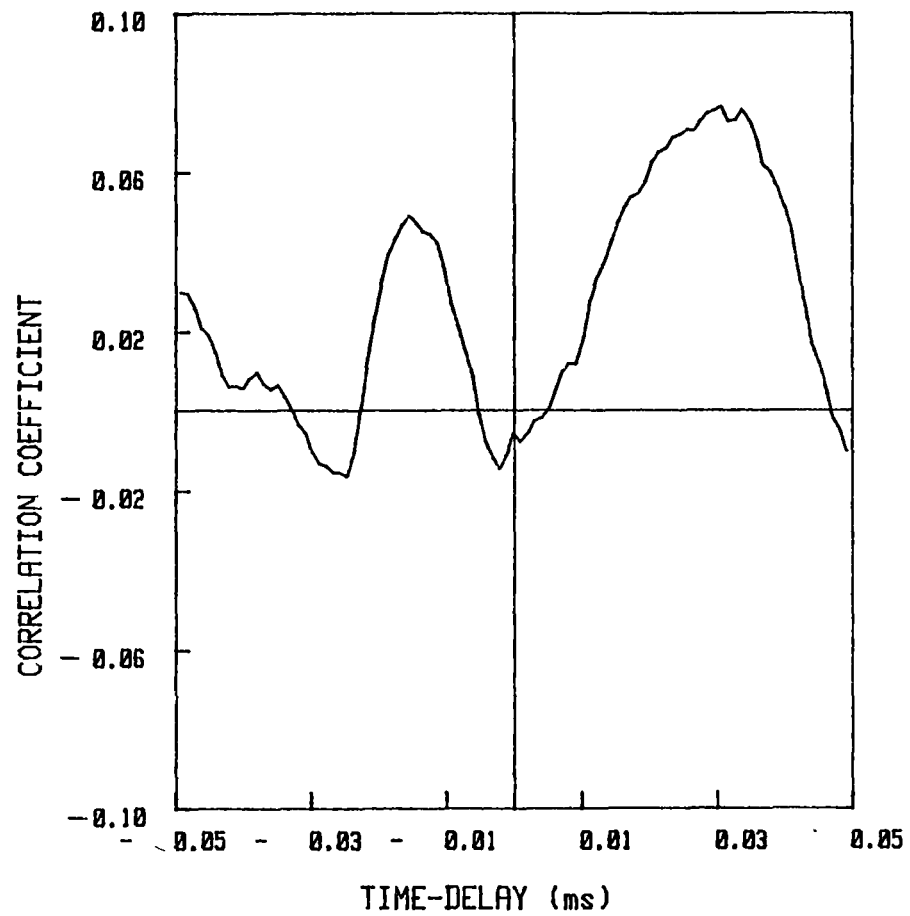


Figure 65. Space-Time Correlation Function
at $x/D = 14$

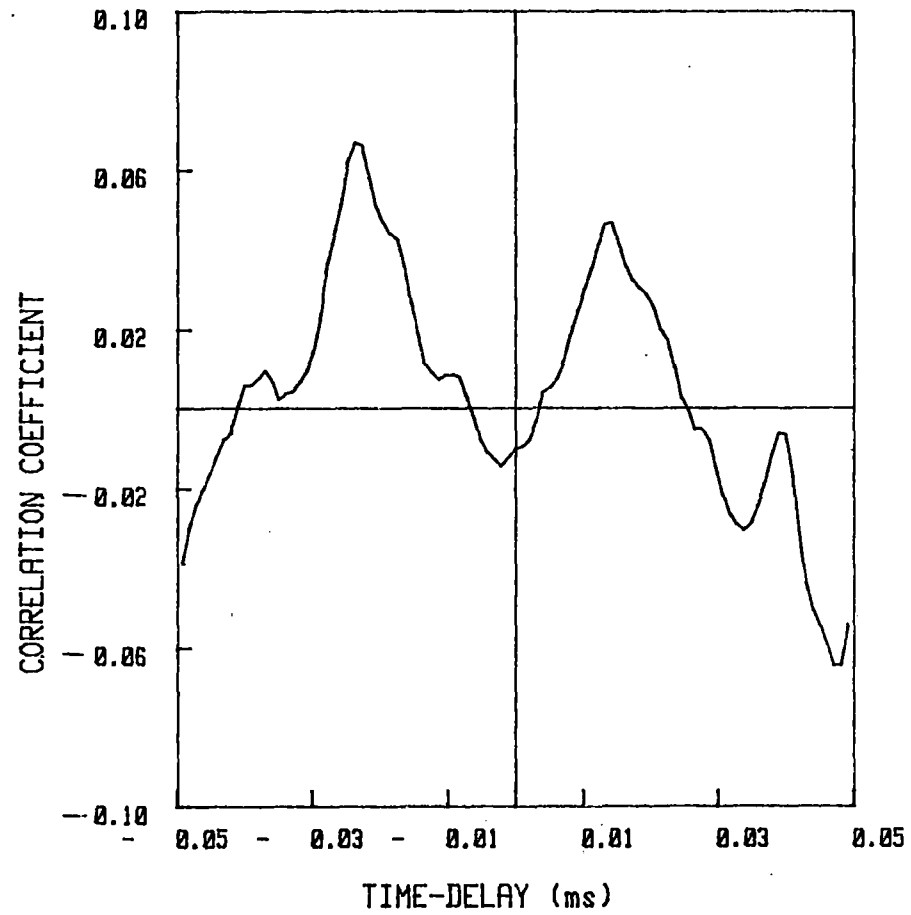


Figure 66. Space-Time Correlation Function
at $x/D = 16$

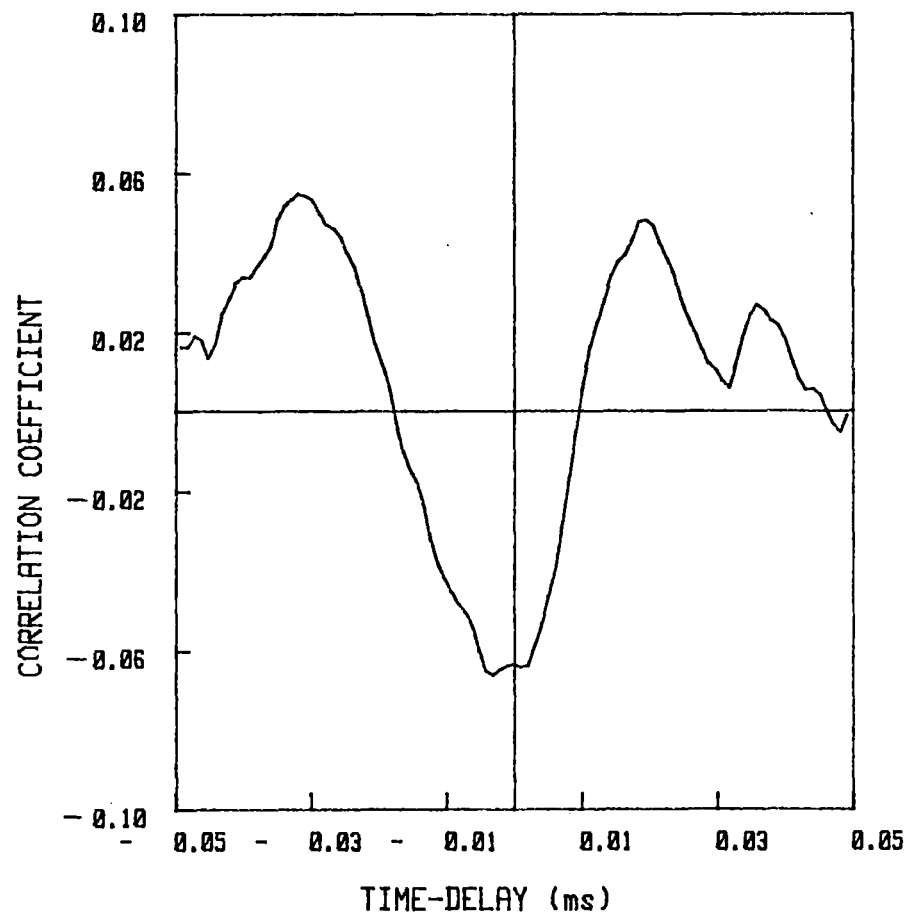


Figure 67. Space-Time Correlation Function
at $x/D = 17$

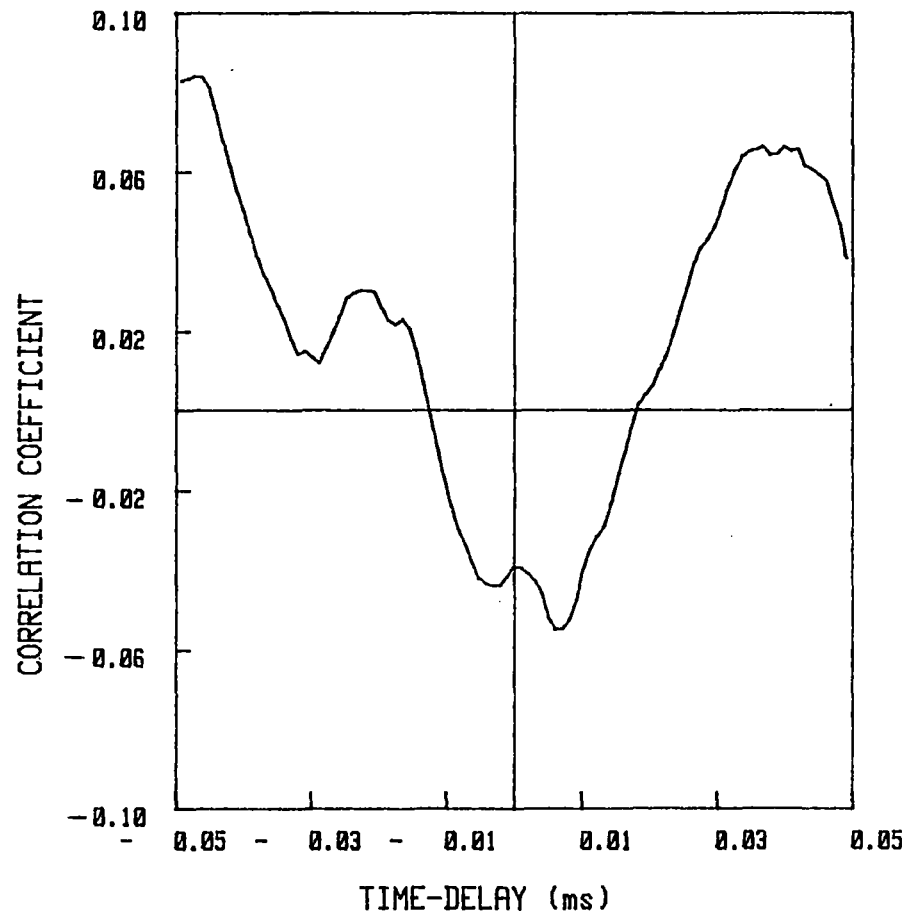


Figure 68. Space-Time Correlation Function
at $x/D = 18$

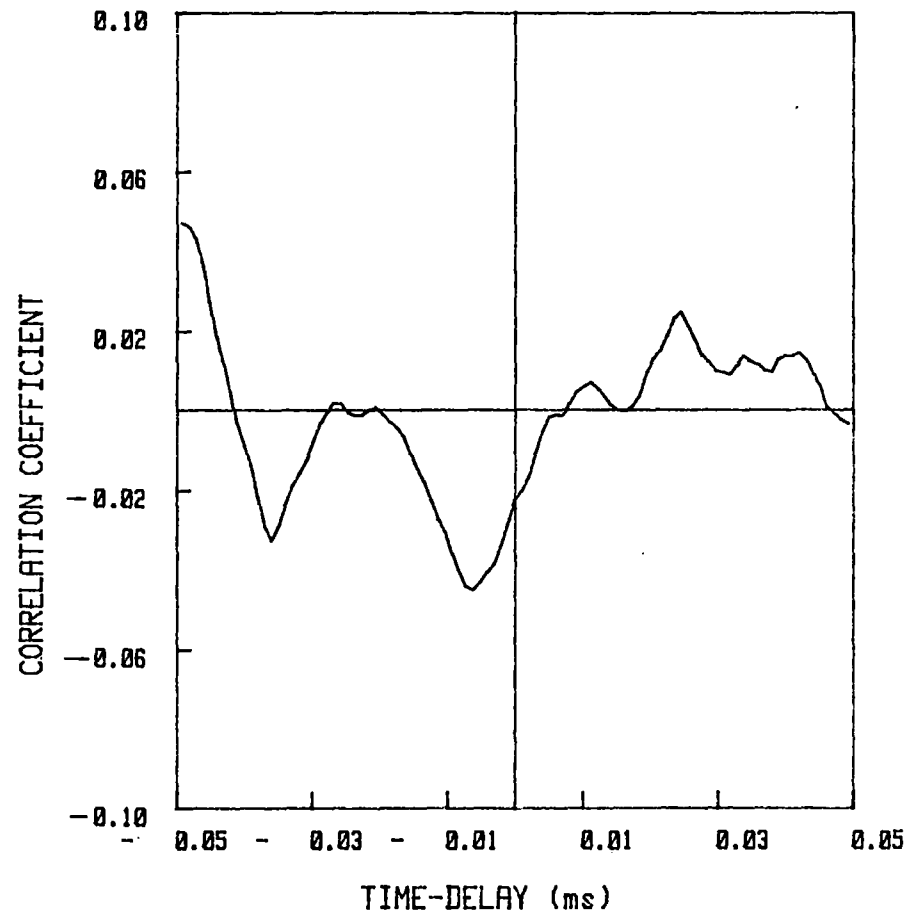


Figure 69. Space-Time Correlation Function
at $x/D = 20$

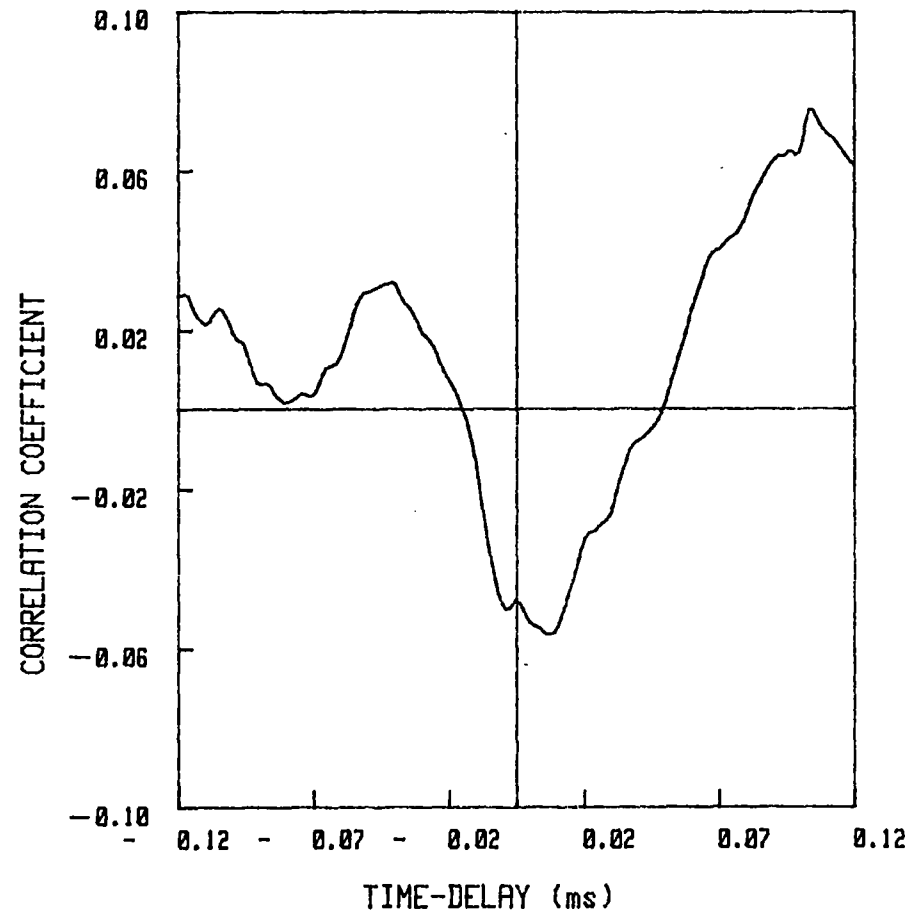


Figure 70. Space-Time Correlation Function
at $x/D = 40$

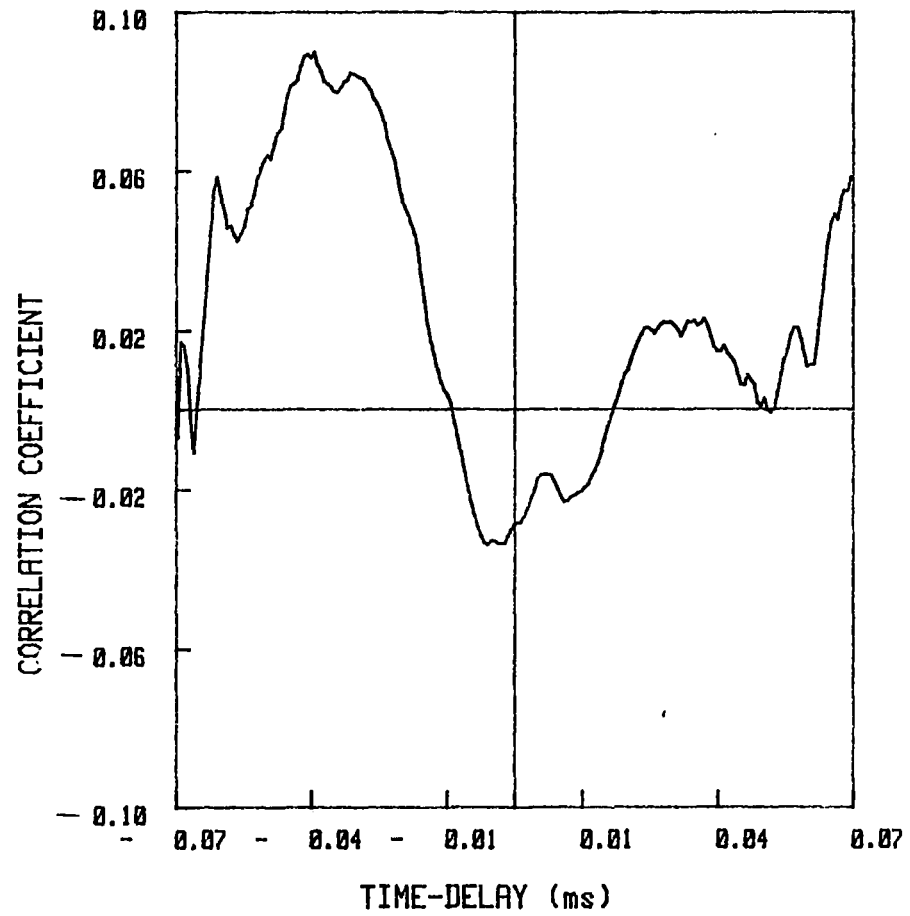


Figure 71. Space-Time Correlation Function
at $x/D = 60$

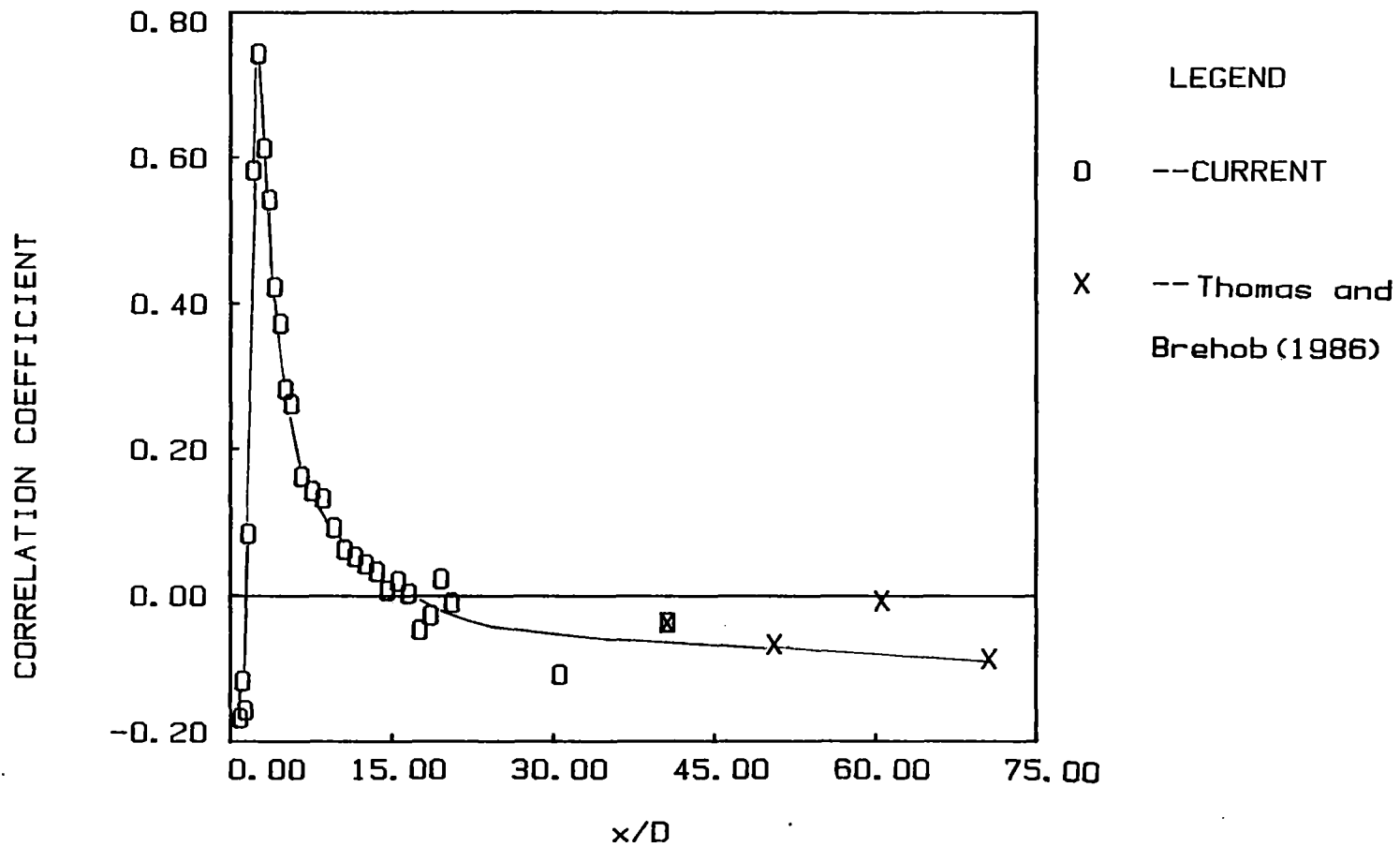


Figure 72. Correlation Coefficient at Zero Time Delay with Downstream Distance

illustrated in this figure. The fluctuations very near the nozzle exit are seen to be asymmetric which with downstream distance develops into a symmetric array of vortices and then the symmetric pattern gradually dies to form an asymmetric structural array by $x/D \approx 16.0$.

4.3 Spectral Coherence and Phase Angle Measurements

The cross-spectrum is a joint statistical measurement which provides information concerning the relationship between corresponding frequency components of two signals (i.e. time series). The cross-spectrum between the two signals $x(t)$ and $y(t)$ is a complex function of frequency which is given by

$$G_{xy}(f) = C_{xy}(f) - i Q_{xy}(f) \quad 4-3.1$$

where $C_{xy}(f)$ is the coincident spectral density function and $Q_{xy}(f)$ is the quadrature spectral density function. The spectral coherence between the two signals is a real valued quantity given by

$$\gamma_{xy}(f) = \frac{|G_{xy}(f)|}{[G_x(f) G_y(f)]^{1/2}} \quad 4-3.2$$

where $|G_{xy}(f)|$ is the magnitude of the cross-spectral density function, G_x and G_y are the power spectral density functions of each of the two signals. When $\gamma_{xy}(f) = 0$ at a particular frequency the two signals $x(t)$ and $y(t)$ are said to be incoherent at that frequency and if $\gamma_{xy}(f) = 1$ then they are said to be fully coherent at that frequency. For values of coherence between 0 and 1 the signals are said to be partially

coherent at that frequency. A phase angle spectrum between the signals $x(t)$ and $y(t)$ may also be computed from the cross-spectrum and is given by

$$\phi_{xy}(f) = \tan^{-1} \left(\frac{Q_{xy}(f)}{C_{xy}(f)} \right) \quad 4-3.3$$

In order to obtain further information regarding the nonlinear transition of the jet, spectral coherence and phase angle measurements were performed. In the measurements to be presented the cross-spectrum and the autospectra were computed via Fast Fourier Transform methods. The PASCAL program which was developed to perform these measurements is listed in Appendix A.

In the first set of measurements to be reported two straight wire probes were placed on opposite sides of the jet centerline with one probe fixed in the nascent jet shear layer at $x/D = 0.25$. This will be referred to as the "fixed probe". The other probe was movable and was placed in the opposite jet shear layer (i.e. $y/b = 1.0$) over streamwise locations $0.25 \leq x/D \leq 20.0$. This probe positioning is shown schematically in Figure 73. The spectral coherence and phase spectrum were computed for selected streamwise positions of the movable probe. In this manner the relationship between downstream spectral modes and the near exit flow field could be investigated. In particular, the existence of a coupling between downstream locations and the near exit field was investigated, with emphasis on determining the particular spectral modes involved. Evidence associating coupling locations with the occurrence of major events in the structural development of the flow was sought.

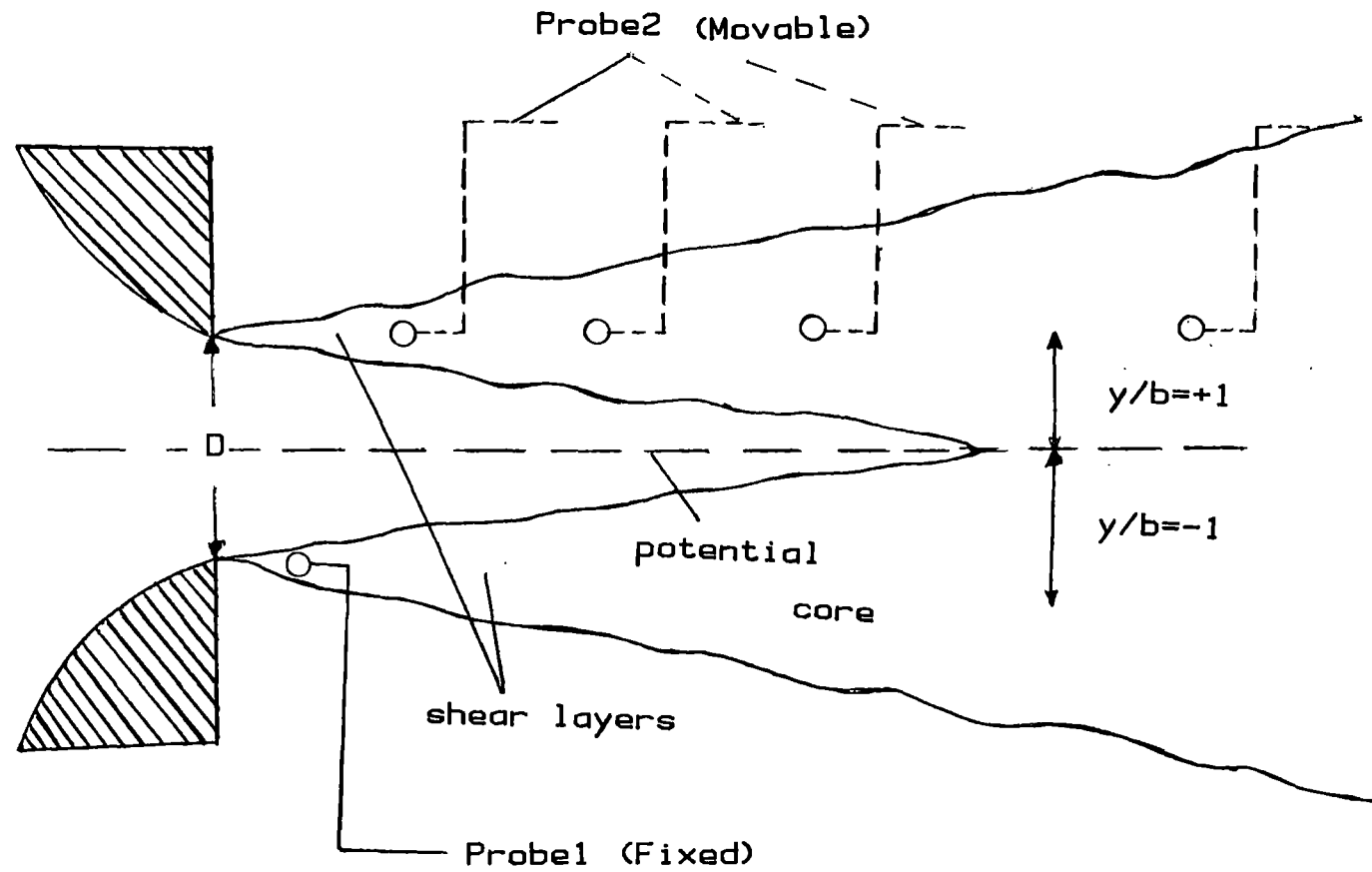


Figure 73. Probe Arrangement for Coherence Measurements

Figure 74 presents the measured frequencies corresponding to the maximum spectral coherence for various downstream locations of the movable probe. A discontinuous distribution involving four nearly constant frequency regimes is noted from this figure. The figure suggests a downstream coupling with the near exit flow at certain discrete preferred frequencies.

The region $0.25 \leq x/D \leq 2.0$ suggests that the spectral modes near 250 Hz and 60 Hz are most coherent with the nascent shear layer flow. As described earlier with regard to the spectral measurements, the 250 Hz mode was interpreted as the vortex roll-up frequency and the roll-up occurred by approximately $x/D = 2.25$. Thus the data of Figure 74 suggests that this roll-up phenomenon is coupled with the nozzle exit. Figure 75 shows the variation of the coherence of the mode centered near 250 Hz (bandwidth of 10 Hz) with downstream distance. The coherence is seen to peak near $x/D = 2.0$ as expected. A second peak near $x/D = 4$ is likely associated with a vortex pairing event previously noted from spectral measurements. The coherence is seen to decrease for $x/D > 4$. The high coherence of the spectral mode near 60 Hz with the nascent shear layer is discussed later in this section.

A sudden drop in maximum coherence frequency from the 250 Hz level to 125 Hz mode is noted to occur soon after roll-up ($x/D = 2.0$) from Figure 74. The 125 Hz mode is seen to exhibit peak coherence up to $x/D = 5.0$. This leads to a general conclusion that the region $2 \leq x/D \leq 5$ is highly coherent with the near exit flow with respect to the spectral mode near 125 Hz. It should be noted here that spectral measurements (see section 4.12) indicated a gradual subharmonic formation (interpreted as a vortex pairing event) at these locations.

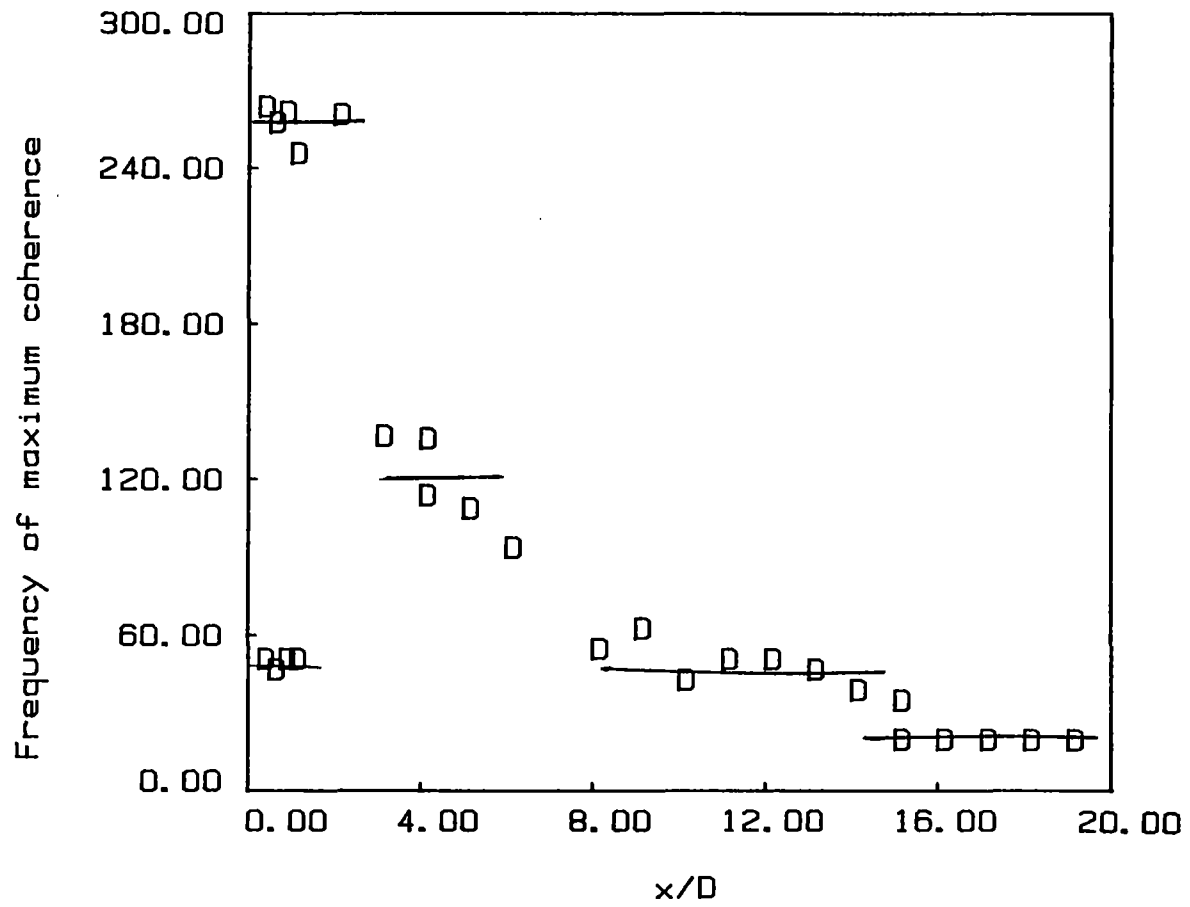


Figure 74. Frequency of Maximum Coherence with Downstream Distance

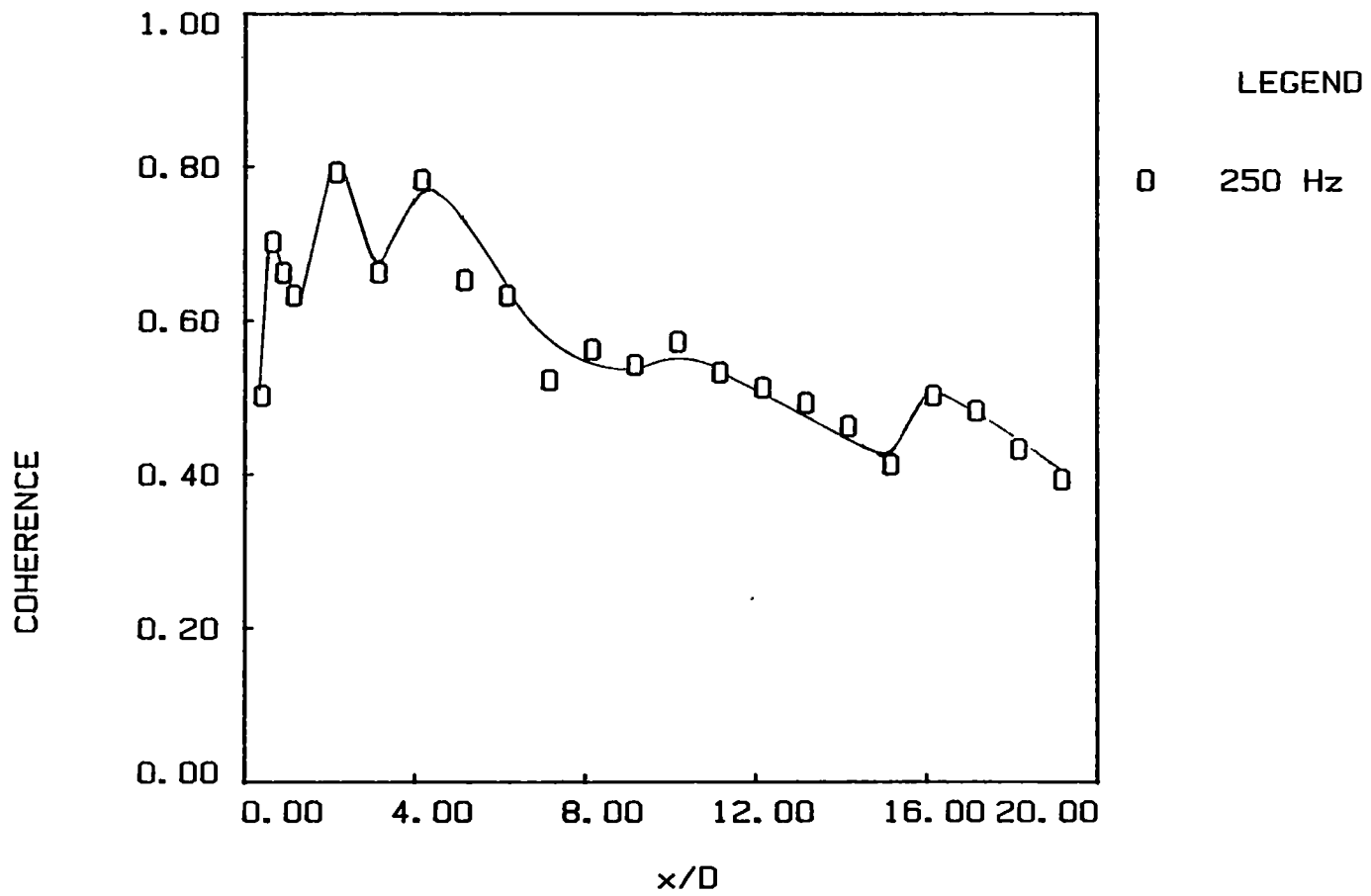


Figure 75. Variation of Coherence of the Mode Near 250 Hz (Bandwidth 10 Hz) with Downstream Distance

This pairing event thus seems to be a likely cause for the presence of the coupling of the 125 Hz mode in the region $0.25 \leq x/D \leq 5.0$. The variation of the frequency centered near 125 Hz (bandwidth = 10 Hz) is shown in Figure 76. The figure shows a maximum coherence at $x/D \approx 4.0$ followed by a gradual decline with downstream distance.

A second halving of the frequency for maximum coherence is noted to gradually occur over the range $5 \leq x/D \leq 8.0$, resulting in a frequency for maximum coherence of approximately 60 Hz. Figure 77 shows the variation of coherence centered near 60 Hz with downstream distance and the peak coherence is seen to occur at approximately $x/D = 7-8$. This suggests that the region $0.25 \leq x/D \leq 8.0$ contains a feedback loop involving a spectral mode near 60 Hz. As described earlier, $x/D \approx 7.0$ was noted to be the location where the shear layers nominally merge and represents the beginning of the "interaction region" of the jet. From previously presented spectral measurements $x/D \approx 7.0$ was noted as the location initiating a double halving of the characteristic structural passage frequency. This was interpreted as evidence of a double merging between structures occurring over the streamwise locations $8.0 \leq x/D \leq 16.0$, and is believed related to the shear layer interactions taking place. Such a double halving is noted in Figure 74 which leads to the formation of maximum coherence at a frequency approximately 20 Hz by $x/D \approx 16.0$. Figure 78 shows the variation of maximum coherence of the mode centered near 20 Hz (bandwidth of 10 Hz) with downstream location. A high degree of coherence is noted in the early similarity region of the flow and in general there is an upward trend in coherence from $x/D \approx 12.0$ as the similarity region is approached. This indicates that the downstream locations are coupled

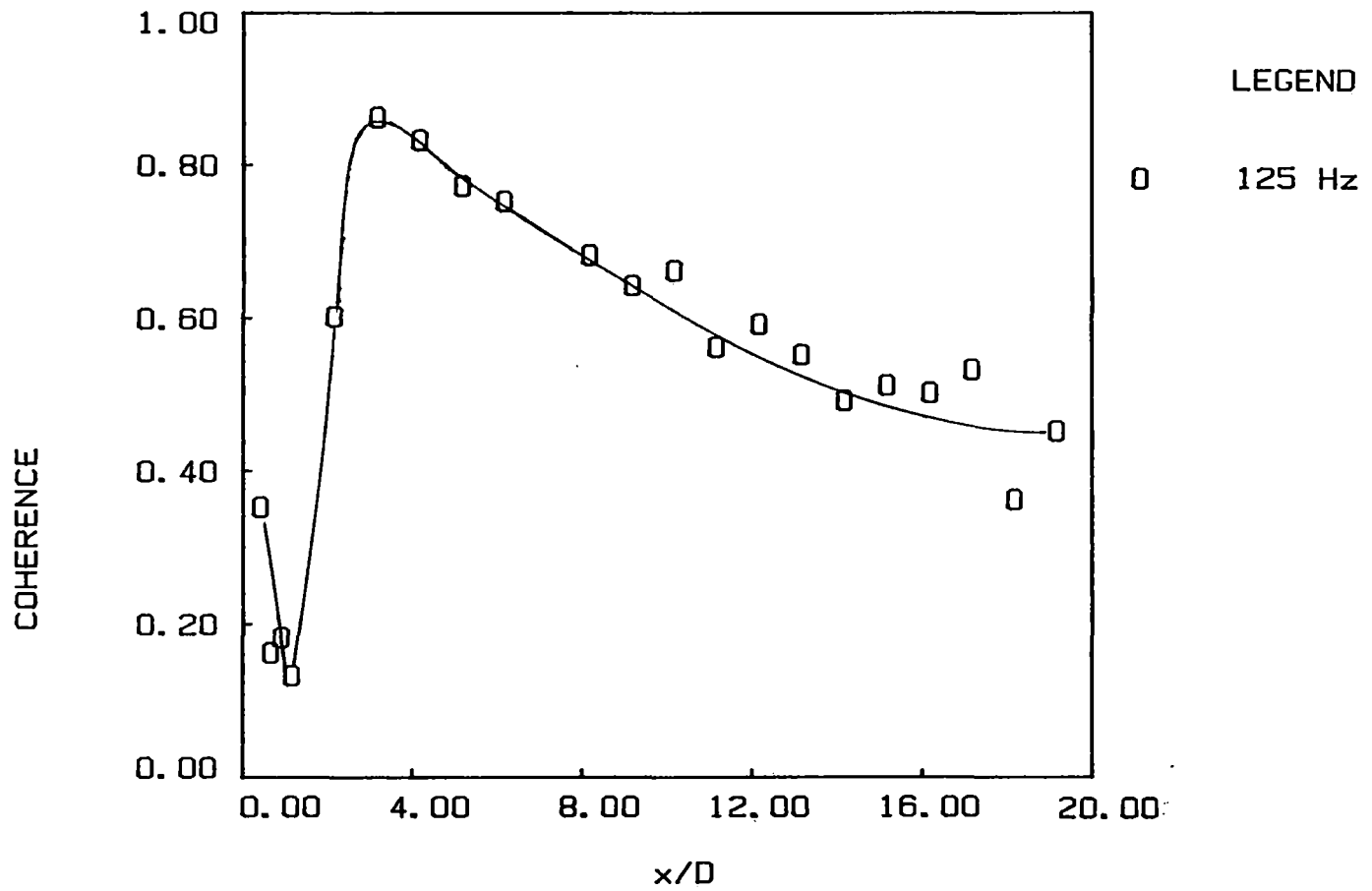


Figure 76. Variation of Coherence of the Mode Near 125 Hz (Bandwidth 10 Hz) with Downstream Distance

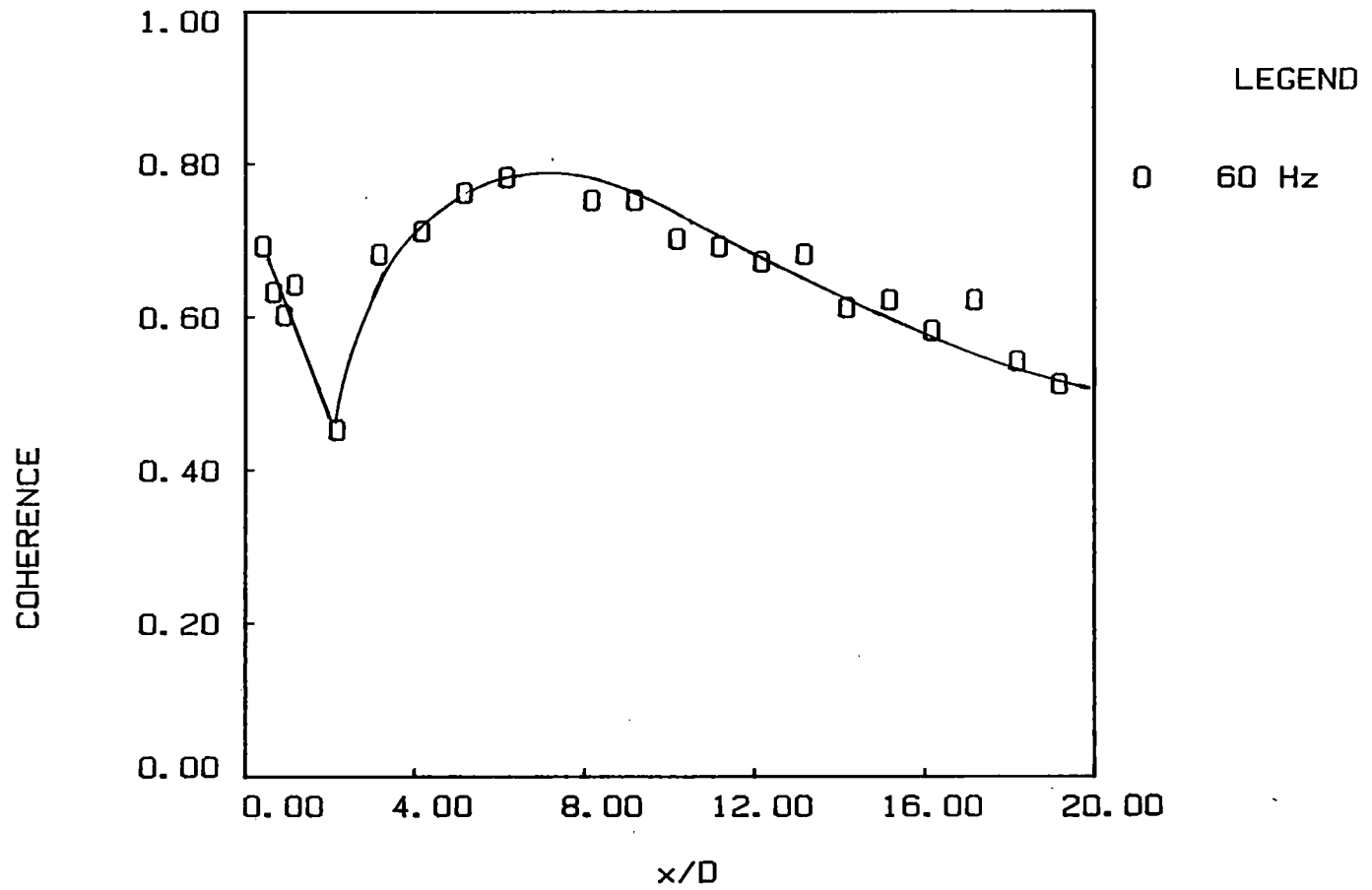


Figure 77. Variation of Coherence of the Mode Near 60 Hz (Bandwidth 10 Hz) with Downstream Distance

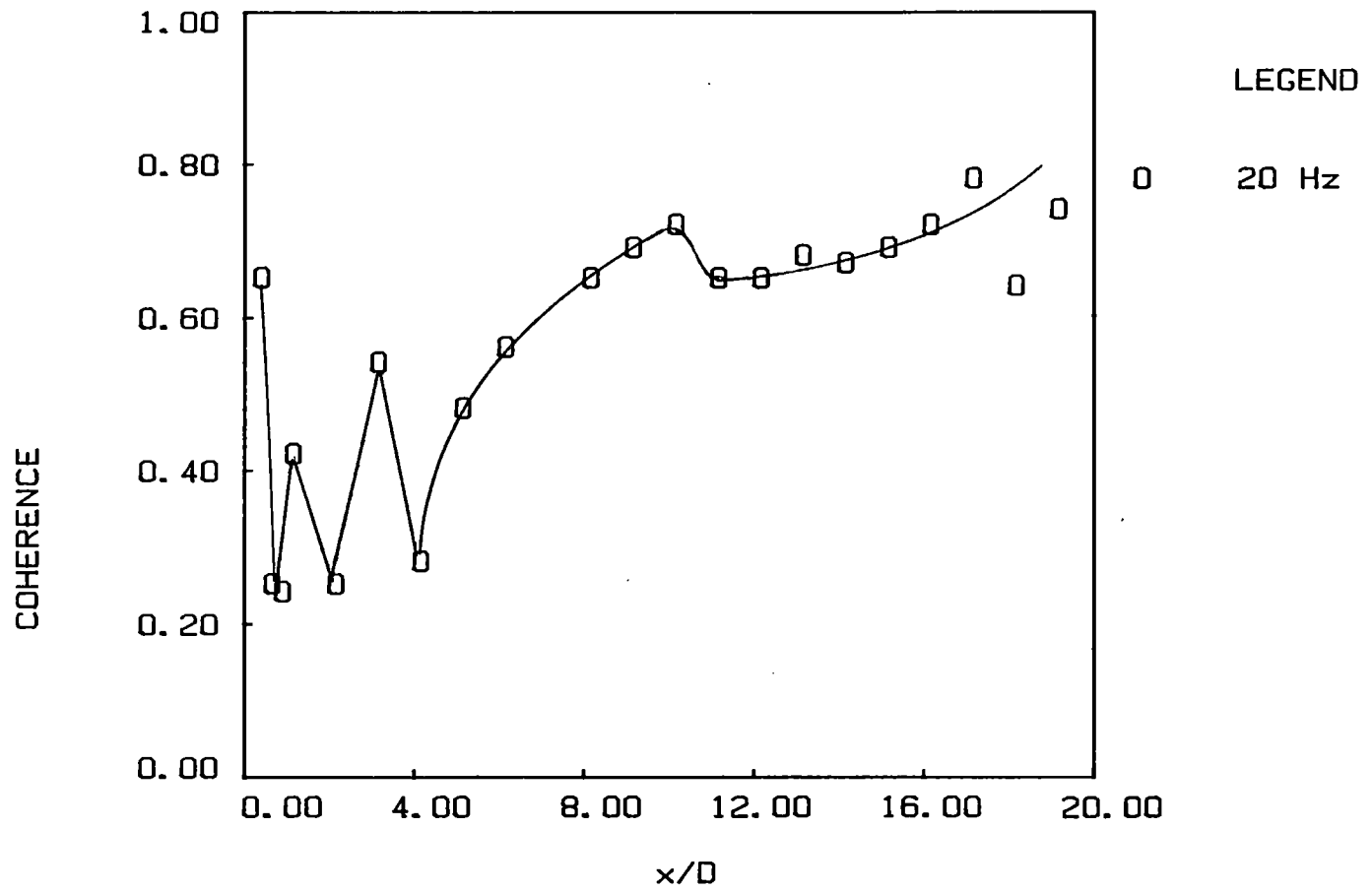


Figure 78. Variation of Coherence of the Mode Near 20 Hz (Bandwidth 5Hz) with Downstream Distance

with the nozzle exit by a spectral mode near 20 Hz. The cause for this coupling could be attributed to the structural rearrangement which seems to take place soon after the end of the potential core ($8 \leq x/D \leq 15$) and, in particular, the event associated with multiple halving which seems completed by $x/D = 16.0$.

It may be noted from Figure 74 that each of the events which lead to a discontinuous shift in frequency for maximum coherence are associated with a consecutive doubling in downstream distance between the occurrence of such events. A similar phenomenon was noted by Ho and Huang (1982) in free shear layer where it was found that the streamwise distance between successive vortex pairing events doubled with increasing downstream distance. In addition, their work illustrated that each vortex pairing event in the flow is linked to the trailing edge via a feedback loop which required just such a distance doubling between pairing events. This will be discussed further in Chapter V.

It is interesting to compare the above measurements with coherence measurements made at corresponding streamwise locations but with the probes side by side at $y/b = \pm 1.0$. Figures 79 and 80 present such a comparison for $x/D = 8$ and 16. Surprisingly, in both cases the coherence levels are much greater when the probes possess large streamwise separation. The coherence measurements for the probes positioned side by side at $\Delta y = 2b$ show very low levels which is due to the high level of randomness that characterize the shear layer interaction region of the jet. The high levels of coherence exhibited for the cases involving streamwise probe separation even in this chaotic region of the flow are further evidence of the presence of a coupling between the near exit flow and downstream locations.

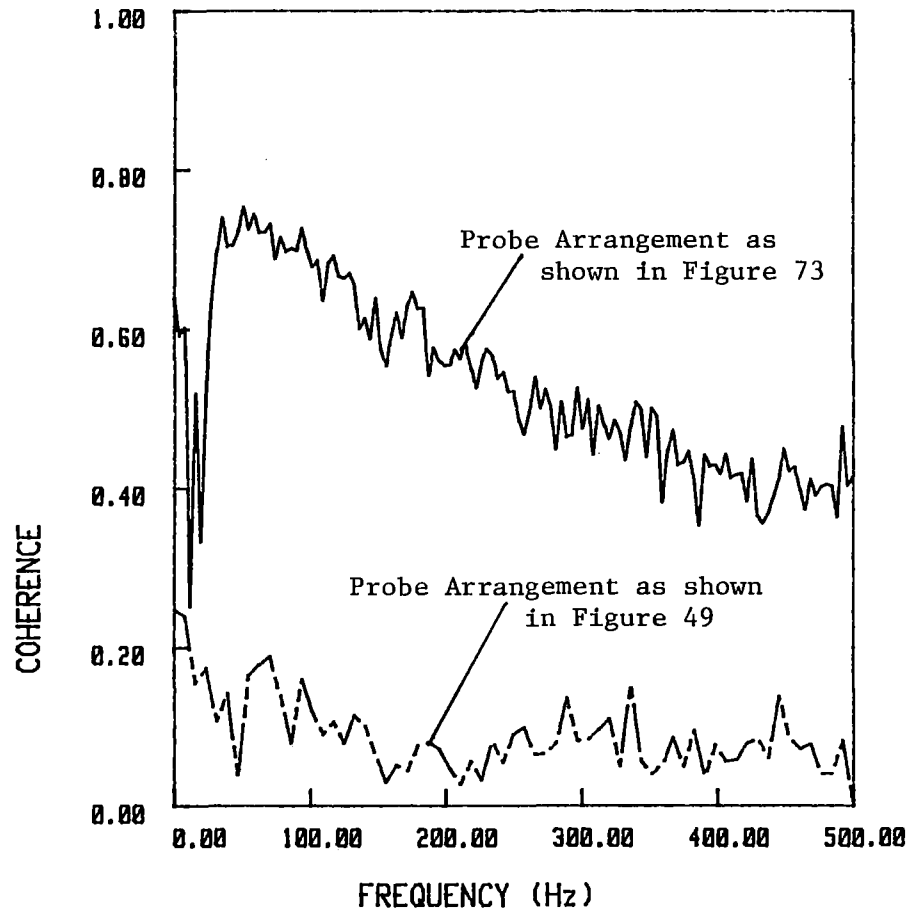


Figure 79. Comparison of Coherence Measurements of the set:Probes placed side by side at $x/D = 8$ with the set:One Probe fixed at Nozzle Exit, the other probe placed at $x/D = 8$

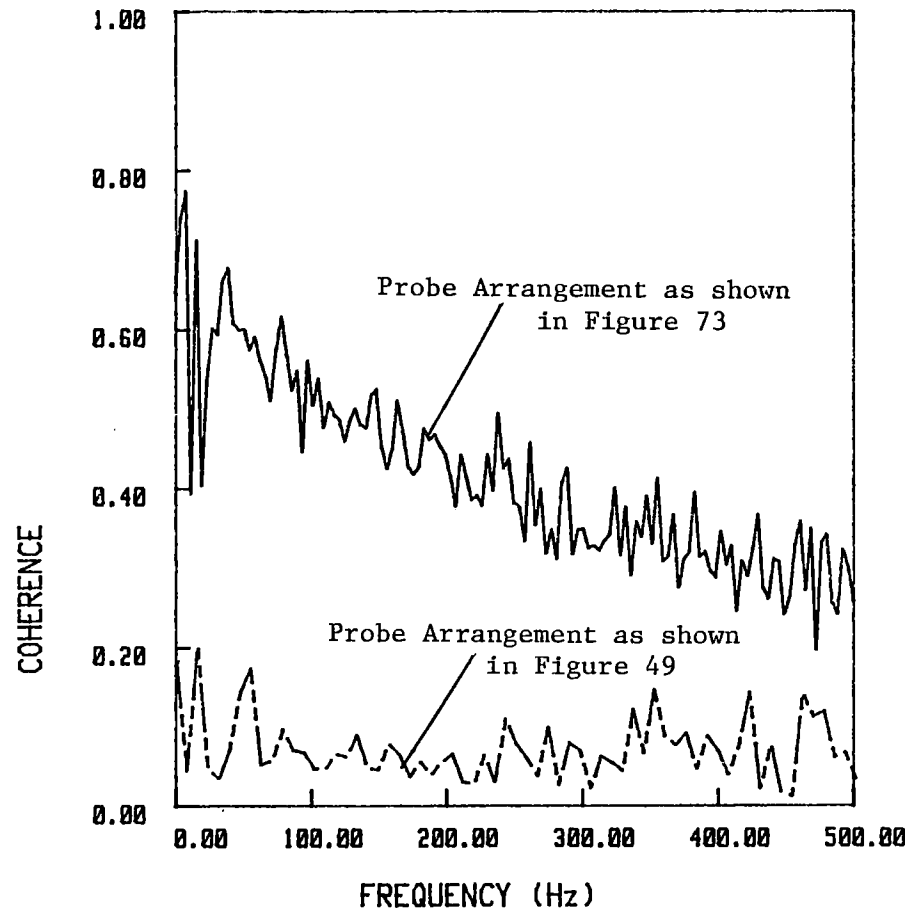


Figure 80. Comparison of Coherence Measurements of the set:Probes placed side by side at $x/D = 16$ with the set:One Probe fixed at Nozzle Exit, the other probe placed at $x/D = 16$

The phase spectra measured at $x/D = 2, 4, 8$ and 16 (which are not presented here) exhibit zero phase shift of the highly coherent spectral modes and this strengthens the conclusion regarding the feedback coupling mentioned above as it would be very likely that any downstream location acting as a source for the feedback should be strongly phase coupled too.

In the next set of measurements to be reported two straight wire probes were placed on opposite sides of the jet centerline at $y/b = \pm 1.0$ (i.e. shear layer) for selected streamwise locations $0.25 \leq x/D \leq 20$ and the coherence and phase spectra were both obtained. The probe positioning is identical to that shown in Figure 49 for the correlation measurements which have been previously reported. The purpose of these measurements was to obtain information regarding the relation between corresponding spectral modes occurring on opposite sides of the jet in the developing and interacting shear layers. The space-time correlation measurements presented in the previous section were performed in time domain and result from a superposition of the multiple spectral modes present. Hence, this measurement is not complete in detailing the relationship between corresponding spectral modes in the developing jet shear layers.

Figures 81 and 82 present the computed coherence function at $x/D = 0.25$ and 0.5 . Both figures show three distinct spectral regions of elevated coherence near 12-20 Hz, 40-80 Hz and 250-300 Hz. The space-time correlations obtained at near exit locations as described earlier showed the presence of a 60 Hz oscillatory component. Near exit power spectra showed the initial dominance of a mode near 20 Hz. Hence, it is not surprising that the coherence measurements initially exhibit strong

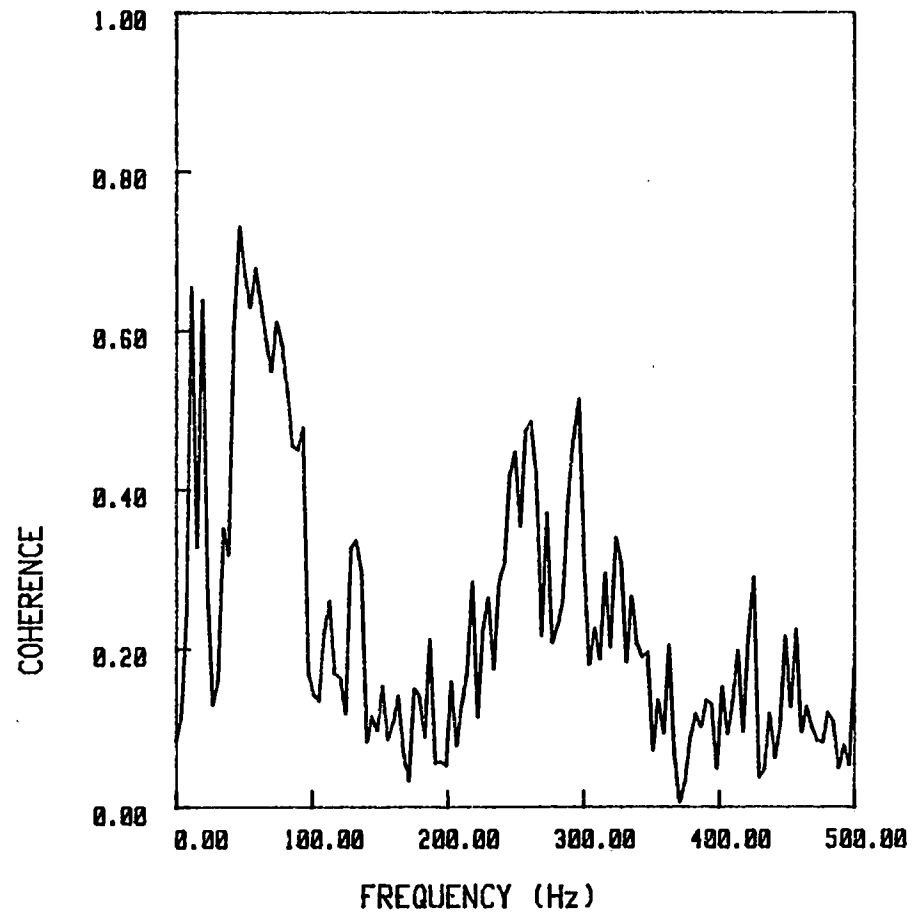


Figure 81. Coherence Spectrum at $x/D = 0.25$

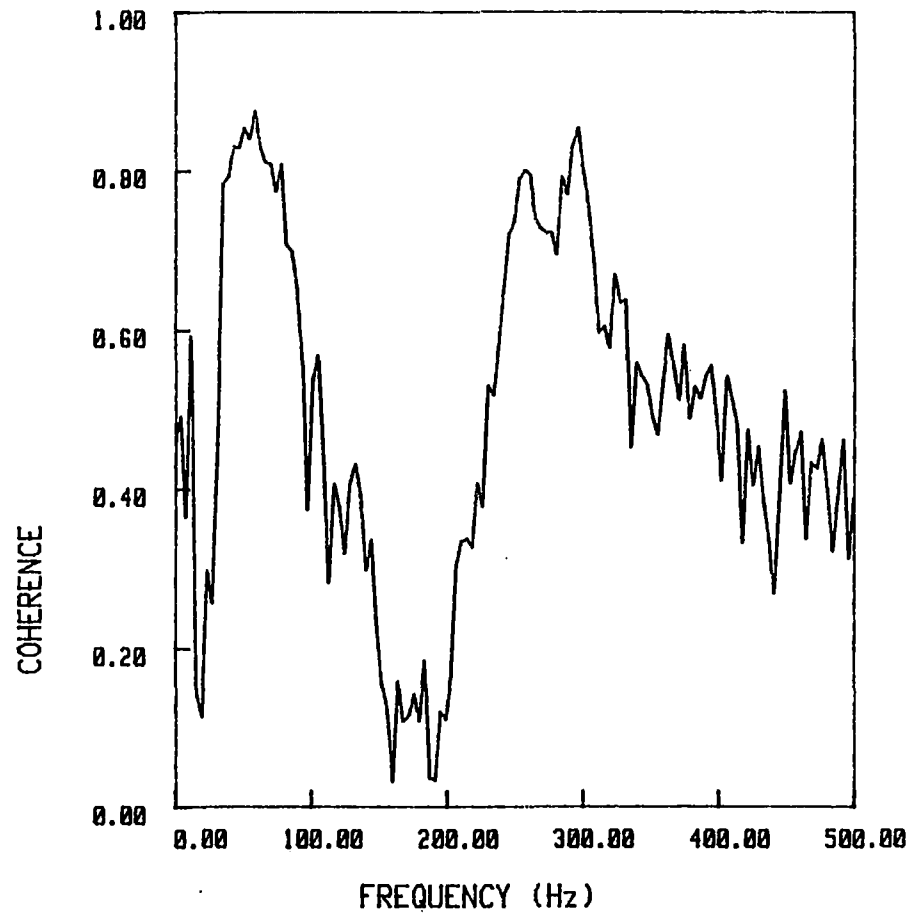


Figure 82. Coherence Spectrum at $x/D = 0.5$

coherence about these frequencies. With increasing downstream distance the coherence measurements as presented in Figures 83 and 84 corresponding to $x/D = 1.0$ and 1.5 , respectively, show strong coherence between 40 Hz and 80 Hz and above 250 Hz. The increase in coherence of mode above 250 Hz is rather expected as according to Figure 8, these correspond to the instability waves that amplify in the shear layers (in accordance with linear theory for $x/D \leq 1.0$).

Figures 85 through 88 present the phase measurements from $x/D = 0.25$ through 1.5 . The phase spectrum at $x/D = 0.25$ exhibits a large amount of scatter due to the extremely low signal amplitude involved. But the figures in general exhibit a high phase shift in the frequency range 15-20 Hz while the modes centered about 60 Hz and 250 Hz show negligible phase shift. From these phase spectra it could be inferred that the modes centered about 60 Hz and 250 Hz are symmetric in nature while the mode centered at 20 Hz is not symmetric.

It may at first appear that the symmetric fluctuation at 60 Hz is not in agreement with the pattern inferred from the space-time correlation measurements previously presented. A strong negative correlation was seen at zero time delay suggesting an antisymmetric pattern with a measured correlation function frequency near 60 Hz. In order to investigate this apparent discrepancy, a simple model involving the space-time correlation between two complex waves made up of 20 Hz and 60 Hz components was performed. The signals were modeled as an interaction between a 20 Hz mode and a 60 Hz mode of form given by

$$A_1(t) = a_1 \sin(\omega_1 t) * a_2 \sin(\omega_2 t) \quad 4-3.4$$

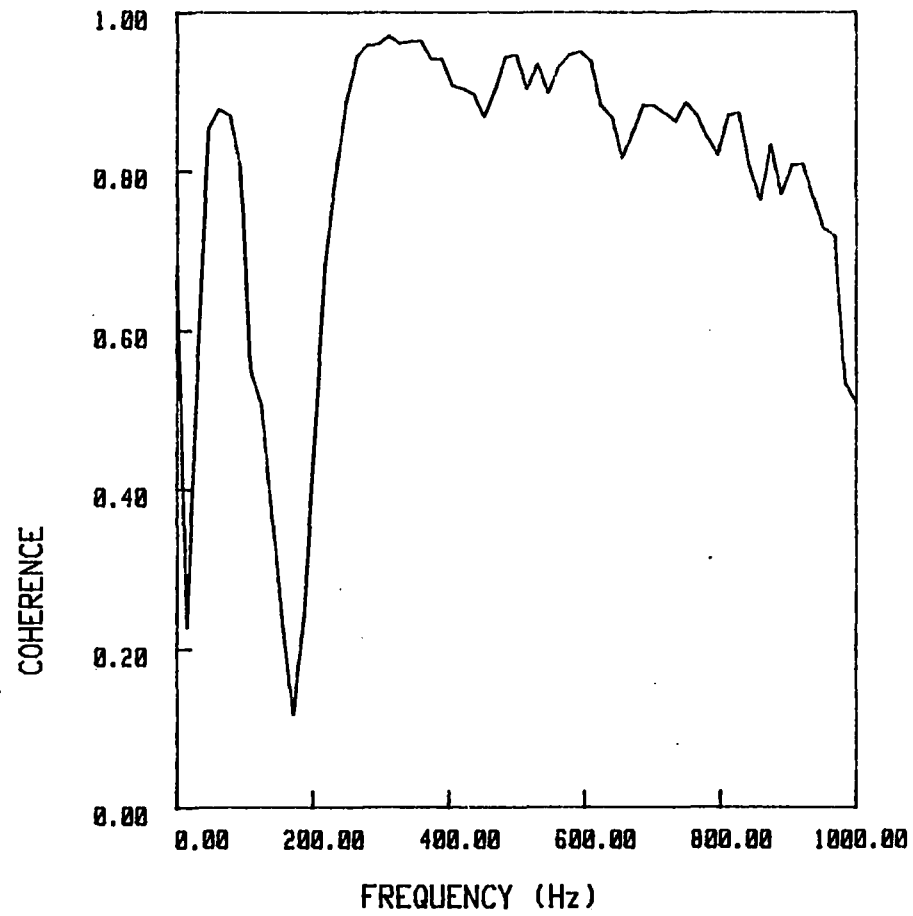


Figure 83. Coherence Spectrum at $x/D = 1$

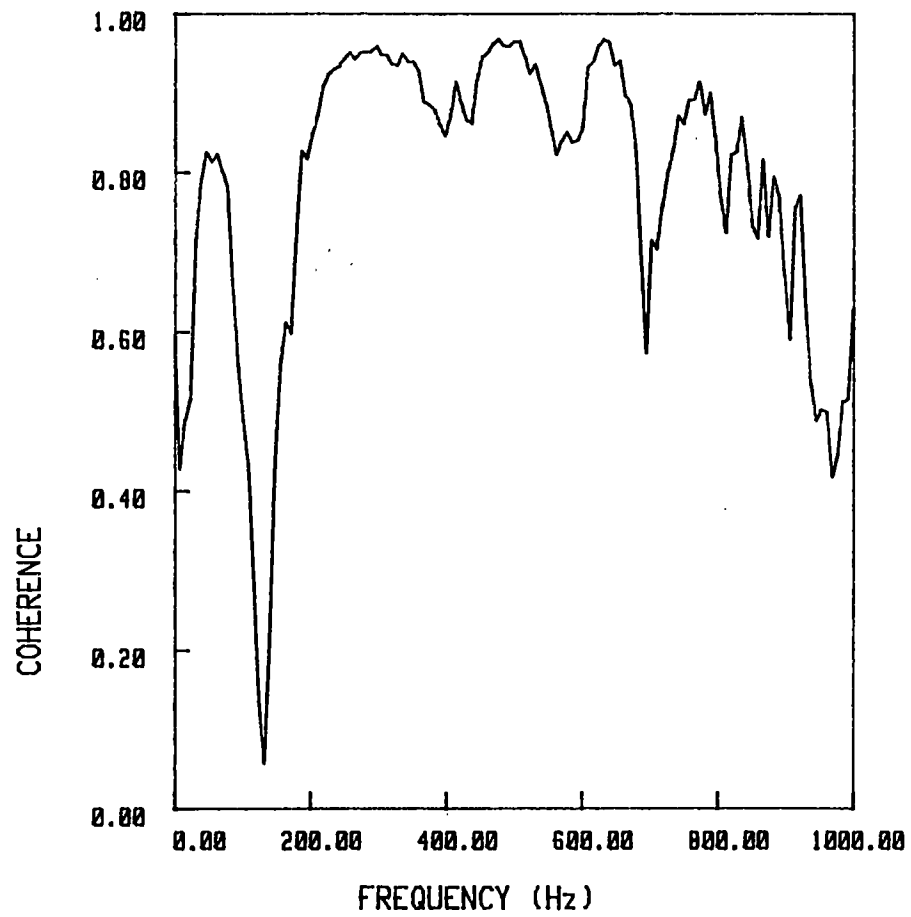


Figure 84. Coherence Spectrum at $x/D = 1.5$

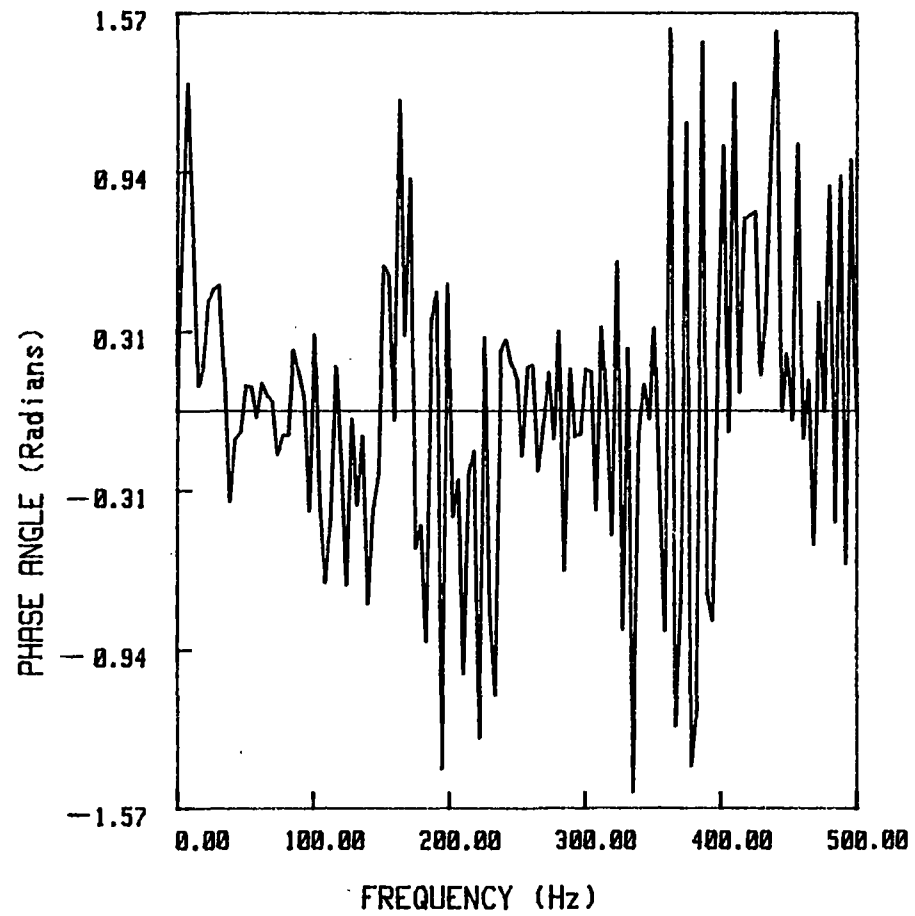


Figure 85. Phase Spectrum at $x/D = 0.25$

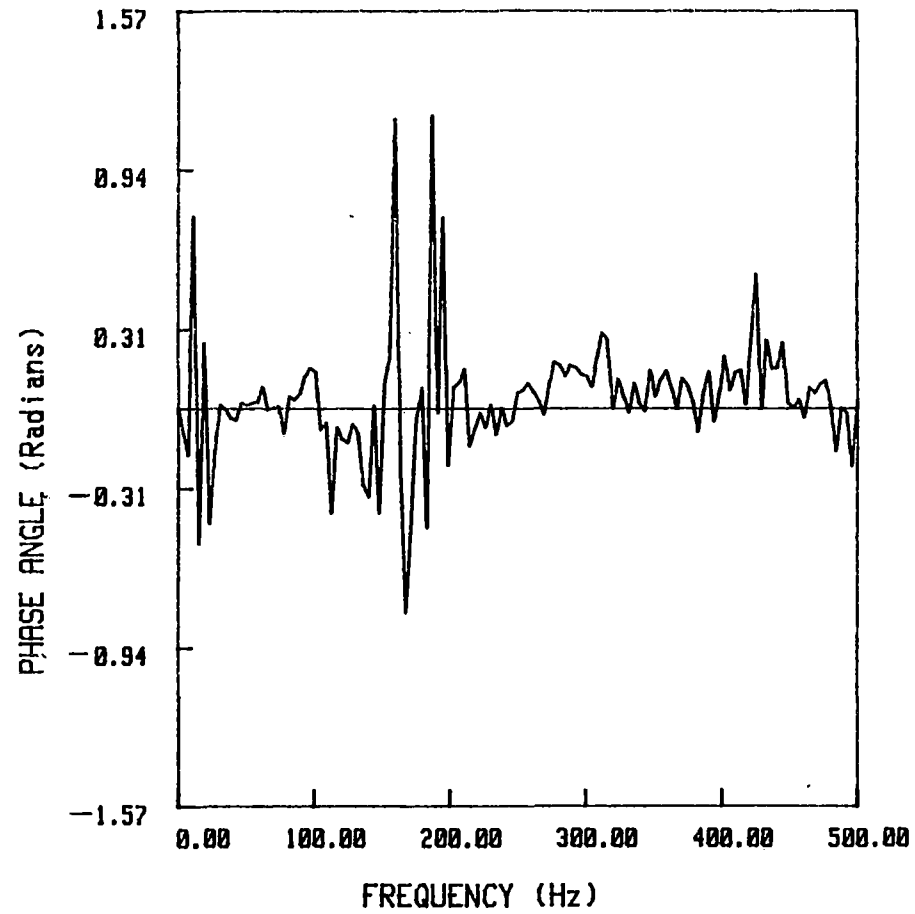


Figure 86. Phase Spectrum at $x/D = 0.5$

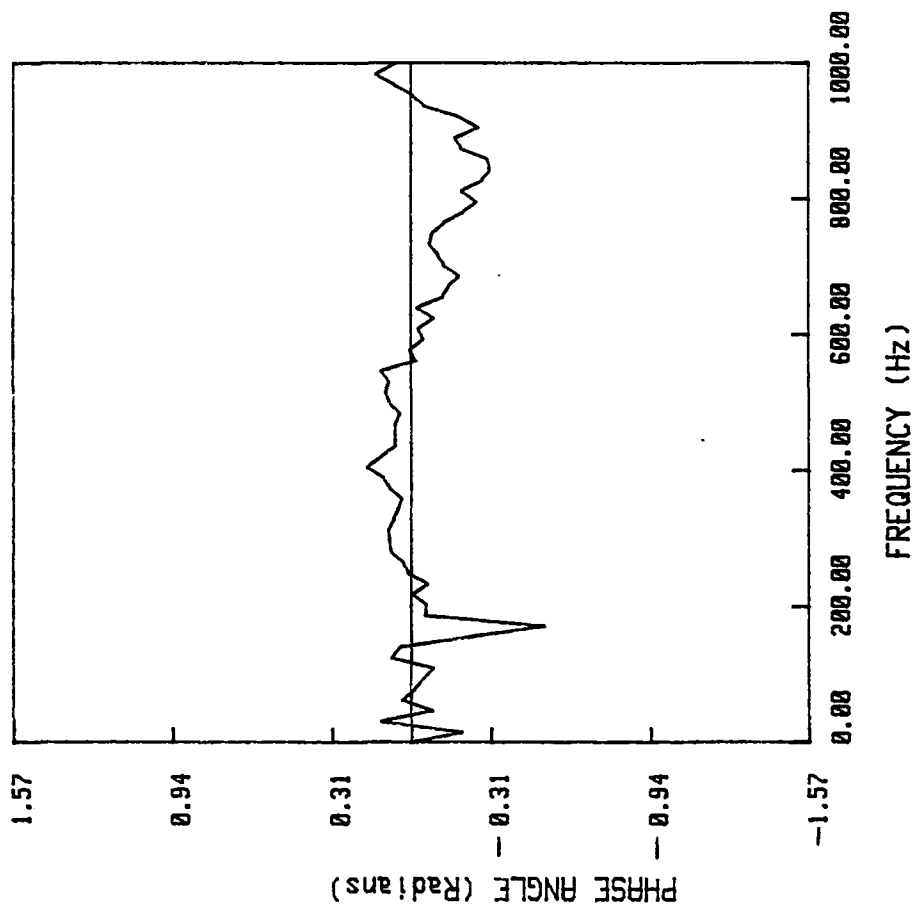


Figure 87. Phase Spectrum at $x/D = 1$

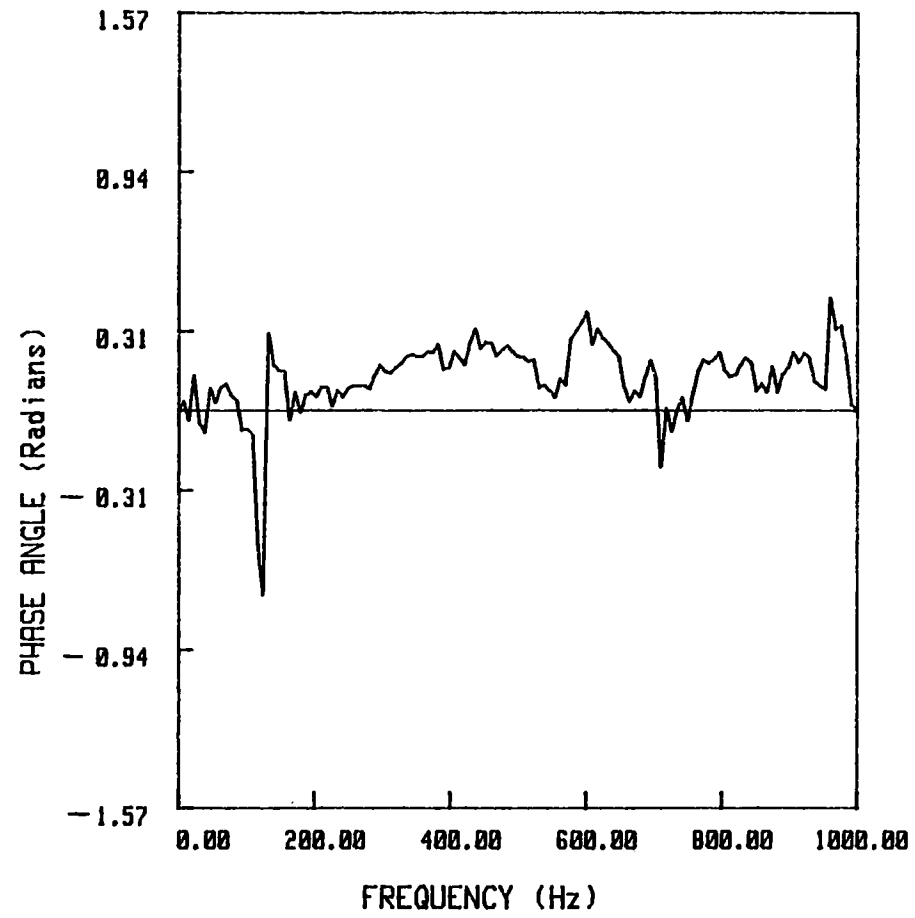


Figure 88. Phase Spectrum at $x/D = 1.5$

$$A_2(t) = a_1 \sin(\omega_1 t + \pi) * a_2 \sin(\omega_2 t) \quad 4-3.5$$

where $\omega_1/2\pi = 20$ Hz, $\omega_2/2\pi = 3\omega_1 = 60$ Hz, $a_1 = 18$, $a_2 = 3.4$.

Note the π phase shift on the ω_1 mode introduced to account for the assumed antisymmetric pattern of this component, while a zero phase shift was assumed on the ω_2 mode as it was assumed to be symmetric. Even though the actual anemometer signal is far more complex, possessing more spectral components and random fluctuation effects, it was thought that incorporating only the major spectral components would be sufficient to investigate the difference in the phase of the 60 Hz mode as inferred from the two types of measurements.

Figure 89 presents the modeled space-time correlation between the two signals (equations 4-3.4 and 4-3.5). Based upon our assumed method for defining correlation function frequency the figure shows a correlation frequency of 60 Hz along with a negative correlation at zero time delay. Hence, it could be concluded that the negative correlation indicated in the actual data shown in Figures 51 and 52 is not necessarily associated with the 60 Hz mode. This is due to the fact that when multiple modes are present (as in the initial jet shear layer) the correlation function contains contributions from all frequency components. It is then impossible to associate the negative correlation as being due to the asymmetry of any one particular mode. This is not the case when a single mode dominates in which case the correlation measurement is much less ambiguous as occurs farther downstream in the similarity region (see Thomas and Brehob (1986)).

The coherence function at $x/D = 2.0$ as seen in Figure 90 shows the formation of spectral peaks quite similar to the power spectral

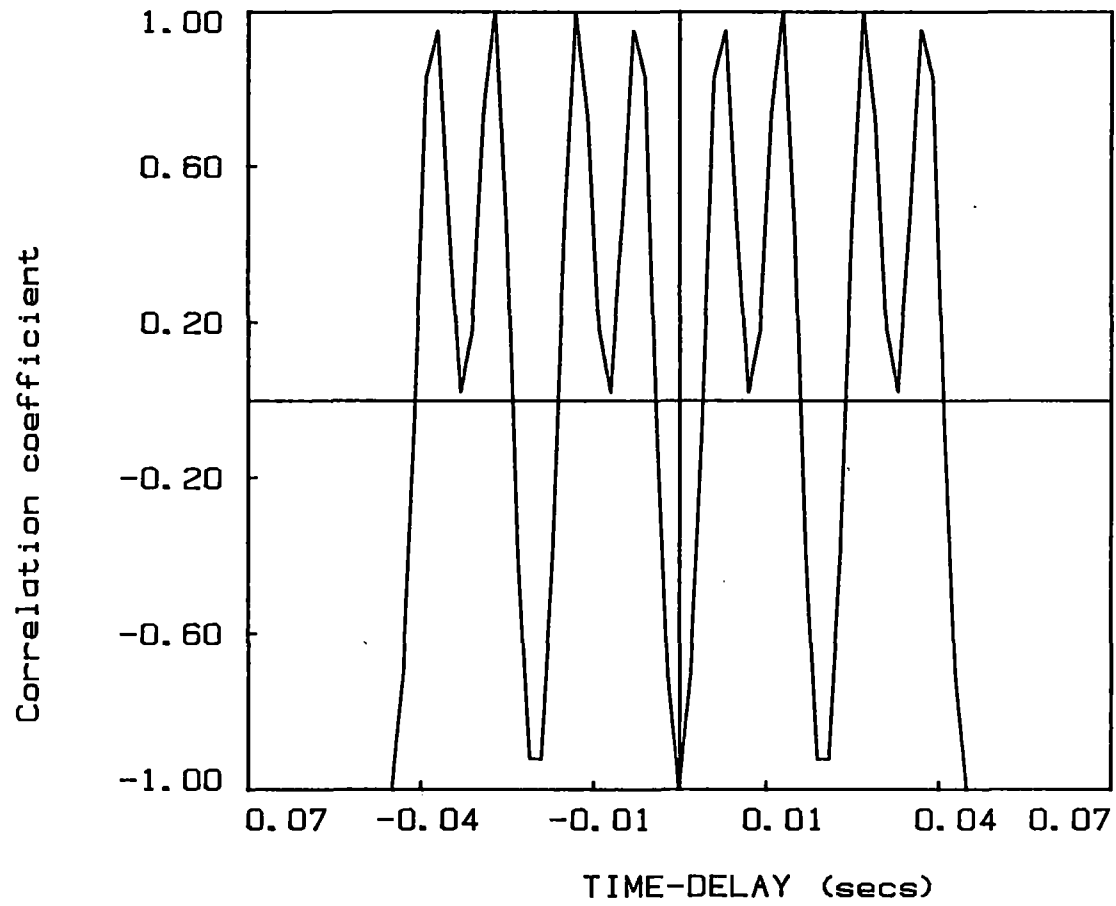


Figure 89. Space-Time Correlation of the Two Signals presented in Equations 4-3.4 and 4-3.5

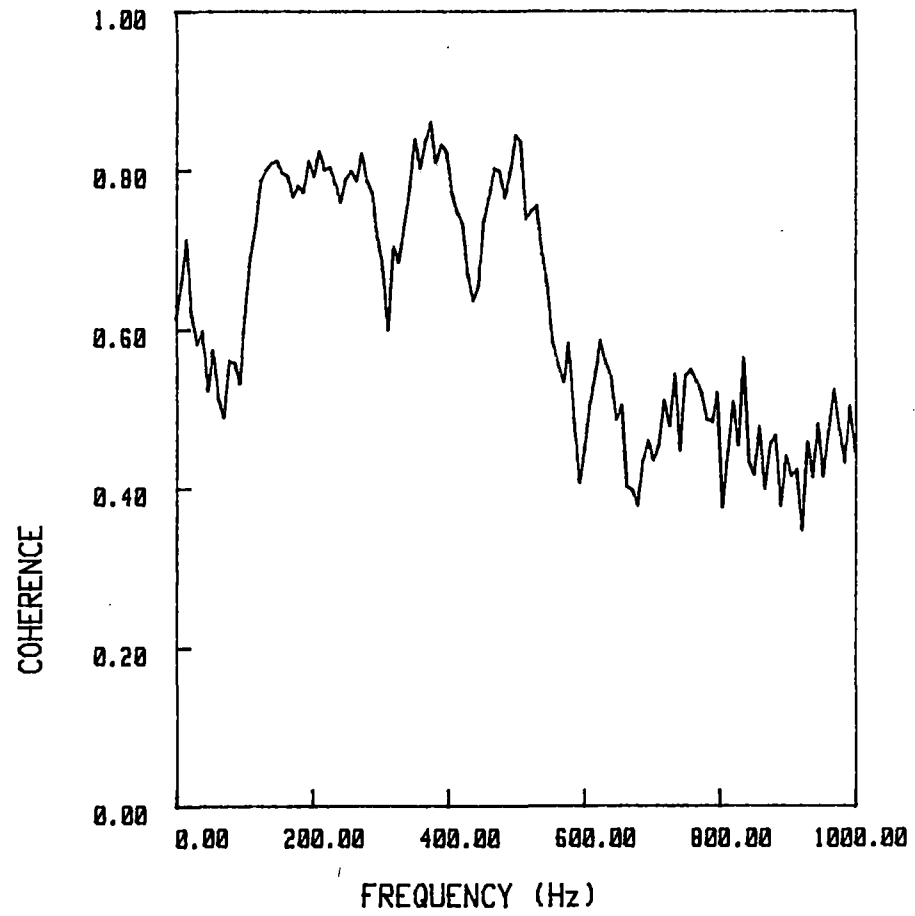


Figure 90. Coherence Spectrum at $x/D = 2$

measurements presented in Figure 26, said to be associated with the roll-up phenomenon. In fact, a drop in the coherence level at all modes is noted which is thought to be due to the inherent phase randomness associated with the rolling up of the instability waves into vortices.

Figures 91 through 94 present the coherence measurement from $x/D = 2.5$ to 5.0 . A gradual shift in the peak coherence function from approximately 250 Hz to 125 Hz is seen to occur between $x/D = 2.5$ to 4.0 (Figures 91 through 93). This phenomenon is in accordance with the halving in frequency noticed in the spectral measurements at downstream locations from $x/D = 2.25$ to 4.5 (Figures 32 and 33). The phase spectra in the region from $x/D = 2.5$ to 4.0 are presented in Figures 95 through 97. A very low phase shift of the modes centered about 250 and 125 Hz is noticed at $x/D = 2.5$ (Figure 95), but the phase shift is seen to increase with downstream distance possibly due to the decay of the 250 Hz mode and the formation of 125 Hz mode. By $x/D = 5$ the 125 Hz mode is seen to exhibit very low phase shift indicating its full development by that location. Figures 98 through 101 show the coherence of the modes centered near 20 Hz, 60 Hz, 125 Hz and 250 Hz with downstream distance. Note that a bandwidth of 10 Hz was used to select the coherence of the frequency modes under consideration. The coherence of these modes is seen to rapidly drop after $x/D \approx 2.0$, which is soon after the roll-up of the instability waves. These figures in comparison with the Figures 75 through 78 (measurements made with one probe fixed at the nozzle exit and the other probe moved downstream) show comparatively low coherence for downstream locations $x/D > 2.0$. Such low coherence between the two signals was thought to be associated with the randomness of the roll-up while the high coherence in Figures 98 through 101

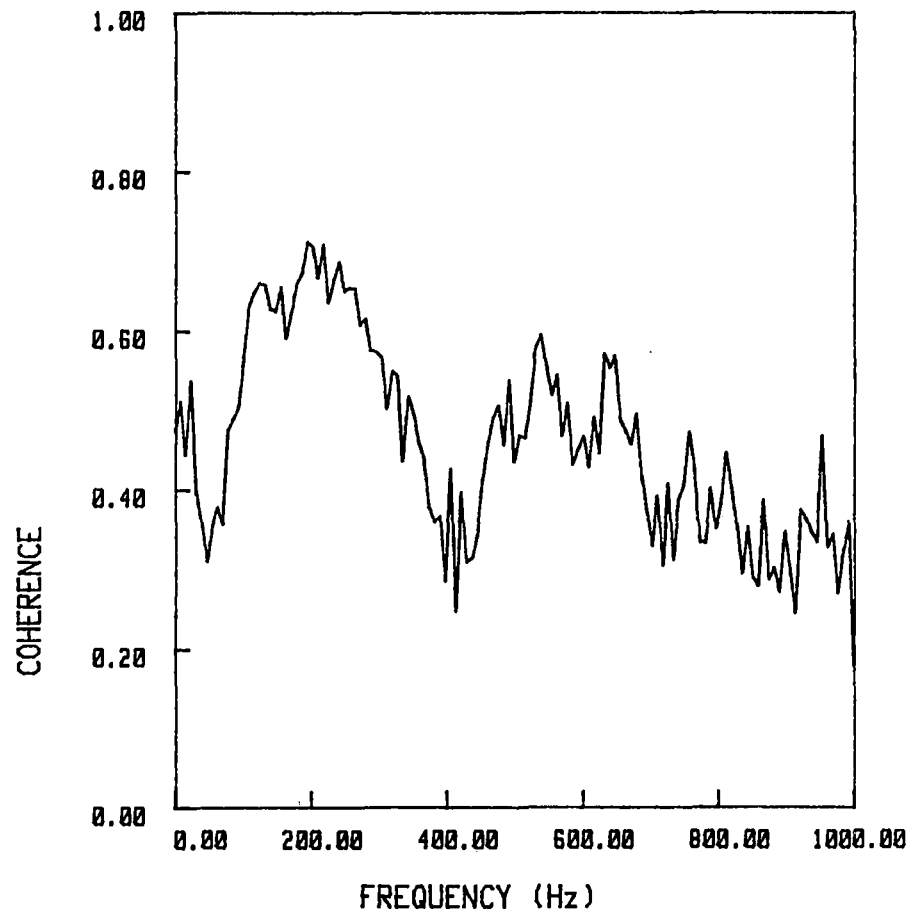


Figure 91. Coherence Spectrum at $x/D = 2.5$

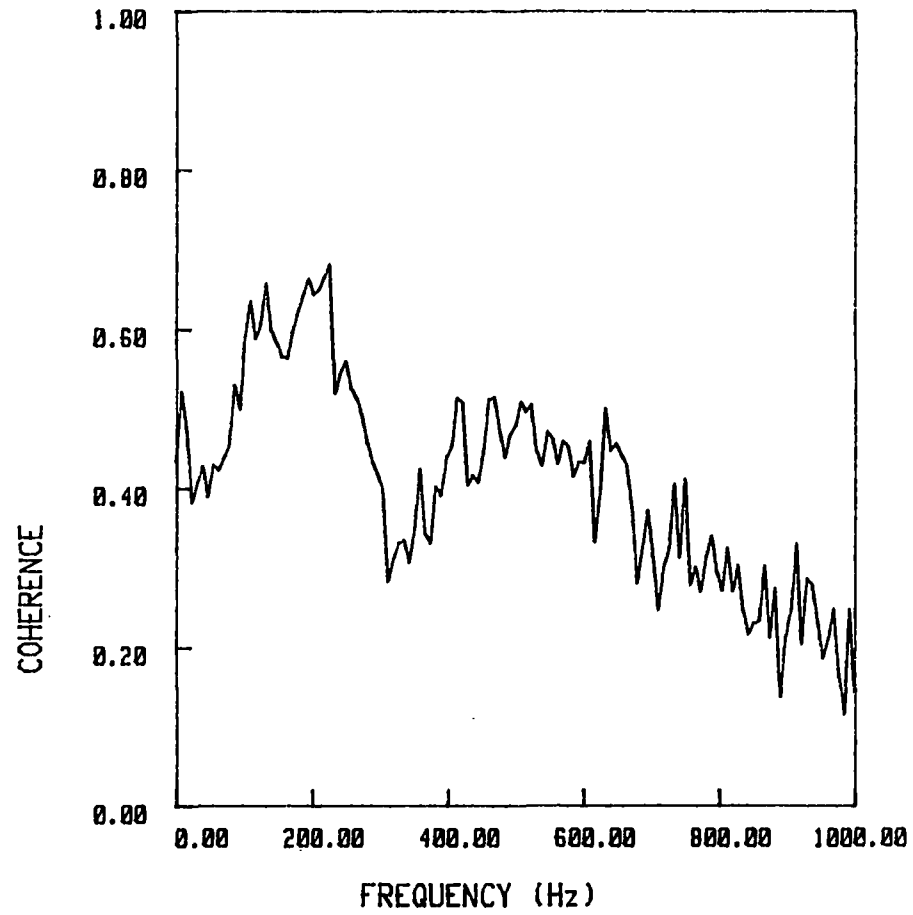


Figure 92. Coherence Spectrum at $x/D = 3$

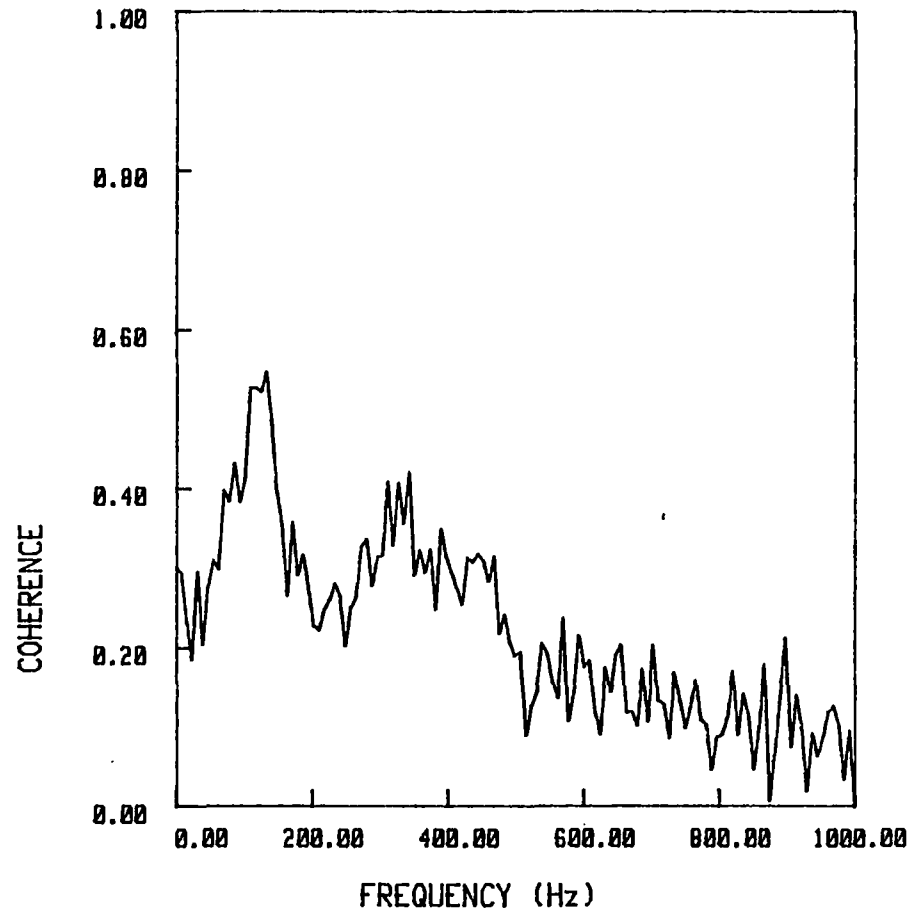


Figure 93. Coherence Spectrum at $x/D = 4$

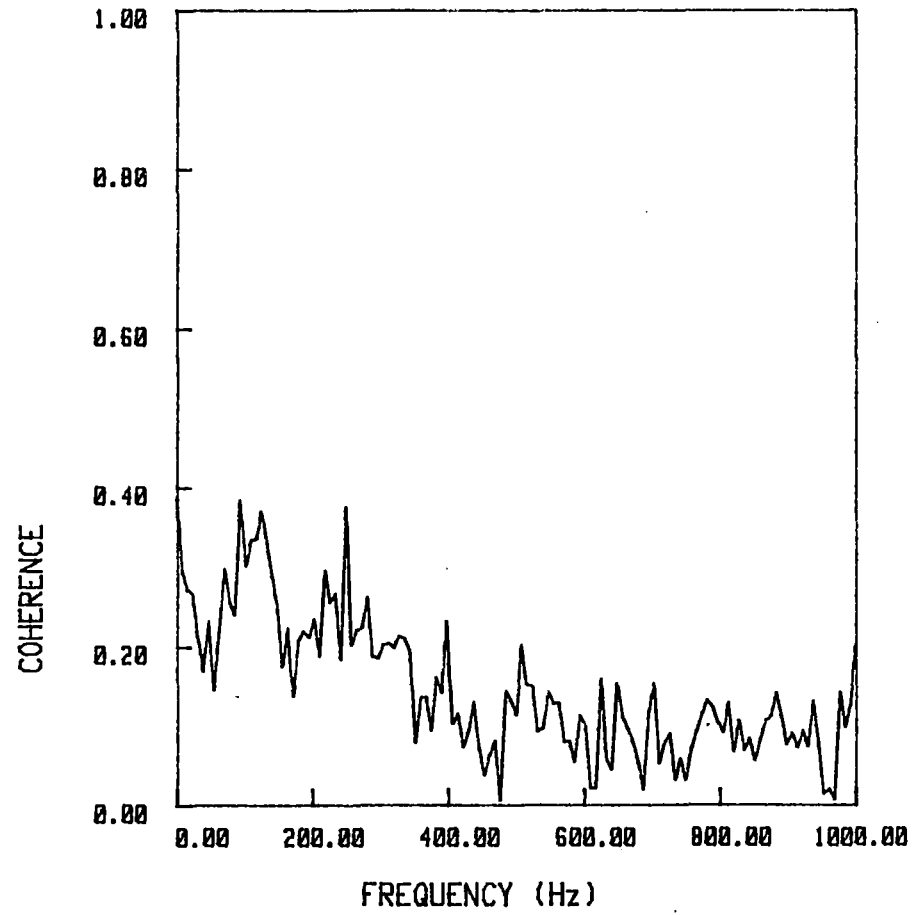


Figure 94. Coherence Spectrum at $x/D = 5$

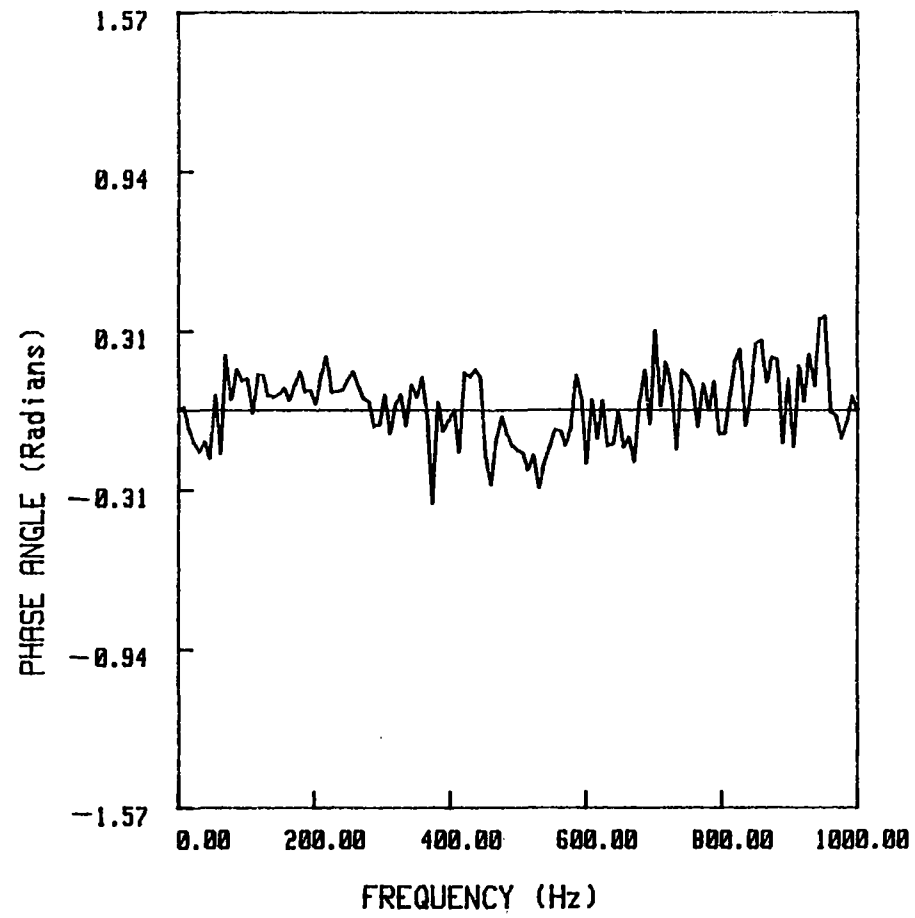


Figure 95. Phase Spectrum at $x/D = 2.5$

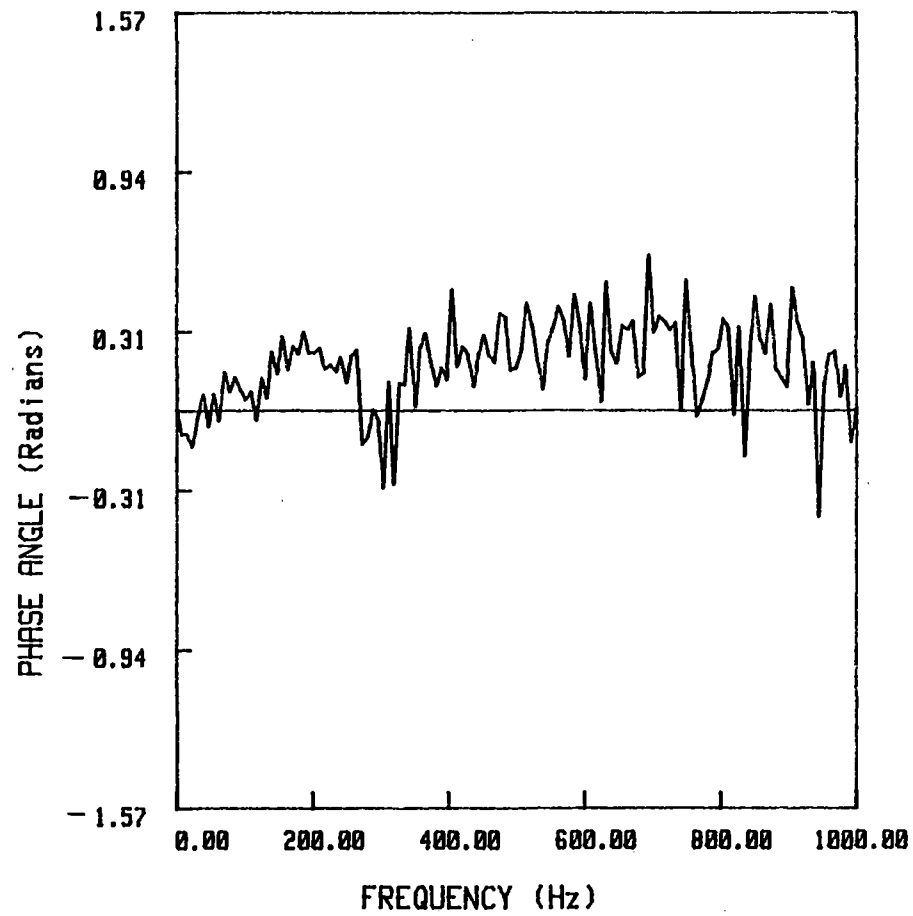


Figure 96. Phase Spectrum at $x/D = 3$

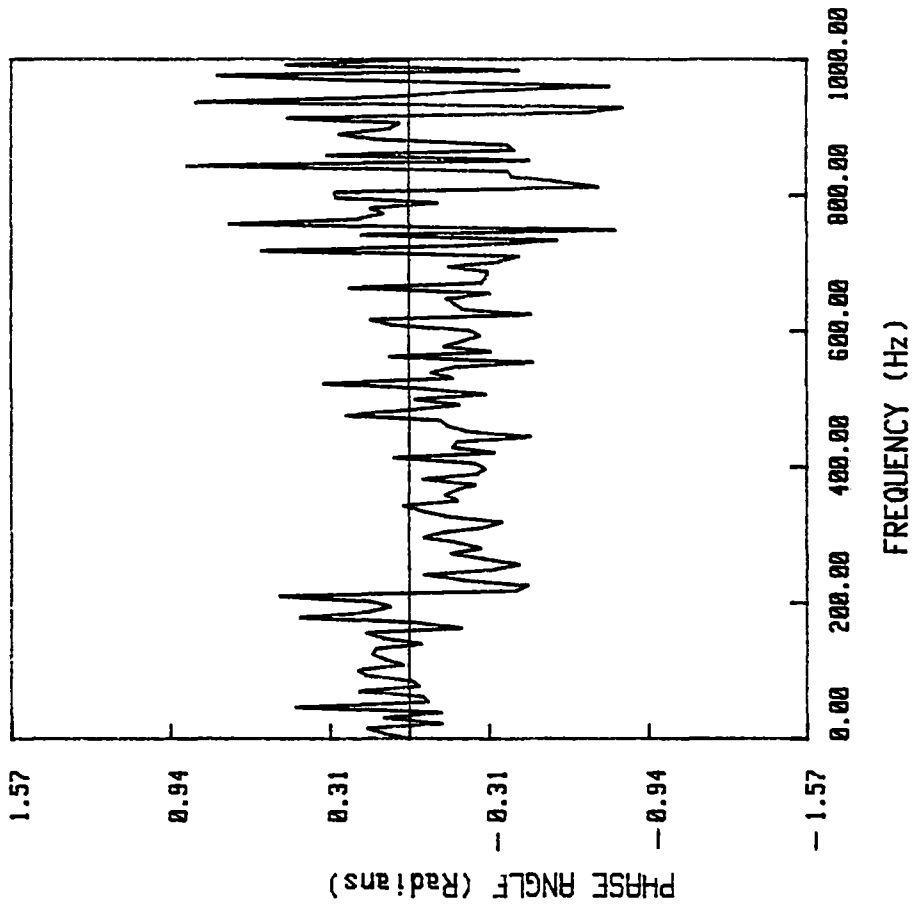


Figure 97. Phase Spectrum at $x/D = 4$

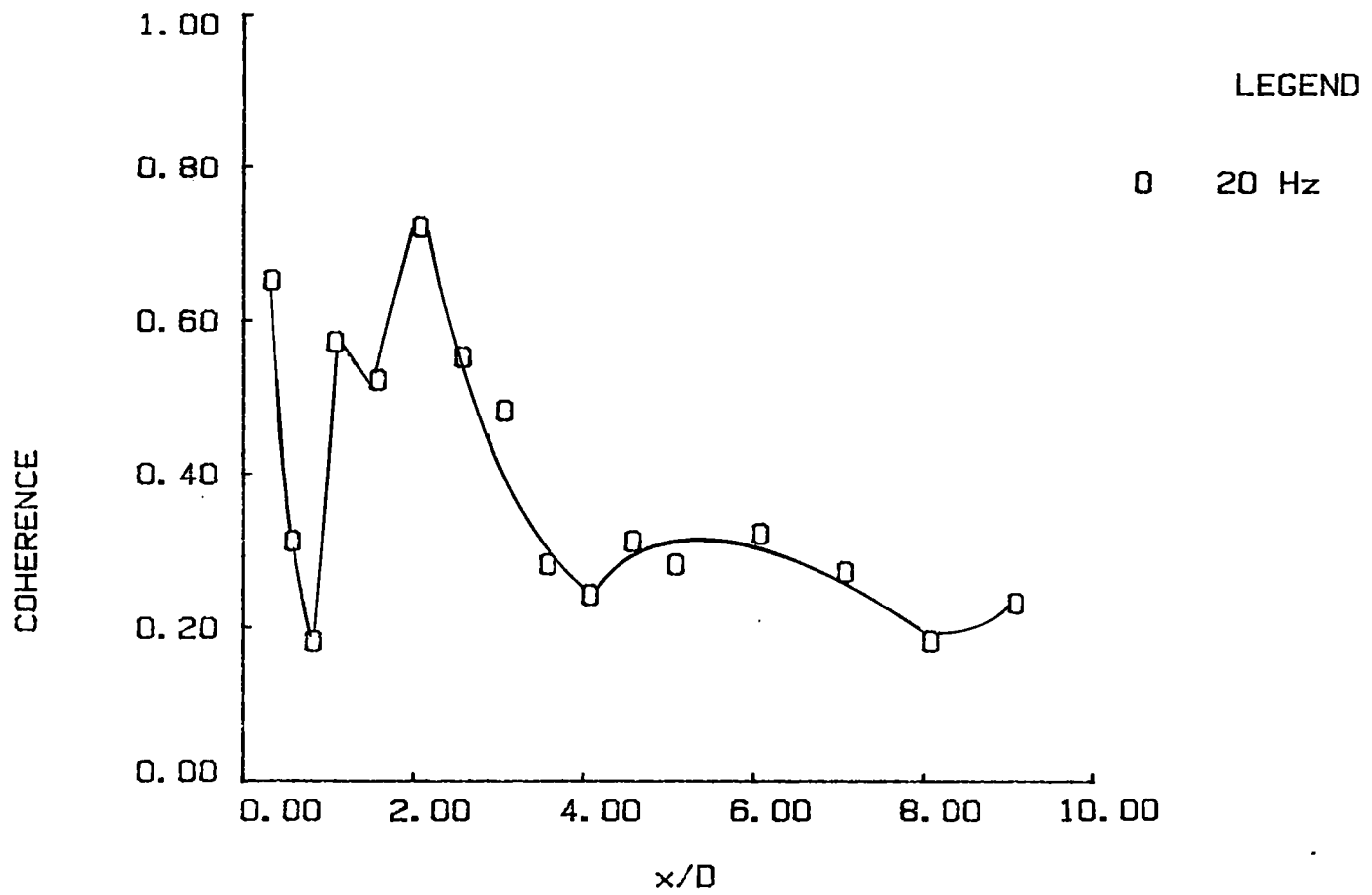


Figure 98. Variation of Coherence of the Mode Near 20 Hz (Bandwidth 5 Hz) with Downstream Distance (Both Probes set Side by Side)

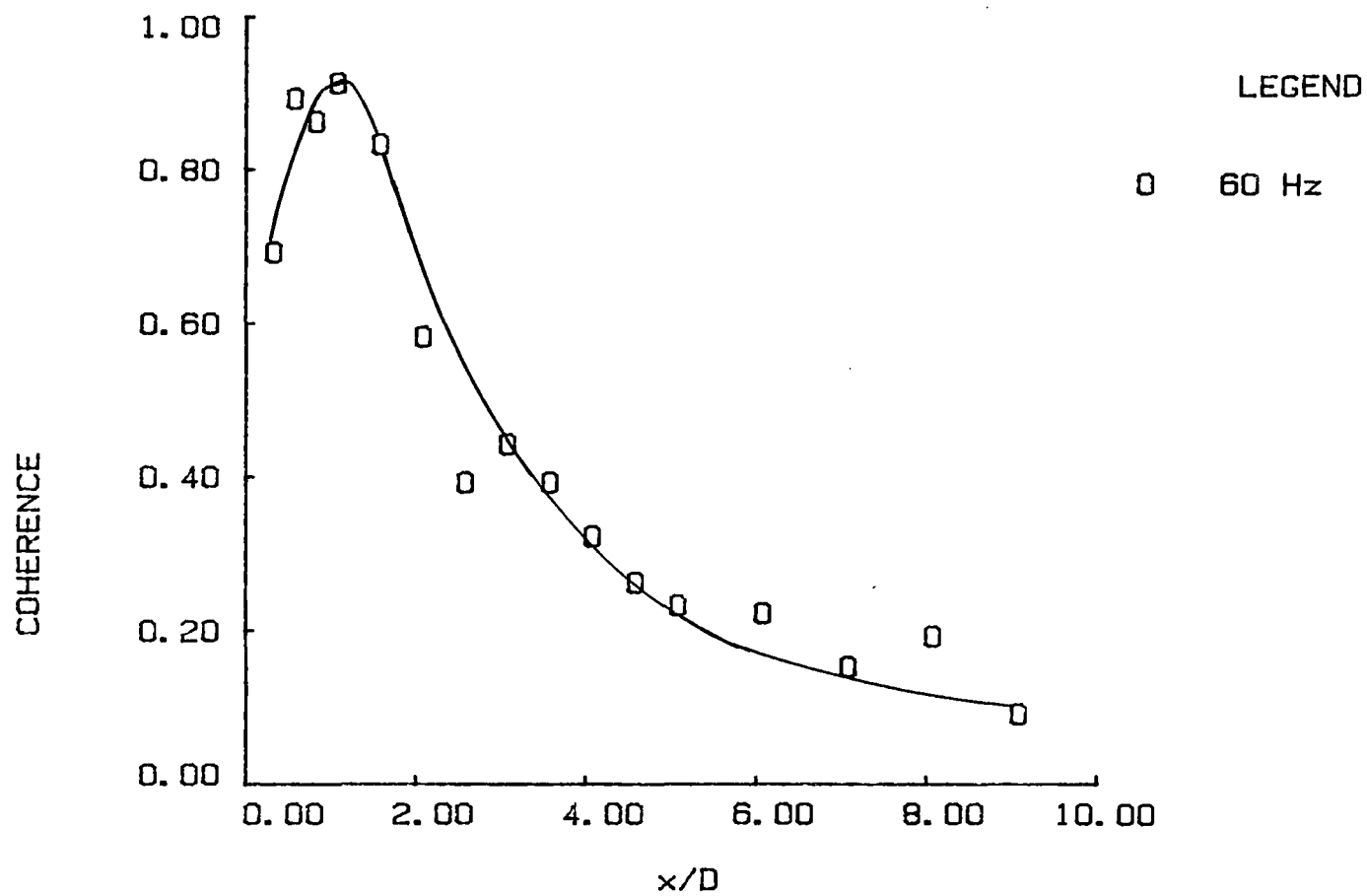


Figure 99. Variation of Coherence of the Mode Near 60 Hz
 (Bandwidth 10 Hz) with Downstream Distance
 (Both Probes set Side by Side)

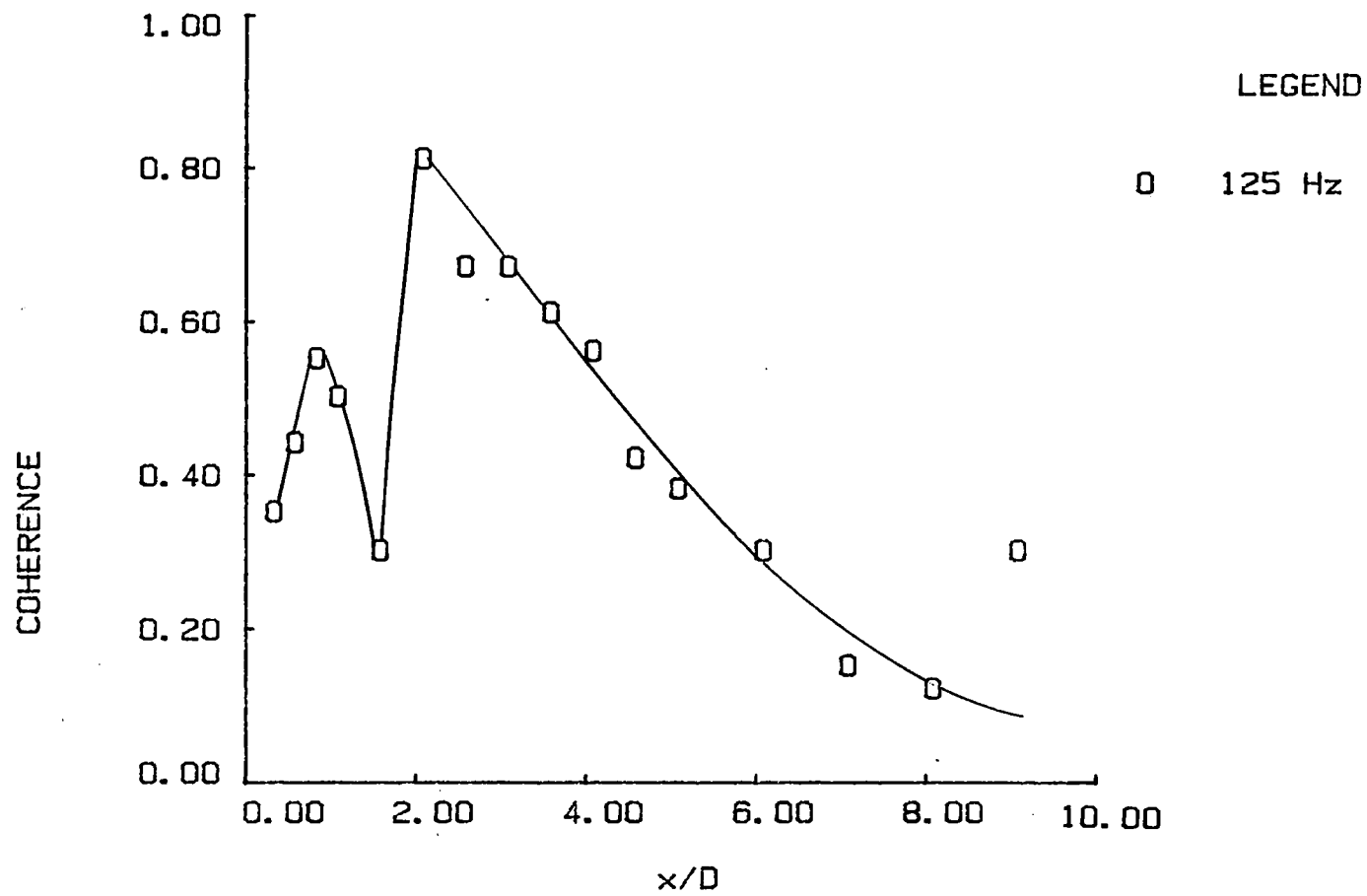


Figure 100. Variation of Coherence of the Mode Near 125 Hz
 (Bandwidth 10 Hz) with Downstream Distance
 (Both Probes set Side by Side)

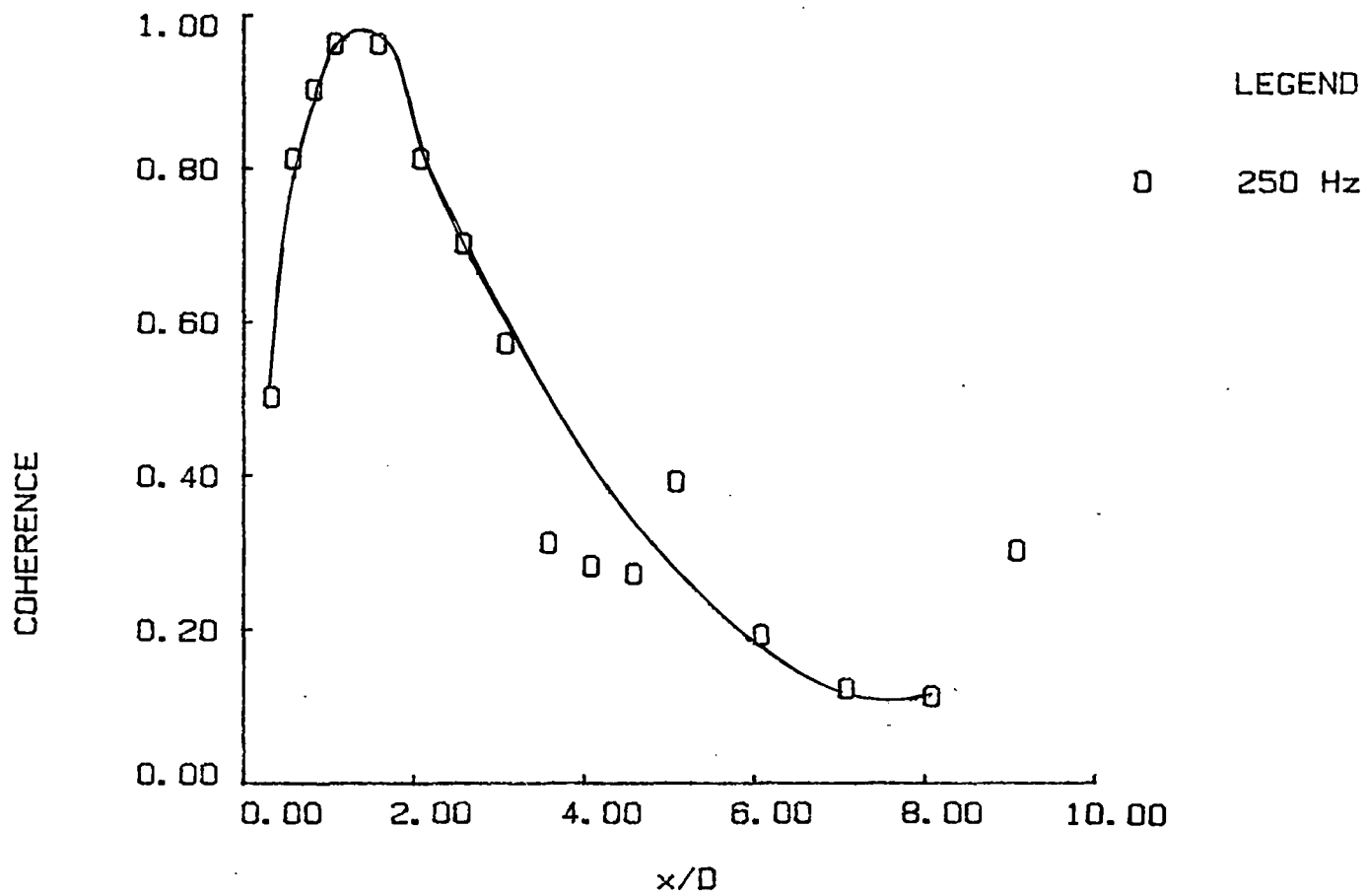


Figure 101. Variation of Coherence of the Mode Near 250 Hz (Bandwidth 10 Hz) with Downstream Distance (Both Probes set Side by Side)

strongly indicates the presence of a coupling between near exit and downstream locations as discussed earlier. Measurements made after $x/D \approx 8$ indicated low coherence between the signals and random phase shifts due to the chaotic nature of the flow. Hence, these measurements are not able to provide much insight as to the events occurring at locations after the end of the potential core.

Thus it could be said that the above sets of coherence and phase measurements have provided additional evidence for the occurrence of each of the following events in the flow: The roll-up of the instability waves complete near $x/D \approx 2$, formation of first subharmonic complete near $x/D \approx 4$, formation of second subharmonic complete near $x/D \approx 8$ and formation of the mode near 15 Hz via a quartering of the dominant frequency by $x/D \approx 16.0$. Further evidence is seen from the variation of the shear layer momentum thickness presented in Figure 102 which shows sharp increases at these approximate locations. These sharp increases are directly related to the occurrence of structural events which cause the shear layer to widen abruptly. Such sharp increases in the momentum thickness are not seen for $x/D \geq 7.0$ but instead a linear variation is noticed. This is due to the fact that the location of vortex pairing events becomes more random with increasing downstream distance. Hence, an average over time results in such a linear variation. Of importance is the recognition that the coherence data indicates that each of the above events is coupled to the near exit flow which suggests the possibility of a resonant feedback effect. This will be examined further in Chapter V.

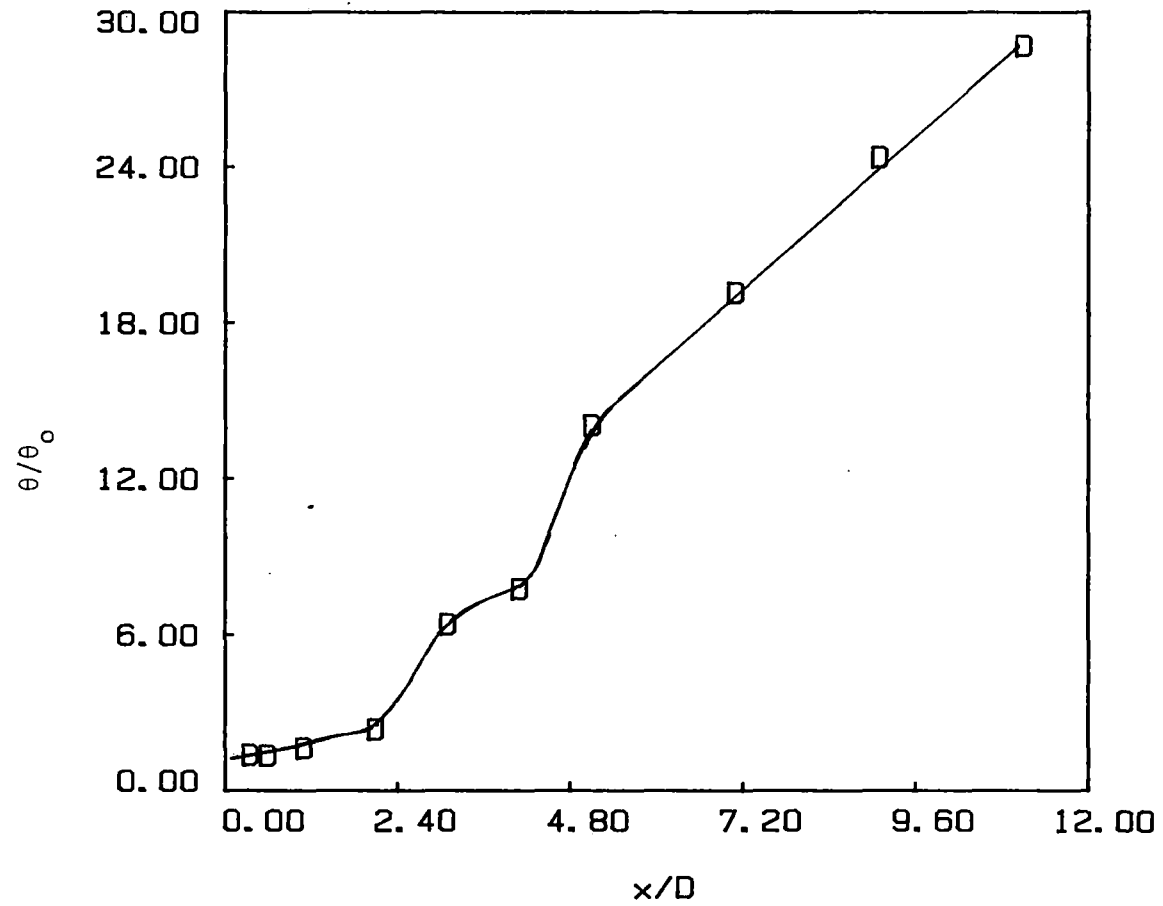


Figure 102. Variation of Momentum Thickness with Downstream Distance

CHAPTER V

EVIDENCE OF FEEDBACK

5.1. Global Resonance Model

The experimental results presented in the previous chapter document the occurrence of localized large-scale structure merging/interaction events in the developing two-dimensional turbulent jet. The experimental measurements have also shown that all these events are strongly coupled with the nozzle exit shear layers. In this chapter an analytical model for global resonance in the two-dimensional jet is presented and is examined in light of the presented experimental measurements. The analytical model described is based on a feedback model proposed by Ho and Nossier (1981) for impinging jet flows and extended by Ho and Huang (1982) to mixing layers. Thomas and Goldschmidt (1985) initially proposed a similar mechanism for the planar turbulent jet.

A requirement for resonance to occur between two streamwise locations in a flow separated by a distance Δx is given by

$$\begin{aligned} & \text{"Time Taken for Convection of} && \text{"Time for acoustic} \\ & \text{large-scale structures downstream"} & + & \text{disturbance to propagate upstream"} \\ & = \text{"some integral multiple of the resonance period."} && (5-1) \end{aligned}$$

This relation assumes that the feedback loop consists of downstream propagating coherent vortical structures whose subsequent interactions

lead to upstream propagating acoustic waves. These are believed to excite the nascent jet shear layers to complete the feedback loop. Mathematically the above relation is then

$$\int_{x_0}^{x_0 + \Delta x} \frac{dx}{KU_m(x)} + \frac{\Delta x}{a} = \frac{N}{f_{res}} \quad (5-2)$$

where $N = \text{integer}$, $K = \text{constant} = U_c(x)/U_m(x) \approx 0.6$, $U_c(x) = \text{structural convective velocity}$, $a = \text{acoustic speed}$, $x_0 = \text{the streamwise near exit location for the feedback node}$ and $f_{res} = \text{the resonant frequency associated with the structural interaction event near the end of the potential core}$ and $x_0 + \Delta x = \text{downstream location associated with the vortex pairing event}$.

Since in our case x_0 is approximately at the nozzle lip the equation (5-2) reduces to

$$\int_0^{x_i} \frac{dx}{KU_m(x)} + \frac{x_i}{a} = \frac{N}{f_{res_i}} \quad (5-3)$$

where x_i is the location of the i^{th} downstream large-scale structural interaction event. For a low speed subsonic flow it follows that

$$\int_0^{x_i} \frac{dx}{KU_m(x)} \gg \frac{x_i}{a} \quad (5-4)$$

hence,

$$\int_0^{x_i} \frac{dx}{KU_m(x)} \approx \frac{N}{f_{res_i}} \quad (5-5)$$

or

$$f_{res_i} \approx \frac{N}{\int_0^{x_i} \frac{dx}{KU_m(x)}} \quad (5-6)$$

If global resonance is to exist in the two-dimensional jet then the above relation must be satisfied throughout the flow field; in both the developing jet shear layers and in the interaction and early similarity regions beyond the jet potential core.

The experimental measurements presented clearly indicated the development of symmetric arrays large-scale structures in the developing shear layers adjoining the potential core. Evidence for symmetry is seen from both the phase spectra and correlation coefficient functions presented. For example, the correlation coefficient function at $x/D = 2.5$ (see Figure 56) shows a maximum value of +0.7 at zero time-delay indicating the presence of symmetrically arranged structures. This is in contrast to results from similar measurements made in the similarity region of planar jet which suggest a self-preserving anti-symmetric array (see Thomas and Brehob (1986)). The shear layer interaction initiated near the end of the potential core thus defines a "symmetry breaking mechanism" which modifies the basic flow structure from a symmetric to an anti-symmetric large-scale structural array. It is thus apparent that the merging of the shear layers near the end of the potential core must result in a vortex pairing/destruction event as the corresponding shear layer structures are forced to interact. This is schematically illustrated in Figure 103. It is now necessary that the characteristic resonance frequency = f_{pc} associated with this structural event should satisfy the requirement of global resonance. Thus it

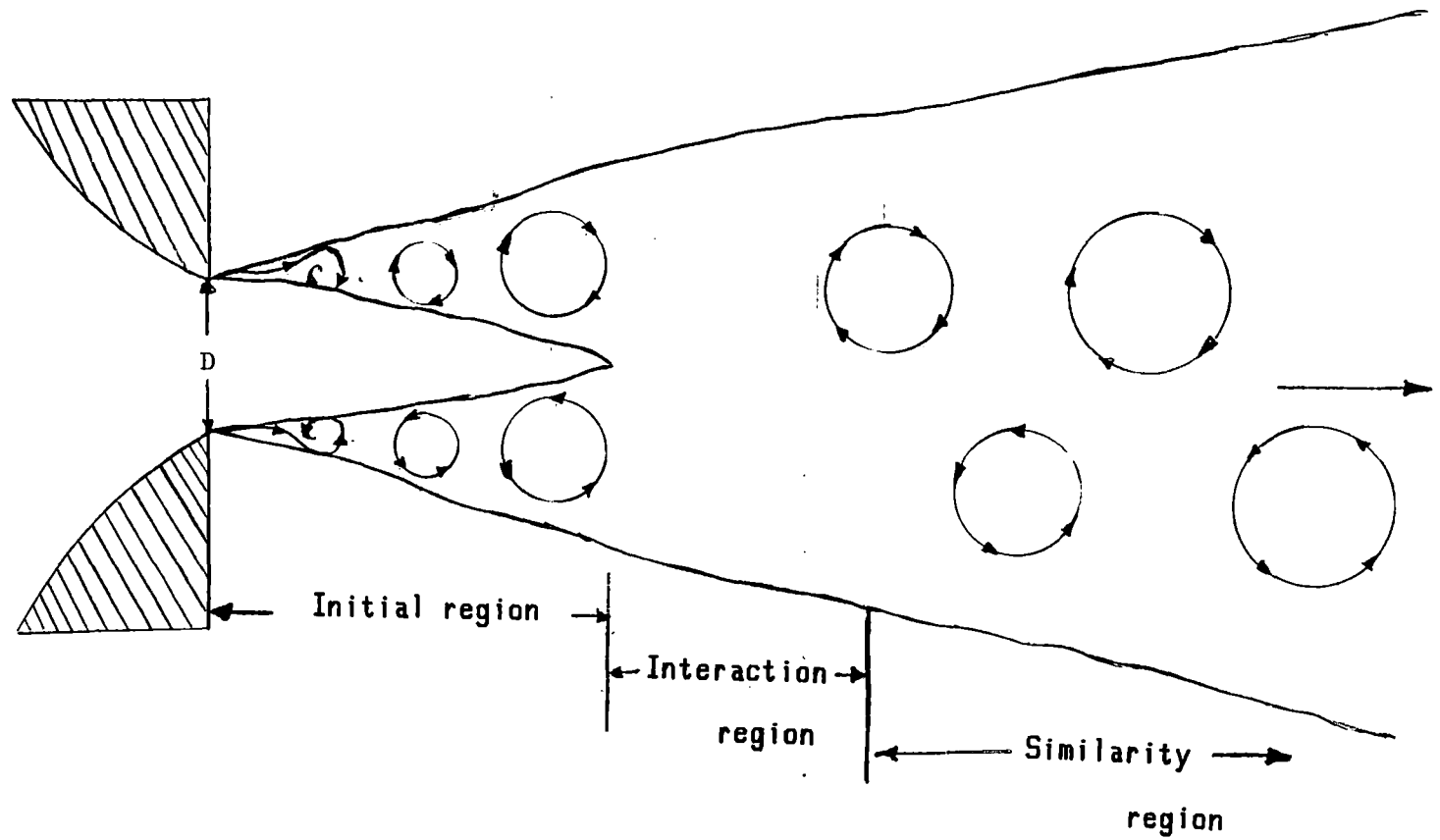


Figure 103. Schematic of Structural Patterns in the flow

follows that

$$f_{pc} = \frac{N}{\int_0^{x_{pc}} \frac{dx}{KU_m(x)}} \quad (5-7)$$

The experimental measurements illustrating the developing shear layer frequency spectra show significant frequency changes with downstream distance (see Figure 74). Such changes seem to result primarily from vortex pairing events as discussed earlier. Since a passage frequency halving occurs at pairing locations, it is possible to predict the occurrence of all vortex pairing events from the requirements of global resonance when one pairing event location along with the corresponding structural frequency is known. With this in mind it could be said that

$$f_i = 2^i f_{pc} \quad (5-8)$$

where i corresponds to the " i^{th} " event prior to the end of potential core and f_i is the structural frequency associated with the completion of the i^{th} pairing event. In this manner negative i values denote events downstream of x_{pc} . Substituting equation (5-8) in equation (5-7) we get an implicit relation for event locations:

$$2^i f_{pc} = \frac{N}{\int_0^{x_i} \frac{dx}{KU_m(x)}} \quad (5-9)$$

Figure 104 shows schematically another parameter of importance, namely the shear layer spreading rate $d\delta/dx$ which will be defined as the maximum slope shear layer thickness. The relationship among the

parameters is established from the geometry of Figure 10⁴ where it is seen that

$$\alpha = \tan^{-1} \left(\frac{D}{2x_{pc}} \right) \quad (5-10)$$

Assuming small angles,

$$\alpha \approx \frac{D}{2x_{pc}} \quad (5-11)$$

and from geometry it is seen that

$$\frac{d\delta}{dx} \approx \frac{D}{x_{pc}} \quad (5-12)$$

A curve fit to the data of Figure 20 indicates a nominal value of $d\delta/dx = 0.118$ in the nonlinear region of the initial jet flow.

Thus the expressions governing the proposed model are summarized as follows:

The approximate location of the end of the potential core is related to slot width D and shear layer widening $d\delta/dx$ by

$$\frac{x_{pc}}{D} = \left(\frac{d\delta}{dx} \right)^{-1} \quad (5-13a)$$

The characteristic frequency associated with the structural interaction near the end of the potential core is obtained from

$$f_{pc} \approx \frac{N}{x_{pc} \int_0^{x_{pc}} \frac{dx}{KU_m(x)}} \quad (5-13b)$$

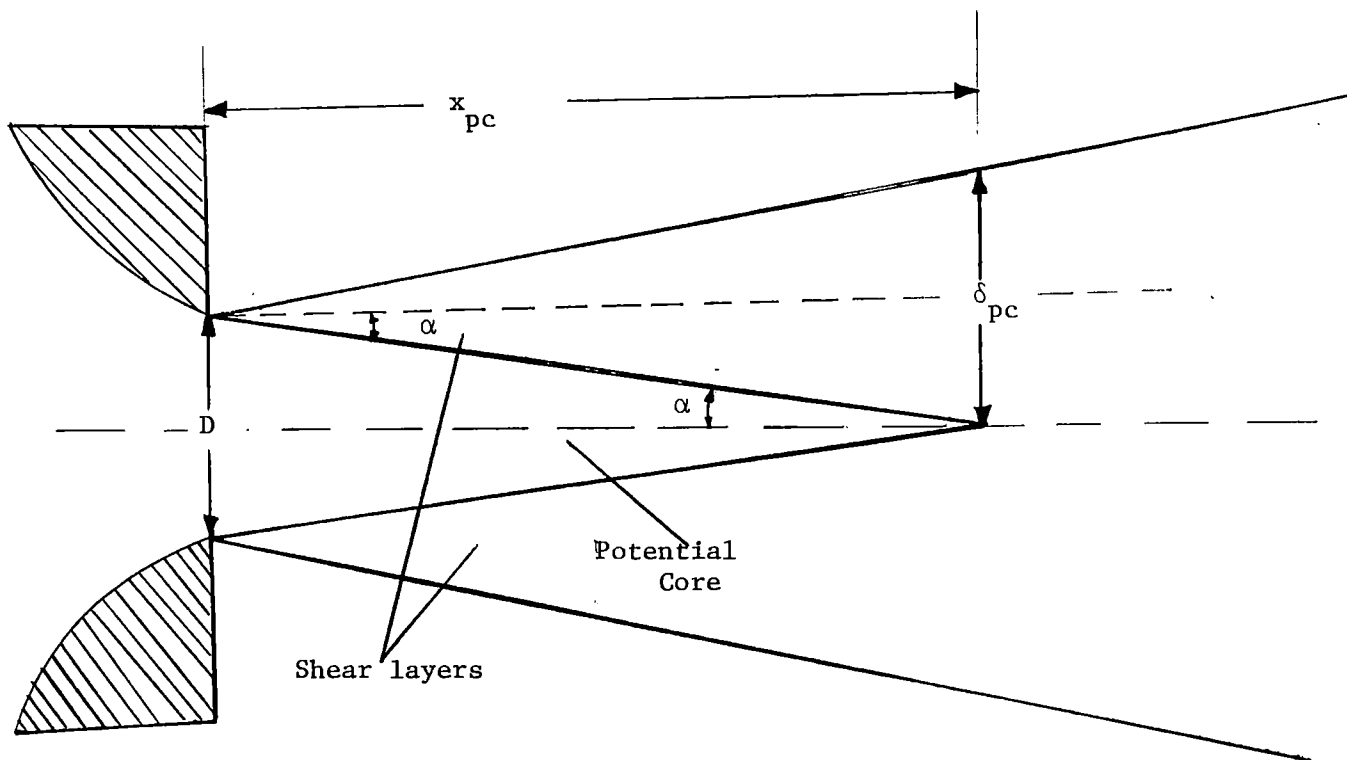


Figure 104. Geometrical Representation of the Shear Layer and the Potential Core Regions

The passage frequency associated with the i^{th} large-scale structural events are then obtained from

$$f_i = 2^i f_{pc} \quad (i = \text{integer}) \quad (5-13c)$$

The location of these events are implicitly given by

$$2^i f_{pc} = \frac{N}{\int_0^{x_i} \frac{dx}{KU_m(x)}} \quad (5-13d)$$

The following section presents a comparison of the model with the experimental data presented in Chapter IV.

5.2. Comparison of Global Resonance

Model Predictions with Experiment

Equation (5-13a), results in a predicted $x_{pc}/D = 8.5$. This is seen to be in good agreement with the value of $x_{pc}/D = 7.0 - 8.0$ inferred from the intensity and mean velocity profiles. The frequency associated with the end of the potential core is then calculated from equation (5-13b) $f_{pc} = 51$ Hz. This too is in good agreement with the spectral and coherence measurements which have shown the presence of a mode near 60 Hz at the above mentioned location. Now with both, the downstream location marking the end of potential core and the frequency associated with the structural pattern at that location known, equation (5-13d) could be employed to predict the merging locations before and after the end of the potential core.

The location of the i^{th} vortex interaction event prior to and after the end of the potential core is obtained by varying $i = -1, 0, 1, 2,$

3... in equation (5-13d). Note $i = 0$ corresponds to the end of the potential core with positive "i" corresponding to upstream locations. The passage frequency corresponding to the i^{th} vortex interaction event is calculated from equation (5-13c) and for $i = -1, 0, 1, 2, 3$ the predicted frequencies are 25.5 Hz, 51 Hz, 102 Hz, 204 Hz and 408 Hz. The downstream locations for the occurrence of vortex interaction events corresponding to the predicted frequencies from equation (5-13d) are as follows:

$$\begin{aligned} (x/D)_{i=-1} &= 16.2 & (x/D)_{i=0} &= 8.0, & (x/D)_{i=1} &= 4.4 \\ (x/D)_{i=2} &= 2.2, & (x/D)_{i=3} &= 1.1. \end{aligned}$$

It was shown earlier that the linear amplification region extended from $0 \leq x/D \leq 1.25$ and its behavior was well predicted by Michalke's linear theory (see Figure 8). The low frequency modes likely related to global resonance merely acted as passive neutral modes in this region exhibiting negligible interaction with the higher frequency shear layer instabilities (which must be true from the definition of linear stability theory). Hence, any structural interaction event must take place beyond the end of the linear growth region, i.e., in the nonlinear transition region. With this in mind examination of the predicted occurrence of events mentioned above results in a limit of $i = 2$ to be imposed. Thus the analytical model predicts the occurrence of events at $x/D = 2.2$ and $x/D = 4.4$ prior to the end of the potential core and at $x/D = 16.2$ after the end of the potential core. Merging locations farther downstream were not inferred from the model since the experimental measurements were restricted for the location $0 \leq x/D \leq 20.0$.

Experimental measurements are in very good accordance with the

above findings. These measurements have predicted the occurrence of the following events during the flow development: the roll-up of instability waves at approximately 250 Hz by $x/D \approx 2.0$, vortex merging resulting in a structural pairing frequency at approximately near 125 Hz by $x/D \approx 4.0$, vortex interaction associated with the end of the potential core by $x/D \approx 8.0$ at a passage frequency at approximately near 60 Hz and another vortex interaction by $x/D \approx 16$ resulting in a structural passage frequency at approximately near 20 Hz. Figure 105 presents a comparison of the theoretically predicted frequencies and locations with experimentally measured coherence based values. A good agreement is seen between the theoretical and experimental values.

A discrepancy noted earlier regarding the roll-up is well explained by the above model. As discussed in section 4.1. the most amplified instability wave is ≈ 750 Hz and it was expected based on similar results for mixing layers that this would correspond to the vortex roll-up frequency. Instead, the jet exhibited roll-up at approximately 250 Hz. The reason for this difference is that the global resonance phenomenon as discussed above requires an event to occur at $x/D \approx 2.2$ near a frequency of 208 Hz and not near 750 Hz in order to satisfy the resonance conditions near the end of the potential core imposed by the length scale, D . The spectral measurements presented in Figures 23, 25 and 28 show how this transformation takes place. Figure 23 ($x/D = 1.25$) shows the growth of the subharmonic (≈ 375 Hz) of the fundamental instability mode (750 Hz). With downstream distance the subharmonic (≈ 375) shows no growth but a sudden growth of the modes at approximately 300 and 422 Hz is noticed by $x/D = 1.75$ (Figure 25). A possible explanation of the presence of these two modes is the formation

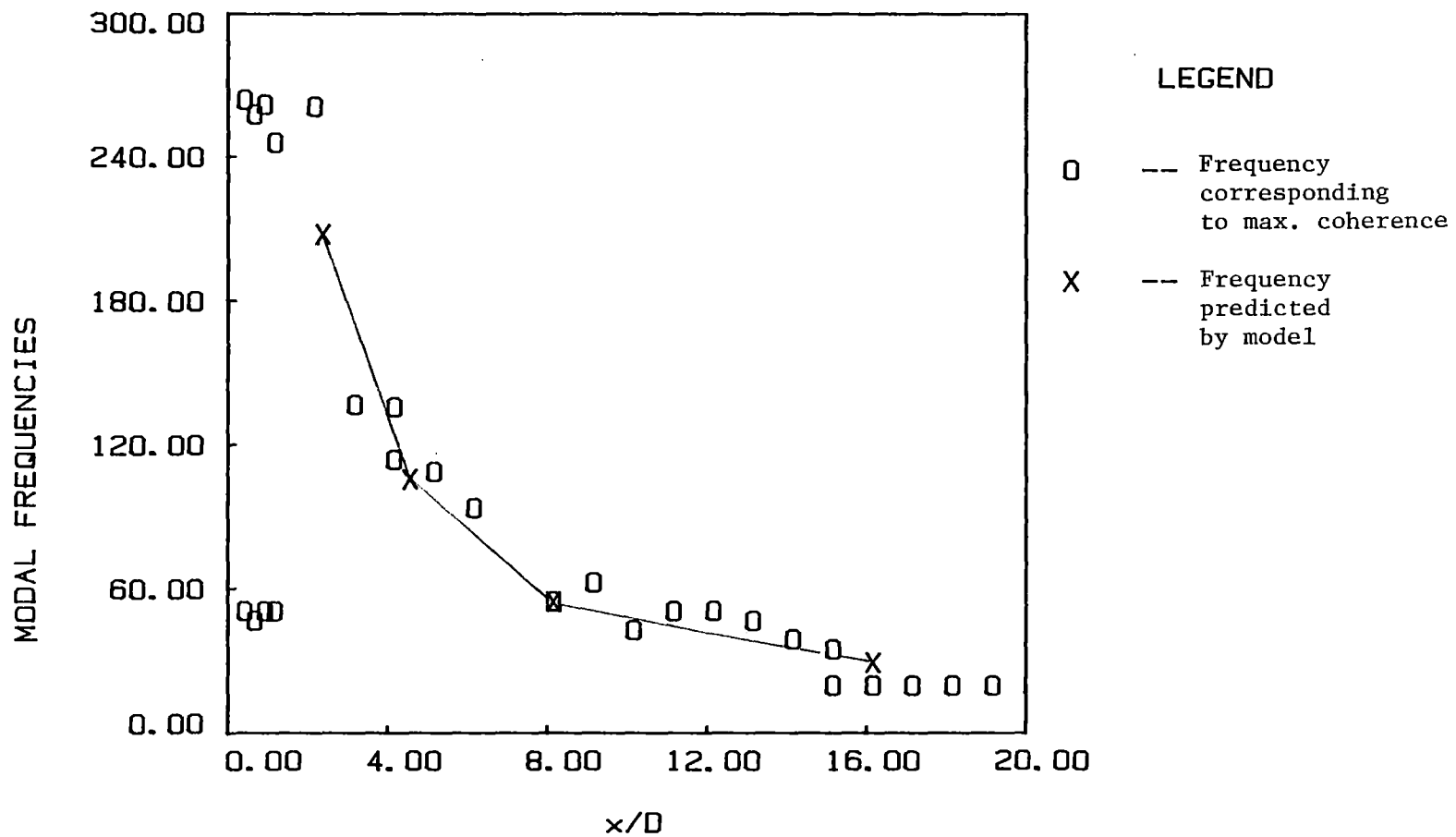


Figure 105. Comparison of Theoretically Predicted Frequencies and Locations for Structural Events with Experimentally Measured Coherence Based Values

of upper and lower sidebands on the subharmonic (≈ 375) by f_{pc} (≈ 60 Hz) which acts as a modulating signal. The lower sideband near 300 Hz decays as rapidly as it formed (see Figure 25 and 28). This decay is associated with the growth of the mode near 250 Hz (again approximately 60 Hz lower than the mode near 300 Hz) which then rolls up into vortices. Though the roll-up frequency is obviously related to the mode f_{pc} the exact dynamic mechanism involved is not presently fully understood.

The selection of 60 Hz as the modulating signal in preference to the other resonance modes seen at the nozzle exit shear layers is well predicted by the model. According to the proposed model the structural interaction taking place at the end of the potential core is the most important event in the flow. Hence, it is rather expected that this structural event should influence the initial flow development in order to match the condition at the end of the potential core. Such an influence is seen in the form of a modulating signal at 60 Hz as mentioned above. The resonance mode near 20 Hz indicated by the power spectral measurements at the nozzle exit (Figure 21) is seen to bring about a faster redistribution of energy for locations $x/D > 5.0$.

In conclusion it could be said that the model presented is truly in agreement with the experimental measurements. Further the effect of the length scale (D) on what otherwise would have been a free shear layer has been clearly demonstrated.

5.3. Conclusions

The measurements presented in this work are in support of the existence of a global resonance mechanism operating in the planar

turbulent jet. Power spectra, space-time correlations and coherence measurements have been used to document the following events which are important in the flow development: The roll-up of the instability waves into vortices near $x/D \approx 2.0$, structural merging at $x/D \approx 4.0$, structural interaction between shear layers just beyond the end of the potential core near $x \approx 8.0$ and a double merging/destruction event near $x/D \approx 16$. Each of these events are coupled to the nozzle exit flow by a feedback loop. In particular, the interaction between shear layers beyond the jet potential core is seen to be the most important event and largely determines the global flow dynamics. This aspect is well predicted by an analytical model presented in Chapter V. The model is found capable of predicting the frequencies and streamwise locations associated with each of the interaction events. Both model and experiments indicate that the structural roll-up in the jet is significantly altered from the behavior seen in single mixing layers and that the shear layer interaction beyond the potential core is primarily responsible for the modification. The location of this shear layer interaction was seen to be dependent on the nozzle slot-width D and the importance of this imposed length scale on the overall flow development was well illustrated by the model.

5.4. Recommendations

Several extensions to the current work would enhance understanding of the reported phenomenon. These are listed below:

1. Investigation regarding the occurrence of structural events could be further substantiated with the help of flow visualization arrangement. Some possible methods are dye injection in the flow, smoke

wire and hydrogen bubble techniques.

2. An additional measurement, namely the bicoherence measurement, would provide more quantitative information regarding nonlinear interactions in the jet. In particular, these measurements provide information as to whether one spectral mode is a result of the nonlinear interaction between two other modes.

3. A parametric study involving different nozzle slot widths (D) and different exit velocities with experiments similar to those reported can be performed to see how it affects the resonance phenomenon and in turn the proposed model.

4. Experimental measurements similar to those reported could be done but with nascent shear layers excited with low level acoustic excitation. Such excitation alters considerably the structural flow development and a study could be made to see how well the model is in agreement with the acoustically modified flow. Experimental measurements in an excited flow would provide better results for the following reason. The flow becomes well organized with a definite reference mode in it and it is easier to follow the occurrence of events with respect to the excited mode than with the flow excited by random background excitation.

5. In all further measurements it is very important to maintain the exit velocity to a very close tolerance as it directly affects the measured passage frequency of the structures.

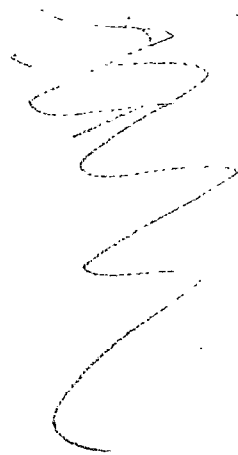
REFERENCES

- Antonia, R. A. Browne, L. W. B., Rajagopalan, S., and Chambers, A. J. "On the Organized Motion of a Turbulent Plane Jet." J. Fluid Mech., 134 (1983), pp. 49-66.
- Bradshaw, P. "The Effects of Initial Conditions on the Development of a Free Shear Layer." J. Fluid Mech., 26 (1966), pp. 255-236.
- Browand, F. K. "An Experimental Investigation of the Instability of an Incompressible Separated Shear Layer." J. Fluid Mech. 26, (1966), pp. 281-307.
- Browand, F. K., and Weidman, P. D. "Large Scales in the Developing Mixing Layer." J. Fluid Mech., 76, 1 (1976), pp. 127-144.
- Brown, G. L., and Roshko, A. "On Density Effects and Large Structure in Turbulent Mixing Layers." J. Fluid Mech., 64, 4 (1974), pp. 775-816.
- Bruun, H. H. "A Time Domain Analysis of the Large Scale Flow Structure in a Circular Jet." J. Fluid Mech., 83, 4 (1977), pp. 641-671.
- Cervantes De Gortari, J. G. "An Experimental Study of the Flapping Motion of a Turbulent Plane Jet". Ph.D. Thesis, School of Mechanical Engineering, Purdue University, (1978):
- Cervantes de Gortari, J. G., and Goldschmidt, V. W. "The Apparent Flapping Motion of a Turbulent Plane Jet--Further Experimental Results." Trans. of ASME, J. Fluids Engr., 103 (1981), pp. 119-126.
- Chambers, F. W. "Acoustic Interaction with a Turbulent Plane Jet". Ph.D. Thesis, School of Mechanical Engineering, Purdue University, (1977):
- Collis, D. C., and Williams, N. J. "Two-Dimensional Convection from Heated Wires at Low Reynolds Number". J. Fluid Mech. 6, (1959), pp. 357-384.
- Dimotakis, P. E., and Brown, G. L. "The Mixing Layer at High Reynolds Number: Large Structure Dynamics and Entrainment." J. Fluid Mech., 78, 3 (1976), pp. 535-560.
- Flora, J. J. Jr., and Goldschmidt, V. W. "Virtual Origins of a Free Plane Turbulent Jet". AIAA Journal, 7, 12 (1969), pp. 2344-2346.
- Foss, J. F. "A Study of Incompressible Bounded Turbulent Jets". Ph.D. dissertation, Purdue University, (1965).

- Freytmuth, P. "On Transition in a Separated Laminar Boundary Layer". J. Fluid Mech. 25, (1966), pp. 683-704.
- Goldschmidt, V. W., and Bradshaw, P. "Flapping of a Plane Jet." Phys. Fluids, 16, 3 (1973), pp. 354-355.
- Gutmark, E., Ho. Bulletin of American Phys. Soc. 25, (1980), p. 1102.
- Gutmark, E., and Wagnanski, I. "The Planar Turbulent Jet." J. Fluid Mech., 73, 3 (1976), pp. 465-495.
- Hegge Zijnen, B. G. van der. "Measurements of the Velocity Distribution in a Plane Turbulent Jet of Air". Appl. Sci. Res., 7, A (1958), pp. 256-276.
- Ho and Huerre. "Perturbed Free Shear Layers." ANN REV. FLUID Mech. (1984), 16: pp. 365-424.
- Ho and Huang. "Subharmonics and Vortex Merging in Mixing Layers." J. Fluid Mech. (1982), 119, pp. 443-473.
- Ho, C. M., and Nossier, N. S. J. Fluid Mech. 105, 119 (1981).
- Jenkins, P. E., and Goldschmidt, V. W. "Study of the Intermittent Region of a Two-Dimensional Plane Jet": Herrick Lab Report. HL 74-75. School of Mechanical Engineering, Purdue University, (1974).
- Jordinson, R. "Design of Wind Tunnel Contractions". Aircraft Eng., 33, 392 (1961), pp. 294-297.
- Kaiser, K. F. "An Experimental Investigation of Interaction of an Acoustic Field and a Plane Turbulent Jet". Purdue University, 1971.
- Kibens, V. "Discrete Noise Spectrum Generated by an Acoustically Excited Jet." Presented at the 5th Aeroacoustics Conference of the American Institute of Aeronautics and Astronautics, Seattle, Washington, 1979.
- Lau, J. C., Fisher, M. J., and Fuchs, H. V. "The Intrinsic Structure of Turbulent Jets." J. of Sound and Vibration, 22, 4 (1972), pp. 379-406.
- Lau, J. C., and Fisher, M. J. "The Vortex-Street Structure of Turbulent Jets. Part 1." J. Fluid Mech., 67 (1975), pp. 299-337.
- Laufer, J., "Transition and Turbulence." Academic, (1981), pp. 63-76.
- Laufer, J. and Monkewitz, P. AIAA meeting, Hartford, CT June, 1980, Paper No. 80-0962.
- Miksad, R. W. "Experiments on the Nonlinear Stages of Free-Shear-Layer Transition". J. Fluid Mech. 56, (1972), pp. 695-719.

- Miksad, R. W. et. al. "Experiments on the Role of Amplitude and Phase Modulations During Transition to Turbulence". J. Fluid Mech. 123, (1982), pp. 1-29.
- Michalke, A. J. Fluid Mech. 23, 521 (1965).
- Moore, C. J. J. Fluid Mech. 80, (1977), p. 321.
- Mulej, D. J. "The Velocity of the Interface". M. S. Thesis, School of Mechanical Engineering, Purdue University, (1975).
- Mumford, J. C. "The Structure of the Large Eddies in Fully Developed Turbulent Shear Flows. Part 1. The Plane Jet." J. Fluid Mech., 118 (1982), pp. 241-268.
- Oler, J. W., and Goldschmidt, V. W. "A Vortex-Street Model of the Flow in the Similarity Region of a Two-Dimensional Free Turbulent Jet." J. Fluid Mech., 123 (1982), pp. 523-535.
- Ott, E. S. "Convective Velocities in a Turbulent Plane Jet". M. S. Thesis, School of Mechanical Engineering, Purdue University, (1972).
- Sato, H. J. Fluid Mech. 1, 53 (1960).
- Thomas, F. O. "Effect of Nozzle Geometry of Acoustic Interaction With a Turbulent Plane Jet". M.S. thesis, Purdue University, (1980).
- Thomas, F. O. "Development of a Two-Dimensional Turbulent Jet Under Natural and Excited Conditions." Ph.D. dissertation, Purdue University, 1983.
- Thomas, F. O., and Brehob, E. Physics of Fluids, Accepted for publication, (1986).
- Thomas, F. O. and Goldschmidt, V. W. "The Possibility of a Resonance Mechanism in the Developing 2-D Jet." Phys. Fluids, (1985), pp. 3510-3514.
- Thomas, F. O., and Goldschmidt, V. W. "Structural Characteristics of a Developing Planar Jet." J. Fluid Mech., (1986).
- Wazzan, A. R., G. Keltner, T. T. Okamura, and A. M. O. Smith. J. Heat Transfer, Vol. 90, pp. 109-114, (1968).
- Weir, A. D., and Bradshaw, P. "Resonance and Other Oscillations in the Initial Region of a Plane Turbulent Jet." I. C. Aero Report 75-07, Imperial College of Science and Technology, Department of Aeronautics, (1975).
- Winant, C. D., and Browand, F. K. "Vortex Pairing: The Mechanism of Turbulent Mixing Layer Growth at Moderate Reynolds Number." J. Fluid Mech., 2 (1974), pp. 237-255.

APPENDICES

A large, stylized handwritten mark, possibly a signature or a scribble, consisting of several overlapping loops and curves. It is positioned centrally below the 'APPENDICES' header.

APPENDIX A

COMPUTER PROGRAM LISTINGS

SPECTRUM PROGRAM

```

program spectrum(input,output);
{This program samples a time varying voltage and computes the frequency}
{spectrum by the Fast Fourier Transform method. The spectrum is
written}
{to disk as "SPECTDATA.TEXT". This program assumes that the D.C.
component}
{of the signal has been removed prior to A/D conversion. If this
is not the}
{case then program spectrum2 should be used.}
import iodeclarations;
import general_2;
import measurement_lib;

const
    name = 'ADC';
    model = '98640A';
select_code = 18;
    error = 'NO';
    units = 'STANDARD';
multiplier = 1.0;
    offset = 0.0;
    p_size = 1;
    g_size = 1;
    c_size = 1;
    n=512; n1=511; r=9; pi=3.14159265;

type
    r_array = ARRAY[1..15000] of real;
    r_ptr = ^r_array;
    i_array = ARRAY[1..7] of shortint;
    i_ptr = ^i_array;
    complex=record x,y: real end;
    datta = ARRAY[0..n1] of complex;
    c_ptr = ^datta;
    a_array=ARRAY[0..n1] of real;

var

    channel: i_ptr;
    gain: i_ptr;
    pace: r_ptr;
    data: r_ptr;
    d_size,rept,i,m,c,p,nn,gane: integer;
    fmax,time,nsamp,pase,sc,deltaf,gan: real;
    w,a:c_ptr;
    txt:text;
    amp,freq:a_array;

procedure reord(var a:c_ptr);
var
    i,j,k,l: integer;

```

```

        q:complex;
begin
  for i:=1 to n1 do begin
    l:=i;
    k:=0;
    for j:=0 to (r-1) do begin
      k:=(2*k)+1 mod 2;
      l:=l div 2
    end;
    if i<k then begin
      q:=a^[l];
      a^[l]:=a^[k];
      a^[k]:=q
    end
  end
end; {reord}

procedure sum(z,w:complex; var s:complex);
begin
  with s do begin
    x:=z.x+w.x;
    y:=z.y+w.y
  end
end;

procedure dif(z,w:complex; var s:complex);
begin
  with s do begin
    x:=z.x-w.x;
    y:=z.y-w.y
  end
end;

procedure prod(z,w:complex; var s:complex);
begin
  with s do begin
    x:=z.x*w.x-z.y*w.y;
    y:=z.x*w.y+z.y*w.x
  end
end;

procedure neg(u:complex; var w:complex);
begin
  w.x:=-u.x;
  w.y:=-u.y
end;

```

```

procedure trf(var x:c_ptr);

var
  lvl,t1,t11,expon,p,i,j,k:integer;
  s,z:complex;

{t1 = 2^lvl}
{t11=2^(lvl-1)}
{p=2^(r-lvl)}
{expon=j*p}

begin
  t1:=2; t11:=1;
  for lvl:=1 to r do
    begin
      p:=n div t1; expon:=0;
      for j:=0 to t11-1 do
        begin
          i:=j; s:=w^[expon];
          while i<n do
            begin
              k:=i+t11;
              if j=0 then z:=a^[k]
              else prod(a^[k],s,z);
              dif(a^[i],z,a^[k]);
              sum(a^[i],z,a^[i]);
              i:=i+t1
            end;
          expon:=expon+p
        end;
      t1:=2*t1; t11:=2*t11
    end
  end; {trf}

function mag(z:complex):real;
begin
  with z do
    mag:=sqr(x)+sqr(y)
end;

```

```

begin {MAIN PROGRAM}
  new(w);
  new(a);
  writeln('ENTER THE MAXIMUM FREQUENCY COMPONENT OF THE SIGNAL');
  readnumber(1,fmax);
  writeln;
  pase:=(1.0/(2.0*fmax));
  if(pase < 0.000018) then
  begin
    writeln('THE PACE VALUE IS TOO SMALL FOR THE HP-98640A!!');
    writeln('*****');
    writeln('IF ALLOWED TO CONTINUE PACE WILL BE SET TO THE
    VALUE 0.000018');
    pase:=0.000018;
  end;
  if (pase>0.0393336) then
  begin
    writeln('THE PACE VALUE IS TOO LARGE FOR THE HP-98640A!!');
    writeln('*****');
    writeln('IF ALLOWED TO CONTINUE PACE WILL BE SET TO THE VALUE
    0.0393336');
    pase:=0.0393336;
  end;
  writeln('THE PACE RATE ON THE HP-98640A WILL BE SET TO:',pase:9:7);
  writeln;
  d_size:=n;
  writeln('THE NUMBER OF ELEMENTS STORED IS ',d_size:5);
  rept:=d_size;
  writeln;
  deltaf:=(2*fmax)/n;
  writeln('THE FREQUENCY RESOLUTION WILL BE ',deltaf:6:4,' HZ');
  writeln;
  writeln('ENTER THE NUMBER OF SAMPLES TO FORM THE SMOOTHED SPECTRUM');
  writeln;
  readnumber(1,nsamp);
new(channel);
channel^[1]:=1;
new(pace);
pace^[1]:=pase;
new(gain);
writeln('ENTER THE GAIN SETTING FOR THE HP-98640A ADC BOARD');
writeln('THE AVAILABLE CHOICES ARE 1, 8, 64, 512');
writeln;
readnumber(1,gan);
gane:=round(gan);
gain^[1]:=gane;
meas_lib_init;

```



```

config_0(name,model,select_code,1,0.02,error,units,multiplier,offset);
init(name);
sc:=(8*arctan(1)/n);
for i:=0 to n1 do
  with w^[i] do begin
    x:=cos(sc*i);
    y:=sin(sc*i)
  end;
for i:=0 to n1 do begin
  amp[i]:=0.0
end;
  calibrate(name,3,0.0001,1000);
new(data);
for p:=1 to round(nsamp) do begin
  writeln(chr(12));
  writeln('DATA SAMPLING IN PROGRESS***SAMPLE ',p:3,' OF ',nsamp:4:0);
  random_scan(name,c_size,channel,d_size,data
  ,rept,p_size,pase,g_size,gain);
  {APPLY COSINE WINDOWING TO THE SAMPLED DATA}
  for i:=1 to round (d_size/10) do begin
    data^[i]:=data^[i]*(1-cos(5*pi*(i-1)/d_size));
  end;
  for i:=round(9*d_size/10) to d_size do begin
    data^[i]:=data^[i]*(1+cos(5*pi*i/d_size));
  end;
  {ASSIGN REAL DATA TO ONE COMPONENT OF COMPLEX NUMBER "a"}
  for i:=0 to n1 do
    with a^[i] do begin x:=data^[i+1]; y:=0.0 end;
  reord(a);
  trf(a);
  for i:=0 to n1 do begin
    amp[i]:=amp[i]+mag(a^[i])
  end;
end;
rewrite(txt,'V18:SPECTDATA.TEXT');
nn:=round(n/2);
for i:=0 to n1 do begin
  amp[i]:=amp[i]*(2*pase/n)*1.14286;
  amp[i]:=amp[i]/nsamp;
  amp[i]:=amp[i]*1.0E08;
  freq[i]:=i*deltaf;
end;
for i:=0 to nn do begin
  writeln(txt,freq[i]:8:4,'      ',amp[i]:20:17);
end;
close(txt,'SAVE');
end.

```

CORRELATION PROGRAM

```

program corr(input,output);
{This program computes the space-time correlation function between}
{two sampled hot-wire anemometer signals. The time-delay is from }
{minus "tau" to plus "tau" and is user selectable.                }
import iodeclarations;
import general_2;
import measurement_lib;

const
    name = 'ADC';
    model = '98640A';
select_code = 18;
    error = 'NO';
    units = 'STANDARD';
multiplier = 1.0;
    offset = 0.0; p_size = 2; g_size = 1;

type
    r_array = ARRAY[1..15000] of real;
    r_ptr = ^r_array;
    i_array = ARRAY[1..7] of shortint;
    i_ptr = ^i_array;
    corr_array = ARRAY[0..7500] of real;
    corr_ptr = ^corr_array;

var
    data: r_ptr;
    cor, corn: corr_ptr;
    channel: i_ptr;
    gain: i_ptr;
    pace: r_ptr;
    c_size,d_size,rept,n,ns,i,j,k,np,p,msamp: integer;
    fmax,m,time,size,tavg,totaltime,sumsqv1,sumsqv2,sumv1
    ,sumv2,tau,
    meanv1,meanv2,pase1,pase2,samplelength,rms1,rms2,d,rns: real;
    x: text;

begin {MAIN PROGRAM}

    pase1:=0.000025;
    writeln('ENTER THE MAXIMUM FREQUENCY COMPONENT OF THE SIGNAL');
    readnumber(1,fmax);
    writeln;
    writeln('ENTER THE PARAMETER "m" WHICH IS A MULTIPLIER OF THE');
    writeln('MINIMUM PACE RATE REQUIRED TO SATISFY THE NYQUIST
    CRITERION');
    writeln('NOTE: FOR GOOD DISCRETIZATION "m" SHOULD BE AT LEAST 5');
    readnumber(1,m);
    pase2:=(1.0/(1.0*m))*(1.0/(2.0*fmax));
    if(pase2 < 0.000018) then
    begin
        writeln('THE PACE VALUE IS TOO SMALL FOR THE HP-98640A!!');
        writeln('*****');
    end

```

```

writeLn('IF ALLOWED TO CONTINUE PACE WILL BE SET TO THE
VALUE 0.000018');
pase2:=0.000018;
end;
if (pase2 > 0.0393336) then
begin
writeLn('THE PACE VALUE IS TOO LARGE FOR THE HP-98640A!!');
writeLn('*****');
writeLn('IF ALLOWED TO CONTINUE PACE WILL BE SET TO THE
VALUE 0.0393336');
pase2:=0.0393336;
end;
writeLn('THE PACE RATE ON THE HP-98640A WILL BE SET TO:',pase2:9:7);
writeLn;
writeLn('ENTER THE MAXIMUM TIME-LAG (seconds)');
readnumber(1,time);
size:=(time/(pase2+pase1))+1.0;
d_size:=2*round(size);
if (d_size mod 4 = 0) then d_size:=d_size+2;writeLn;
writeLn('d_size:= ',d_size:4);
writeLn;
if (d_size > 7500) then begin
writeLn('THE INCREMENTAL TIME IS TOO LARGE!!');
writeLn('*****');
writeLn('STOP PROGRAM EXECUTION AND RESTART WITH A SMALLER
INCREMENTAL');
writeLn('TIME.....');writeLn;
end;
rept:=round(d_size/2.0);
writeLn('ENTER THE NUMBER OF ENSEMBLES FOR COMPUTING THE AVERAGE');
writeLn('SPACE-TIME CORRELATION FUNCTION');
writeLn;
readnumber(1,rns);
ns:=round(rns);
writeLn;
c_size:=2;
new(channel);
for i:=1 to 2 do begin
channel^[i]:=i
end;
new(pace);
pace^[1]:=pase2;
pace^[2]:=pase1;
new(gain);
gain^[1]:=8;
meas_lib_init;
config_0(name,model,select_code,1,0.02,error,units,multiplier,offset);
init(name);
calibrate(name,3,0.0001,1000);

```

```

new(cor);
new(corn);
new(data);
sumv1:=0.0;
sumv2:=0.0;
sumsqv1:=0.0;
sumsqv2:=0.0;
for i:= 0 to (round(d_size/2)-1) do begin
    cor^[i]:=0.00;
    corn^[i]:=0.00
end;
writeln;
writeln('NOW CALCULATING THE MEAN VOLTAGE TO BE SUBTRACTED FROM ALL');
writeln('TIME SERIES DATA ELEMENTS');
writeln;
writeln('ENTER THE AVERAGING TIME FOR COMPUTING THE MEAN VOLTAGE');
writeln;

```

```

readnumber(1,tavg);
msamp:=round(tavg/((pase1+pase2)*(d_size/2)));
writeln(msamp:3);
for i:= 1 to msamp do begin
    writeln(chr(12));
    writeln;
writeln('MEAN VOLT CALCULATION IN PROGRESS...REPETITION ',i:3,
' OF ',msamp:3);
random_scan(name,c_size,channel,d_size,data,rept,p_size,pase
,g_size,gain);
for j:=1 to (d_size) do begin
    sumv1:=sumv1+data^[j];
    sumv2:=sumv2+data^[j+1];
    sumsqv1:=sumsqv1+sqr(data^[j]);
    sumsqv2:=sumsqv2+sqr(data^[j+1]);
    j:=j+1;
end;
end;
meanv1:=(2.0*sumv1)/(d_size*msamp);
meanv2:=(2.0*sumv2)/(d_size*msamp);
sumsqv1:=(sumsqv1/(((d_size/2.0)*msamp))-(sqr(meanv1)));
sumsqv2:=(sumsqv2/(((d_size/2.0)*msamp))-(sqr(meanv2)));
rms1:=sqrt(sumsqv1);
rms2:=sqrt(sumsqv2);

```

```

writeln('*****BEGIN CORRELATION MEASUREMENT*****');
  for i:=1 to ns do
    begin
      writeln(chr(12));
      writeln;
      writeln('CORRELATION SAMPLE NUMBER ',i:4,' OF ',ns:4);
      random_scan(name,c_size,channel,d_size,data,rept,p_size,pace
,g_size,gain);
      for k:=1 to (d_size-1) do begin
        data^[k]:=data^[k]-meanv1;
        data^[k+1]:=data^[k+1]-meanv2;
        k:=k+1;
      end;

      for k:= 0 to (round(d_size/2)-1) do begin
        p:=1;
        for j:=1 to (round(d_size/2)-k) do begin
          cor^[k]:=cor^[k]+data^[p]*data^[p+(2*k)+1];
          p:=p+2;
        end;
      end;
      for k:=0 to (round(d_size/2)-2) do begin
        p:=2;
        for j:=1 to (round(d_size/2)-k-1) do begin
          corn^[k]:=corn^[k]+(data^[p]*data^[p+(2*k)+1]);
          p:=p+2;
        end;
      end;
    end;
  end;
  for k:= 0 to (round(d_size/2)-1) do begin
    cor^[k]:=cor^[k]/(ns*((d_size/2)-k))/(rms1*rms2);
  end;
  for k:=0 to (round(d_size/2)-2) do begin
    corn^[k]:=corn^[k]/(ns*((d_size/2)-1-k))/(rms1*rms2);
  end;
  for k:=0 to(round(d_size/2)-1) do begin
    cor^[k+round(d_size/2)]:=cor^[k];
  end;
  {SHIFT DATA ONE ELEMENT TO THE LEFT}
  for k:=(round(d_size/2)-1) to (d_size-2) do begin
    cor^[k]:=cor^[k+1]
  end;
  for k:=0 to (round(d_size/2)-2) do begin
    cor^[k]:=corn^[round(d_size/2)-2-k];
  end;

```

```
    end;
rewrite(x,'V20:CORRDATA.TEXT');
tau:=-((d_size/2)-1)*(pase1+pase2);
np:=d_size-1;
writeln(x,np);
for k:=0 to d_size-2 do begin
writeln(x,tau:9:6,'    ',cor^[k]:7:4);
tau:=tau+(pase2+pase1);
end;
close(x,'SAVE');
end.
```

COHERENCE PROGRAM

```

program COHERENCE(input,output);
{This program uses the FFT method to compute the coherence}
{function between two sampled anemometer signals}
import iodeclarations;
import general_2;
import measurement_lib;

const
    name = 'ADC';
    model = '98640A';
    select_code = 18;
    error = 'NO';
    units = 'STANDARD';
    multiplier = 1.0;
    offset = 0.0;
    p_size = 2;
    q_size = 1;
    c_size = 2;
    n=256;
    n1=255;
    r=8;
    pi=3.14159265;

type
    r_array = ARRAY[1..2*n] of real;
    r_ptr = ^r_array;
    i_array = ARRAY[1..7] of shortint;
    i_ptr = ^i_array;
    complex=record x,y: real end;
    datta = ARRAY[0..(2*n)-1] of complex;
    c_ptr = ^datta;
    a_array=ARRAY[0..n1] of real;
    l_array=ARRAY[1..n] of real;

var
    channel: i_ptr;
    gain: i_ptr;
    pace: r_ptr;
    data: r_ptr;
    d_size,rept,i,j,m,c,p,msamp,k: integer;
    fmax,time,nsamp,pase1,pase2,sc,sumv1,sumv2,meanv1,meanv2
    ,temp,tau,
    f:real;
    w,a,b,g:c_ptr;
    txt:text;
    theta,sumx,sumy,gxy,gx,gy,gamma:a_array;
    q,qq:complex;
    v:l_array;

procedure reord1(var a:c_ptr);
var

```

```

    i,j,k,l:integer;
    q:complex;
begin
  for i:=1 to n1 do begin
    l:=i;
    k:=0;
    for j:=0 to (r-1) do begin
      k:=(2*k)+1 mod 2;
      l:=l div 2
    end;
    if i<k then begin
      q:=a^[i];
      a^[i]:=a^[k];
      a^[k]:=q
    end
  end
end; {reord1}

procedure reord2(var b:c_ptr);
var
  i,j,k,l:integer;
  q:complex;
begin
  for i:=1 to n1 do begin
    l:=i;
    k:=0;
    for j:=0 to (r-1) do begin
      k:=(2*k)+1 mod 2;
      l:=l div 2
    end;
    if i<k then begin
      q:=b^[i];
      b^[i]:=b^[k];
      b^[k]:=q
    end
  end
end; {reord2}

procedure sum(z,w:complex; var s:complex);
begin
  with s do begin
    x:=z.x+w.x;
    y:=z.y+w.y
  end
end;

```



```

procedure dif(z,w:complex; var s:complex);
begin
with s do begin
  x:=z.x-w.x;
  y:=z.y-w.y
end
end;

procedure prod(z,w:complex; var s:complex);
begin
with s do begin
  x:=z.x*w.x-z.y*w.y;
  y:=z.x*w.y+z.y*w.x
end
end;

procedure neg(u:complex; var w:complex);
begin
  w.x:=-u.x;
  w.y:=-u.y
end;

procedure trfl(var x:c_ptr);

var
  lvl,tl,tll,expon,p,i,j,k:integer;
  s,z:complex;

{tl = 2^lvl}
{tll=2^(lvl-1)}
{p=2^(r-lvl)}
{expon=j*p}

begin
tl:=2; tll:=1;
for lvl:=1 to r do
  begin
  p:=n div tl; expon:=0;
  for j:=0 to tll-1 do
    begin
    i:=j; s:=w^[expon];
    while i<n do
      begin
      k:=i+tll;
      if j=0 then z:=a^[k]
      else prod(a^[k],s,z);
      dif(a^[il],z,a^[k]);
      sum(a^[il],z,a^[il]);
      i:=i+tl
      end;
      expon:=expon+p
    end;
  tll:=2*tll; tll:=2*tll
  end
end

```

```

end: {trf1}

procedure trf2(var x:c_ptr);

var
  lvl,tl,tll,expon,p,i,j,k:integer;
  s,z:complex;

{tl = 2^lvl}
{tll=2^(lvl-1)}
{p=2^(r-lvl)}
{expon=j*p}

begin
  tl:=2; tll:=1;
  for lvl:=1 to r do
    begin
      p:=n div tl; expon:=0;
      for j:=0 to tll-1 do
        begin
          i:=j; s:=w^[expon];
          while i<n do
            begin
              k:=i+tll;
              if j=0 then z:=b^[k]
              else prod(b^[k],s,z);
              dif(b^[i],z,b^[k]);
              sum(b^[i],z,b^[i]);
              i:=i+tl
            end;
            expon:=expon+p
          end;
          tll:=2*tll; tll:=2*tll
        end
      end
    end
  end: {trf2}

procedure conj(u:complex; var w:complex);
begin
  w.x:=u.x;
  w.y:=-u.y
end:

function mag(z:complex):real;
begin
  with z do
    mag:=sqr(x)+sqr(y)
  end:
end:

```

```

begin {MAIN PROGRAM}
  new(w);
  new(a);
  new(data);
  new(b);
  new(g);
  writeln('ENTER THE MAXIMUM FREQUENCY COMPONENT OF THE DATA (HZ)');
  writeln;
  readnumber(1,fmax);
  writeln;
  pase1:=0.000025;
  pase2:=1.0/(2.0*fmax);
  d_size:=2*n;
  writeln('THE TOTAL NUMBER OF ELEMENTS STORED IS ',d_size:5);
  writeln;
  rept:=n;
  writeln('ENTER THE NUMBER OF SAMPLES TO FORM THE AVERAGE
  COHERENCE');
  writeln;
  readnumber(1,nsamp);
new(channel);
for i:= 1 to 2 do
begin
  channel^[i]:=i
end;
new(pace);
pace^[1]:=pase2;
pace^[2]:=pase1;
new(gain);
gain^[1]:=8;
meas_lib_init;
config_0(name,model,select_code,1,0.02,error,units,multiplier,offset);
init(name);
calibrate(name,3,0.0001,1000);
sc:=(8*arctan(1)/n);
for i:=0 to n1 do
  with w^[i] do begin
    x:=cos(sc*i);
    y:=sin(sc*i)
  end;
writeln('* * * * *');
writeln('NOW CALCULATING THE MEAN VOLTAGE TO BE SUBTRACTED FROM ALL');
writeln('TIME SERIES DATA ELEMENTS');
writeln('* * * * *');
writeln;
writeln('ENTER THE AVERAGING TIME FOR COMPUTING THE MEAN VOLTAGE');
writeln;
readnumber(1,time);

```

```

msamp:=round((2*time)/((pase1+pase2)*d_size));
sumv1:=0.0;
sumv2:=0.0;
for i:= 1 to msamp do begin
    writeln(chr(12));
    writeln;
    writeln('MEAN VOLT CALCULATION IN PROGRESS...REPETITION ',i:3
,' OF',msamp:3);
    random_scan(name,c_size,channel,d_size,data,rept,p_size,pace
,g_size,gain);
    for j:=1 to (d_size-1) do begin
        sumv1:=sumv1+data^[j];
        sumv2:=sumv2+data^[j+1];
        j:=j+1;
    end;
end;
meanv1:=(2.0*sumv1)/(d_size*msamp);
meanv2:=(2.0*sumv2)/(d_size*msamp);
{*****}
for k:=0 to ni do begin
    gxy[k]:=0.0;
    gx[k]:=0.0;
    gy[k]:=0.0;
    theta[k]:=0.0;
    gamma[k]:=0.0;
end;
for p:=1 to round(nsamp) do begin
    writeln(chr(12));
    writeln('*****');
    writeln('COHERENCE MEASUREMENT IN PROGRESS.....');
    writeln('SAMPLE ',p:3,' OF ',nsamp:4:0);
    writeln('*****');
    writeln;
    random_scan(name,c_size,channel,d_size,data,rept,p_size,pace
,g_size,gain);
    for i:=1 to (d_size-1) do begin
        data^[i]:=data^[i]-meanv1;
        data^[i+1]:=data^[i+1]-meanv2;
        i:=i+1;
    end;
    i:=1;
    for j:=1 to round(d_size/2) do begin
        v[j]:=data^[i];
        i:=i+2;
    end;
    for i:=1 to round(d_size/20) do begin
        v[i]:=v[i]*(1-cos(10*pi*(i-1)/d_size));
    end;
    for i:=round(9*d_size/20) to round(d_size/2) do begin
        v[i]:=v[i]*(1+cos(10*pi*i/d_size));
    end;
    i:=1;
    for j:=1 to round(d_size/2) do begin
        data^[i]:=v[j];

```

```

i:=i+2      end;
i:=1;
for j:=1 to round(d_size/2) do begin
v[j]:=data^[i+1];
i:=i+2
end;
for i:=1 to round(d_size/20) do begin
v[i]:=v[i]*(1-cos(10*pi*(i-1)/d_size));
end;
for i:=round(9*d_size/20) to round(d_size/2) do begin
v[i]:=v[i]*(1+cos(10*pi*i/d_size));
end;
i:=1;
for j:=1 to round(d_size/2) do begin
data^[i+1]:=v[j];
i:=i+2
end;

j:=1;
for i:=0 to n1 do begin
with a^[i] do begin x:=data^[j]; y:=0.0; j:=j+2 end;
end;

j:=1;
for i:=0 to n1 do begin
with b^[i] do begin x:=data^[j+1]; y:=0.0; j:=j+2 end;
end;

reord1(a);
trf1(a);
reord2(b);
trf2(b);
for k:=0 to n1 do begin
gx[k]:=gx[k]+mag(a^[k]);
gy[k]:=gy[k]+mag(b^[k]);
end;
for i:=0 to n1 do begin
conj(a^[i],q);
prod(q,b^[i],g^[i]);
with g^[i] do begin sumx[i]:=sumx[i]+x;
sumy[i]:=sumy[i]+y end;
end;
end;
for i:=0 to n1 do begin
gxy[i]:=sqrt(sqrt(sumx[i])+sqrt(sumy[i]));
theta[i]:=arctan(sumy[i]/sumx[i]);
end;
writeln;
for k:=0 to n1 do begin
gx[k]:=gx[k]*(2*pase2/n)*1.14286*1/nsamp;
gy[k]:=gy[k]*(2*pase2/n)*1.14286*1/nsamp;
gxy[k]:=gxy[k]*(2*pase2/n)*1.14286*1/nsamp;
gamma[k]:=sqrt(gxy[k])/(gx[k]*gy[k]);
end;

```

```
rewrite(txt,'V20:COHERENCE.TEXT');
for j:=0 to round(n/2) do begin
f:=j/(n*pase2);
writeln(txt,f:9:6,' ',gamma[j]:9:6);
end;
close(txt,'SAVE');
rewrite(txt,'V20:FAZE.TEXT');
for j:=0 to round(n/2) do begin
f:=j/(n*pase2);
writeln(txt,f:9:6,' ',theta[j]:9:6);
end;
close(txt,'SAVE');
end.
```

APPENDIX B
UNCERTAINTY ANALYSIS

In order to determine the experimental uncertainties associated with measurements performed in this investigation, an analysis based on the method of Kline and McClintock (1953) was used. The following results were obtained:

1. Uncertainty in setting the Reynolds Number

$$Re_D = \pm 3.6\%$$

2. Uncertainty in Mean Velocity Measurements

$$U = U \pm 2.5\%$$

3. Uncertainty in RMS Velocity Measurements

$$\sqrt{\overline{u^2}} = \pm 5\%$$

4. Uncertainty in Correlation Coefficients

$$\rho = \pm 8\%$$

VITA

Kombupalayam Malayanan Kumaravel Prakash

Candidate for the Degree of

Master of Science

Thesis: AN EXPERIMENTAL INVESTIGATION OF A RESONANCE MECHANISM IN A
TWO-DIMENSIONAL TURBULENT JET

Major Field: Mechanical Engineering

Biographical:

Personal Data: Born in Madras, India, September 23, 1961, the son
of Mr. and Mrs. Malayanan

Education: Graduated from Don Bosco Matriculation High School,
Madras, India, May 1978; received the Bachelor in Engineering
in Mechanical Engineering degree from Anna University, May
1984; completed the requirements for Master of Science degree
at Oklahoma State University, May 1986.

Professional Experience: On the job training as a Manufacturing
Engineer at Engineering Products and Services, 1983; Teaching
Assistant, Oklahoma State University, School of Mechanical
Engineering, September 1984 - May, 1985; Research Assistant at
Oklahoma State University, School of Mechanical Engineering,
May 1985 - May 1986.